10-16-2014 12:00 AM

Quantitative MRI correlates of hippocampal and neocortical pathology in intractable temporal lobe epilepsy

Maged Goubran
The University of Western Ontario

Supervisor
Terry Peters
The University of Western Ontario

Graduate Program in Biomedical Engineering
A thesis submitted in partial fulfillment of the requirements for the degree in Doctor of Philosophy

QUANTITATIVE MRI CORRELATES OF HIPPOCAMPAL AND NEOCORTICAL PATHOLOGY IN INTRACTABLE TEMPORAL LOBE EPILEPSY

(Thesis format: Integrated article)

by

Maged Goubran

Graduate Program in Biomedical Engineering

A thesis submitted in partial fulfillment
of the requirements for the degree of
Doctor of Philosophy

The School of Graduate and Postdoctoral Studies
The University of Western Ontario
London, Ontario, Canada

Abstract

Intractable or drug-resistant epilepsy occurs in over 30% of epilepsy patients, with many of these patients undergoing surgical excision of the affected brain region to achieve seizure control. Advances in MRI have the potential to improve surgical treatment of epilepsy through improved identification and delineation of lesions. However, validation is currently needed to investigate histopathological correlates of these new imaging techniques. The purpose of this work is to investigate histopathological correlates of quantitative relaxometry and DTI from hippocampal and neocortical specimens of intractable TLE patients. To achieve this goal I developed and evaluated a pipeline for histology to *in-vivo* MRI image registration, which finds dense spatial correspondence between both modalities. This protocol was divided in two steps whereby sparsely sectioned histology from temporal lobe specimens was first registered to the intermediate *ex-vivo* MRI which is then registered to the *in-vivo* MRI, completing a pipeline for histology to *in-vivo* MRI registration. When correlating relaxometry and DTI with neuronal density and morphology in the temporal lobe neocortex, I found T1 to be a predictor of neuronal density in the neocortical GM and demonstrated that employing multi-parametric MRI (combining T1 and FA together) provided a significantly better fit than each parameter alone in predicting density of neurons. This work was the first to relate in-vivo T1 and FA values to the proportion of neurons in GM. When investigating these quantitative multimodal parameters with histological features within the hippocampal subfields, I demonstrated that MD correlates with neuronal density and size, and can act as a marker for neuron integrity within the hippocampus. More importantly, this work was the first to highlight the potential of subfield relaxometry and diffusion parameters (mainly T2 and MD) as well as volumetry in predicting the extent of cell loss per subfield pre-operatively, with a precision so far unachievable. These results suggest that high-resolution quantitative MRI sequences could impact clinical practice for pre-operative evaluation and prediction of surgical outcomes of intractable epilepsy.

Keywords: Temporal lobe epilepsy, MRI, histology, correlation, hippocampus, relaxometry, DTI, neuronal density

If our brains were simple enough for us to understand them, we'd be so simple that we couldn't.

Ian Stewart

Acknowlegements

I cannot be more grateful to my supervisor, Terry Peters, for introducing me to the world of neuroimaging and image guided interventions, and for the continuous support and encouragement throughout my summer internships and graduate years. I am very thankful for providing me with the opportunity to work on this exciting project and perform cutting edge research at Robarts, for providing all the possible resources a student can ask for to succeed, and for his superb mentorship personally and professionally.

I also want to emphasize how grateful I am to Ali Khan -then post-doctoral fellow, now professor- who for the past three years mentored me and micromanaged the project on daily-basis. I am very thankful for all the knowledge, whether technical or research methodology, that he shared with me over the past years, for directing all aspects of the project to reach its current form, for his constant guidance and for being an exceptional mentor and friend.

Deep admiration and gratitude to the patients who, despite the difficult times they are going through and their debilitating disease, agreed to undergo lengthy and often-times multiple scanning sessions and agreed as well for their resected specimens to be imaged and processed through our research pipeline.

I would also like to thank Catherine Currie and Cathie Crukley for managing the tedious work of handling the tissue and histological processing, and for all their technical support during the project. Moreover, I want to greatly thank Trevor Szekeres for scanning the patients and for teaching me how to operate a magnet, Joe Gati for his guidance and help in developing a 7T protocol and troubleshooting/testing the sequences, and David Rudko for his help on the QSM project.

This thesis would not have been in this form if it was not for our many, outstanding, clinical collaborators, specifically: Sandrine de Ribaupierre, Rob Hammond, Seyed Mirsattari, Jorge Burneo, David Steven, Andrew Parrent and Jonathan Lau. I am thankful for your openness to novel research methodologies, for the many hours you put in developing the project and teaching me the clinical aspects of epilepsy, and for your feedback to improve the quality of this thesis. Many thanks to Aaron Ward for being on my committee and for his continuous encouragement. In addition, I want to thank the summer students, Brendan Santyr and Susan Buchanan, for all their hard work on the project.

I would like to thank the CIHR and NSERC agencies for financial support.

Furthermore, I would like to mention all my colleagues at the Peters VASST lab specifically: Martin Rajchl, Abraam Soliman, Kamyar Abhari, Golafsoun Ameri, and the epilepsy team: Diego Cantor, Charlotte Blinston and Jonathan Mcleod for sharing the ups and downs along the way and for sharing their knowledge with me; and John Moore, Elvis Chen and Chris Wedlake, for providing a collaborative work environment in the lab and for their support.

The biggest thank you goes to my mom and my sister who have been the pillars in my life. Without you I would not have had the chance to get here and I owe my success to your love. Lastly, words cannot express my gratitude to my close friends (whether in Canada or Egypt) and girlfriend for their immense care and support.

Contents

Abstract ii

Acknowlegements iii

List of Figures x

List of Tables xvii

List of Abbreviations, Symbols, and Nomenclature xx

1 I Introduction & Background 1
- 1.1 Temporal Lobe Epilepsy . . . 1
- 1.2 Epilepsy surgery . . . 3
  - 1.2.1 Temporal lobe function, anatomy and connections . 3
  - 1.2.2 Anterior Temporal Lobectomy . . . 7
- 1.3 Pathological substrates of TLE . . . 9
  - 1.3.1 Hippocampal sclerosis . . . 9
  - 1.3.2 Malformations of cortical development . . . 10
- 1.4 Diagnostic techniques for pre-operative evaluation . . . 12
  - 1.4.1 Electroencephalography . . . 12
  - 1.4.2 Imaging modalities . . . 14
  - 1.4.3 Magnetic Resonance Imaging . . . 14
    - MRI in epilepsy . . . 18
  - 1.4.4 Novel MRI techniques . . . 20
    - Diffusion Tensor Imaging . . . 20
    - Functional MRI . . . 24
    - Quantitative Susceptibility Mapping . . . 26
    - High resolution 3D Relaxometry . . . 26
- 1.5 MRI-Histology correlation . . . 28
- 1.6 Image Registration . . . 30
- 1.7 Thesis objectives . . . 32
- 1.8 Thesis outline . . . 32
  - 1.8.1 Chapter II Histology to *ex-vivo* registration . . . 33

1.8.2 Chapter III *in-vivo* to *ex-vivo* registration, Histology to *in-vivo* pipeline . . . 33
1.8.3 Chapter IV MRI-Histology neocortical correlation 34
1.8.4 Chapter V MRI-Histology hippocampal correlation 34
1.8.5 Chapter VI Conclusions and future work . . . 35
1.8.6 Appendix A Quantitative Atlas of hippocampal subfields . . . 35

2 II Registration of Histology to Ex-vivo MRI 51
2.1 Introduction . . . 51
2.2 Methods & Materials . . . 55
2.2.1 Recruitment, surgery & specimen acquisition . . . 55
2.2.2 Specimen *ex-vivo* MR Imaging . . . 56
Scan Protocol I . . . 58
Scan Protocol II . . . 58
2.2.3 Histological processing . . . 59
2.2.4 Image registration . . . 60
2.2.5 Iterative registration algorithm . . . 63
MR image pre-processing . . . 64
Histology image pre-processing . . . 67
Rigid registration . . . 67
Non-rigid registration . . . 68
Coregistration of additional staining . . . 69
2.2.6 Registration validation . . . 70
Landmark-based validation . . . 70
Localization error and statistical analysis . . . 71
2.3 Results . . . 73
2.4 Discussion . . . 75

3 III Registration of Ex-vivo to In-vivo MRI 88
3.1 Introduction . . . 88
3.2 Methods & Materials . . . 90
3.2.1 Recruitment, surgery & specimen acquisition . . . 90
3.2.2 Patient *in-vivo* MR imaging & map generation . . . 92
3.2.3 Specimen *ex-vivo* MR imaging . . . 94
3.2.4 Histological processing . . . 96
3.2.5 Image registration . . . 96
Initialization . . . 98
Landmark-based similarity transformation . . . 100
Non-rigid registration: Hippocampus . . . 101
Non-rigid registration: Neocortex . . . 104

In-vivo MRI to Histology registration 105
3.2.6 Registration validation & statistical analysis 105
3.3 Results 107
3.4 Discussion 112

4 IV Correlation of Neocortical MRI and histology 123
4.1 Introduction 123
4.2 Materials & Methods 125
4.2.1 Patients and Samples 125
4.2.2 *In-vivo* Magnetic Resonance Imaging 125
4.2.3 Histological processing and quantitative histology . 127
4.2.4 ROI Placement and Image Registration 129
4.2.5 Statistical analysis 133
4.3 Results 134
4.3.1 MRI parameters-Histology features correlation . . 134
4.3.2 Multivariate vs. univariate MRI 134
4.3.3 Correlation with clinical variables 138
4.3.4 MRI-MRI parameters correlation 138
4.3.5 Histology-Histology features correlation 138
4.4 Discussion 139
4.4.1 Neurobiological interpretations and considerations 139
4.4.2 Benefit of registration-based correlation 144
4.4.3 Limitations and future work 145

5 V Correlation of Hippocampal MRI and histology 154
5.1 Introduction 154
5.2 Materials & Methods 156
5.2.1 Patients and Samples 156
5.2.2 *In-vivo* MRI and Qualitative classification 157
5.2.3 Histological processing and quantitative histology . 157
5.2.4 Histology subfields segmentation 160
5.2.5 MRI subfields segmentation 162
5.2.6 Statistical analysis 164
5.3 Results 166
5.3.1 MRI-histology correlation analysis 167
5.3.2 Correlations with clinical variables 167
5.3.3 Multiple linear regressions 170
5.3.4 Discriminant function analysis 172
5.4 Discussion 175
5.4.1 Biological Interpretations 175
5.4.2 Clinical findings and insights 177

5.4.3 Limitations and technical considerations 179

6 VI Conclusions and future work **188**
6.0.4 Current Limitations & Future Directions 190

A App. A - In vivo atlas of the hippocampal subfields **194**
A.1 Introduction 194
A.2 Methods 197
A.2.1 Materials & Imaging 197
A.2.2 MRI Phase Processing 198
A.2.3 Susceptibility Weighted Image Calculation 199
A.2.4 Quantitative Susceptibility Maps 200
A.2.5 Subfield Labeling 202
A.2.6 Average Atlas construction 204
A.2.7 R2* validation 205
A.2.8 Quantitative susceptibility validation 206
A.2.9 Statistical comparison 206
A.3 Results 207
A.4 Discussion & conclusion 212

Copyright Licenses **229**

CV **243**

List of Figures

1.1 Anatomy of the temporal lobe highlighting some of its prominent structures: the hippocampus, parahippocampal gyrus, uncus, fimbria and fornix. These images are modified from the original work of Henry Gray's anatomy: "Gray739", "Gray747" and "Gray 740". Licensed under Public domain via Wikimedia Commons. 5

1.2 Characterization of the hippocampus into different subfields (CA1-4,DG and subiculum). Left: Delineation of the subfields on a high field 7T MRI average (Top) and NeuN IHC (bottom). Right: 3D surface rendering of the hippocampus with the subfield segmentations of the hippocampal body. . 6

1.3 Comparison of normal and pathologic hippocampi, presenting hippocampal sclerosis on a FLAIR MRI scan and a histology NeuN IHC. Hippocampal atrophy and increased T_2-weighted signal are visible on the FLAIR image and prominent neuronal loss within the different subfields specifically CA1, CA3 and CA4 is visible on the histology slide. 10

1.4 Example visualization of the diffusion maps FA and MD (with the first eigen vector overlaid on the maps), as well as fibers from deterministic (bottom left) and probabilistic tractography (bottom right) of the cortico-spinal tract. . . . 23

1.5 Comparison of MRI T_1 & T_2-weighted images (acquired at 1.5T & 3T) and relaxometry maps of the same subject. . . 28

2.1 Example of encountered deformations. Red arrows represent cortical sulci on the pre-operative MRI and blue arrows represent the corresponding sulci on the resected neocortex specimen. a) Photograph of surgical view before resection, b) Volume rendering of a pre-operative MRI of the patient with a zoomed view showing the temporal pole, c) Coronal view of the pre-operative MRI demonstrating temporal gyri with red arrows, d) Photograph of the temporal lobe neocortex post resection, e) Surface rendering of the resected neocortex with blue arrows showing the corresponding sulci to part b), and f) Coronal view of the *ex-vivo* MRI with blue arrows indicating sulci corresponding to part c); the small window in the top left corner demonstrates the mesial (interior) side of the neocortex with an intersection of the shown MRI slice. 53

2.2 Overview of histological processing from specimen generation to digitization. Processed performed at in a standard clinical work flow at the hospital are included in dashed boxes. 61

2.3 Registration pipeline showing pre-processing steps of the data and our iterative 2D-3D approach. The left column demonstrates the pre-processing steps applied to the histology slides sequentially from top to bottom. Likewise, the right column represents the pre-processing steps applied to the MRI of the specimens. The resulting histology stack acts as a fixed image to transform the MR image in a 3D rigid registration. The transformed image as well as the stack are split into slices 4.4 mm apart where each histology slice has a corresponding MRI slice. These MR slices act as fixed images to deform the histology slices rigidly then non-rigidly. The resulting deformed histology slices are stacked and fed back into the 3D rigid registration for the next iteration. 66

2.4 Example of the chosen intrinsic landmarks on histology and their localized corresponding landmark on a neocortical *ex-vivo* MRI specimen. The arrows in blue pinpoint the micro vasculature used as targets for the TLE calculations on both histology and MRI. A zoomed in window demonstrates the targets on both modalities with cross hairs indicating the target coordinates on MRI and a circle showing the chosen coordinates on histology. 70

2.5 3D visualization revealing the wide spatial distribution of validation landmarks (blue spheres) within an exemplar neocortical specimen in sagittal and coronal views. 72

2.6 Boxplots with 5-95% whiskers of Hippocampal and Neocortical registration target registration errors at each stage of the iterative registration scheme. 76

2.7 Example of a neocortex rigid and deformable registration showing: a) photograph of a neocortical specimen after resected with orientation labels placed by the operating surgeon, b) volume rendering of the MRI of the specimen showing the location of three consecutive histology slices. c) rendering of both sides of the specimen where the middle slice of histology was cut, d) the three histology slices shown in b), e) the corresponding MRI slices after 3D rigid registration, and f) the deformed histology slices after non-rigid registration to their corresponding MRI slices. 77

2.8 Example of a hippocampal rigid and deformable registration showing: a) photograph of a hippocampus before grossing, b) volume rendering of the MRI of the hippocampus demonstrating the location of a histology slice through the specimen, c) rendering of both sides of the hippocampus where the histology slice was cut, and d) three orthogonal views of the hippocampal MRI (left to right: coronal, sagittal, axial). The bottom row depicts: e) a coronal view of the same histological slice with a registration mask over a breakage region shown in blue, f) a checkerboard image showing the MRI and histology before non-rigid registration, and g) a checkerboard image showing the MRI and non-rigidly deformed histology slice. 78

3.1 In-vivo MRI to histology registration scheme depicting the transformations obtained through each registration step and the resulting images. 99

3.2 Landmark placement for *in-vivo* to *ex-vivo* registration of hippocampal specimens. a) An example hippocampus before grossing. b) Surface rendering of the *ex-vivo* MR of the specimen. c) Distribution of landmarks (green) within the volume of the specimen. d) Three pairs of corresponding landmarks chosen on orthogonal planes of *in-vivo* (blue) and *ex-vivo* (red) images. 102

3.3 Landmark placement for rigid registration of neocortical specimens. The white arrows point to homologous points and their corresponding gyri. a) Neocortex specimen before grossing. b) Volume rendering of the *in-vivo* MR image of the patient with registration landmarks overlaid on top (red). c) Surface rendering of the *ex-vivo* MR image of the specimen with registration landmarks overlaid on top (blue). 103

3.4 Boxplots with standard deviation of Hippocampal and Neocortical registration target registration errors at rigid and non-rigid registration stages. 108

3.5 Comparison of landmark-based rigid and non-rigid registrations for the hippocampus. The white arrows depict areas where deformable registration outperformed rigid registration. a) Cropped *in-vivo* MR image, I_c, b) Rigidly registered *ex-vivo* specimen (purple), c) Merged view of rigidly registered *ex-vivo* to *in-vivo* image, d) Non-rigidly registered *ex-vivo* specimen (red), e) Merged view of non-rigidly registered *ex-vivo* to *in-vivo* image, f) Difference in shape and volume between the hippocampus specimen after rigid transformation and deformable warping. 110

3.6 Comparison of landmark-based rigid and non-rigid registrations for the neocortex. The white arrows depict areas where deformable registration outperformed rigid registration. a) Cropped *in-vivo* MR image, I_c, b) Rigidly registered *ex-vivo* specimen, c) Merged view of rigidly registered *ex-vivo* to *in-vivo* image, d) Non-rigidly registered *ex-vivo* specimen, e) Merged view of non-rigidly registered *ex-vivo* to *in-vivo* image. 111

3.7 Mapping of *in-vivo* MR images to the *aligned* space for a neocortical specimen. The spatial resolution decreases vertically (top to bottom) in the figure. The top row depicts the *ex-vivo* MR (left) and three stains of a histological section (right). The 2^{nd}, 3^{rd} and 4^{th} rows show warped images taken at 7, 3 and 1.5 Tesla respectively. The last row demonstrates warped diffusion maps (FA= fractional anisotropy, MD= mean diffusivity). 113

3.8 3D histological reconstruction and registration to MR. a) A resected temporal lobe neocortical specimen from epilepsy surgery. b) Rendering of the specimen from a 9.4T MR image registered to histological slices. c) 3D consecutive histology slices in the MR space. d) Rendering of both sides of the specimen where a histology slice was cut. e) Registered MRI slice to the cut histology slice. Four different immunohistochemistry and staining techniques are shown as well for the cut histology section: f) Hematoxylin & Eosin (H&E), g) Neuronal Nuclei (NeuN), h) Microtubule associated protein (MAP)2 and i) Luxol fast blue (LFB). . 115

4.1 Histological processing and semi-quantitative features extraction, for both NeuN and GFAP IHC stains. 129

4.2 ROI placement and MRI parameters extraction. A) Grey matter and white ROI on 100um H&E histology slice in histology native space. B) Registered ex-vivo MRI slice corresponding to the histology slice in Hist3D space. C) Warped ROIs overlaid on the registered and obliquely resampled T1 map in Hist3D space where MRI parameters extraction is performed. The registered histology slice is shown in the top left corner. D) Warped ROIs in the native in-vivo MRI space overlaid on three consecutive slices of the T1 map for illustration purposes. 132

4.3 Overview of our registration pipeline depicting registration results and the four different spaces of MRI and histology including the intermediate Hist 3D space where reconstructed histology slices are stacked parallel to the A-P axis. 132

4.4 Relationships between quantitative MRI parameters (T1 and FA) and neuronal density in GM (Top left: Total neuronal density, Top right: Neuronal density for small-caliber neurons, Bottom: Neuronal density for large-caliber neurons). 135

4.5 Representation of T1-FA multi-parametric space, revealing that combining T1 and FA provides better discrimination of normal and abnormal neuron density in neocortical grey matter. Each dot in this plot refers to a grey matter ROI on a histology slide, with representative dots being labeled with patient IDs from Table 1. It is clear from the figure that low and high neuron densities are not well separated when using T1 or FA (see projections on horizontal and vertical axes), but in the two-dimensional space the data demonstrate are more clearly separable (demonstrated by the dashed line), suggesting that multivariate or multiparametric analysis would be more beneficial in predicting or classifying pathology in-vivo. Since the presented ROIs are extracted from sparsely sectioned histology slices (4 mm apart), this figure highlights the potential of imaging parameters in detecting local pathology within the neocortex. 137

4.6 Significant relationships between diffusion and relaxometry MRI parameters, as well as the association between neuronal density and NeuN field fraction. 140

4.7 Summary of MRI parameters and histological features correlations in both tissues of the temporal lobe neocortex, along with possible neurobiological explanations for the highlighted relations. 143

5.1 Overview of some of the quantitative histological features including: neuron density (for both CA and DG), mean neuron size, and GFAP field fraction. 160

5.2 Subfield delineation on histology slices from three patients from our cohort (Top: Mild sclerosis, Middle: Moderate sclerosis, Bottom: Severe sclerosis). The labeling scheme (colour representing each subfield) is described at the bottom of the figure. 163

5.3 In-vivo MRI parameter extraction scheme. A target region was chosen around the corresponding (registered) MRI slice to the cut histology slice for parameter extraction. Manual segmentation of the subfields was employed within the target region and a sagittal weighting kernel was applied, whereby slices closer to the corresponding MRI slice in the sagittal plane had higher weighting. 165

5.4 Boxplots of in-vivo MRI parameters (Volume, T1, T2, FA and MD) as well as histological neuronal density categorized by the qualitative HS subtype classification. 168
5.5 Most significant associations from Spearman's correlation analysis for subfield-specific MRI parameters with histological features. 171
5.6 Multiple linear regression results for subfield-specific parameters depicting predicted vs. actual percent neuron loss for each of the four CA subfields. 173

A.1 Single subject (Middle) as well as atlas-based images of average magnitude across echoes (Top Left), R2* (Top Right), qualitative SWI (Bottom Left) and QS maps (Bottom Right). The adjacent image to each map shows a zoomed-in representation of a hippocampal slice in the coronal view. The same slice is chosen for all maps to compare CNR and SNR across the different maps. 208
A.2 Two sets of three consecutive coronal slices as seen in atlas space in the magnitude across echoes, R2* and QS maps, with the top row of each block showing segmentation labels overlaid on the images. The location of the slices is indicated on a sagittal view of the hippocampus at the top of the figure. 211
A.3 Validation of pre-operative R2* with 9.4T ex-vivo imaging of a resected hippocampus. Left: Coronal slice of the pre-op R2* at 7T with a zoomed-in view of the sclerotic hippocampus before epilepsy surgery excision. Middle: Magnitude image of the patient's resected hippocampus imaged at 9.4T resulting in a 0.1 mm isotropic resolution (top); R2* image of the hippocampus, where the subfield delineation was performed (bottom). Right: Graph of comparison between pre-op (blue) and ex-vivo (purple) R2* values within the subfields. 214
A.4 Figure 4. Validation of our QS values in the basal ganglia with Deistung et al. [31] and Wharton and Bowtell [32]. Left: Axial slice of a QS map from a single subject showing the outlines of the basal ganglia structures. Right: Graph demonstrating QS values within the basal ganglia for three papers. 215

List of Tables

2.1 Summary of demographics and clinical data, including MRI and histopathological findings, for the seven recruited patients in the study. Registration was performed on both hippocampus and neocortex specimens for all patients. In two cases (denoted by ⋆) registration was only performed on the neocortex due to a missed scan and a fragmented hippocampus specimen. MTS: Mesial Temporal Sclerosis. FCD : focal cortical dysplasia. 57

2.2 Summary of *ex-vivo* subvolumes, the numbers of histological blocks and sections, as well as NeuN and GFAP sections. 62

2.3 TRE values for hippocampal registration across iterations. H.B.E: Non-rigid with a High Bending Energy penalty, L.B.E: Non-rigid with a Low Bending Energy penalty. † : $P \leq 0.01$ between means registration step and Rigid Iteration 1. ‡ : $P \leq 0.01$ between means of registration step and Rigid Iteration 5. 75

2.4 TRE values for neocortical registration across iterations.H.BE: Non-rigid with a High Bending Energy penalty,L. B.E: Non-rigid with a Low Bending Energy penalty. † : $P \leq 0.01$ between means registration step and Rigid Iteration 1. ‡ : $P \leq 0.01$ between means of registration step and Rigid Iteration 5. 76

3.1 Overview of the studies reporting algorithms for *in-vivo* MRI to histology of the brain in the last 15 years. 91

3.2 Summary of demographics and clinical data, including MRI and histopathological findings, for the ten recruited patients in the study. Registration was performed on both hippocampus and neocortex specimens eight patients. Registration was only performed on the neocortex for cases denoted by ⋆. HS: Hippocampal Sclerosis. FCD : Focal Cortical Dysplasia. TS: Tuberous Sclerosis. 94

3.3 Summary of *ex-vivo* subvolumes, the numbers of histological blocks and sections, as well as NeuN and GFAP sections. In two cases (denoted by $*$) registration was only performed on the neocortex 97
3.4 Summary of Dice similarity metric coefficient and root mean squared error (RMSE) for both tissue types (GM & WM) . 107

4.1 Patient demographics and clinical information including age, gender, onset age, seizure origin as well as clinical MRI and pathology findings for our patient cohort. MTS = mesial temporal sclerosis, MAA= minor architectural abnormalities, Neo. Path. = Neocortical Pathology, Hp. Path. = Hippocampal Pathology,† Previous resection of left temporal lobe tumour (DNET), * not enough tissue to make diagnosis of MTS 126
4.2 Results of the linear mixed-effects models with random effects for subjects, showing parameter estimates (β), standard error (SE) and p-values for all variables. Density (L.N)= Large Neurons, Density (S.N) = Small Neurons, NeuN F.F = Field Fraction. * Variable with fixed effect significant at $p < 0.05$, ** Variable with fixed effect significant at $p < 0.01$ 136
4.3 Significance of Spearman Rho correlations between MR parameters. All p-values were corrected for family wise error. 139

5.1 Patient demographics and clinical information including age, gender, onset age, seizure origin as well as clinical MRI and pathology findings for our patient cohort. HS = mesial temporal sclerosis, MAA= minor architectural abnormalities, Neo. Path. = Neocortical Pathology, Hp. Path. = Hippocampal Pathology † Previous resection of left temporal lobe tumour (DNET), ‡ not enough tissue to make diagnosis of HS 158
5.2 Percent neuron loss per subfield and qualitative and Quantitative HS subtype classifications. 161
5.3 Significance of Spearman's correlations between MR parameters and histological features for whole hippocampus and subfield-specific analyses. 169
5.4 Model fit of multiple linear regression analysis for predicting percent neuron loss per subfield using whole hippocampus MRI parameters. 172

5.5 Model fit of multiple linear regression analysis for predicting percent neuron loss per subfield using subfield-specific MRI parameters. 174

A.1 Table I: Dice similarity coefficient, absolute percentage volume error and Intra-class correlation coefficient metrics in conducted patient space 209
A.2 Table II: Hippocampal subfield volumes normalized by intracranial volume (ICV), reported in mm^3. 209
A.3 Table III: Subfield volumes, R2* and QS values as a mean across all subject in subject space 212
A.4 Table IV: One-way analysis of variance (ANOVA) between all subfields for R2* and QS maps 213

List of Abbreviations, Symbols, and Nomenclature

AD	Alzheimer's Disease
AD	Axial Diffusivity
ADC	Apparent Diffusion Coefficient
ANOVA	ANalysis Of VAriance
ATL	Anterior Temporal Lobectomy
bSSFP	balanced Steady-State Free Precession
BOLD	Blood-Oxygen-Level Dependant
CA	Cornu Ammonis
CC	Cross Correlation
CHARMED	Composite Hindered And Restricted ModEl of Diffusion
COSMOS	Calculation Of Susceptibility through Multiple Orientation Sampling
CR	Correlation Ratio
CT	Computerized Tomography
CGNR	Conjugate Gradient Normal Residual
CUSA	Cavitron Ultrasonic Surgical Aspirator
DBS	Deep Brain Stimulation
DESPOT1	Driven Equilibrium Single Pulse Observation of T1
DG	Dentate Gyrus
DNET	Dysembryoplastic NEuroepithelial Tumour
DSC	Dice Similarity Coefficient
DTI	Diffusion Tensor Imaging
DWI	Diffusion Weighted Imaging
EEG	ElectroEncephaloGraphy
ERP	Event Related Potentials
ET	Echo Time
ETL	Echo Train Length
ERC	Entorhinal Cortex
EPI	Echo-Planar Umaging
FA	Fractional Anisotropy
FCD	Focal Cortical Dysplasia
FDG	Fludeoxyglucose
FIESTA	Fast Imaging Employing Steady sTate Acquisition
FLAIR	Fluid Attenuated Inversion Recovery
FLASH	Fast Low Angle SHot
FM	Frequency Mask
FMRI	Functional Magnetic Resonance Imaging
FOV	Field Of View
FSE	Fast Spin Echo
FWER	Family-Wise Error Rate
FWHM	Full Width Half Maximum

GFAP	Glial Fibrillary Acidic Protein
GM	Gray Matter
GRE	GRadient-Echo
H&E	Hematoxylin and Eosin
HP	Hippocampus
HS	Hippocampal Sclerosis
ICC	Intraclass Correlation Coefficient
ICV	IntraCranial Volume
IED	Interictal Epileptiform Discharges
IHC	ImmunoHistoChemistry
IR	Inversion Recovery
IVIM	IntraVoxel Incoherent Motion
LFB	Luxol Fast Blue
LFS	Local Frequency Shift
MAP	Microtubule Associated Protein
MCD	Malformations of Cortical Development
MD	Mean Diffusivity
MEDI	Morphology Enabled Dipole Inversion
MI	Mutual Information
MPRAGE	Magnetization Prepared RApid Gradient Echo
MRI	Magnetic Resonance Imaging
MTLE	Mesial Temporal Lobe Epilepsy
MTS	Mesial Temporal Sclerosis
NCC	Normalized Cross Correlation
NEUN	NEUronal Nuclei
NF	NeuroFilament
NMI	Normalized Mutual Information
NODDI	Neurite Orientation Dispersion and Density Imaging
NR	Non-rigid Registration
NRM	Nuclear Magnetic Resonance
PET	Positron Emission Tomography
PD	Proton Density
PDF	Projection onto Dipole Fields
QSM	Quantitative Susceptibility Mapping
RBF	Radial Basis Functions
RD	Radial Diffusivity
RF	Radio-Frequency
ROI	Region Of Interest
RMS	Root-Mean Square
SAH	Selective AmygdaloHippocampectomy
SE	Spin-Echo

SHARP	Sophisticated Harmonic Artifact Reduction on Phase data
SNR	Signal-to-Noise Ratio
SPECT	Single Photon Emission Computed Tomography
SPGR	SPoiled Gradient Echo
SSD	Sum of Squared Differences
SSFP	Steady State Free Precession
SWI	Susceptibility Weighted Imaging
SUB	SUBiculum
SyN	Symmetric traNsformation
TKD	Truncated K-space Division
TLE	Temporal Lobe Epilepsy
TLE	Target Localization Error
TR	Repetition Time
TRE	Target Registration Error
TrueFISP	True Fast Imaging with Steady state Precession
TSE	Turbo Spin Echo
VBM	Voxel Based Morphometry
WH	Whole Hippocampus
WM	White Matter

Chapter 1

Introduction & Background

1.1 Temporal Lobe Epilepsy

Epilepsy is a chronic neurological disorder characterized by recurrent seizures. Epileptic seizures are alteration in neurological function resulting from episodes of excessive or synchronous neuronal electrical activity [1]. There are two main categories of seizures based on the International League Against Epilepsy ILAE classification [1]: generalized or partial (focal), depending on their clinical type, interictal electroencephalography findings and propagation. Generalized seizures involve both hemispheres often from the onset of the attack, with tonic-clonic/grand mal (involving muscle spasm and jerking movements) and absence seizures/petit mal (involving lapses of consciousness) being the most common subtypes. Partial seizures start in a specific region of the brain and may be contained or spread to the whole brain, and are subdivided into focal seizure with consciousness preserved (old terminology: simple partial) or

with loss of consciousness (complex partial/dyscognitive). Epilepsy affects around 50 million people worldwide [2]. In Canada, epilepsy is one of the most common chronic neurological disorders with a prevalence of about 1% in the population (approximately 350,000 people)[3].

Anticonvulsant or antiepileptic pharmacotherapy is for the vast majority of cases the primary means of treatment. However, over 30% of epileptic patients suffer from intractable seizures (that are drug-resistant or medically refractory) despite multiple trials of drugs [3, 4, 5]. These uncontrolled seizures are associated with a decreased quality of life (inability to work, drive and complete schooling), as well as increased psychiatric co-morbidities [6], mortality [7] and a higher risk of suicide [8], placing a significant burden on the patients, families, and the Canadian health care system and services.

Temporal lobe epilepsy (TLE) is the most common, and best-defined, form of symptomatic adult focal epilepsy [9]. TLE can originate from either mesial or lateral structures. Mesial temporal lobe seizures typically involve limbic structures, specifically the hippocampus, the amygdala and the parahippocampal gyrus, while lateral temporal lobe seizures involve the temporal neocortex. The common features of these seizures are auras (somatosensory, auditory, visual, or olfactory), memory distortions (deja vu or jamais vu), epigastric sensations or anxiety [10]. The etiology of temporal lobe seizures remains unknown; however they can be caused by a number of factors including hippocampal sclerosis, infections (such as meningitis or encephalitis), traumatic brain injury, cerebral tumours or stroke [10]. While mesial TLE (mTLE) commonly starts in adolescence and even adulthood, the initial insult is believed to be neurodevelopmental and to occur after prolonged febrile seizures in early life [11]. Numerous histopathological and electrophysiological studies have suggested that the sclerotic hippocampus

and closely related structures may be the origin of epileptic activity common to the disorder, possibly arising from the reorganization of networks in the dentate gyrus [12] and subiculum [13]. When there is a localized seizure focus, the standard of care for refractory patients is surgical excision of the affected brain region in order to achieve seizure control [14]. Intractable TLE patients form the majority of surgical candidates for epilepsy surgery [15].

1.2 Epilepsy surgery

Understanding the anatomy and connectivity of the temporal lobe is a key prerequisite for interpretation of the surgical protocols and pathological substrates of the TLE syndrome.

1.2.1 Temporal lobe function, anatomy and connections

The temporal cortex comprises regions concerned with the perception of written and spoken language, as well as auditory, vestibular, olfactory and visual senses [16]. The medial side of the temporal lobe consists of areas involved in semantic memory and olfaction, namely the the hippocampal formation and amygdala [17], as well as the uncus and nearby cortex respectively [16]. The hippocampus is not only responsible for encoding and consolidation of short-term memories, but also for their retrieval [18]. The amygdala responds to sensory stimuli that have been analyzed in other regions of the brain, such as feelings, emotions and involuntary responses mediated by the autonomic system [17]. Figure 1.1 presents an overview of the anatomy of the human

temporal lobe highlighting some of its main structures: the uncus, parahippocampal gyrus, fimbria, hippocampus (an enfolded gyrus next to the parahippocampal gyrus), fornix and neocortical gray and white matter. This section focuses on the hippocampal formation and the cerebral cortex (neocortex) of the temporal lobe. The constituents of the hippocampal formation include the hippocampus, the dentate gyrus, the fimbria, alveus and fornix [16]. The entorhinal cortex is the cortex neighbouring the hippocampus and it is found along the length of the parahippocampal gyrus. The subiculum is a transitional region located between the hippocampal and entorhinal cortices. The hippocampus proper is divided into multiple subfields, the dentate gyrus and the cornu ammonis (CA), or Amun's horn (from the Egyptian deity, Amun, with a ram's head) [19]. The dentate gyrus is made up of the hilus and fascia dentata, while CA is divided into four fields CA1, CA2, CA3, and CA4 (based on their anatomical location, cytoarchitecture and fiber connections), as shown in Figure 1.2.

Many structures of the temporal lobe are constituents of the limbic system, a collection of brain areas that regulate endocrine as well as autonomic function, namely in response to emotional stimuli, including the hippocampus, amygdala and parahippocampal gyrus [20]. The two major efferent and afferent pathways of the hippocampus within the limbic system are the fornix and entorhinal cortex (via the cingulate cortex), which are part of the Papez circuit. Many structures such as temporal lobe neocortex, amygdala and cingulate cortex are major sources of afferent pathways to the hippocampus via the entorhinal cortex [21]. The hippocampus also receives inputs through the pre-commissural and post-commissural branches of the fornix. The amygdala receives pathways from visceral inputs, mainly the hypothalamus, as well as auditory, visual and somatosensory inputs from the temporal and anterior cingulate cortices [22, 21]. It also has major efferent pathways to the hippocampus, entorhinal cortex and thalamus. The

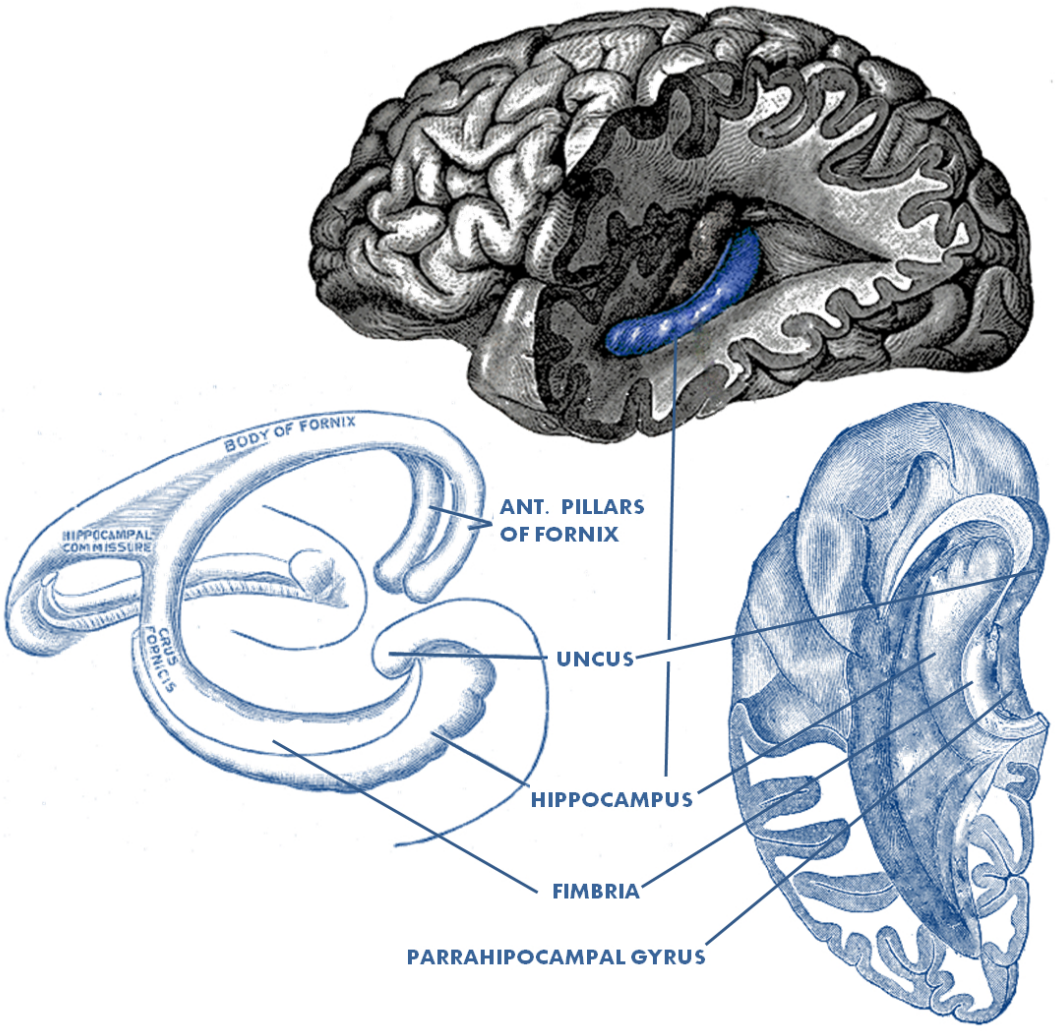

Figure 1.1: Anatomy of the temporal lobe highlighting some of its prominent structures: the hippocampus, parahippocampal gyrus, uncus, fimbria and fornix. These images are modified from the original work of Henry Gray's anatomy: "Gray739", "Gray747" and "Gray 740". Licensed under Public domain via Wikimedia Commons.

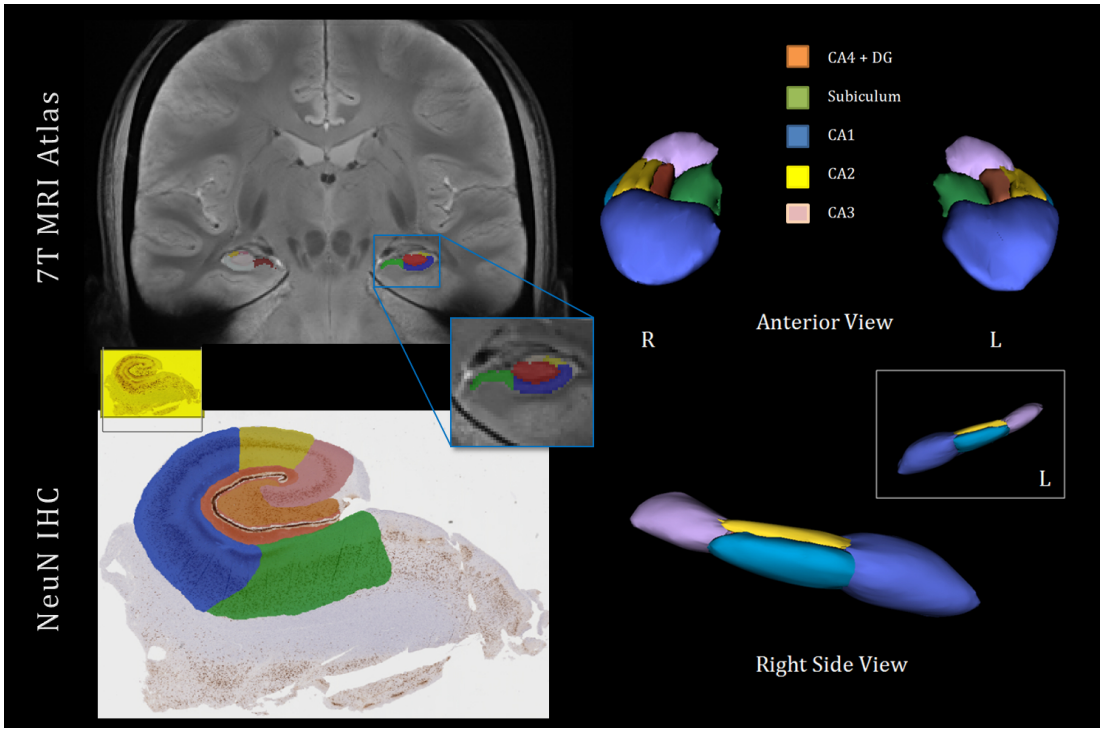

Figure 1.2: Characterization of the hippocampus into different subfields (CA1-4,DG and subiculum). Left: Delineation of the subfields on a high field 7T MRI average (Top) and NeuN IHC (bottom). Right: 3D surface rendering of the hippocampus with the subfield segmentations of the hippocampal body.

three principal pathways within the hippocampus are: 1) The perforant pathway which connects the dentate gyrus, as well as the remaining subregions of the hippocampal formation to the entorhinal cortex, 2) Mossy fiber pathways from the granular cells of the dentate gyrus to the pyramidal cells of the CA3 subfields and finally 3) the Schaffer collaterals which are the most prominent projections from CA3 to CA1.

There are three main populations of neural tracts in the brain: Association fibers connect regions in the cerebral cortex in the same hemisphere, commissural fibers generally link regions between hemispheres (not exclusively), and finally projection fibers provide a connectional route from subcortical regions to cortical regions. As for the white matter circuitry of the temporal lobe, the arcuate fasciculus (part of the superior longitudinal fasciculus) provides a two-way communication between posterior region of the superior temporal gyrus (Wernicke's language comprehension area) and the frontal cortex, namely Broca's speech development area. The uncinate fasciculus connects the temporal pole cortex with the pre-frontal cortex. The most notable association bundle in the temporal lobe is the anterior commissure which connects the middle and inferior temporal gyri of both hemispheres and runs anterior to the fornix. An important projection fiber bundle as well in the temporal lobe is Meyer's loop, which connects the upper quadrants visual fields to their associated, contralateral primary visual cortex of the inferior bank within the calcarine sulcus [16].

1.2.2 Anterior Temporal Lobectomy

Surgical excision of the affected brain region, the seizure focus, is the standard of care for the majority of cases of drug-resistant focal epilepsy [14, 23]. A randomized controlled trial that was carried out in 2001 demonstrated this to be an effective

treatment [24]. Anterior temporal lobectomy (ATL) remains the most common procedure performed for adults suffering from hippocampal sclerosis, with other options including more limited removal of only the medial structures such as selective amygdalohippocampectomy (SAH) [23]. In the ATL procedure, the mesial structures, the hippocampus and amygdala, and up to 3-5 cm of the temporal neocortex are removed [23]. Surgical risks commonly comprise neurological deficits, as well as a 6% chance of temporary complications, a 2% chance of severe chronic complications, and a 0.24% chance of death [25]. These common neurological deficits may include superior quadrant visual field defects contralateral to the side of surgery, verbal memory deficits (if the operated hemisphere is language dominant), non verbal/spatial memory deficits (if right sided) as well as language and speech deficits (dysphasia) such as word-finding ability and reading difficulties [26]. Other neurosurgical operative complications such as the risk of wound infections needing antibiotics, cerebrospinal fluid leaks or stroke are comparable to other neurosurgical operations [27].

However, seizure outcomes for epilepsy patients following surgical resection remain suboptimal, despite advances in localizing techniques, with a recent long-term study of surgical outcomes reporting that only half of such patients are seizure-free at 10 years follow-up [26]. It is believed that early seizure recurrence is mainly due to inadequate removal of the epileptic lesion itself or a critical component of the epileptic network [28]. Novel techniques have emerged to perform minimally invasive procedures for seizure control of TLE patients, such as stereotactic radio frequency amygdalohippocampectomy (where thermocoagulation of the hippocampus and amygdala is performed using a string electrode) [29] or selective laser hippocampectomy (where hippocampal ablation is conducted through a laser fiber under real-time MR monitoring) [30]. However, the long-term outcomes and effectiveness of such procedures on

seizure freedom and remission, as well as complications are yet to be established.

1.3 Pathological substrates of TLE

The findings in excised specimens from ATL surgery characterize different pathologies, including hippocampal sclerosis, congenital lesions, ischemic or inflammatory lesions, traumatic brain injuries and tumors. In this work, we focus on hippocampal sclerosis and malformations of cortical development.

1.3.1 Hippocampal sclerosis

Hippocampal sclerosis (HS), the hallmark of TLE and originally named mesial temporal sclerosis (MTS) to include amygdala and mesial structures, is the most common underlying pathology and the most common epileptogenic lesion encountered in patients with focal epilepsy [31]. The prevalence of HS varies between different reports, ranging from about 48% up to 73% [32]. HS is characterized by atrophy in the hippocampal formation associated with neuronal loss and gliosis of the CA1 (Sommer sector), CA3 and CA4 (end folium) subfields, as well as the dentate gyrus with a relative sparing of the CA2 subfield [33]. Moreover, the dentate gyrus shows reorganization of excitatory and inhibitory neuronal networks, which is characterized by granule cell dispersion, axonal sprouting of excitatory and inhibitory neurons as well as loss of interneurons [31]. HS presents a broad spectrum of structural and molecular changes, which are categorized into different subtypes based on a neuropathologic grading system [33, 34, 35]. Each distinct pattern or subtype demonstrates a different postsurgical seizure outcome, as

well as different clinical correlates such as memory impairment postoperatively [33]. Immunohistochemistry for neuronal nuclei (NeuN) has proven effective in detecting loss of neurons in the hippocampal subfields (Figure 1.3), and immunohistochemistry for glial fibrillary acidic protein (GFAP) commonly delineates gliosis related to neuronal loss [31]. Dual pathology, or the coexistence of an extra-hippocampal pathology in patients suffering from HS, has a reported incidence of 5% to 34% [32].

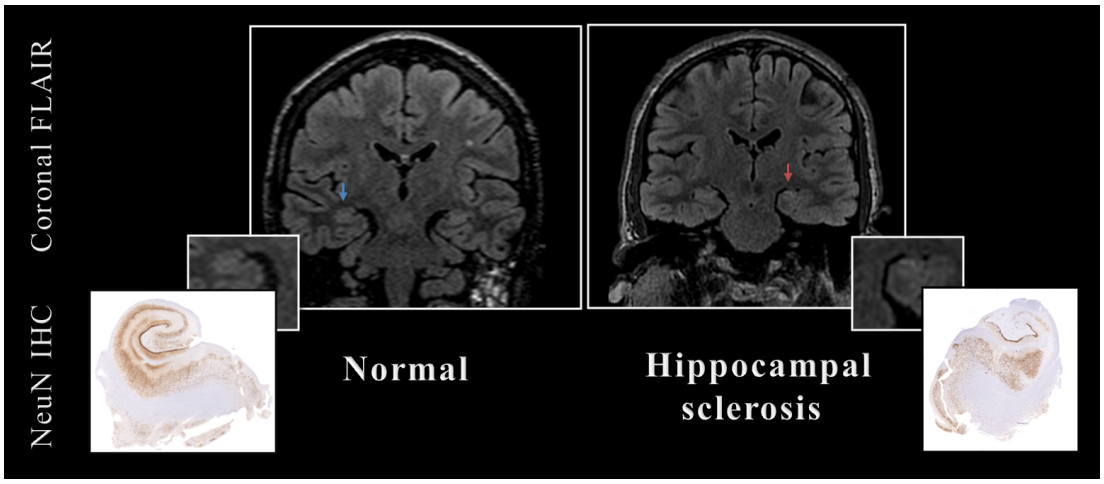

Figure 1.3: Comparison of normal and pathologic hippocampi, presenting hippocampal sclerosis on a FLAIR MRI scan and a histology NeuN IHC. Hippocampal atrophy and increased T_2-weighted signal are visible on the FLAIR image and prominent neuronal loss within the different subfields specifically CA1, CA3 and CA4 is visible on the histology slide.

1.3.2 Malformations of cortical development

Malformations of cortical development (MCD) are developmental abnormalities of the neocortex representing pathological processes throughout prenatal and postnatal brain development [36]. These mechanisms can influence different developmental processes such as cell proliferation or neuronal migration, apoptosis and cortical organization.

Focal cortical dysplasia (FCD) is the most common subtype of MCD that causes medically intractable, chronic epilepsy in children and young adults [37]. It encompasses a broad range of lesions, including cytoarchitectural abnormalities, dyslamination of the cerebral cortex, as well as underlying white matter pathology. Other subtypes of MCD include grey matter heterotopia, polymicrogyria, agyria, pachygyria or porencephaly [32].

FCD is categorized into three distinct clinicopathological types [38]. FCD Type I describes isolated lesions that are either radial or tangential cortical dyslamination (Type Ia and Ib respectively). FCD Type II are lesions, which present as cortical dyslamination plus dysmorphic neurons not including balloon cells (Type IIa) or including them (Type IIb) [39]. Whereas FCD Type III, can be diagnosed as cortical lamination abnormalities in association with other epileptogenic lesions such as hippocampal sclerosis (Type IIIa), tumors (Type IIIb), neighbouring vascular malformations (Type IIIc), or lesions acquired in early life, that is ischemic injury, traumatic brain injury or encephalitis (Type IIId) [38].

Surgical failures or seizure remission, may in some cases suggest the presence of dual pathology or error in localizing/resecting subtle neocortical lesions, thus identification and delineation of epileptogenic lesions in the neocortex is crucial to improving surgical outcomes. Moreover, the landscape of epilepsy surgery is changing with more neocortical lesions and focal cortical dysplasia (FCD) resections being performed [40], as well as an increased demand for intracranial studies and invasive evaluations within the neocortex. Patients with neocortical lesions present a higher degree of complexity than mesial TLE since they may undergo invasive surgeries due to diffuse cortical abnormalities or be denied surgery as non-surgical candidates [41].

1.4 Diagnostic techniques for pre-operative evaluation

1.4.1 Electroencephalography

Electroencephalography (EEG), first recorded by Hans Berger in 1924, is a technique for measuring spontaneous neuronal electrical activity using electrodes placed on or under the scalp. EEG detects voltage fluctuations from ionic currents in the neurons [42]. It is a vital tool for analyzing the temporal dynamics of the human brain due to its high intrinsic temporal resolution (on the order of milliseconds) [43]. EEG is conventionally analyzed as temporal waveforms over multiple channels, by looking at power of rhythms, latency and amplitude of the peaks and troughs within event related potentials (ERPs) [44]. The main limitation of EEG is its poor spatial resolution (centimeters) and that the measured signal at the surface of the scalp surface does not directly point to the site of the active neurons within the brain [45]. In addition, the signal at a given electrode is the superposition of many different sources, hence it is difficult to localize. EEG is mandatory to diagnose epilepsy though the characterization of interictal epileptiform discharges (IED) and their propagation patterns. Accuracy of EEG is limited and is neither sufficiently sensitive nor specific for localization of the seizure focus [20]. However, imaging findings on their own cannot determine the epileptogenicity of structural lesions. The accuracy of ictal findings of scalp EEG in predicting the side of the ipsilateral temporal lobe seizure onset (lateralization) is around 80% [46, 47].

Mesial temporal lobe epilepsy associated with hippocampal sclerosis commonly presents either anterior or mid temporal interictal spikes that are ipsilateral to the affected temporal lobe. The common epileptiform abnormality is the classic spike or

sharp wave having a negative polarity and preceding a slow wave. The maximum negativity of spikes originating from the anterior temporal lobe is present over the basal and sphenoidal electrodes (F7, F8, T1 and T2) [48]. In a mTLE surgical series, these anterior temporal spikes were found in over 90% of cases [49]. The characteristic ictal discharge is a buildup of sharp lateralized rhythmic activity (5-10 Hz) accompanying seizures. Ictal onset in nTLE patients is commonly in the 2-5Hz frequency range. As noted by Javidan [50], differentiating between nTLE and mTLE using scalp/clinical EEG characteristics is a challenging task. It should be noted however, that in the former the EEG may have more variable amplitude and frequency at the onset, as well as more widely spread changes, with more contribution of the fronto-central electrodes [49].

Surgical insertion of intracranial electrodes, termed intracranial EEG, can provide additional electrographic evidence for seizure focality. Techniques include placement of subdural electrodes over cortical regions of interest and/or insertion of depth electrodes for deeper neuronal structures. Since these techniques are invasive, and thus associated with potential risks, they cannot reasonably be employed for the investigation of all epilepsy patients. Intracranial EEG is mainly used to validate findings for patients with bi-temporal scalp EEG spikes (from both hemispheres) and when no visible lesion is identified on the imaging findings. Patients with epileptogenic lesions and concordant findings from analysis of semiology, MRI, video-EEG and neuropsychology undergo surgery without invasive recordings.

1.4.2 Imaging modalities

Alternative imaging methods for diagnosis of TLE include Magnetic resonance imaging (MRI), which will be discussed in details in the next subsection, interictal positron emission tomography (PET), single photon emission computed tomography (SPECT) and functional MRI (fMRI) which can be used for language laterization. PET and SPECT methods rely on detecting gamma rays emitted from an injected radioactive isotope (tracer) such as fludeoxyglucose ($^{18}F-FDG$) (an analogue to glucose) or (^{11}C flumanzenil) [51]. Ictal SPECT studies are performed at the time of seizures to detect hyper-metabolic areas (of increased blood flow) which reflect increased neuronal activation, whereas inter-ictal PET relies on the detection of hypo-metabolic areas in the brain. The localizing rates of PET and SPECT for seizure foci are about 75% and 60% respectively [52] but ictal SPECT can be interpreted with higher certainty than PET when MRI findings are negative [53]. However, the in-plane resolution of these functional imaging techniques remains on the order of few millimeters ($> 2mm$) with thick slices along the field of view [52].

1.4.3 Magnetic Resonance Imaging

MRI is a non-invasive tomographic imaging technique, which generates images of internal physical as well as chemical characteristics of an object employing externally measured nuclear magnetic resonance (NMR) signals [54]. MRI can produce 2D sectional images at any orientation, volumetric 3D scans, or even 4D volumes including spatial and time domains [55]. It operates in the radio-frequency (RF) range, and therefore does not employ ionizing radiation nor possesses its related detrimental effects. It

relies on detecting an RF signal emitted by excited nuclei, which receive energy through the application of a precessing RF pulse (oscillating magnetic field) at the proper resonant frequency [56]. The dominant (most frequently imaged) nucleus in MRI is the proton in hydrogen.

Briefly, MRI relies on the phenomenon of nuclear spin, a magnetic property of nuclei (protons) where they behave like small rotating magnets represented by magnetic moment vectors. At rest, the net magnetization (sum of all spins) is null since they are randomly distributed, however within a large external magnetic field a small fraction of the spins align with and precess about the field direction, producing a net magnetization. The magnetic vector of spinning protons (net magnetization) can be broken down into two orthogonal components: a longitudinal component M_z in the direction of the external magnetic field, and a transverse component M_{xy} or $M_{\perp}$, lying on the XY plane. The precession angular frequency, also called Larmor frequency, for the proton magnetic moment vector is given by [54]

$$\omega(x) = \gamma B(x),$$

where γ is a constant called the gyromagnetic ratio and B(x) is the magnetic field. The net magnetization, as well as energy levels and spin phases of these protons, can be altered by applying an electromagnetic excitation RF pulse precessing at the same Larmor frequency. The altered or tipped net magnetization returns to equilibrium in a process called relaxation. During relaxation, electromagnetic energy is retransmitted from excited nuclei, as the NMR signal that can be employed to induce current in the MR coils.

Longitudinal (T_1) and transverse (T_2) relaxation times are measures of the time taken for the magnetization of water protons to revert back to equilibrium, following RF excitation [55]. T1 (spin-lattice) relaxation time is the decay constant for the recovery of the M_z component to its equilibrium M_0, and is denoted by:

$$M_z(t) = M_0(1 - e^{-t/T_1}),$$

T_2 (spin-spin) relaxation is the decay constant of the M_{xy} component and is caused by a de-phasing of individual magnetic moments of the protons, and starts immediately following the application of the RF pulse. It is denoted by:

$$M_{xy}(t) = M_{xy}(0)(1 - e^{-t/T_2}),$$

The transverse relaxation arises from magnetic particles found within tissues, as well as magnetic field inhomogeneities generated by the external magnet [55]. Protons de-phase, or rotate at different frequencies, as they experience a slightly different magnetic field. T_2 is always shorter than T_1 for a given tissue [56]. T_2^*, the observed time constant of the free induction decay, is a measure of the combination of magnetic field inhomogeneities and transverse relaxation times. Both T_1 and T_2 times are tissue specific, and are dependent on the biophysical and chemical properties of tissue. By altering the time-point of MRI signal acquisition during relaxation, contrast can be created between different tissue types.

Most commonly, MRI can be weighted in T_1 and/or T_2 or proton density (PD), whereby the contrast of the image is derived from comparative contributions of different

tissues [54]. All MRI sequences comprise a series of excitation pulses that are separated by repetition times (TR). The echo time (TE) is the time at which data are acquired after applying the excitation pulses [57]. The contrast in the image changes with variations to both TE and TR [57], with the MRI signal modeled as:

$$M_{\perp}(TE) = M_0(1 - e^{-TR/T_1})e^{-TE/T_2},$$

Proton density is related to the number of hydrogen atoms in a particular volume [54]. In PD images, high PDs give high signal intensities. In $T_2 - weighted$ images, tissues with long T_2 give the highest signal intensities, producing a hyper-intense appearance. In $T_1 - weighted$ images long T_1 tissues are the most hypointense, that is bright pixels on T_1 are associated with short T_1s. One can also generate a quantitative map, derived from the relaxation time, referred to as relaxometry, which will be discussed in further detail in the following subsection. Selection of the slice plane and spatial encoding of image voxels is performed through the use of magnetic field gradients. The field gradients permit the encoding of spatial data as spatial frequency information and mapping it into k-space (frequency domain). An inverse 2D Fourier transform is employed to reconstruct the image [54]. The Fourier transform of a spatial function $f(x)$ is denoted by:

$$F(k) = \int_{-\infty}^{\infty} f(x)e^{-2\pi ikx}dx,$$

To create an image the data are acquired using a combination of gradient and RF pulses in a specific order, as part of an MRI acquisition sequence. There are two principal types of pulse sequences, gradient echo (GRE) and spin echo (SE) [55]. Gradient

echo (GRE) is the simplest type of MRI sequence, employing a single RF pulse followed by a gradient pulse to create the echo [57]. The spin echo (SE) sequence is analogous to the GE sequence with the addition of a 180° refocusing pulse. This pulse is applied between the excitation pulse and the echo at exactly half TE. Other types of sequences, such as inversion recovery, begins with a 180° inversion pulse [54]. There are many more advanced types of sequences such as Fast or Turbo Spin Echo (FSE/TSE), inversion recovery (IR), fluid attenuated inversion recovery (FLAIR) or advanced GE sequences as, spoiled gradient echo (SPGR) and steady state free precession (SSFP) [57].

MRI in epilepsy

A patient is considered a potential surgical candidate if they suffer from medically refractory seizures, the seizure is focal in origin and an accurate pre-operative localization on the ipsilateral side has been performed (based on concordant data from clinical history and exams, EEG, semiology and imaging findings). Localization of the seizure focus is therefore a major task in preoperative evaluation of surgical candidates with intractable epilepsy. In addition to EEG monitoring, MRI has the potential to identify and detect lesions related to seizure onset, and surgical outcomes are more favorable if an underlying lesion can be detected [58, 59]. Recent advances in MRI have revolutionized the management and evaluation of intractable epilepsy. The advantages of MRI, other than elimination of radiation dose, include excellent soft tissue contrast over computerized tomography (CT), as well as the ability to acquire high resolution images as compared to EEG sampling.

The clinical standard MRI protocol for pre-operative localization of seizure focus in TLE patients varies according to institutional practice and resources. The MRI protocol commonly includes a combination of the following sequences perpendicular to the hippocampal axis: 1) a coronal SPGR ($T_1 - weighted$) image, 2) a coronal FLAIR image, 3) an axial relatively higher resolution FSE ($T_2 - weighted$) through temporal lobe, 4) an axial FSE IR ($T_1 - weighted$) image and 5) a diffusion weighted imaging (DWI) sequence (this list is by no means exclusive) [20]. The imaging parameters (image resolution, slice thickness, number of averages, etc.) also vary according to the epilepsy center and are dictated by the length of the scan and the sequence. However, for structural sequences, the slices are commonly a few millimeters apart, and the intrinsic in-plane resolution ranges on average from 1 mm to 2 mm for higher resolution scans.

Since the early 1990s, hippocampal sclerosis (HS) has been detectable on pre-operative MRI [60]. The classic hallmark of HS on MRI is reduced hippocampal volume and increased signal intensity on $T_2 - weighted$ images and T_2 relaxometry, and a large body of research has established their reliability in reflecting hippocampal atrophy [60, 61, 62, 63], however, the exact causal relationship between structural changes and epileptogenesis in the hippocampus is still unclear. The radiological diagnostic criteria for HS on MRI are as follows: hippocampal atrophy and malrotation, signal alterations (mainly hyperintensity on T_2 and FLAIR), loss of internal architecture [20]. Secondary findings within temporal lobe are loss of hippocampal head digitations, dilation of temporal horn, white matter changes and entorhinal cortex atrophy. Extratemporal lobe findings include atrophy in the fornix, mammillary bodies or thalamus. In addition, the MRI features for MCD include cortical thickening, blurring or irregularity of gray matter/white matter junction, hyperintensity of gray matter, hyperintense signal in sub-

cortical white matter and altered sulcal morphology.

However, more than 30% of TLE patients are MRI-negative, presenting no evidence of brain lesions (non-lesional) [64, 65]. Histological evaluation of excised tissue in these cases often reveals reactive changes or malformations of cortical development (MCD) that were not detected in preoperative imaging [66, 67].

1.4.4 Novel MRI techniques

Current clinical imaging protocols and surface EEG techniques for epileptogenic focus localization may not be sufficient for pre-operative planning due to limited sensitivity to deeper brain structures, and low resolution of source localization techniques [68]. Novel magnetic resonance imaging (MRI) techniques such as diffusion tensor imaging (DTI), relaxometry mapping, high resolution functional MRI (fMRI), voxel-based morphometry (VBM), and cortical thickness analysis can detect abnormalities not identified with conventional or diagnostic MRI protocols [69, 70, 71]. This is important since it has been shown that post-operative outcomes can be predicted more accurately in patients where lesions can be identified [26, 72]. These techniques also have the potential to improve pre-operative localization of the focus, paving the way towards less invasive procedures and better surgical outcomes.

Diffusion Tensor Imaging

Diffusion tensor imaging (DTI) is an MRI technique that allows the study of brain microstructure by mapping the diffusion process of water molecules [73]. Water diffusion in the brain is a three-dimensional anisotropic process believed to originate from

specific organization of fiber bundles, neural axons, membranes and macromolecules. Diffusion anisotropy patterns in the white matter can therefore reveal tissue microstructure and architecture for both diseased and healthy states [74]. Diffusion is encoded in the MR signal by using diffusion sensitizing magnetic field gradients and only molecular diffusion that occurs along the direction of the gradient is visible [73]. If diffusion was isotropic, it would be fully described by a single (scalar) parameter, the diffusion coefficient, D. The effect of diffusion on the MRI signal is an attenuation, A, such as:

$$A = exp(-bD),$$

where b is a factor characterizing the gradient pulses (duration (δ), strength (g), time between the gradient pair (Δ) and shape) of the MRI sequence, and can be simplified for a rectangular pulse pair as:

$$b = \gamma^2 g_D^2 \delta^2 (\Delta - \delta/3)$$

Since diffusion is anisotropic it requires a tensor D, which fully describes molecular mobility in each direction and the correlation between them, to be characterized.

$$\underline{\mathbf{D}} = \begin{matrix} D_{xx} & D_{xy} & D_{xz} \\ D_{yx} & D_{yy} & D_{yz}, \\ D_{zx} & D_{zy} & D_{zz} \end{matrix}$$

The tensor is commonly calculated from six or more different diffusion weighted acquisitions, each obtained with a different orientation of the diffusion sensitizing gradients [74]. The directional information is encoded as eigen vectors and can be used to follow, whether in a deterministic or a probabilistic fashion, the orientations of the fiber tracts through the brain, in a process called DTI tractography. Tractography can be used to map eloquent fiber tracts for surgical planning. Figure 1.4 demonstrates an example of the corticospinal tract mapped using deterministic and probabilistic tractography for surgical planning of a tumour resection case. A standard clinical DTI sequences varies across centers and has an image resolution on the order of a few millimeters, a b-value of 1000 and 12 to 30 diffusion directions.

Several diffusion indices (maps) have been proposed to characterize anisotropy or diffusivity within the brain. Fractional anisotropy (FA) and mean diffusivity (MD) are the most commonly used indices in the epilepsy literature: They are described as follows:

$$FA = \frac{\sqrt{3[(\lambda_1 - \langle\lambda\rangle)^2 + (\lambda_2 - \langle\lambda\rangle)^2 + (\lambda_3 - \langle\lambda\rangle)^2]}}{\sqrt{2(\lambda_1^2 + \lambda_2^2 + \lambda_3^2)}},$$

where

$$\langle\lambda\rangle = MD = \frac{(\lambda_1 + \lambda_2 + \lambda_3)}{3},$$

and λ_1, λ_2, λ_3, are the eigen values of the tensor. Previous studies have demonstrated reduced FA and increased MD in the ipsilateral white matter in TLE [75, 76, 77, 78].

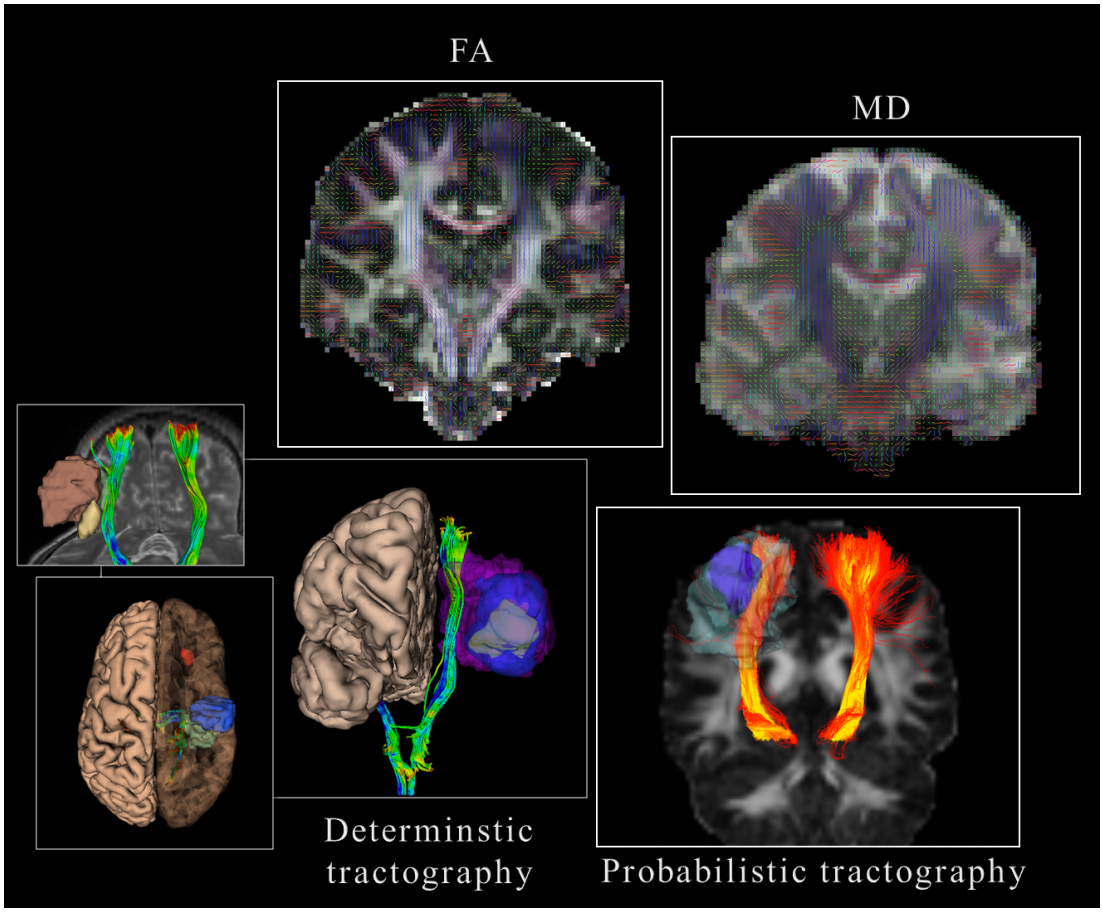

Figure 1.4: Example visualization of the diffusion maps FA and MD (with the first eigen vector overlaid on the maps), as well as fibers from deterministic (bottom left) and probabilistic tractography (bottom right) of the cortico-spinal tract.

These changes may be due to degeneration of axons, reduced packing, or demyelination [79]. The measured diffusion weighted (DW) signal in each voxel (estimate of rate of water diffusion at that voxel) combines the signal arising from a variety of heterogeneous microstructural environments including multiple cell types, sizes, geometries and orientations and extra-cellular space [80]. Most diffusion MR studies rely on simplistic single-compartment models to model the DW signal, such as apparent diffusion coefficient (ADC) or intravoxel incoherent motion (IVIM). Several models have been proposed to characterize the white matter microstructure by modeling the underlying biophysical mechanisms into multiple compartments. Most notably, the composite hindered and restricted water diffusion (Charmed) model [81] represents the intra-cellular compartment as impermeable parallel cylinders with a gamma distribution of radii; and the neurite orientation dispersion and density imaging (NODDI) approach [82] estimates the microstructural complexity using a three compartment (neurite density, orientation dispersion and extra-cellular volume fraction) with a spherical Watson distribution. Although these multi-compartment models have the potential to better investigate the tissue microstructure and supplement standard clinical tractography results, they require more time-consuming MRI acquisitions (with multiple b-values), which may limit their efficacy in a clinical setting.

Functional MRI

Functional MRI, or fMRI, is a technique for measuring brain activity through the detection of changes in blood flow that occur in response to neural activity (hemodynamic response). fMRI uses the blood-oxygen-level dependent (BOLD) method which relies on the different reactions between oxygen-rich (oxyhemoglobin) and oxygen-poor

(deoxyhemoglobin) blood to the magnetic field [83]. Cerebral blood flow and neuronal activation are coupled, in that oxygenated blood flows at a greater rate to inactive neurons and hence the difference in magnetic susceptibility between oxy and deoxyhemoglobin leads to signal variations detectable using an MRI scanner [84]. However, the hemodynamic response lags the neuronal events or the stimulus by a few seconds [83].

Advances in MRI hardware and post-processing statistical analysis techniques lead to the possibility of acquiring a high-resolution fMRI sequence (typically on the order of 2 mm resolution). In the standard fMRI paradigm, task and control states are carefully constructed to isolate one component of brain function, and the analysis then investigates areas that correlate with the known stimulus [84]. These states are alternated in blocks, with each block also event related having a number of fMRI scans and within each only one condition is presented [83]. Another paradigm is to map brain networks correlations between spontaneous fluctuations of the BOLD signal during the "resting state" of the brain. The idea of resting state fMRI, or rsFMRI, is to allow for the exploration of functional connectivity between spatially remote areas based on their synchronous BOLD activity [85]. While not assessed in this thesis, fMRI can have a role in language mapping or lateralization of the seizure for epileptic patients. It can also provide higher spatial resolution to complement the high temporal resolution of EEG in EEG/fMRI studies, where EEG spikes are correlated with the fMRI time series to determine regions in which a change in the BOLD signal resulted from an epileptic discharge observed on scalp EEG [86].

Quantitative Susceptibility Mapping

Quantitative susceptibility mapping (QSM) is a novel MRI technique that provides measurements of the apparent tissue magnetic susceptibility from measurements of the magnetic field perturbation. It requires filtering of the MR phase data and relies on regularization techniques to solve the magnetic field to susceptibility ill-posed problem. QSM provides a different contrast than the traditional susceptibility weighted imaging (SWI) and can be useful in the quantification and identification of magnetic biomarkers such as iron and calcium. QSM and qualitative SWI have demonstrated enhanced contrast and sensitivity compared to traditional T2-weighted imaging in several clinical applications, including imaging of vascular malformations, calcifications, and iron deposition [87, 88]. Furthermore, susceptibility-weighted contrast has demonstrated clinical potential in the assessment of epilepsy [89] and Alzheimer's disease [90]. Moreover, QSM can detect cerebral microbleeds with a higher sensitivity than gradient echo (GRE) magnitude imaging [91] and can be used to accurately quantify iron content in deep grey matter nuclei [92].

High resolution 3D Relaxometry

Relaxometry is a voxel-wise quantification of intrinsic relaxation times from MR images. T_1, T_2 and T_2^* can be estimated using the appropriate pulse sequence and parameters. Its advantages over qualitative T_1 or $T_2 -$ *weighted* imaging is the relative insensitivity to acquisition parameters and improved sensitivity to biochemical tissue changes, and more importantly, the ability to acquire MRI data with consistent tissue contrast at multiple time points and across different imaging centers, making it a quantitative mapping technique. Data measured during a conventional T_1- or T_2- weighted

image acquisition is a function of a combination of numerous properties of the tissue (T_1, T_2, and proton density), as well as extraneous effects associated with hardware such as amplifier gains and RF coil sensitivity [93]. Quantitative T_1 voxel-wise maps present 'pure' T_1 relaxation times that are not contaminated with T_2 effects as compared to T_1-weighted images. However, conventional relaxometry techniques such as inversion recovery (IR) for T_1 mapping and spin-echo for T_2, are rarely used in a clinical setting due to the long scan times. In this work we employed the driven equilibrium single pulse observation of T_1 and T_2, or $DESPOT1, 2$ [94, 95], which provide accurate mapping with high image resolution (1 mm isotropic) in clinically feasible time. The method derives T_1 maps from a series of two or more spoiled gradient recalled echo (SPGR) or spoiled fast low angle shot (FLASH) scans with constant TR and incremented flip angle (α) [96], as follows:

$$S_{SPGR} = \frac{M_0(1 - E_1)sin\alpha_T}{1 - E_1 cos\alpha_T},$$

where $E_1 = exp(-TR/T_1)$, which results in T_1 being calculated as $T_1 = -TR/ln$(m) and m being the slope of $S_{spgr}/\sin\alpha$ vs $S_{spgr}/\tan\alpha$

and T_2 maps from a series of five balanced steady-state free precession (bSSFP) using flip angles 5°, 35° and 68° with phase cycling patterns $\theta_{RF} = 0°$ and 180°. The signal from SSFP images is:

$$\frac{S_{SSFP}}{sin\alpha} = \frac{S_{SSFP}}{tan\alpha}\left(\frac{E_1 - E_2}{1 - E_1E_2}\right) + M_0\frac{(1 - E_1)E_2}{1 - E_1E_2}$$

where $E_2 = exp(-TR/T_2)$, which allows calculation of T_2 as $T_2 = -TR/ln[(m$-$E_1)/(mE_1$ -1)]. Figure1.5 demonstrates a visual comparison between weighted images

and relaxometry maps. It should be noted however, that the simple T1 and T2 relaxometry sequences assume a uni-exponential model for the relaxation mechanism in each case, which may not always be a true representation of the underlying phenomena creating the relaxation. For this reason, more complex sequences have also been developed that allow for multi-exponential decay [95].

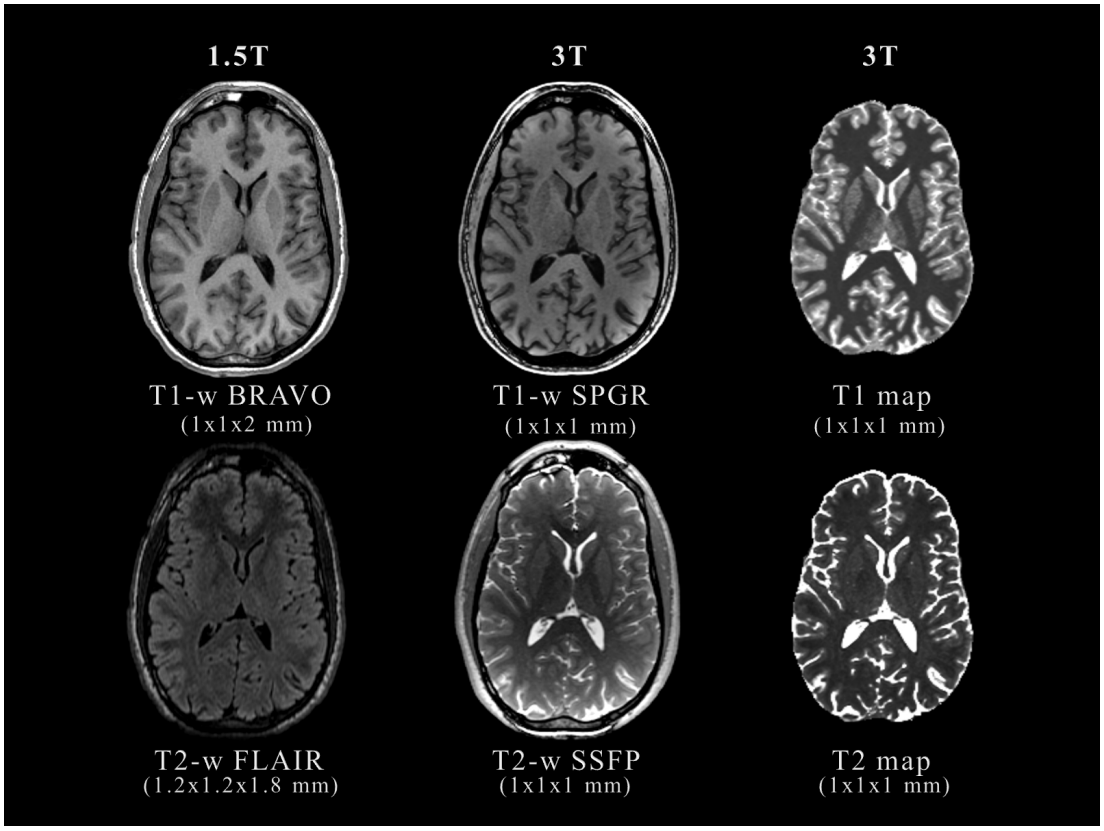

Figure 1.5: Comparison of MRI T_1 & T_2-weighted images (acquired at 1.5T & 3T) and relaxometry maps of the same subject.

1.5 MRI-Histology correlation

With the plethora of MRI sequences and analysis techniques available, the challenge then becomes how to verify and evaluate the sensitivity and specificity of these tech-

niques for detection of abnormal brain tissue. Prospective studies involving pre-operative imaging and collection of resected tissue from surgery [97, 98] provide a unique opportunity for verification and tuning of these image analysis techniques, since direct comparison can be made against high-resolution *ex-vivo* imagery, histology and immunohistochemistry. Histological verification of MRI is rare since tissue from surgeries or postmortem specimens are required, and when available validation is not a straightforward task (many surgeons employ a cavitron ultrasonic surgical aspirator - CUSA - that mitigates against intact resected surgical samples.

To carry out this validation effectively, accurate registration, or alignment, must be performed to obtain a dense spatial correspondence between in-vivo MR images and histology images of surgical specimens. Performing an accurate full image registration allows for the spatially-localized and quantitative assessment of pathological correlates in MRI by the fusion of information from both modalities. This in turn provides the ability to evaluate the effectiveness of high resolution MRI to resolve underlying pathologies of focal epilepsy, such as focal cortical dysplasia (FCD), gliosis or hippocampal subfield sclerosis (which could be on the order of a few millimeters). Several challenges are met in the process of finding spatial correspondence, or registration, between resected tissue and preoperative MRI. One of the main difficulties encountered is tissue deformation introduced due to the physical stresses experienced during surgery, as well as distortions to the tissue during histological processing. These deformations can be divided into two types: those occurring during surgical resection, and those occurring during histological processing . By obtaining an intermediate *ex-vivo* MRI of the tissue specimen after surgical resection, we can divide this challenging registration problem into two independent sub-problems that can be tackled individually.

1.6 Image Registration

Registration is the process of aligning two images so that their features correspond or can be related, by mapping a source image I_s (or its coordinates) to the space of a target image I_t using a geometrical transformation, or a deformation field, ϕ [99]. Image registration has numerous applications in brain image analysis such as registering different imaging modalities of the same subject (multi-modal registration), or computing atlases to spatially normalize anatomy across a group of subjects, or bringing in-vivo information to the operating room in image guided interventions. In our work, image registration was employed for registration of different MR sequences for the same patient, and more importantly for multi-modal registration between MR and histology. Registration algorithms involve a similarity metric, an optimizer and also a transformation model that specifies how the source (moving) image is to be deformed and what constraints are placed on such deformations [99]. Depending on the dimensionality of this transformation, registration can account for translation or rotation (rigid), global scale and shear (affine) or local shape and volume changes (non-rigid) [100]. Low-dimensional transformations (rigid or affine) are often used as an initial pre-processing step before high-dimensional registration, to align the overall anatomy.

In order to learn the optimal transformation parameters using an automated process, image registration utilizes similarity measures or metrics to determine when two images have achieved the best alignment (optimal result). There are many choices in the literature for similarity metrics including, sum of squared differences (SSD), correlation ratio (CR), cross correlation (CC) and mutual information (MI). The sum-of-squared differences (SSD) [100] is the simplest and most straightforward similarity metric and is denoted by,

$$SSD(S,T) = \sum_{i}^{N} (S(i) - T(i))^2,$$

However, it requires that the intensities between both images be matched, that is no shifting or scaling of intensities exists. Hence the SSD similarity metric would not be a good choice for multi-modal registration or registration of MR weighted images from different scanning sessions. To adjust for this discrepancy, one may use a normalized version of the metric. Another normalized metric, is the normalized cross correlation (NCC): [101]

$$NCC(S,T) = \frac{1}{N} \sum \frac{(S - \overline{S})(T - \overline{T})}{\sigma_s \sigma_t},$$

which is more robust for rapid optimization, however, it may not be suitable for multi-modal registration as it requires the source and target images to contain corresponding intensity profiles. The most commonly used metric for multi-modal registration is mutual information. In information theory, mutual information (MI), or relative entropy, is a measure of statistical dependence and information redundancy (amount of shared information) between two variables. In image registration, the local MI between two images is estimated using entropies obtained from spatially-local histograms of each images and their joint histogram. However, the standard MI metric wrongly encourages large overlap between images where the optimal output involves a small one. The normalized version of the metric accounts for the discrepancy [102], and is expressed as:

$$NMI(S,T) = \frac{H(S) + H(T)}{H(S,T)},$$

Where H(i) is the entropy of the random variable (image) and H(i,j) is the joint entropy of both variables.

1.7 Thesis objectives

The overall goals of this work were defined as follows:

1. Develop and validate an accurate pipeline for histology to *in-vivo* MRI image registration, which finds dense spatial correspondence between both modalities.

2. Investigate histopathological correlates of quantitative relaxometry and DTI from neocortical specimens of intractable TLE patients.

3. Investigate quantitative MRI predictors of neuronal loss and gliosis within the hippocampal subfields of intractable TLE patients and test the efficacy of their prediction from *in-vivo* images.

1.8 Thesis outline

The following four chapters in this thesis describe how these objectives were achieved.

1.8.1 Chapter II Histology to *ex-vivo* registration

This chapter focuses on finding spatial correspondence between the *ex-vivo* MR images and tissue-derived histology images, by modelling the transformations and deformations that occur due to surgical resection and tissue handling (such as slicing, slide mounting, fixation and other histological processing). It presents methodology and validation for the specific application of automatically registering MRI images to sparsely sampled histology images. The proposed method, based on an iterative 3D and 2D image registration scheme, does not require implanted landmarks, block-face images, or serially sectioned histology images.

1.8.2 Chapter III *in-vivo* to *ex-vivo* registration, Histology to *in-vivo* pipeline

In the third chapter I focus on the problem of registering the *in-vivo* MRI to the intermediate *ex-vivo* MRI, and completing a pipeline for histology to *in-vivo* MRI registration in temporal lobe epilepsy. The registration pipeline finds dense and accurate spatial correspondence between in-vivo MRI and histology and allows for the spatially-local and quantitative assessment of pathological correlates in MRI. The *ex-vivo* MRI is used as intermediate reference between *in-vivo* and histology images. The registration approach for *in-vivo* to *ex-vivo* MRI registration uses an automated initialization as well as a landmark-based rigid registration, followed by a landmark deformable registration for hippocampal specimens and an image-based non-rigid warping for neocortical specimens.

1.8.3 Chapter IV MRI-Histology neocortical correlation

Studies involving MRI and histology correlation from neocortical specimens in TLE are employed to better understand the relationships between the two. Quantitative MRI sequences and image processing techniques such as T2 relaxometry mapping, diffusion tensor imaging (DTI) and voxel based morphometry may present correlations with neocortical pathology that are absent with clinical MRI. In this chapter, I make use of a validated non-rigid image registration protocol (from Chapter II & III) to obtain accurate correspondences between quantitative in-vivo MRI and histology images to investigate quantitative imaging-histopathological correlations within the temporal neocortex. First quantitative histology parameters from the grey and white matter in each NeuN (representing neuron integrity) and GFAP (representing gliosis) IHC slide are sampled, and then used via image registration to obtain the corresponding MRI parameters from high-resolution quantitative T1 and T2 maps along with DTI.

1.8.4 Chapter V MRI-Histology hippocampal correlation

Chapter 5 attempts to establish the pathological substrates of hippocampal volume and intensity changes in TLE, as well as to correlate quantitative MRI parameters, including relaxation and diffusion maps, with neuronal loss and gliosis within the subfields. Furthermore, I investigate the efficacy of these quantitative MRI measures in predicting subfield pathology from in-vivo imaging. The hippocampal subfields were manually delineated on histology slices and an atlas-based segmentation protocol was employed to extract the subfields on pre-operative maps.

1.8.5 Chapter VI Conclusions and future work

This chapter summarizes the main findings of this work and their significance in the field. It also includes comments and notes for future directions and possible research questions to be investigated.

1.8.6 Appendix A Quantitative Atlas of hippocampal subfields

The hippocampus and its substructures are of great importance in the pre-operative evaluation of neurological disorders. This appendix is based on work focusing on the construction of a normative atlas of the hippocampal subfields from in vivo susceptibility weighted images of seventeen healthy volunteers on 7T MRI.

Bibliography

[1] Robert S Fisher, Walter van Emde Boas, Warren Blume, Christian Elger, Pierre Genton, Phillip Lee, and Jerome Engel. Epileptic seizures and epilepsy: definitions proposed by the international league against epilepsy (ilae) and the international bureau for epilepsy (ibe). *Epilepsia*, 46(4):470–472, 2005.

[2] WZ Wang, JZ Wu, DS Wang, XY Dai, B Yang, TP Wang, CL Yuan, RA Scott, LL Prilipko, HM De Boer, et al. The prevalence and treatment gap in epilepsy in china an ilae/ibe/who study. *Neurology*, 60(9):1544–1545, 2003.

[3] Samuel Wiebe. Brain surgery for epilepsy. *The Lancet*, 362:s48–s49, 2003.

[4] J Engel. Etiology as a risk factor for medically refractory epilepsy: a case for early surgical intervention. *Neurology*, 51(5):1243–4, 1998.

[5] Patrick Kwan and Martin J Brodie. Early identification of refractory epilepsy. *New England Journal of Medicine*, 342(5):314–319, 2000.

[6] Bruce Hermann, Michael Seidenberg, and Jana Jones. The neurobehavioural comorbidities of epilepsy: can a natural history be developed? *The Lancet Neurology*, 7(2):151–160, 2008.

[7] José F Téllez-Zenteno, Lizbeth Hernández Ronquillo, and Samuel Wiebe. Sudden unexpected death in epilepsy: evidence-based analysis of incidence and risk factors. *Epilepsy research*, 65(1):101–115, 2005.

[8] Jakob Christensen, Mogens Vestergaard, Preben Bo Mortensen, Per Sidenius, and Esben Agerbo. Epilepsy and risk of suicide: a population-based case–control study. *The Lancet Neurology*, 6(8):693–698, 2007.

[9] Jerome Engel. Mesial temporal lobe epilepsy: what have we learned? *The Neuroscientist*, 7(4):340–352, 2001.

[10] Jerome Engel Jr. Introduction to temporal lobe epilepsy. *Epilepsy research*, 26 (1):141–150, 1996.

[11] Nathalie T Sanon, Sébastien Desgent, and Lionel Carmant. Atypical febrile seizures, mesial temporal lobe epilepsy, and dual pathology. *Epilepsy research and treatment*, 2012, 2012.

[12] Robert S Sloviter. The functional organization of the hippocampal dentate gyrus

and its relevance to the pathogenesis of temporal lobe epilepsy. *Annals of neurology*, 35(6):640–654, 1994.

[13] Ivan Cohen, Vincent Navarro, Stéphane Clemenceau, Michel Baulac, and Richard Miles. On the origin of interictal activity in human temporal lobe epilepsy in vitro. *Science*, 298(5597):1418–1421, 2002.

[14] J Engel, M F Levesque, and W D Shields. Surgical treatment of the epilepsies: presurgical evaluation. *Clin Neurosurg*, 38:514–34, 1992.

[15] F Semah, M-C Picot, C Adam, D Broglin, A Arzimanoglou, B Bazin, D Cavalcanti, and M Baulac. Is the underlying cause of epilepsy a major prognostic factor for recurrence? *Neurology*, 51(5):1256–1262, 1998.

[16] JA Kiernan. Anatomy of the temporal lobe. *Epilepsy research and treatment*, 2012, 2012.

[17] Katrin Amunts, O Kedo, M Kindler, P Pieperhoff, H Mohlberg, NJ Shah, U Habel, F Schneider, and K Zilles. Cytoarchitectonic mapping of the human amygdala, hippocampal region and entorhinal cortex: intersubject variability and probability maps. *Anatomy and embryology*, 210(5-6):343–352, 2005.

[18] Howard Eichenbaum, AR Yonelinas, and Charan Ranganath. The medial temporal lobe and recognition memory. *Annual review of neuroscience*, 30:123, 2007.

[19] Henri M Duvernoy. *The human hippocampus: functional anatomy, vascularization and serial sections with MRI*. Springer, 2005.

[20] Scott W Atlas. *Magnetic resonance imaging of the brain and spine*, volume 1. Lippincott Williams & Wilkins, 2009.

[21] V Rajmohan and E Mohandas. The limbic system. *Indian journal of psychiatry*, 49(2):132, 2007.

[22] Rudolf Nieuwenhuys, Jan Voogd, and Christiaan Van Huijzen. *The human central nervous system: a synopsis and atlas*. Springer, 2007.

[23] Faisal Al-Otaibi, Saleh S Baeesa, Andrew G Parrent, John P Girvin, and David Steven. Surgical techniques for the treatment of temporal lobe epilepsy. *Epilepsy research and treatment*, 2012, 2012.

[24] S Wiebe, W T Blume, J P Girvin, M Eliasziw, Effectiveness, and Efficiency of Surgery for Temporal Lobe Epilepsy Study Group. A randomized, controlled trial of surgery for temporal-lobe epilepsy. *N Engl J Med*, 345(5):311–8, 2001.

[25] Maria Thom, Gary W Mathern, J. Helen Cross, and Edward H Bertram. Mesial temporal lobe epilepsy: How do we improve surgical outcome? *Ann Neurol.*, 68 (4):424–434, 2010.

[26] Jane de Tisi, Gail S Bell, Janet L Peacock, Andrew W McEvoy, William F J Harkness, Josemir W Sander, and John S Duncan. The long-term outcome of adult epilepsy surgery, patterns of seizure remission, and relapse: a cohort study. *Lancet*, 378(9800):1388–95, 2011.

[27] Jerome Engel Jr. Surgery for seizures. *New England Journal of Medicine*, 334 (10):647–653, 1996.

[28] Imad Najm, Lara Jehi, Andre Palmini, Jorge Gonzalez-Martinez, Eliseu Paglioli, and William Bingaman. Temporal patterns and mechanisms of epilepsy surgery failure. *Epilepsia*, 54(5):772–782, 2013.

[29] Roman Liscak, Hana Malikova, Miroslav Kalina, Zdenek Vojtech, Tomas Prochazka, Petr Marusic, and Vilibald Vladyka. Stereotactic radiofrequency amygdalohippocampectomy in the treatment of mesial temporal lobe epilepsy. *Acta neurochirurgica*, 152(8):1291–1298, 2010.

[30] Daniel J Curry, Ashok Gowda, Roger J McNichols, and Angus A Wilfong. Mr-guided stereotactic laser ablation of epileptogenic foci in children. *Epilepsy & Behavior*, 24(4):408–414, 2012.

[31] Maria Thom, Sofia Eriksson, Lillian Martinian, Luis O Caboclo, Andrew W McEvoy, John S Duncan, and Sanjay M Sisodiya. Temporal lobe sclerosis associated with hippocampal sclerosis in temporal lobe epilepsy: neuropathological features. *J Neuropathol Exp Neurol*, 68(8):928–38, 2009.

[32] Fahd Al Sufiani and Lee Cyn Ang. Neuropathology of temporal lobe epilepsy. *Epilepsy research and treatment*, 2012, 2012.

[33] Ingmar Blümcke, Elisabeth Pauli, Hans Clusmann, Johannes Schramm, Albert Becker, Christian Elger, Martin Merschhemke, Heinz-Joachim Meencke, Thomas Lehmann, Andreas Deimling, Christian Scheiwe, Josef Zentner, Benedikt Volk, Johann Romstöck, Hermann Stefan, and Michelle Hildebrandt. A new clinico-pathological classification system for mesial temporal sclerosis. *Acta Neuropathol*, 113(3):235–244, 2007.

[34] Ingmar Blümcke, Roland Coras, Hajime Miyata, and Cigdem Ozkara. Defining clinico-neuropathological subtypes of mesial temporal lobe epilepsy with hippocampal sclerosis. *Brain Pathol*, 22(3):402–11, 2012.

[35] Ingmar Blümcke, Maria Thom, Eleonora Aronica, Dawna D Armstrong, Fabrice

Bartolomei, Andrea Bernasconi, Neda Bernasconi, Christian G Bien, Fernando Cendes, Roland Coras, et al. International consensus classification of hippocampal sclerosis in temporal lobe epilepsy: a task force report from the ilae commission on diagnostic methods. *Epilepsia*, 54(7):1315–1329, 2013.

[36] Sanjay M Sisodiya. Malformations of cortical development: burdens and insights from important causes of human epilepsy. *The Lancet Neurology*, 3(1): 29–38, 2004.

[37] Ingmar Blümcke, Harry V Vinters, Dawna Armstrong, Eleonora Aronica, Maria Thom, and Roberto Spreafico. Malformations of cortical development and epilepsies: neuropathological findings with emphasis on focal cortical dysplasia. *Epileptic Disord*, 11(3):181–93, 2009.

[38] Ingmar Blümcke, Maria Thom, Eleonora Aronica, Dawna D Armstrong, Harry V Vinters, Andre Palmini, Thomas S Jacques, Giuliano Avanzini, A James Barkovich, Giorgio Battaglia, Albert Becker, Carlos Cepeda, Fernando Cendes, Nadia Colombo, Peter Crino, J Helen Cross, Olivier Delalande, François Dubeau, John Duncan, Renzo Guerrini, Philippe Kahane, Gary Mathern, Imad Najm, Ciğdem Ozkara, Charles Raybaud, Alfonso Represa, Steven N Roper, Noriko Salamon, Andreas Schulze-Bonhage, Laura Tassi, Annamaria Vezzani, and Roberto Spreafico. The clinicopathologic spectrum of focal cortical dysplasias: a consensus classification proposed by an ad hoc Task Force of the ILAE Diagnostic Methods Commission. *Epilepsia*, 52(1):158–74, 2011.

[39] Sanjay M Sisodiya, Susanne Fauser, J Helen Cross, and Maria Thom. Focal cortical dysplasia type II: biological features and clinical perspectives. *The Lancet Neurology*, 8(9):830–843, 2009.

[40] Christian G Bien, Anna L Raabe, Johannes Schramm, Albert Becker, Horst Urbach, and Christian E Elger. Trends in presurgical evaluation and surgical treatment of epilepsy at one centre from 1988–2009. *Journal of Neurology, Neurosurgery & Psychiatry*, pages jnnp–2011, 2012.

[41] Eduard Bercovici, Balagobal Santosh Kumar, and Seyed M Mirsattari. Neocortical temporal lobe epilepsy. *Epilepsy research and treatment*, 2012, 2012.

[42] Ernst Niedermeyer and FH Lopes da Silva. *Electroencephalography: basic principles, clinical applications, and related fields*. Lippincott Williams & Wilkins, 2005.

[43] Paul L Nunez and Ramesh Srinivasan. *Electric fields of the brain: the neurophysics of EEG*. Oxford university press, 2006.

[44] Frédéric Grouiller, Rachel C Thornton, Kristina Groening, Laurent Spinelli, John S Duncan, Karl Schaller, Michael Siniatchkin, Louis Lemieux, Margitta Seeck, Christoph M Michel, et al. With or without spikes: localization of focal epileptic activity by simultaneous electroencephalography and functional magnetic resonance imaging. *Brain*, 134(10):2867–2886, 2011.

[45] Christoph M Michel, Micah M Murray, Göran Lantz, Sara Gonzalez, Laurent Spinelli, and Rolando Grave de Peralta. Eeg source imaging. *Clinical neurophysiology*, 115(10):2195–2222, 2004.

[46] MW Risinger, J Engel, PC Van Ness, TR Henry, and PH Crandall. Ictal localization of temporal lobe seizures with scalp/sphenoidal recordings. *Neurology*, 39(10):1288–1288, 1989.

[47] Thaddeus S Walczak, Rodney A Radtke, and Darrel V Lewis. Accuracy and interobserver reliability of scalp ictal eeg. *Neurology*, 42(12):2279–2279, 1992.

[48] Alois Ebner and Matthias Hoppe. Noninvasive electroencephalography and mesial temporal sclerosis. *Journal of clinical neurophysiology: official publication of the American Electroencephalographic Society*, 12(1):23–31, 1995.

[49] PD Williamson, JA French, VM Thadani, JH Kim, RA Novelly, SS Spencer, DD Spencer, and RH Mattson. Characteristics of medial temporal lobe epilepsy: Ii. interictal and ictal scalp electroencephalography, neuropsychological testing, neuroimaging, surgical results, and pathology. *Annals of neurology*, 34(6):781–787, 1993.

[50] Manouchehr Javidan. Electroencephalography in mesial temporal lobe epilepsy: a review. *Epilepsy research and treatment*, 2012, 2012.

[51] P Ryvlin, S Bouvard, D Le Bars, G De Lamerie, MC Gregoire, P Kahane, JC Froment, and F Mauguiere. Clinical utility of flumazenil-pet versus [18f] fluorodeoxyglucose-pet and mri in refractory partial epilepsy. a prospective study in 100 patients. *Brain*, 121(11):2067–2081, 1998.

[52] Terence J O'Brien, Ken Miles, Robert Ware, Mark J Cook, David S Binns, and Rodney J Hicks. The cost-effective use of 18f-fdg pet in the presurgical evaluation of medically refractory focal epilepsy. *Journal of Nuclear Medicine*, 49(6): 931–937, 2008.

[53] Susan S Ho, Samuel F Berkovic, Salvatore U Berlangieri, Mark R Newton, Gary F Egan, Henri J Tochon-Danguy, and W John McKay. Comparison of ictal

spect and interictal pet in the presurgical evaluation of temporal lobe epilepsy. *Annals of neurology*, 37(6):738–745, 1995.

[54] Donald W McRobbie, Elizabeth A Moore, Martin J Graves, and Martin R Prince. *MRI from Picture to Proton*. Cambridge University Press, 2006.

[55] Zhi-Pei Liang and Paul C Lauterbur. *Principles of magnetic resonance imaging*. SPIE Optical Engineering Press, 2000.

[56] E Mark Haacke, Robert W Brown, Michael R Thompson, and Ramesh Venkatesan. Magnetic resonance imaging. *Physical principles and sequence design*, 1999.

[57] Matt A Bernstein, Kevin F King, and Xiaohong Joe Zhou. *Handbook of MRI pulse sequences*. Elsevier, 2004.

[58] Warren T Blume, Gobi R Ganapathy, David Munoz, and Donald H Lee. Indices of resective surgery effectiveness for intractable nonlesional focal epilepsy. *Epilepsia*, 45(1):46–53, 2004.

[59] LE Jeha, IM Najm, WE Bingaman, F Khandwala, P Widdess-Walsh, HH Morris, DS Dinner, D Nair, N Foldvary-Schaeffer, RA Prayson, et al. Predictors of outcome after temporal lobectomy for the treatment of intractable epilepsy. *Neurology*, 66(12):1938–1940, 2006.

[60] Gregory D Cascino, Clifford R Jack, Joseph E Parisi, Frank W Sharbrough, Kathryn A Hirschorn, Frederic B Meyer, W Richard Marsh, and Peter C O'Brien. Magnetic resonance imaging–based volume studies in temporal lobe epilepsy: pathological correlations. *Annals of neurology*, 30(1):31–36, 1991.

[61] Ana Carolina Coan, Eliane Kobayashi, Li Min Li, and Fernando Cendes. Quantification of hippocampal signal intensity in patients with mesial temporal lobe epilepsy. *J Neuroimaging*, 13(3):228–33, 2003.

[62] W Van Paesschen, T Revesz, J S Duncan, M D King, and A Connelly. Quantitative neuropathology and quantitative magnetic resonance imaging of the hippocampus in temporal lobe epilepsy. *Ann Neurol*, 42(5):756–66, 1997.

[63] AC Coan, B Kubota, FPG Bergo, BM Campos, and F Cendes. 3t mri quantification of hippocampal volume and signal in mesial temporal lobe epilepsy improves detection of hippocampal sclerosis. *American Journal of Neuroradiology*, 35(1):77–83, 2014.

[64] Aaron A Cohen-Gadol, Christopher C Bradley, Anne Williamson, Jung H Kim, Michael Westerveld, Robert B Duckrow, and Dennis D Spencer. Normal magnetic resonance imaging and medial temporal lobe epilepsy: the clinical syndrome of paradoxical temporal lobe epilepsy. *J Neurosurg*, 102(5):902–9, 2005.

[65] PN Sylaja, K Radhakrishnan, C Kesavadas, and PS Sarma. Seizure outcome after anterior temporal lobectomy and its predictors in patients with apparent temporal lobe epilepsy and normal mri. *Epilepsia*, 45(7):803–808, 2004.

[66] Sang Kun Lee, Seo Young Lee, Kwang-Ki Kim, Kkeun-Sik Hong, Dong-Soo Lee, and Chun-Kee Chung. Surgical outcome and prognostic factors of cryptogenic neocortical epilepsy. *Annals of neurology*, 58(4):525–532, 2005.

[67] Peter Widdess-Walsh, Beate Diehl, and Imad Najm. Neuroimaging of focal cortical dysplasia. *Journal of Neuroimaging*, 16(3):185–196, 2006.

[68] S J M Smith. EEG in the diagnosis, classification, and management of patients with epilepsy. *Journal of Neurology, Neurosurgery & Psychiatry*, 76 Suppl 2: ii2–7, 2005.

[69] A Bernasconi, N Bernasconi, Z Caramanos, D C Reutens, F Andermann, F Dubeau, D Tampieri, B G Pike, and D L Arnold. T2 relaxometry can lateralize mesial temporal lobe epilepsy in patients with normal MRI. *Neuroimage*, 12(6):739–46, 2000.

[70] N Bernasconi, S Duchesne, A Janke, J Lerch, D L Collins, and A Bernasconi. Whole-brain voxel-based statistical analysis of gray matter and white matter in temporal lobe epilepsy. *Neuroimage*, 23(2):717–23, 2004.

[71] B C Bernhardt, K J Worsley, H Kim, A C Evans, A Bernasconi, and N Bernasconi. Longitudinal and cross-sectional analysis of atrophy in pharmacoresistant temporal lobe epilepsy. *Neurology*, 72(20):1747–54, 2009.

[72] D R Fish, S J Smith, L F Quesney, F Andermann, and T Rasmussen. Surgical treatment of children with medically intractable frontal or temporal lobe epilepsy: results and highlights of 40 years' experience. *Epilepsia*, 34(2):244–7, 1993.

[73] Denis Le Bihan, Jean-François Mangin, Cyril Poupon, Chris A Clark, Sabina Pappata, Nicolas Molko, and Hughes Chabriat. Diffusion tensor imaging: concepts and applications. *Journal of magnetic resonance imaging*, 13(4):534–546, 2001.

[74] Andrew L Alexander, Jee Eun Lee, Mariana Lazar, and Aaron S Field. Diffusion tensor imaging of the brain. *Neurotherapeutics*, 4(3):316–329, 2007.

[75] Christoph WU Leuze, Alfred Anwander, Pierre-Louis Bazin, Bibek Dhital, Carsten Stüber, Katja Reimann, Stefan Geyer, and Robert Turner. Layer-specific intracortical connectivity revealed with diffusion mri. *Cerebral Cortex*, 24(2): 328–339, 2014.

[76] Gwenaëlle Douaud, Saâd Jbabdi, Timothy EJ Behrens, Ricarda A Menke, Achim Gass, Andreas U Monsch, Anil Rao, Brandon Whitcher, Gordon Kindlmann, Paul M Matthews, et al. Dti measures in crossing-fibre areas: *Increased* diffusion anisotropy reveals early white matter alteration in mci and mild alzheimer's disease. *Neuroimage*, 55(3):880–890, 2011.

[77] Fergus J Rugg-Gunn, Sofia H Eriksson, Mark R Symms, Gareth J Barker, Maria Thom, William Harkness, and John S Duncan. Diffusion tensor imaging in refractory epilepsy. *Lancet*, 359(9319):1748–51, 2002.

[78] Ali R Khan, Maged Goubran, Sandrine de Ribaupierre, Robert R Hammond, Jorge G Burneo, Andrew G Parrent, and Terry M Peters. Quantitative relaxometry and diffusion MRI for lateralization in MTS and non-MTS temporal lobe epilepsy. *Epilepsy Research*, 108:506–516, 2014.

[79] Niels K Focke, Mahinda Yogarajah, Silvia B Bonelli, Philippa A Bartlett, Mark R Symms, and John S Duncan. Voxel-based diffusion tensor imaging in patients with mesial temporal lobe epilepsy and hippocampal sclerosis. *Neuroimage*, 40(2):728–37, 2008.

[80] D Le Bihan, E Breton, D Lallemand, P Grenier, E Cabanis, and M Laval-Jeantet. MR imaging of intravoxel incoherent motions: application to diffusion and perfusion in neurologic disorders. *Radiology*, 161(2):401–7, 1986.

[81] Yaniv Assaf and Peter J Basser. Composite hindered and restricted model of diffusion (CHARMED) MR imaging of the human brain. *Neuroimage*, 27(1): 48–58, 2005.

[82] Hui Zhang, Torben Schneider, Claudia A Wheeler-Kingshott, and Daniel C Alexander. NODDI: practical in vivo neurite orientation dispersion and density imaging of the human brain. *Neuroimage*, 61(4):1000–16, 2012.

[83] Scott A Huettel, Allen W Song, and Gregory McCarthy. *Functional magnetic resonance imaging*, volume 1. Sinauer Associates Sunderland, MA, 2004.

[84] Richard B Buxton. *Introduction to functional magnetic resonance imaging: principles and techniques*. Cambridge university press, 2009.

[85] Bharat Biswal, F Zerrin Yetkin, Victor M Haughton, and James S Hyde. Functional connectivity in the motor cortex of resting human brain using echo-planar mri. *Magnetic resonance in medicine*, 34(4):537–541, 1995.

[86] Jean Gotman. Epileptic networks studied with eeg-fmri. *Epilepsia*, 49(s3):42–51, 2008.

[87] Alexander Rauscher, Jan Sedlacik, Markus Barth, Hans-Joachim Mentzel, and Jürgen R Reichenbach. Magnetic susceptibility-weighted mr phase imaging of the human brain. *American journal of neuroradiology*, 26(4):736–742, 2005.

[88] Govind B Chavhan, Paul S Babyn, Bejoy Thomas, Manohar M Shroff, and E Mark Haacke. Principles, techniques, and applications of t2*-based mr imaging and its special applications 1. *Radiographics*, 29(5):1433–1449, 2009.

[89] Jitender Saini, Chandrasekhran Kesavadas, Bejoy Thomas, Tirur Raman Kapilamoorthy, Arun Kumar Gupta, Ashalatha Radhakrishnan, and Kurupath Radhakrishnan. Susceptibility weighted imaging in the diagnostic evaluation of patients with intractable epilepsy. *Epilepsia*, 50(6):1462–73, 2009.

[90] Tsutomu Nakada, Hitoshi Matsuzawa, Hironaka Igarashi, Yukihiko Fujii, and Ingrid L Kwee. In vivo visualization of senile-plaque-like pathology in alzheimer's disease patients by mr microscopy on a 7t system. *Journal of Neuroimaging*, 18 (2):125–129, 2008.

[91] Jan Klohs, Andreas Deistung, Ferdinand Schweser, Joanes Grandjean, Marco Dominietto, Conny Waschkies, Roger M Nitsch, Irene Knuesel, Jürgen R Reichenbach, and Markus Rudin. Detection of cerebral microbleeds with quantitative susceptibility mapping in the arcabeta mouse model of cerebral amyloidosis. *Journal of Cerebral Blood Flow & Metabolism*, 31(12):2282–2292, 2011.

[92] Christian Langkammer, Ferdinand Schweser, Nikolaus Krebs, Andreas Deistung, Walter Goessler, Eva Scheurer, Karsten Sommer, Gernot Reishofer, Kathrin Yen, Franz Fazekas, et al. Quantitative susceptibility mapping (qsm) as a means to measure brain iron? a post mortem validation study. *Neuroimage*, 62(3):1593–1599, 2012.

[93] Sean C L Deoni, Brian K Rutt, and Terry M Peters. Rapid combined T1 and T2 mapping using gradient recalled acquisition in the steady state. *Magn Reson Med*, 49(3):515–26, 2003.

[94] Sean C L Deoni. High-resolution T1 mapping of the brain at 3T with driven equilibrium single pulse observation of T1 with high-speed incorporation of RF

field inhomogeneities (DESPOT1-HIFI). *J Magn Reson Imaging*, 26(4):1106–11, 2007.

[95] Sean C L Deoni, Brian K Rutt, Tarunya Arun, Carlo Pierpaoli, and Derek K Jones. Gleaning multicomponent T1 and T2 information from steady-state imaging data. *Magn Reson Med*, 60(6):1372–87, 2008.

[96] Sean C L Deoni, Melanie J C Josseau, Brian K Rutt, and Terry M Peters. Visualization of thalamic nuclei on high resolution, multi-averaged T1 and T2 maps acquired at 1.5 T. *Human Brain Mapping*, 25(3):353–9, 2005.

[97] S H Eriksson, S L Free, M Thom, L Martinian, M R Symms, T M Salmenpera, A W McEvoy, W Harkness, J S Duncan, and S M Sisodiya. Correlation of quantitative MRI and neuropathology in epilepsy surgical resection specimens–T2 correlates with neuronal tissue in gray matter. *Neuroimage*, 37(1):48–55, 2007.

[98] K L Howe, D Dimitri, C Heyn, T-R Kiehl, D Mikulis, and T Valiante. Histologically confirmed hippocampal structural features revealed by 3T MR imaging: potential to increase diagnostic specificity of mesial temporal sclerosis. *AJNR American journal of neuroradiology*, 31(9):1682–9, 2010.

[99] Barbara Zitova and Jan Flusser. Image registration methods: a survey. *Image and vision computing*, 21(11):977–1000, 2003.

[100] D Rueckert, L I Sonoda, C Hayes, D L Hill, M O Leach, and D J Hawkes. Nonrigid registration using free-form deformations: application to breast MR images. *IEEE Transactions on Medical Imaging*, 18(8):712–21, 1999.

[101] Mark Holden, Derek LG Hill, Erika RE Denton, Jo M Jarosz, Tim CS Cox, Torsten Rohlfing, Joanne Goodey, and David J Hawkes. Voxel similarity measures for 3-d serial mr brain image registration. *Medical Imaging, IEEE Transactions on*, 19(2):94–102, 2000.

[102] Frederik Maes, Andre Collignon, Dirk Vandermeulen, Guy Marchal, and Paul Suetens. Multimodality image registration by maximization of mutual information. *Medical Imaging, IEEE Transactions on*, 16(2):187–198, 1997.

Chapter 2

Registration of Histology to Ex-vivo MRI

2.1 Introduction

The fundamental operation underlying all of the research presented in this thesis is the accurate registration of histology to pre-operative images. However, several challenges are met in the process of finding spatial correspondence, or registration, between resected tissue and preoperative MRI. One of the main difficulties encountered is tissue deformation introduced due to the physical stresses experienced during surgery, as well as distortions to the tissue during the histological processing (Figure 2.1). These deformations can be divided into primary and secondary categories [1]. Primary deformations can be thought of as three dimensional changes, such as mechanical distortions

This chapter is adapted from Goubran et al. "Image registration of ex-vivo MRI to sparsely sectioned histology of hippocampal and neocortical temporal lobe specimens." Neuroimage 2013;83:770-781

during brain extraction once the resected specimen is detached from surrounding brain tissue, when cutting the specimen in blocks, or non uniform shrinkage induced by formalin fixation. Secondary deformations are within-slice distortions which are due to stretching of microtome cut sections on a water bath, spreading histology slices over glass slides and staining. Breakage of histology slices, is a major manifestation of the deformations encountered during histological processing of the tissue [2]. Specifically, irregularities in the block surface due to different temperature and humidity can possibly lead to loss of sections from the face of the blocks. Furthermore, differential shrinkage of the tissue is another challenge that is due to the different intrinsic properties of white and grey matter. Registration of histology from surgically resected brain specimens to MRI is more challenging than registration of post-mortem or animal tissue, as the tissue must be sparsely sectioned, in comparison to the possibility of serially sectioning the entire specimen. This limitation is imposed by the clinical requirement of pathology departments to retain parts of the resected specimen in tissue archives. The very different anatomy between sparsely sectioned adjacent histology slices (several mm apart) presents itself as another significant problem. To address the challenge of non-rigidly registering sparsely sectioned histology slides of brain resections from epilepsy surgery to *in-vivo* 3D MRI, I propose a full image registration protocol that relies on *ex-vivo* imaging of the specimen, to enable accurate correlation of histopathology with MRI. This chapter focuses on the intermediate registration of histology images to *ex-vivo* imaging of hippocampal and temporal lobe resections from anterior temporal lobectomies (ATL). The remaining 3D registration from *ex-vivo* to *in-vivo* MRI is dealt with in chapter 3 and involves a set of unique challenges related to the primary deformations occurring during brain resection and variability of the resection boundary.

A previous method has been devised to manually match histopathology of temporal

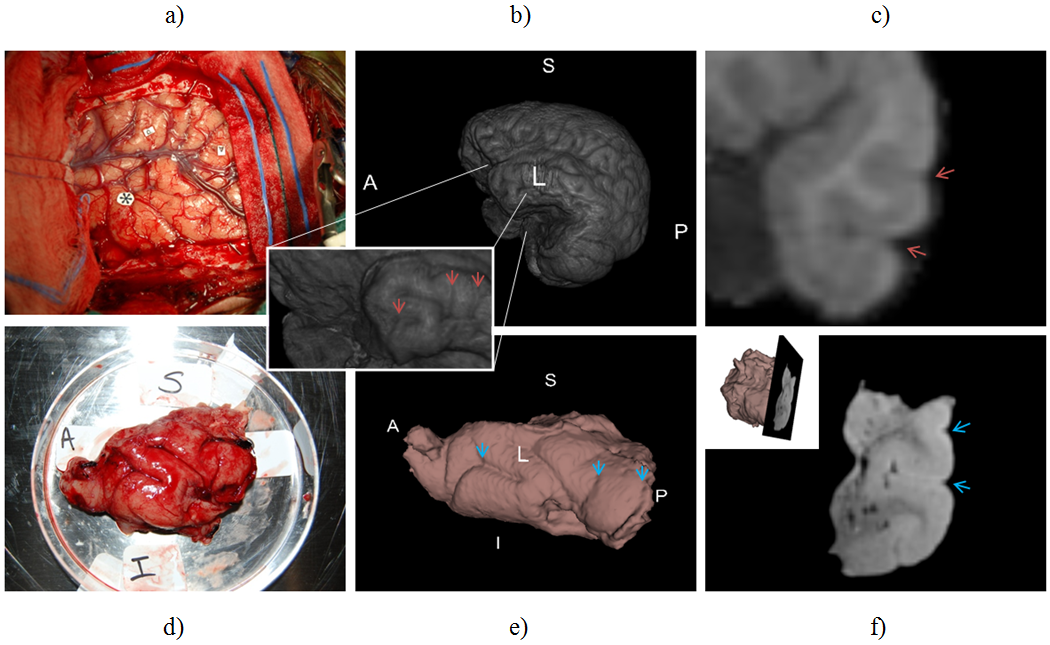

Figure 2.1: Example of encountered deformations. Red arrows represent cortical sulci on the pre-operative MRI and blue arrows represent the corresponding sulci on the resected neocortex specimen. a) Photograph of surgical view before resection, b) Volume rendering of a pre-operative MRI of the patient with a zoomed view showing the temporal pole, c) Coronal view of the pre-operative MRI demonstrating temporal gyri with red arrows, d) Photograph of the temporal lobe neocortex post resection, e) Surface rendering of the resected neocortex with blue arrows showing the corresponding sulci to part b), and f) Coronal view of the *ex-vivo* MRI with blue arrows indicating sulci corresponding to part c); the small window in the top left corner demonstrates the mesial (interior) side of the neocortex with an intersection of the shown MRI slice.

lobe resections to MRI using a cutting cradle to resample the MRI to the orientation of histology [3]. However no image registration was performed and only visual assessment of the correspondence between the MRI and photographs of histology slices was accomplished. Previous studies on registration of histopathology to *in-vivo* imaging were reported mostly for rodents [4, 5, 6, 7, 2] and primates [8, 9, 1, 10]. Relatively few studies report attempts to register human brain MRI to histology, with the majority being performed on whole-brain or single-hemisphere postmortem data [11, 12, 13]. These landmark-based and image-based registration algorithms, however, are not likely to be applicable to the registration of specimens from lobectomies to full preoperative MR images, due to the drastic change in shape and coherence when the specimen is separated from neighbouring tissue. Other methods have been proposed that allow co-registration of histology to other modalities through the use of stereotactic systems using target points [14, 5], however the design of these systems is tissue-specific and is not broadly applicable to other brain resections. To the best of our knowledge, this is the first instance where human brain surgery specimens were registered to histology using an image-based algorithm in a clinical setting, with a target registration error reported and validated.

Presently, there are no automated histology to MRI image registration protocols that could be widely applicable to focal resections of human brain, such as tissue resected during epilepsy surgery. I present here a protocol to register *ex-vivo* scans of hippocampal and neocortical temporal lobe resections to histology as an intermediate step that reduces the complexity of the preoperative MRI to 2D sparse histology problem. Specifically I describe a novel landmark-free algorithm for simultaneous reconstruction and alignment of sparsely sectioned histological data to *ex-vivo* MRI, and a quantitative validation for our registration method. Performing this intermediate step

addresses most of the challenges of registration to *in-vivo* imaging due to the higher resolution and reduced deformations of the *ex-vivo* images. Furthermore, the higher resolution of specimen imaging is advantageous for examining the correlation between MRI and histology. The proposed method represents a significant step towards *in-vivo* MRI to histology registration in the clinical setting and can be broadly applicable to MRI and histopathology correlations of resections other than epilepsy surgery.

2.2 Methods & Materials

2.2.1 Recruitment, surgery & specimen acquisition

Seven patients suffering from intractable temporal lobe epilepsy (TLE) were recruited as part of an ongoing study. This project has been cleared by the Health Sciences Research Ethics Board of Western University, and informed consent was obtained from all patients prior to their participation in the study. All such patients were recommended for ATL surgery by the department of clinical neurological sciences at the University Hospital (UH) of the London Health Sciences Centre, and had preoperative investigations including neuropsychological testing and 1.5T clinical MRI scans which included T1w, T2w, FLAIR, and diffusion-weighted sequences. Patients were monitored with scalp-based electroencephalogram (EEG) video telemetry for seizure characterization, with three patients having to undergo monitoring with subdural placement of strip electrodes. In addition to the 1.5T clinical MRI scans performed at the hospital, patients underwent a series of scans on 3T and 7T MRI research scanners,

including high-resolution structural imaging, diffusion-tensor imaging, relaxation mapping and resting-state functional imaging prior to surgery. Following surgery, the resected tissue specimens were transferred to the Robarts Research Institute for *ex-vivo* specimen imaging on the same 3T scanner and then to the pathology technologist for histological processing. From the seven patients, fourteen resected specimens were collected (7 neocortex and 7 hippocampus), whereas all 7 neocortical specimens were fully analyzed, only 5/7 hippocampal specimens were analyzed, due to a fragmented hippocampus specimen and missed *ex-vivo* hippocampus scan. All the specimens used in this chapter were en bloc resections, however the size of the neocortex specimens were smaller if the resection was on the language-dominant side. The mean volume of the hippocampal specimens was 4.30 ± 0.41 mL; and the mean volumes of the neocortical specimens for language-dominant side resections and non-language-dominant resections were 12.9 ± 1.78 mL and 23.2 ± 6.41 mL respectively. It should be noted however, that different surgeons use slightly different techniques, which could account for the variability in the volume of specimens. Table 2.1 summarizes the patients' demographic data, as well as, their clinical MRI and histopathological findings.

2.2.2 Specimen *ex-vivo* MR Imaging

After resection, each specimen was placed in a large petri dish within a specialized sealed cooler for specimen transport, and orientation labels were marked on the container by the operating neurosurgeon, with photographs taken for future reference. MR imaging was carried out on the specimens in two sessions: immediately following surgical resection, and after overnight fixation in 10% formalin. For the initial session, referred to as the pre-fixation session, the specimens were immediately transferred from

Subj.	Sex	Age	Onset age	Seizure origin	MRI	Path.	Scan Protocol
1	F	51	10	Right	Normal	dysplasia	I
2	F	22	15	Right	Normal	mild MTS	I
3	F	52	12	Left	Non-specific	mild FCD	I
4⋆	F	26	20	Right	Tuberous Sclerosis	Cortical tubers	II
5	F	22	15	Right	R. MTS	MTS	II
6	M	20	3	Left	L. MTS	MTS	II
7⋆	M	19	5	Right	Normal	Gliosis	II

Table 2.1: Summary of demographics and clinical data, including MRI and histopathological findings, for the seven recruited patients in the study. Registration was performed on both hippocampus and neocortex specimens for all patients. In two cases (denoted by ⋆) registration was only performed on the neocortex due to a missed scan and a fragmented hippocampus specimen. MTS: Mesial Temporal Sclerosis. FCD : focal cortical dysplasia.

the operating room to the scanning suite at the Robarts Research Institute and prepared for imaging. Each specimen was wrapped in gauze for stabilization, transferred to suitably-sized containers for imaging, and immersed in a fluorine-based lubricant 'Christo-lube MCG 1046' (Lubrication Technology, Inc) prior to imaging to avoid susceptibility artifacts at the tissue boundaries. Identical preparation was performed for the second post-fixation session.

Specimen imaging was performed on a 3T Discovery MR750 scanner (GE Medical Systems, Milwaukee, WI, U.S.A.). Initially, an in-house developed gradient-insert coil was employed in the scanning setup with each specimen imaged sequentially using different coils. For improved time-efficiency in scanning and setup, the gradient-insert coil was not employed in later studies, and both specimens were imaged in the same field of view. Post-fixation T2-weighted scans were used in the subsequent image processing and registration. Both scanning protocols are described in detail below:

Scan Protocol I

The first protocol utilized a gradient-insert with a 4 channel TORO coil for the neocortex and a solenoid coil for the hippocampus, with specimens scanned sequentially. T2-weighted images with a multi-phase balanced SSFP FIESTA sequence with 4 cycled phases were acquired for the neocortex (TR=3.5ms, TE=1.75ms, flip angle=40°, N=4, matrix=200×200, slice thickness=0.3, FOV=60mm) and the hippocampus (TR=3.97ms, TE=1.98ms, flip angle=40°, N=4, matrix=200×200, slice thickness=0.3, FOV=60mm).

Scan Protocol II

For the second protocol, a 6 channel coil, designed to image the carotid artery, was used instead of the gradient-insert coil of the previous configuration. Similar T2-weighted fast imaging employing steady state acquisition (FIESTA) images (TR=8.17ms, TE=4.08ms, flip angle=40°, N=2, matrix=200 × 200, slice thickness=0.4, FOV=70mm) with a resolution of 0.35 × 0.35 × 0.4mm, as well as, Fast gradient echo (fastGRE) scans with sixteen echoes (TR=65.0ms, TE=38.9ms, flip angle=40°, matrix=200×200, slice thickness=0.4, FOV=70 mm) were acquired for the study for a total scan time of less than two hours. A switch was made to the second protocol due to the significant time savings achieved during the setup and gradient shimming processes (from ~45 min to ~65 min) with minimal loss of image resolution. Note that similar SSFP FIESTA sequences were used in both protocols to provide the images used in registration.

2.2.3 Histological processing

Following pre-fixation and post-fixation MRI imaging, the specimens underwent accessioning and grossing at the Department of Pathology at the University Hospital of London Health Sciences Centre, and were then cut into two halves midway, anterior-posterior, through the specimen in the coronal plane. Each half of the specimen was then embedded in agar for a stabilization effect during slicing. The half-specimens were then sectioned parallel to the initial cut, into 4.4 mm pieces in the anterior to posterior direction using a deli slicer (Globe Food Equipment Company, Dayton, OH, U.S.A). Each block was embedded in paraffin and mounted on a microtome where 8 μ m thick sections were cut from the face of each block and mounted on slides. The constraint of cutting only one section from each block stems from two limitations. The first being the requirement set forth by the committee governing tissue use, which requires the remaining part of the blocks be reserved in their tissue archive in case further analysis is needed. The second factor is the significantly increased cost associated with acquiring serial sections of all our blocks for both types of specimens, which would restrict the number of subjects we could recruit for this ongoing study.

One slide from each block was stained with hematoxylin and eosin (H&E) according to standard clinical neuropathology protocols, and additional stains or immunohistochemistry (IHC), mainly glial fibrillary acidic protein (GFAP) (polyclonal antibody) and neuronal nuclei (NeuN) (monoclonal antibody), as well as neurofilament (NF), luxol fast blue (LFB) and cluster of differentiation antibody (CD34) were ordered when deemed necessary by the neuropathologist on duty. Batch IHC processing was performed on a Dako Autostainer Link 48 (Dako Corporation, Glostrup, Denmark) to minimize variability between slides.The median number of hippocampus (Hp) and

neocortex (Neo) blocks was 8 and 12 respectively. For the hippocampus, on average about a quarter of the blocks were additionally stained with GFAP. As for the neocortex, about half of the blocks were additionally stained with a combination of the previously mentioned stains and immunohistochemistry; while GFAP and NeuN being the two most common additional stains. The *ex-vivo* subvolumes, the numbers of histological blocks and sections, as well as NeuN and GFAP sections, are summarized in table 2.2. The average physical size of the hippocampal histological sections (slide area ($\hat{mm2}$)) was 96.5 ± 60.9, and 281.0 ± 168.9 for neocortical sections.

The resulting slides were digitized on a ScanScope GL (Aperio Technologies, Vista, CA, USA) bright field slide scanning system at a maximum of 20x optical zoom, and stitched to form full-frame multi-resolution images stored in BigTIFF file format (maximum pixel resolution 0.5μm).The full resolution BigTIFF histology images were retained for future quantitative analysis. Since each specimen was sectioned into blocks of 4.4mm thickness, the corresponding H&E stained images have a physical spacing of effectively 4.4mm in the coronal (anterior-posterior) direction. Figure 2.2 shows an overview of all these histological processing steps.

2.2.4 Image registration

To motivate our registration approach we first describe how the numerous physical processing steps between *ex-vivo* MR imaging and slide digitization affect the specimen, and how these steps could be accounted for with registration. As outlined in the previous section, after imaging, the tissue specimen is sectioned coronally, but this slicing plane is not enforced to be along the orthogonal axes corresponding to the MRI coordinate system. We therefore need to obtain a transformation between the MRI axes

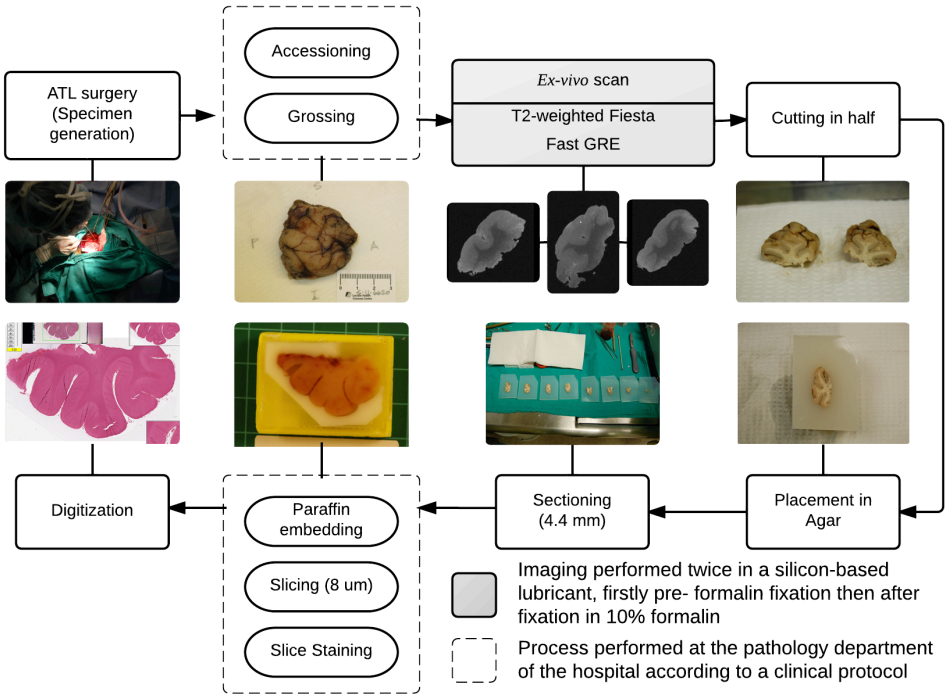

Figure 2.2: Overview of histological processing from specimen generation to digitization. Processed performed at in a standard clinical work flow at the hospital are included in dashed boxes.

Subject	Hp volume (mm^2)	Hp blocks	Hp sections	Neo volume (mm^2)	Neo blocks	Neo sections
1	4808.4	9	18 (9 GFAP)	21331.0	16	20 (4 GFAP)
2	4140.3	9	11 (2 GFAP)	20363.1	10	14 (2 NeuN, 2 GFAP)
3*	3896.1	10	10 (No IHC)	14087.3	16	20 (1 NeuN, 1 GFAP)
4	-	-	-	32669.3	14	37 (13 NeuN, 3 GFAP)
5	3992.4	6	6 (No IHC)	18472.0	12	21 (3 NeuN, 3 GFAP)
6*	4677.0	7	8 (1 GFAP)	13830.8	12	15 (2 NeuN)
7*	-	-	-	10885.8	9	15 (3 NeuN, 2 GFAP)

Table 2.2: Summary of *ex-vivo* subvolumes, the numbers of histological blocks and sections, as well as NeuN and GFAP sections.

and tissue slicing axes. Next, when the specimen is mounted on the microtome, there may be variability in the angle at which sections are taken and in the number of partial sections removed before a full section is retained. This effectively leads to variability in the angle and spacing between sections. For similar procedures carried out on prostate specimens, Gibson et al. [15] quantified the variability to be $1.7 \pm 1.1^\circ$ and 1.0 ± 0.5 mm in angle and spacing respectively. Because of the relatively small magnitude of variability, which presumably would be similar for brain sections, as well as the ease of working with parallel sections, we do not explicitly account for this and and instead assume sections are parallel and spaced by 4.4mm. The tissue being sectioned in the microtome is highly folded after the blade is brought down, thus to mount the section on a slide, it is first placed in a water bath to unfold, then eased onto the glass slide. This procedure can introduce folds or tears in the mounted section, and placement on the slide is variable. Histological processing and staining of the section can introduce

further distortions, such as differential shrinkage or expansion of tissue. Since all these deformations are present in the thin (8μm) section of tissue mounted on the slide, these can be modelled as transformations and warps constrained to the 2D plane.

In summary, we require a registration approach that can model: 1) the transformation between the 3D MRI axes to the specimen slicing axes (3D rigid transformation), and 2) the transformations and deformations of each slide-mounted section constrained to the 2D space of the slide (2D rigid transformations and non-rigid deformations).

2.2.5 Iterative registration algorithm

In this section we outline our iterative registration approach to attain the transformations and deformations and to establish correspondence between the MRI and histology images. Note that the registration procedures for hippocampus and neocortex images were carried out separately in each case. Preliminary results for neocortex registration were shown in Goubran et al. [16].

If a 3D reconstruction of the histology were given, 3D rigid image registration could be used to align the MRI to the histology. However, to generate a 3D reconstruction of the histology, the individual histology slices would need to be corrected, using the registered MRI as a reference. Thus we see that obtaining the 3D rigid transformation is dependent on having a 3D histology reconstruction, and this is in turn dependent on the 2D histology registration with the MRI for a reference. To resolve this circularity, we propose an iterative registration scheme that alternates between 1) finding the 3D rigid transformations given the current histology reconstruction, and 2) finding the 2D

rigid transformations and non-rigid deformations to reconstruct the histology volume given the current 3D rigid transformations.

Figure 2.3 presents a block diagram overview of our overall registration algorithm. First, the histology and MRI images are pre-processed separately to obtain image pairs of the same resolution and field of view suitable for image registration. Then the images are fed into an iterative registration algorithm that alternates between registration of the MRI volume to the current estimate of the histology volume (3D Rigid Registration), and registration of the histology slides to the reference MRI slides for histology volume reconstruction (2D Rigid Registration and 2D Non-rigid Registration). The details of this registration are shown in Algorithm 1.

MR image pre-processing

Prior to image registration, the images underwent a series of pre-processing steps, carried out with command-line tools from the FSL image analysis suite (FSL, `http://fsl.fmrib.ox.ac.uk`) and scripts written in MATLAB (The MathWorks Inc., Natick, MA, USA). First, *ex-vivo* MRI images scanned with *Scan Setup II*, containing both neocortex and hippocampus specimens in the same field of view, were converted from the scanner output Dicom (dcm) format to the standard Nifti (nii) format, then bisected to produce separate volumes. Since the orientation of these specimens in the scanner bore did not correspond to the anatomical orientation, the orientation matrices of the images volumes were updated to reflect the correct pose. This operation was performed using photographs of the annotated specimens and 3D models of *ex-vivo* images, and the resulting orientation matrices were applied to all the acquired images in the session.

Input: Histology and MRI volumes: $\mathbf{H}^0 = \{H_j\}_{j=1\ldots N}$, $\mathbf{M}$
Output: Final volume and transformations: $\mathbf{H}^{i_{\max}}$, $T_{3D}^{i_{\max}}$, $T_{2D,j=1\ldots N}^{i_{\max}}$, $\Phi_{2D,j=1\ldots N}^{i_{\max}}$

for $i = 0$ **to** i_{max} **do**
  // 3D rigid registration between histology and MRI volume:
  $T_{3D}^{i} = \text{RigidReg3D}\left(\mathbf{H}^{i}, \mathbf{M}\right)$
  // Transformed MRI volume:
  $\mathbf{M}^{T^i} = T_{3D}^{i} \circ \mathbf{M}$
  // For each histology slice:
  for $j = 1$ **to** N **do**
    // 2D rigid registration between histology and MRI slice:
    $T_{2D,j}^{i} = \text{RigidReg2D}\left(M_j^{T^i}, H_j^{i}\right)$
    if $i > 2$ **then**
      // 2D non-rigid registration between histology and MRI slice:
      $\Phi_{2D,j}^{i} = \text{NonRigidReg2D}\left(M_j^{T^i}, T_{2D,j}^{i} \circ H_j^{i}\right)$;
    else
      $\Phi_{2D,j}^{i} = Id$;
    end
    // Deformed histology slice
    $H_j^{i+1} = \Phi_{2D,j}^{i} \circ T_{2D,j}^{i} \circ H_j^{i}$;
  end
  // Updated histology volume
  $\mathbf{H}^{i+1} = \{H_j^{i+1}\}_{j=1\ldots N}$;
end

Algorithm 1: Iterative 3D and 2D registration of input histology volume $\mathbf{H}^0 = \{H_j\}_{j=1\ldots N}$ and MRI volume $\mathbf{M}$. Here, we represent image volumes in boldface ($\mathbf{H}$) and the corresponding slices with subscripts (H_j). In the first part of each iteration, 3D registration is carried out on the current estimate of the histology volume and the MRI volume to obtain the transformation between the MRI axes to the specimen slicing axes. In the second part, 2D registration is carried out to obtain the transformations and deformations of each slide-mounted histology section using the current estimate of the aligned reference MRI.

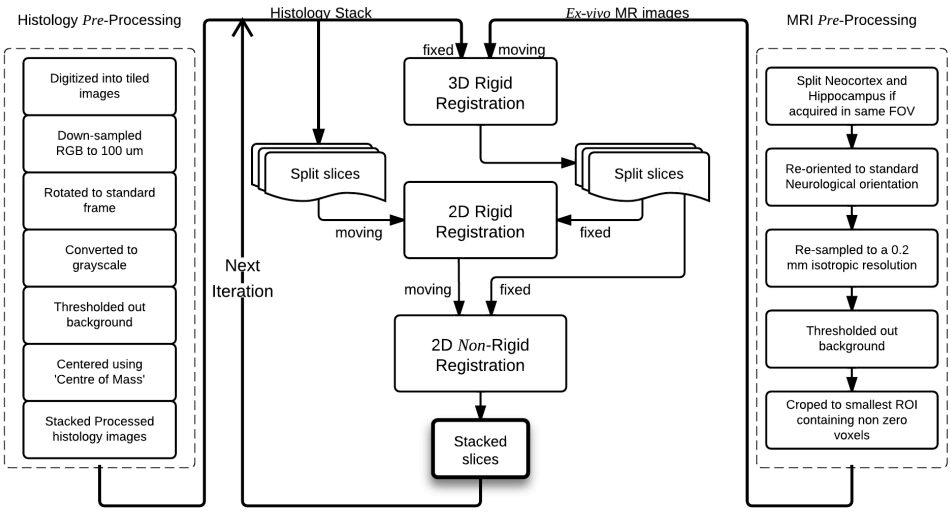

Figure 2.3: Registration pipeline showing pre-processing steps of the data and our iterative 2D-3D approach. The left column demonstrates the pre-processing steps applied to the histology slides sequentially from top to bottom. Likewise, the right column represents the pre-processing steps applied to the MRI of the specimens. The resulting histology stack acts as a fixed image to transform the MR image in a 3D rigid registration. The transformed image as well as the stack are split into slices 4.4 mm apart where each histology slice has a corresponding MRI slice. These MR slices act as fixed images to deform the histology slices rigidly then non-rigidly. The resulting deformed histology slices are stacked and fed back into the 3D rigid registration for the next iteration.

The images were then background masked using a percentile threshold, resampled to 0.2 mm isotropic resolution, and cropped around the perimeter of the specimen.

Histology image pre-processing

The digitized histology images were similarly reoriented into a standard orientation, with the origin in the top-left image corner corresponding to superior-right in anatomical orientation, using the Aperio ImageScope software and the corresponding MRI as a reference. The images were then down-sampled to 200 μm in-plane resolution and converted into NIFTI format, where each RGB channel was represented as a slice in a 3D volume, to match the resolution of the acquired *ex-vivo* MRI. We converted the images to grayscale by extracting the green channel, since this channel was found to possess the best gray/white matter contrast in the H&E stained slides. Finally, the images were background masked and centered in a standard 60mm field of view using the image-based center-of-mass in each slide.

Rigid registration

Rigid registration in our iterative scheme was carried out with the *flirt* tool from [17] (FSL, `http://fsl.fmrib.ox.ac.uk/flirt`) to perform the 3D and 2D registration. The default multi-modal cost function (correlation ratio) was applied and the registration was constrained to a rigid transform model with 6 and 3 degrees of freedom respectively for the 3D and 2D steps. The default correlation ratio cost function was found to produce accurate results, and the use of normalized mutual information (NMI) in the rigid registration was found to produce comparable results.

Non-rigid registration

A deformable registration between corresponding histology and MRI slices was employed to account for any anisotropic tissue deformations that can occur during histological processing, sectioning, and staining. We used a fast non-rigid registration that makes use of a B-spline deformation field and a normalized mutual information cost-function [18, 19] (NiftyReg,`http://sourceforge.net/projects/niftyreg/`).

The B-spline image registration used a three-level multi-resolution image pyramid with final control point spacing of 2 mm. This control point spacing was chosen after a number of different control point spacings (0.1 , 0.5 ,1 , 2, 4, 6mm) were qualitatively evaluated on representative sections on multiple specimens and the 2mm spacing was found to perform best, as it is small enough to account for local deformations encountered and large enough to avoid noise and provide a smooth deformation. Non-rigid registration was carried out starting at iteration 3 of the algorithm and not having been employed in the first two iterations to ensure the sufficient convergence of the rigid registration step. Furthermore, for slices where foreground of the MRI image or histology image were below a specified threshold, non-rigid registration was not performed and a zero deformation was assumed for the slice. The deformation penalty term (bending energy of the spline at a control point), was successively relaxed after each iteration to allow for greater deformations as the alignment is improved over each iteration. Specifically the sequence of bending energies employed at the iterative registration steps were {0.5,0.025,0.01}, for iterations 3-5.

Due to histology tissue breakage and loss, a final registration step was added where binary 'ignore' masks defined on the registered histology slices were included in the deformable registration scheme. These ignore masks were manually-defined in 3D Slicer

(`http://www.slicer.org`) using a large 2 mm radius paintbrush on regions of the MRI image where tissue loss is readily apparent in corresponding regions of the histology image, preventing these regions from contributing to the registration, which would result in incorrect deformations since one-to-one tissue correspondence is unattainable. The average percentage of sections requiring registration masks was 75% and 82.5% for the neocortex and hippocampus respectively. An example of a registration mask for a hippocampal section is shown on Figure 2.8-e.

Coregistration of additional staining

As noted previously additional IHC staining was performed on a subset of blocks for clinical diagnostic purposes. To make use of these IHC stained images in future quantitative analysis, a supplementary registration step was carried out in order to register the sections with additional IHC to the sections with H&E stains. This registration step must be performed for these additional stains or IHC since additional sections were cut, placed on slides, and processed for each stain. We performed 2D affine registration between the H&E and the each IHC stained image with the *flirt* tool [17] on histology images downsampled to 200 μm resolution and converted to grayscale. We performed this registration for NeuN and GFAP IHC since these were the most common and relevant in diagnosis or quantification of neuronal loss, cytoarchitectural abnormalities, and gliosis.

2.2.6 Registration validation

Landmark-based validation

To validate our registration protocol, we computed target registration error (TRE) based on manually-identified corresponding intrinsic landmarks on MR images and histology slices. These landmarks were used as independent targets to assess the accuracy of the registration at each iteration of the iterative registration scheme, as well as after deformable warping of the images. We found that micro-vasculature or micro-bleeds that were visible on the H&E histology slides appeared as dark hypo-intense regions in the *ex-vivo* T2-weighted MRI, as demonstrated in Figure 2.4. First, one rater identified landmarks on histology slides (downsampled to 10μm per pixel), restricting selection to vasculature with a transverse diameter of more than 35 pixels wide, assuming an ellipsoid shape.

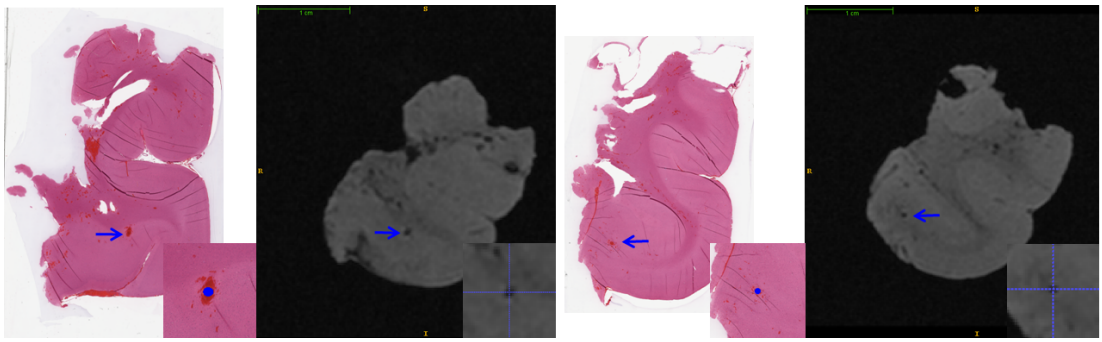

Figure 2.4: Example of the chosen intrinsic landmarks on histology and their localized corresponding landmark on a neocortical *ex-vivo* MRI specimen. The arrows in blue pinpoint the micro vasculature used as targets for the TLE calculations on both histology and MRI. A zoomed in window demonstrates the targets on both modalities with cross hairs indicating the target coordinates on MRI and a circle showing the chosen coordinates on histology.

The most anterior and posterior histology slices in many cases of both specimens did not contain sufficient intact tissue for reliable placement of anatomical landmarks.

The landmarks were 20 per neocortical specimen and 12 per hippocampal specimen on average. Figure 2.5 demonstrates the distribution of landmarks within a neocortical specimen. Three raters then independently searched through the *ex-vivo* MRI to locate corresponding landmarks in the MRI images representing the centroid of these micro-vasculature or micro-bleeds. Since tissue contrast varies throughout the specimen, other MR scans of the specimen were used to facilitate the localization process. To compute the TRE the coordinates for all three raters were averaged to generate a consensus set of MRI landmarks. A total of 215 pairs of corresponding landmarks were identified for the TRE calculations in the twelve specimens. Note that, to ensure consistent landmark locations, only a single set of the histology landmarks was used. For the separate registration between the original H&E stain and the additional IHC (NeuN, GFAP), the target registration error of the 2D affine registration was evaluated for 2 subject neocortical specimens, in a total of 5 blocks, placing a total of 40 pairs of intrinsic landmarks. These histology intrinsic landmarks consisted of micro-vasculature or micro-bleeds visible on the different types of stains and IHC, resembling the histology landmarks used to validate our MRI to histology registration. The 2D euclidean distance was measured between these corresponding landmarks to compute the TRE.

Localization error and statistical analysis

Target localization incorporates human error in localizing the coordinates which combines with the image registration error to produce the TRE measurements. The target localization error (TLE) was calculated on *ex-vivo* MRI images as an unbiased estimator of the standard deviation of repeated localizations of the same landmark by the same rater [20], described by the equation below:

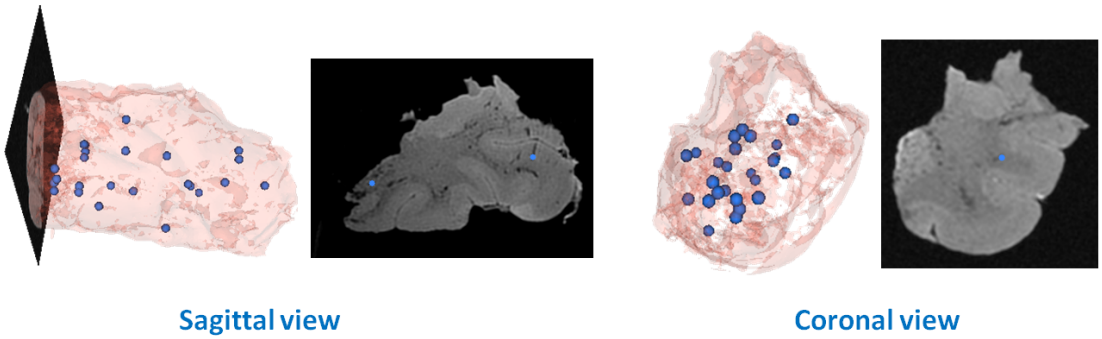

Figure 2.5: 3D visualization revealing the wide spatial distribution of validation landmarks (blue spheres) within an exemplar neocortical specimen in sagittal and coronal views.

$$TLE = \sqrt{\frac{1}{J}\sum_{j=1}^{J}\frac{1}{K-1}\sum_{K=1}^{K}\|P_{j,k} - \frac{1}{K}\sum_{k=1}^{K}P_{j,k}\|^2}$$

where $P_{j,k}$ is the $k-$th localization of the $j-$th landmark. A total of five localization ($K = 5$) of twenty landmarks ($J = 20$) was performed.

Inter-rater variability was measured as an estimator of the standard of deviation of repeated localization of the same landmarks by different raters, where a hundred and twenty eight landmarks ($J = 128$) were placed by three different raters ($K = 3$). Statistical analyses were performed in Prism 5.04 (GraphPad Software, San Diego, CA). To assess for significant differences between the several iterations of the algorithm and across rigid and non-rigid steps , we computed a repeated-measures analysis of variance (ANOVA) of the mean TRE value of each of these steps followed by Bonferroni multiple-comparison correction. A Bartlett's test for equal variances was conducted between all iterations (rigid and non-rigid) of the algorithm to verify the equal variance assumption of the ANOVA tests.

2.3 Results

The proposed methodology required ~ 85 min (including setup) for *ex-vivo* imaging and < 10 min for execution of both the rigid and non rigid components of the algorithm (excluding the manual re-orientation step in the pre-processing scheme and the time for definition of ignore masks). Evaluation of the protocol was performed by localization of micro vasculature landmarks seen on both modalities by three raters. The localization protocol yielded 2-4 homologous landmarks on each of 8-12 sections per neocortex specimen and 1-3 landmarks on each of 6-8 sections per hippocampus specimen. Our registration protocol produced a mean target registration error of 0.76 ± 0.66 for hippocampal specimens, as shown in table 2.3, and 0.98 ± 0.60 for neocortical specimens. The mean TRE was below 1.2 mm after the last step of the registration algorithm in all cases including both specimens. The mean landmark localization error for the three raters was 0.21 mm, relative to an MRI voxel size of 0.35×0.35×0.4 mm, while the inter-rater reliability between the raters was 0.33 mm. Figure 2.6 shows the registration errors across all steps of the algorithm including both rigid and non-rigid components for both specimens. The errors are shown first along iterations 1, 3 and 5 of the rigid component then the non-rigid steps beginning with a step using a high bending energy regularization penalty; then a low penalty weight and finally deformable registration utilizing ignore masks, that account for tissue breakage and differential shrinkage. The mean error of the rigid iterations reaches a plateau around iteration 5 for both specimens. The masked imaged based step outperformed the non-masked registration as expected by avoiding tissue breakage. For the supplemental 2D affine registration between sections with the original H&E stain and sections with the additional IHC (NeuN, GFAP), the target registration error was 0.46 ± 0.31 and 0.41 ± 0.23 for NeuN and

GFAP respectively. This validation demonstrates our ability to accurately align, and potentially correlate, MRI with additional stains and immunohistochemistry.

Figure 2.7 shows three neocortical slices with their corresponding MRI slices, that represent the locations where the histology cuts were made with respect to the MRI scans of the resections, as well as the transformations of the slices after deformable registration. A picture of the resected specimen along with a volume rendering demonstrating the location of these histology slices in respect to the whole specimen are also shown in the figure. Checkerboard images of both rigid and non-rigid registration for a hippocampal slice are displayed in figure 2.8, which also shows a rendered representation of both sides of the hippocampus where the histology slice was cut.

The Bartlett's test confirmed the validity of the equal variance assumption for the ANOVA analyses of both specimens ($P > 0.05$). The significant results of the ANOVA analysis are shown in the 'Mean' row of tables 2.3 and 2.4. The ANOVA analysis, between the first deformable registration step (High Bending Energy) and the last rigid step (Iteration 5), failed to show a statistically significant difference of the mean TREs for both the hippocampus ($P > 0.05$, 95 % Confidence Interval [CI] of difference -0.2666 to 1.653) and neocortex ($P > 0.05$, 95 % CI -0.0147 to 1.54). However, this test did demonstrate a significant decrease in TRE between (High Bending Energy) and the first rigid iteration (Iteration 1) for the hippocampus and neocortex respectively ($P \leq 0.01$, 95 % CI 0.143 to 1.69 and $P \leq 0.05$, 95 % CI -0.2040 to 1.715). In comparison, decreasing the bending energy weight penalty produced significantly lower mean TRE than the final rigid iteration step (Iteration 5) for the hippocampus and neocortex respectively ($P \leq 0.001$, 95 % CI 0.449 to 2.00 and $P \leq 0.01$, 95 % CI 0.3516 to 2.271). The proposed masked non-rigid scheme (Masked NR) had as well significantly

lower TRE ($P \leq 0.0001$) than Iteration5 for both the hippocampus (95 % CI 0.590 to 2.14 mm) and neocortex (95 % CI 0.5143 - 2.434).

	It.1	It.3	It.5	H.B.E	L.B.E	Masked N.R
Subj 1	2.07±0.96	2.05±0.97	2.05±0.98	1.35±0.85	0.88±0.67	0.73±0.85
Subj 2	2.81±0.54	2.87±0.63	2.74±0.80	2.52±0.94	1.42±0.94	1.03±0.94
Subj 3	2.13±1.78	2.12±1.74	2.09±1.73	1.30±0.78	0.73±0.42	0.62±0.40
Subj 4	2.19±1.02	2.09±1.02	2.07±1.21	1.01±0.54	0.68±0.37	0.68±0.42
Subj 5	2.05±0.84	1.86±0.85	1.78±0.95	1.15±0.68	0.75±0.43	0.72±0.45
Mean	2.25±1.10	2.18±1.11	2.15±1.14	1.46 ± 0.77†	0.89 ± 0.61‡	0.76 ± 0.66‡

Table 2.3: TRE values for hippocampal registration across iterations. H.B.E: Non-rigid with a High Bending Energy penalty, L.B.E: Non-rigid with a Low Bending Energy penalty. † : $P \leq 0.01$ between means registration step and Rigid Iteration 1. ‡ : $P \leq 0.01$ between means of registration step and Rigid Iteration 5.

2.4 Discussion

In this article, we have described a method to reliably register *ex-vivo* MRI and sparsely sliced histology slides of neocortex and hippocampus specimens. Our protocol is a landmark free algorithm that produced sub-millimeter accuracy for hippocampal registration and close to 1-mm of error for temporal lobe neocortical registration. Correlating MRI with histopathology is imperative in the validation of new imaging sequences, since verification of pathological anomalies underlying signal changes is needed to enable these sequences to ultimately gain clinical acceptance. The intrinsic higher resolution of *ex-vivo* MR images provides a superior opportunity to further examine the

	It.1	It.3	It.5	H.B.E	L.B.E	Masked N.R
Subj 1	2.97±0.86	2.98±0.86	2.96±0.87	1.55±1.21	1.26±0.66	1.08±0.52
Subj 2	2.36±0.83	1.92±0.84	1.91±0.94	1.69±1.17	0.83±0.85	0.72±0.68
Subj 3	2.23±1.40	2.08±1.37	2.07±1.37	1.15±1.15	0.98±0.99	0.83±0.70
Subj 4	2.41±1.61	2.40±1.76	2.38±1.89	2.17±0.88	1.17±0.68	1.05±0.65
Subj 5	2.19±1.02	2.08±1.02	2.06±1.01	1.01±0.43	1.02±0.45	0.87±0.38
Subj 6	2.23±1.63	2.24±1.65	2.25±1.65	2.06±0.61	1.35±0.57	1.12±0.52
Subj 7	2.16±1.41	2.14±1.44	2.11±1.44	1.42±0.55	1.15±0.49	1.15±0.35
Mean	2.37±1.19	2.26±1.22	2.25±1.28	1.60 ± 1.01†	1.11 ± 0.75‡	0.98 ± 0.60‡

Table 2.4: TRE values for neocortical registration across iterations.H.BE: Non-rigid with a High Bending Energy penalty,L. B.E: Non-rigid with a Low Bending Energy penalty. † : $P \leq 0.01$ between means registration step and Rigid Iteration 1. ‡ : $P \leq 0.01$ between means of registration step and Rigid Iteration 5.

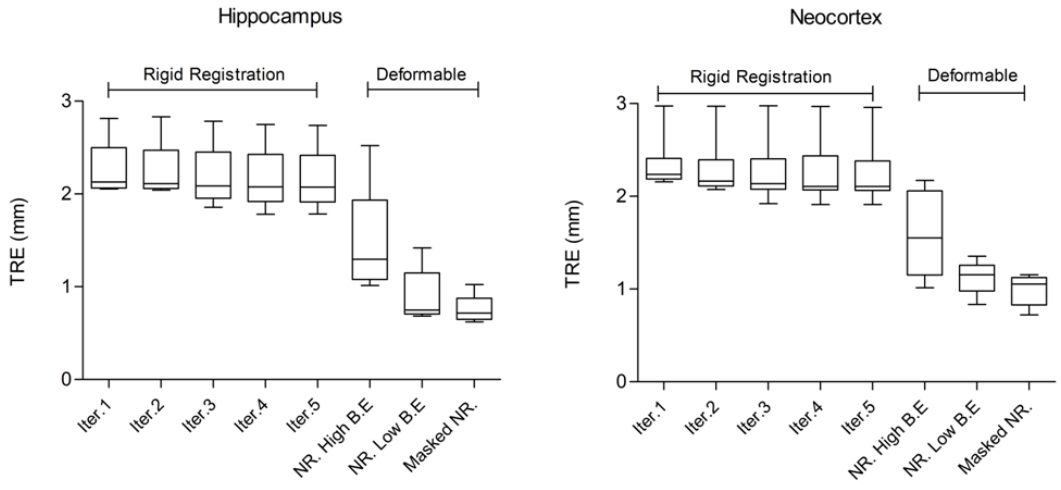

Figure 2.6: Boxplots with 5-95% whiskers of Hippocampal and Neocortical registration target registration errors at each stage of the iterative registration scheme.

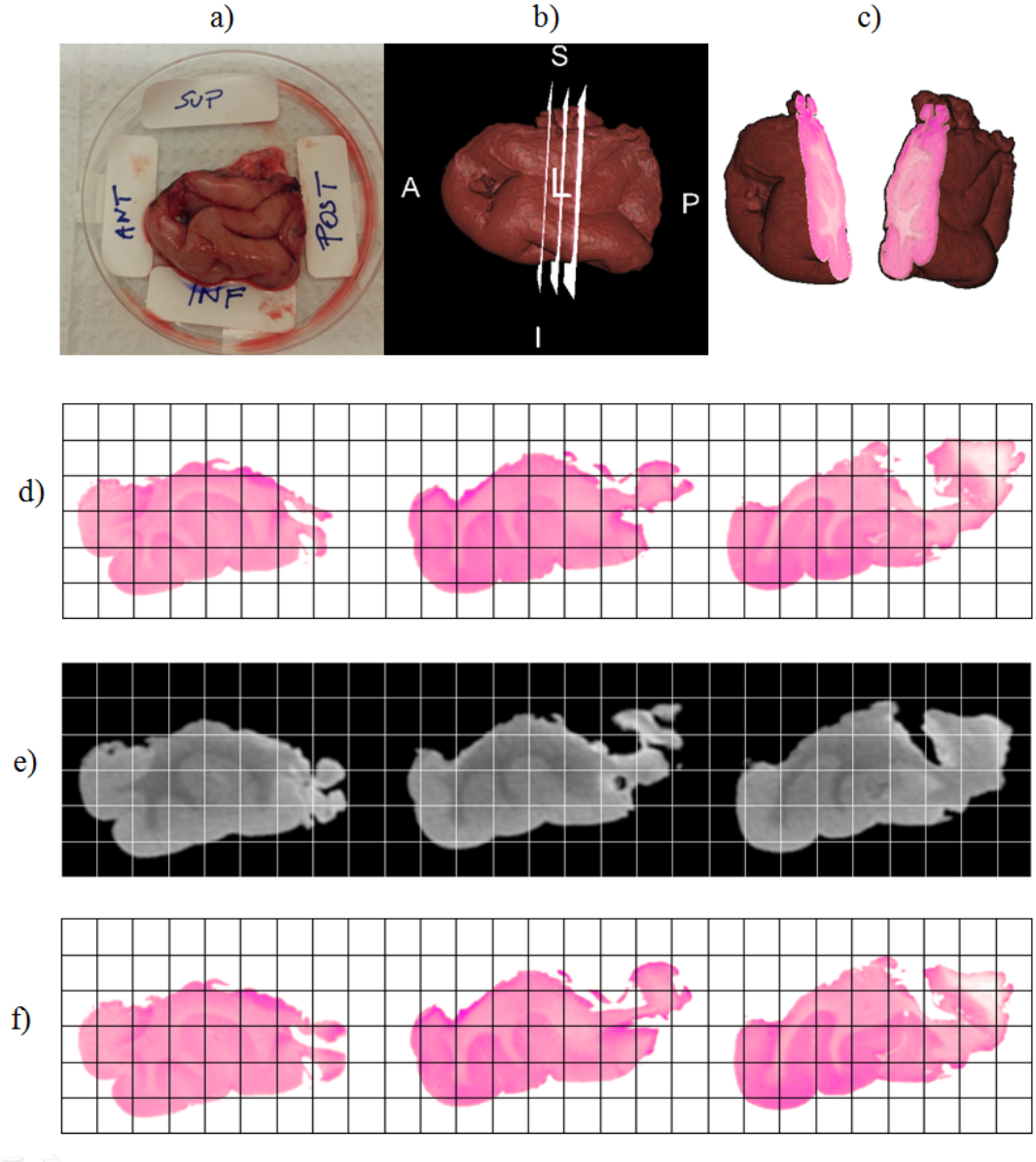

Figure 2.7: Example of a neocortex rigid and deformable registration showing: a) photograph of a neocortical specimen after resected with orientation labels placed by the operating surgeon, b) volume rendering of the MRI of the specimen showing the location of three consecutive histology slices. c) rendering of both sides of the specimen where the middle slice of histology was cut, d) the three histology slices shown in b), e) the corresponding MRI slices after 3D rigid registration, and f) the deformed histology slices after non-rigid registration to their corresponding MRI slices.

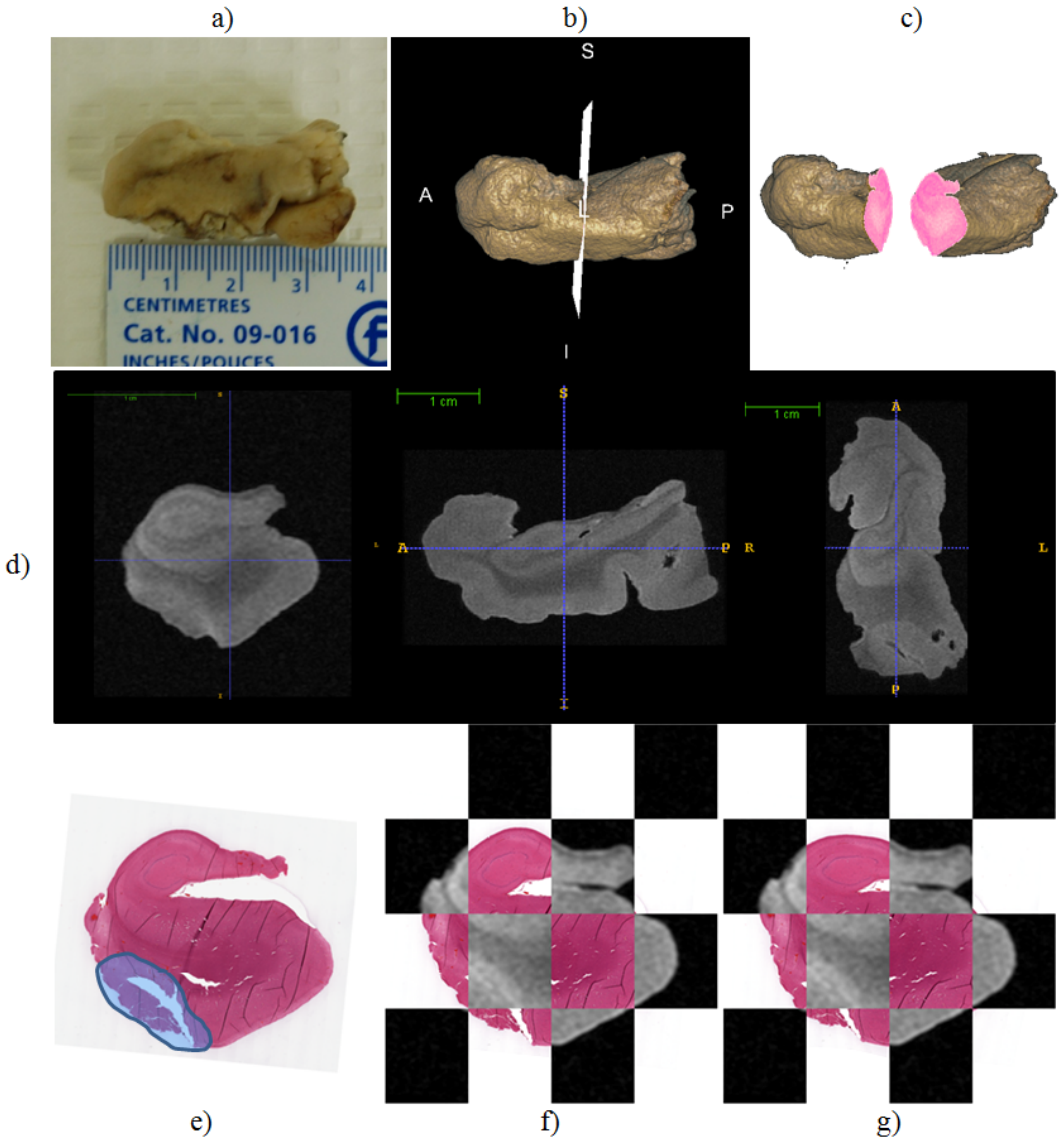

Figure 2.8: Example of a hippocampal rigid and deformable registration showing: a) photograph of a hippocampus before grossing, b) volume rendering of the MRI of the hippocampus demonstrating the location of a histology slice through the specimen, c) rendering of both sides of the hippocampus where the histology slice was cut, and d) three orthogonal views of the hippocampal MRI (left to right: coronal, sagittal, axial). The bottom row depicts: e) a coronal view of the same histological slice with a registration mask over a breakage region shown in blue, f) a checkerboard image showing the MRI and histology before non-rigid registration, and g) a checkerboard image showing the MRI and non-rigidly deformed histology slice.

correlation between MRI and histology. By addressing many challenges of the in-vivo MRI to histology registration, our protocol leaves single modality registration between specimen and preoperative MRI scans as the remaining step. In addition, *ex-vivo* to MRI registration can be used to validate specimen imaging, as it has been shown by Madabhushi et al. [21] in prostate *ex-vivo* imaging examples. While using an intermediate *ex-vivo* registration interrupts the clinical flow for specimen imaging, our algorithm requires ~9 min ±37 seconds on average (for the automated iterative 3D/2D rigid approach plus the non-rigid steps) to register 100 μm coronally sliced (anterior to posterior) histology slices to *ex-vivo* MRI images.

The vast majority of previous attempts at registering MRI and histology using a combination of 2D and 3D transformations, or alternating between 2D and 3D registration, were performed with a reconstructed 3D histology volume from serially sectioned brain specimens at < 700μm [22, 5, 1, 7, 23]. This technique, while producing accurate results, is not compatible with the clinical work flow of pathology departments, where the tissue is sparsely sectioned at a thickness of more than a few mm. Previous registration work flow with sparsely sectioned histology focused on non-brain tissue such as the prostate [24, 25]. Brain tissue has different mechanical characteristics than other tissue in the body, and is more susceptible to deformation as compared to non-brain tissue, such as the prostate. These characteristics cause the brain to deform significantly during surgery and histological processing, increasing the complexity of the registration and the need for deformable registration. For example, it has been shown that sub-millimeter accuracy for registering *ex-vivo* prostate MRI with histology could be achieved using only affine transformations [24]. This finding is very unlikely to be reproduced in brain tissue. In addition, sparsely sectioned brain tissue shows high anatomical variability between consecutive histology slices which may not be true for

other tissue due to the tissue overall shape. This difference in anatomy adds another layer to the complexity of the histology reconstruction and in turn the registration as a whole.

To achieve correlation of MRI and histology at a voxel-wise level, where the highest resolution of the pre-operative MRI is 1-mm isotropic, the registration error would ideally be less than 1mm. This required registration accuracy depends on the physical scale of the pathology being correlated, and in turn the scale at which the image analysis is being performed. However, detection of pathology at single voxels is impractical and thus voxel-based analysis techniques typically involve the use of a smoothing kernel to improve signal-to-noise and be reduce sensitivity to registration error. Recent studies of voxel-based analysis in temporal lobe epilepsy have used smoothing kernels from 4-8 mm (FWHM) [26, 27], thus the overall pre-operative MRI to histology error should be in this range.

The measurement of TRE requires the identification of homologous landmarks on images of both modalities used for registration and is frequently lacking in analyses of these methods. A few articles have quantified and reported TRE in brain histology to MRI. Jacobs et al. [4] reported a registration residual root-mean square (RMS) error of 0.83 mm between histological sections and MRI of ischemic rats and Humm et al. [5] obtained a 0.25 mm registration error for tumor xenografts of one mice using stereotactic fiduciary markers. Both studies could not be extrapolated or compared to human cases due to the methodological differences between these protocols and resected human specimens, as well as the mechanical differences between excised human and whole primate brain. Singh et al. [13] reported a 5.1 mm TRE computed as 3D coordinates of centroid of marked lesions in both modalities, which exceeds the desired

error range for correlation between histopathology and MRI in focal epilepsy as underlying pathologies may be found on the scale of millimeters. Our method produced a mean TRE of 0.76 ± 0.66 and 0.98 ± 0.60 for hippocampal and neocortical specimens respectively, which is sufficient for exploring underlying pathologies of focal epilepsy. For a very small FCD with a volume of $128mm^3$ [28], the mean TRE obtained from our algorithm is able to achieve a 70% overlap of the FCD, assuming it is a sphere. Our mean TLE of 0.21 mm is indicative that the localization variability is not dominating in the TRE measurements. The significantly lower mean TRE for the latter deformable registration found by our ANOVA analysis motivates the use of the hierarchal bending energies as well as the incorporation of ignore masks. It should be noted however that the variability in orientation and depth of the actual section relative to the block face in section is not specifically accounted for in our registration procedure and thus would contribute in part to our target registration error.

A previous method proposed visual comparison of photographs of temporal lobe neocortex tissue slices to MRI, and reported a < 2 mm difference between two observers in most cases [3]. This manual matching technique suffers from a major limitation that is the lack of image registration between the histology and MRI, which in turn dictates the use of region of interest (ROI) based analysis in further studies of correlation [26, 29, 27]. This operator-based method incorporates human bias in locating the corresponding slice of MRI, which explains the 4-mm difference between raters in their last case. Only two ROIs in temporal lobe neocortical specimen were assessed in Lockwood-Estrin's and Eriksson's work to analyze histopathology to MRI correlation. In one instance a negative correlation was seen between grey matter T2 values of fast Flair (fFT2) and NeuN field fraction [26], and another no correlation was found between normalized FLAIR signal intensity (nFSI) and NeuN field fraction within these

ROIs [27]. While the differences between fFT2 and nFSI may not necessarily explain this discrepancy, averaging across the whole area of the ROI may mask signal changes of pathologies smaller than the size of the ROI. Moreover, unlike our protocol, Eriksson et al. [3] focused on matching temporal lobe neocortical specimen and no hippocampal correspondence was performed. Registration of the hippocampus is very challenging due to the smaller size of the resection and the higher susceptibility of the tissue to deform and the histology slices to break apart. Furthermore, performing an image-based registration allows exploratory hypothesis-free analysis at a voxel-wise level and does not require ROI definition, which may be more sensitive to subtle pathologies. Our protocol will be complemented with 3D *in-vivo* to *ex-vivo* MR registration in order to explore the correlations between MRI and histology at greater depth, and provide histopathological validation of multi-modal MRI analysis techniques.

Bibliography

[1] Julien Dauguet, Thierry Delzescaux, Françoise Condé, Jean-François Mangin, Nicholas Ayache, Philippe Hantraye, and Vincent Frouin. Three-dimensional reconstruction of stained histological slices and 3D non-linear registration with in-vivo MRI for whole baboon brain. *Journal of neuroscience methods*, 164(1): 191–204, 2007.

[2] Zhengyi Yang, Kay Richards, Nyoman D Kurniawan, Steven Petrou, and David C Reutens. Mri-guided volume reconstruction of mouse brain from histological sections. *Journal of neuroscience methods*, 211(2):210–217, 2012.

[3] Sofia H Eriksson, Samantha L Free, Maria Thom, William Harkness, Sanjay M Sisodiya, and John S Duncan. Reliable registration of preoperative MRI with histopathology after temporal lobe resections. *Epilepsia*, 46(10):1646–53, 2005.

[4] M A Jacobs, J P Windham, H Soltanian-Zadeh, D J Peck, and R A Knight. Registration and warping of magnetic resonance images to histological sections. *Med Phys*, 26(8):1568–78, 1999.

[5] J L Humm, D Ballon, Y C Hu, S Ruan, C Chui, P K Tulipano, A Erdi, J Koutcher, K Zakian, M Urano, P Zanzonico, C Mattis, J Dyke, Y Chen, P Harrington, J A O'Donoghue, and C C Ling. A stereotactic method for the three-dimensional registration of multi-modality biologic images in animals: NMR, PET, histology, and autoradiography. *Med Phys*, 30(9):2303–14, 2003.

[6] Charles R Meyer, Bradford A Moffat, Kyle K Kuszpit, Peyton L Bland, Paul E Mckeever, Timothy D Johnson, Thomas L Chenevert, Alnawaz Rehemtulla, and Brian D Ross. A methodology for registration of a histological slide and in vivo MRI volume based on optimizing mutual information. *Mol Imaging*, 5(1):16–23, 2006.

[7] J Lebenberg, A S Hérard, A Dubois, J Dauguet, V Frouin, M Dhenain, P Hantraye, and T Delzescaux. Validation of MRI-based 3D digital atlas registration with histological and autoradiographic volumes: An anatomofunctional transgenic mouse brain imaging study. *Neuroimage*, 51(3):1037–1046, 2010.

[8] Grégoire Malandain, Eric Bardinet, Koen Nelissen, and Wim Vanduffel. Fusion of autoradiographs with an MR volume using 2-D and 3-D linear transformations. *Neuroimage*, 23(1):111–27, 2004.

[9] Michael S Breen, Tanya L Lancaster, and David L Wilson. Correcting spatial distortion in histological images. *Comput Med Imaging Graph*, 29(6):405–17, 2005.

[10] Can Ceritoglu, Lei Wang, Lynn D Selemon, John G Csernansky, Michael I Miller, and J Tilak Ratnanather. Large Deformation Diffeomorphic Metric Mapping Registration of Reconstructed 3D Histological Section Images and in vivo MR Images. *Front Hum Neurosci*, 4:43, 2010.

[11] T Schormann, A Dabringhaus, and K Zilles. Statistics of deformations in histology and application to improved alignment with MRI. *IEEE Transactions on Medical Imaging*, 14(1):25–35, 1995.

[12] T.S Kim, M Singh, W Sungkarat, C Zarow, and H Chui. Automatic registration of postmortem brain slices to MRI reference volume. *Nuclear Science, IEEE Transactions on*, 47(4):1607–1613, 2000.

[13] M Singh, A Rajagopalan, T-S Kim, D Hwang, H Chui, X-L Zhang, A-Y Lee, and C Zarow. Co-registration of In-Vivo Human MRI Brain Images to Postmortem Histological Microscopic Images. *Int. J. Imaging Syst. Technol.*, 18(5-6):325–335, 2008.

[14] K Schmierer, F Scaravilli, G J Barker, R Gordon, D G MacManus, and D H Miller. Stereotactic co-registration of magnetic resonance imaging and histopathology in post-mortem multiple sclerosis brain. *Neuropathol Appl Neurobiol*, 29(6):596–601, 2003.

[15] Eli Gibson, José A Gómez, Madeleine Moussa, Cathie Crukley, Glenn Bauman, Aaron Fenster, and Aaron D Ward. 3d reconstruction of prostate histology

based on quantified tissue cutting and deformation parameters. In *SPIE Medical Imaging*, pages 83170N–83170N. International Society for Optics and Photonics, 2012.

[16] Maged Goubran, Ali R Khan, Cathie Crukley, Susan Buchanan, Brendan Santyr, Sandrine deRibaupierre, and Terry M Peters. Robust registration of sparsely sectioned histology to ex-vivo mri of temporal lobe resections. In *SPIE Medical Imaging*, pages 83141V–83141V. International Society for Optics and Photonics, 2012.

[17] M Jenkinson and S Smith. A global optimisation method for robust affine registration of brain images. *Medical Image Analysis*, 5(2):143–56, 2001.

[18] D Rueckert, L I Sonoda, C Hayes, D L Hill, M O Leach, and D J Hawkes. Non-rigid registration using free-form deformations: application to breast MR images. *IEEE Transactions on Medical Imaging*, 18(8):712–21, 1999.

[19] Marc Modat, Gerard R Ridgway, Zeike A Taylor, Manja Lehmann, Josephine Barnes, David J Hawkes, Nick C Fox, and Sébastien Ourselin. Fast free-form deformation using graphics processing units. *Computer methods and programs in biomedicine*, 98(3):278–84, 2010.

[20] J M Fitzpatrick, J B West, and C R Maurer. Predicting error in rigid-body point-based registration. *IEEE Trans Med Imaging*, 17(5):694–702, 1998.

[21] Anant Madabhushi, Michael D Feldman, Dimitris N Metaxas, John Tomaszeweski, and Deborah Chute. Automated detection of prostatic adenocarcinoma from high-resolution ex vivo MRI. *IEEE Transactions on Medical Imaging*, 24(12):1611–25, 2005.

[22] E Bardinet, S Ourselin, D Dormont, G Malandain, D Tandé, K Parain, N Ayache, and J Yelnik. Co-registration of histological, optical and mr data of the human brain. *Medical Image Computing and Computer-Assisted Intervention—MICCAI 2002*, pages 548–555, 2002.

[23] M Mallar Chakravarty, Gilles Bertrand, Charles P Hodge, Abbas F Sadikot, and D Louis Collins. The creation of a brain atlas for image guided neurosurgery using serial histological data. *Neuroimage*, 30(2):359–76, 2006.

[24] Eli Gibson, Cathie Crukley, Mena Gaed, José A Gómez, Madeleine Moussa, Joseph L Chin, Glenn S Bauman, Aaron Fenster, and Aaron D Ward. Registration of prostate histology images to ex vivo mr images via strand-shaped fiducials. *Journal of Magnetic Resonance Imaging*, 36(6):1402–1412, 2012.

[25] Jonathan Chappelow, B. Nicolas Bloch, Neil Rofsky, Elizabeth Genega, Robert Lenkinski, William DeWolf, and Anant Madabhushi. Elastic registration of multimodal prostate mri and histology via multiattribute combined mutual information. *Medical Physics*, 38(4):2005, February 2011. doi: 10.1118/1.3560879. URL `http://link.aip.org/link/MPHYA6/v38/i4/p2005/s1{&}Agg=doi`.

[26] S H Eriksson, S L Free, M Thom, L Martinian, M R Symms, T M Salmenpera, A W McEvoy, W Harkness, J S Duncan, and S M Sisodiya. Correlation of quantitative MRI and neuropathology in epilepsy surgical resection specimens–T2 correlates with neuronal tissue in gray matter. *Neuroimage*, 37(1):48–55, 2007.

[27] Georgia Lockwood-Estrin, Maria Thom, Niels K Focke, Mark R Symms, Lillian Martinian, Sanjay M Sisodiya, John S Duncan, and Sofia H Eriksson. Correlating

3T MRI and histopathology in patients undergoing epilepsy surgery. *Journal of Neuroscience Methods*, 205(1):182–9, 2012.

[28] Pierre Besson, Frederick Andermann, Francois Dubeau, and Andrea Bernasconi. Small focal cortical dysplasia lesions are located at the bottom of a deep sulcus. *Brain*, 131(Pt 12):3246–55, 2008.

[29] S H Eriksson, S L Free, M Thom, M R Symms, L Martinian, J S Duncan, and S M Sisodiya. Quantitative grey matter histological measures do not correlate with grey matter probability values from in vivo MRI in the temporal lobe. *Journal of neuroscience methods*, 181(1):111–8, 2009.

Chapter 3

Registration of Ex-vivo to In-vivo MRI

3.1 Introduction

MRI to histology registration is far from trivial due to the significant deformations undergone by the brain tissue during surgery, handling, and histological processing. As mentioned in chapter 2, these deformations can be split into two main categories, those occurring during surgical resection and those during histological processing [1]. Those due to surgical resection, are three dimensional mechanical deformations that take place once brain tissue is resected, due to its tendency to deform when separated from neighbouring tissue. The histological processing deformations are three dimensional, occurring during sectioning or due to non uniform shrinkage induced by formalin fixation, as well as two dimensional (within-slice) distortions due to stretching of microtome

This chapter is adapted from Goubran et al. "Registration of pre-operative to it ex-vivo MRI of resected specimens: a pipeline for histology to pre-op registration." Journal of neuroscience methods. Under-review

cut sections on a water bath, spreading histology slices over glass slides and staining. The deformations induced during histological processing can be isolated from those from surgery and handling by employing an intermediary MRI image of the specimen or using blockface images for histological reconstruction, splitting the *in-vivo* MRI to histology registration procedure into two distinct problems (*in-vivo* to reference and reference to histology). As described in chapter 2, which focused on registering *ex-vivo* MRI to sparsely sectioned histology hippocampal and neocortical temporal lobe specimens, the intermediate *ex-vivo* MRI or blockface stack can function as an anatomical reference with which the 2D histological slices can be corrected against [2]. In this chapter, however, I focus on the first problem of registering the *in-vivo* MRI to the intermediate *ex-vivo* MRI, and completing a pipeline for histology to *in-vivo* MRI registration in temporal lobe epilepsy.

There have been many attempts in the literature to register *in-vivo* MR images of many organs, such as the prostate [3, 4], to histology slices. Extrapolating these registration techniques to the brain may not be practical since the brain has very different biomechanical properties than other organs and is prone to deformation. Moreover, algorithms optimized for registering other resected organs generally do not deal with part-to-whole registration, and thus may not be applicable in our problem. In the past two decades, there have also been many studies specifically dealing with *in-vivo* brain MRI to post-mortem histology. The majority of these studies focused on primates [5, 6, 1, 7, 8] or rodents [9, 10, 11, 12, 13, 14]. The few studies that registered human brain MRI to histology were performed on whole-brain [15, 16, 17], or single hemisphere [18, 19] postmortem serially sectioned data. Amunts et al. [20] created a 3D model of single subject's brain using post-mortem histological sections reconstructed at 20 μm isotropic resolution and registered it to a T1 average atlas created from 24

subjects. [21] reported registering histology of neocortical specimens from anterior temporal lobectomies to *in-vivo* MRI, however, their approach only involved visually selecting the closest coronal MRI slice for each histology slide, and did not attempt to find a dense correspondence between each histology slide and the corresponding MRI slice. Table 3.1 presents a summary of the studies reporting algorithms for *in-vivo* MRI to histology of the brain in the last 15 years.

The registration approach for *in-vivo* to *ex-vivo* MRI registration uses an automated initialization as well as a landmark-based rigid registration, followed by a landmark deformable registration for hippocampal specimens and an image-based non-rigid warping for neocortical specimens. Using anatomical landmarks is a reliable technique for registration that exploits the operator's anatomical expertise and enforces registration constraints based on the placed landmarks.

3.2 Methods & Materials

3.2.1 Recruitment, surgery & specimen acquisition

Temporal lobe epilepsy patients who were candidates for anterior temporal lobectomy (ATL) surgery were recruited for this study. Patients had preoperative investigations including neuropsychological testing and 1.5T clinical MRI scans which included T1w, T2w, FLAIR, and diffusion-weighted sequences. Patients were monitored with scalp-based electroencephalogram (EEG) video telemetry for seizure characterization, with three patients requiring subdural electrodes placement. In addition to the 1.5T clinical MRI scans performed at the hospital, patients underwent a series of scans on 3T and

Study	Reg features	Trans model	Dim.	Brain section	Mammal	Cohort	Interm. Ref.	Block slice (mm)	TRE (mm)
Kim et al. (1997)	Images+Landmarks	TPS	2D	Whole	Rodent	1	Block	0.02	3 px (2D)
Schormann et al. (1998)	Images	Linear+Elastic	2D+3D	Whole	PM Human	1	Block+Ex MRI	1.8	N/A
Jacobs et al. (1999)	Surfaces+Contours	TPS	3D	Whole	Rodent	15	No	1	0.71
Bardinet et al. (2002)	Images	Affine	2D+3D	Hemi	PM Human	1	Block	0.7	N/A
Lazebnik et al. (2003)	Landmarks	Rigid	2D+3D	Whole	Rabbit	1	No	3	0.52
Malandin et al. (2004)	Images	Affine	2D+3D	Hemi	Primate	1	No	0.04	N/A
Meyer et al. (2006)	User Init+Images	TPS	2D (one slice)	Whole	Rodent	1	Block+Ex MRI	-	N/A
Yelnik et al. (2007)	Contours/Images	Affine	2D+3D	Hemi	PM Human	1	Block	0.7	N/A
Dauguet et al. (2007)	Images	Elastic	2D+3D	Whole	PM Human	2	Block	0.72	N/A
Singh et al. (2008)	Images	Elastic	3D (4 slices)	Whole	PM Human	11	Block	0.03	5.1
Lebenberg et al. (2010)	Images	Affine+Elastic	2D+3D	Hemi	Rodent	7	Block	0.08	N/A
Ceritoglu et al. (2010)	Contours/Images	LDDMM	2D+3D	Hemi	Primate	9	No	0.8	0.39
Osechinskiy et al. (2010)	Landmarks	TPS	3D	Hemi	PM Human	1	No	150	N/A
Choe et al. (2011)	Landmarks	TPS	2D+3D	Whole	Primate	1	Block	0.5	0.32
Yang et al. (2012)	Contours+Images	Rigid+B-spline	2D+3D	Whole	Rodent	4	No	0.04	0.27
Liu et al. (2012)	Landmarks	TPS	3D	Whole	Rodent	5	No	0.04	3

Table 1: Overview of the studies reporting algorithms for *in-vivo* MRI to histology of the brain in the last 15 years. TPS: Thin Plate Spline. LDDMM: Large Deformation Diffeomorphic Metric Mapping.

Table 3.1: Overview of the studies reporting algorithms for *in-vivo* MRI to histology of the brain in the last 15 years.

7T MRI research scanners, described in the *in-vivo* MRI subsection. The study cohort included 10 temporal lobe patients who underwent epilepsy surgery and the resection of two specimens, temporal lobe neocortex and hippocampus, as part of an ongoing project at the Robarts Research Institute. Two hippocampal specimens were not obtained en-bloc due to the use of the cavitron ultrasonic surgical aspirator (CUSA) device during surgery, and were thus excluded from this study. This project was cleared by the Health Sciences Research Ethics Board of Western University, and informed consent was obtained from all patients prior to their participation in the study. Table 3.2 summarizes the age, sex, onset age, seizure origin as well as clinical MRI and pathology findings for our patient cohort.

3.2.2 Patient *in-vivo* MR imaging & map generation

All patients underwent pre-operative imaging on a 3 Tesla Discovery MR750 scanner (General Electric , Milwaukee, WI, U.S.A.) with a 32 channel head coil and consisted of relaxation mapping, diffusion-tensor imaging and resting-state functional imaging. For T1 mapping the 'DESPOT1-HIFI' approach [22] was employed and involved acquisition of two 3D SPGR sagittal T1-weighted images (TR=8.36ms, TE=3.712ms, flip angles =4° & 18°, matrix=220 × 220, slice thickness=1, FOV=220 mm), as well as an additional inversion-prepared SPGR for B1 mapping (TR = 6.46ms, TE = 3.1ms, flip angle = 5°, matrix = 220 × 128, slice thickness = 0.5, FOV = 220 mm). For T2 mapping the 'DESPOT2-FM' approach [23], whereby five balanced steady-state free precession (bSSFP) images were acquired with flip angles 5°, 35° and 68° with phase cycling patterns θ_{RF} = 0° and 180° (TR = 4.608ms, TE = 2.356ms, matrix = 220 × 220, slice thickness = 1, FOV = 220 mm). Images were co-registered to the

first T1-weighted scan in the session using the *Flirt* tool from [24] of the FSL image analysis suite (FSL, `http://fsl.fmrib.ox.ac.uk`) offline to correct for motion between scans. Subsequently, T1 and T2 quantitative maps were reconstructed from their respective weighted images using their signal equations as described in Deoni [22, 23]. The T1 map was subsequently used for the registration protocol for all the patients. Diffusion tensor imaging (DTI), though not used to guide the registration, was performed using an axial spin-echo echo-planar imaging (EPI) sequence with 41 diffusion directions and a b-value of 1000 (TR = 1100ms, TE = 63.2ms, flip angle = 90°, matrix = 96×96, slice thickness = 2.5, FOV = 240 mm). Eddy-current correction and diffusion tensor estimation were performed using FMRIB's Diffusion Toolbox *(FDT)* and maps of fractional anisotropy (FA), mean diffusivity (MD), radial diffusivity (RD) and axial diffusivity (AD) were computed after tensor estimation, transformed and resampled to the coordinate system defined by the 1mm isotropic T1 map.

Patients also underwent high resolution structural imaging at 7T (Agilent Technologies, Santa Clara, CA, U.S.A/ Siemens, Erlangen, Germany), and are also shown in conjunction with the histology for a qualitative comparison. The 7T imaging protocol comprised a T1-weighted magnetization prepared rapid gradient echo (MPRAGE) sequence with a 0.75 mm isotropic resolution (TR = 8.42ms, TE = 3.9ms, flip angles = 11°, matrix = $220 \times 294 \times 230$, FOV = $150 \times 220 \times 172$ mm) and a T2-w turbo spin echo (TSE) sequence with a 0.6 mm isotropic resolution (TR = 3750ms, Effective TE = 470.83ms, Echo spacing=4.73ms, flip angles = 90°, matrix = $260 \times 366 \times 266$, FOV = $156 \times 220 \times 160$ mm, echo train length(ETL) = 199, n.avg = 4)

Patient	Sex	Age	Onset age	Seizure origin	MRI	Path.	Scan Protocol
1⋆	F	26	20	Right	TS	Cortical tubers	3T
2	F	22	15	Right	R. HS	HS	3T
3	M	20	3	Left	L. HS	HS	3T
4⋆	M	19	5	Right	Normal	Gliosis	3T
5	M	49	13	Left	Normal	mild HS	3T
6	F	21	13	Right	Non-specific	mild FCD	3T
7	F	47	8	Right	Normal	dysplasia	9.4T
8	M	19	5	Right	L. HS	HS	9.4T
9	F	43	3	Right	R. HS	HS	9.4T
10	M	34	15	Left	L. HS	HS	9.4T

Table 3.2: Summary of demographics and clinical data, including MRI and histopathological findings, for the ten recruited patients in the study. Registration was performed on both hippocampus and neocortex specimens eight patients. Registration was only performed on the neocortex for cases denoted by ⋆. HS: Hippocampal Sclerosis. FCD : Focal Cortical Dysplasia. TS: Tuberous Sclerosis.

3.2.3 Specimen *ex-vivo* MR imaging

Following surgery, the resected tissue specimens were transferred to the Robarts Research Institute for *ex-vivo* specimen imaging followed by processing in Pathology. After resection, each specimen was oriented by the operating neurosurgeon, photographed and transported on ice to the imaging lab. The *ex-vivo* scanning was performed after overnight fixation in 10% formalin. We have initially tested specimen imaging before and after overnight fixation and found that post-fixation provided superior gray matter-white matter contrast to the pre-fixation images. Each specimen was wrapped in gauze for stabilization, transferred to suitably-sized containers for imaging, and immersed in a fluorine-based lubricant 'Christo-lube MCG 1046' (Lubrication Technology, Inc) prior to imaging to avoid susceptibility artifacts at the tissue boundaries. The specimen scan-

ning was performed on the 3 T scanner used for patient imaging with both hippocampal and neocortical specimens imaged in the same field of view using a 6 channel coil designed to image the carotid artery. The protocol sequences and imaging parameters are described under 'Scan Protocol II' in chapter 2, and included T2-weighted FIESTA images with a resolution of $0.35 \times 0.35 \times 0.4$mm, as well as, fastGRE scans with sixteen echoes.

For cases where overnight imaging was feasible and not disruptive to the clinical work flow (N=4), scanning was performed on a 9.4T small bore Varian MR magnet (Varian, Palo Alto, CA, U.S.A) for improved image resolution and signal-to-noise (SNR), as an alternative to the 3T scan. Each specimen was imaged separately using different coils for a total time of sixteen hours per specimen. The hippocampal specimens were imaged in a millipede birdcage MP30 coil (Agilent, Santa Clara, CA, U.S.A) and the neocortical specimens were scanned with an in-house developed coil. True fast imaging with steady state precession (TrueFisp) images (TR = 7.6 ms, TE = 3.8 ms, flip angle = 30°) were acquired with a resolution of 0.1 mm isotropic, a FOV of $38. \times 25.6 \times 19.2$ mm; and a resolution of 0.2 mm isotropic (FOV of $50 \times 26 \times 44$), for hippocampal and neocortical specimens respectively. Spin-echo diffusion sequences were also acquired (TR = 7.6 ms, TE = 3.8 ms, slice thickness = 0.4mm) with an in-plane resolution of 0.1×0.1 mm and FOV of $38. \times 25.6$ mm, and an in-plane resolution of 0.2×0.2 mm and FOV of 50×26, for hippocampal and neocortical specimens respectively. The T2-weighted images from either protocol were used in the registration pipeline.

3.2.4 Histological processing

Following *ex-vivo* imaging, the specimens underwent histological processing as described in chapter 2. Briefly, the specimens were accessioned and examined prior to coronal blocking every 4.4 mm. Each block was embedded in paraffin and mounted on a microtome where 8 μm thick sections were cut from the face of each block and mounted on slides. One slide from each block was stained with hematoxylin and eosin (H&E) and select blocks processed for immunohistochemistry (IHC) as determined on clinical grounds. The resulting slides were digitized on a ScanScope GL (Aperio Technologies, Vista, CA, USA) bright field slide scanning system at a maximum of 20x optical zoom, and stitched to form full-frame multi-resolution images stored in BigTIFF file format (maximum pixel resolution 0.5 μm). The *ex-vivo* subvolumes, the numbers of histological blocks and sections, as well as NeuN and GFAP sections, are summarized in Table 3.3.

3.2.5 Image registration

The goal of the image registration for a given specimen is to find correspondence between the 3D in-vivo MRI, denoted as I_{in}, and the set of N 2D histology slides, denoted as $\{I^i_{h2D}\}_{i=1...N}$. We divide this process into two distinct steps through the use of an intermediate 3D *ex-vivo* MRI of the specimen, I_{ex}. Chapter 2 [2] described and validated methodology for generating a 3D reconstruction of the histology slides, I_{h3D}, with an iterative approach that alternates between aligning I_{ex} to I_{h3D}, and correcting for within-slices deformations using the aligned I_{ex} as a reference. The registration detailed in this work relates to finding the transformations between I_{in} and I_{ex}, thus connecting images

Subject	Hp vol (mm^3)	Hp blocks	Hp sections	Neo vol (mm^3)	Neo blocks	Neo sections
1*	-	-	-	32669.3	14	37 (13 NeuN, 3 GFAP)
2	3992.4	6	6 (No IHC)	18472.0	12	21 (3 NeuN, 3 GFAP)
3	4677.0	7	8 (1 GFAP)	13830.8	12	15 (2 NeuN)
4*	-	-	-	10885.8	9	15 (3 NeuN, 2 GFAP)
5	3705.1	9	13 (4 GFAP)	20371.0	14	18 (4 GFAP)
6	4373.2	9	11 (2 GFAP)	20896.6	11	15 (2 NeuN, 2 GFAP)
7	3748.6	8	8 (No IHC)	16067.5	15	22 (1 NeuN, 1 GFAP)
8	4588.4	7	8 (1 NeuN)	22719.9	12	14 (1 NeuN, 1 GFAP)
9	3545.0	8	13 (2 GFAP, 3 NeuN)	17225.5	13	28 (8 NeuN, 7 GFAP)
10	3147.5	8	10 (2 GFAP)	19368.6	12	22 (5 NeuN, 5 GFAP)
Mean	3972.2	7	9	19126.2	12	19

Table 3.3: Summary of *ex-vivo* subvolumes, the numbers of histological blocks and sections, as well as NeuN and GFAP sections. In two cases (denoted by $*$) registration was only performed on the neocortex

obtained *in-vivo* with histological slides, as depicted in Figure 3.1. These transformations are obtained in a hierarchical fashion, beginning with an initial translation, $\mathbf{T}^{\mathbf{trans}}_{\mathbf{ex,in}}$, a landmark-based similarity transformation, $\mathbf{T}^{\mathbf{sim}}_{\mathbf{ex,in}}$, and finally a non-rigid deformation, $\phi_{\mathbf{ex,in}}$. To avoid oblique resampling of the highly anisotropic histology images for the purposes of visualization and analysis, the in-vivo and ex-vivo images are ultimately transformed to the space of the 3D reconstructed histology, *Hist3D*, where the reconstructed coronal histology slides are stacked parallel to the anterior-posterior axis.

Initialization

Prior to image registration, the images underwent a series of pre-processing steps, carried out with command-line tools from the FSL image analysis suite (FSL, `http://fsl.fmrib.ox.ac.uk`) and scripts written in MATLAB (The MathWorks Inc., Natick, MA, USA). First, all MR images were converted from the scanner output Dicom (dcm) format to the standard Nifti (nii) format. Since the anatomical orientation of the *ex-vivo* specimens in the scanner bore may not correspond to the head-based scanner orientation, we first updated the orientation matrices of I_{ex} to encode the actual anatomical orientation. We used photographs of the anatomical specimens labeled in the operating room along with 3D models to assist in this process and to obtain the correct pose. The same orientation correction was applied to all images in the same *ex-vivo* scan session.

The goal of the first transformation obtained between I_{ex} and I_{in}, as depicted in Figure 3.1, is to translate the resected specimen into *in-vivo* space, in close proximity to the relevant anatomical structures in the anterior temporal lobe. We performed this step in an automated fashion by computing a translation matrix, $\mathbf{T}^{\mathbf{trans}}_{\mathbf{ex,in}}$ between standardized

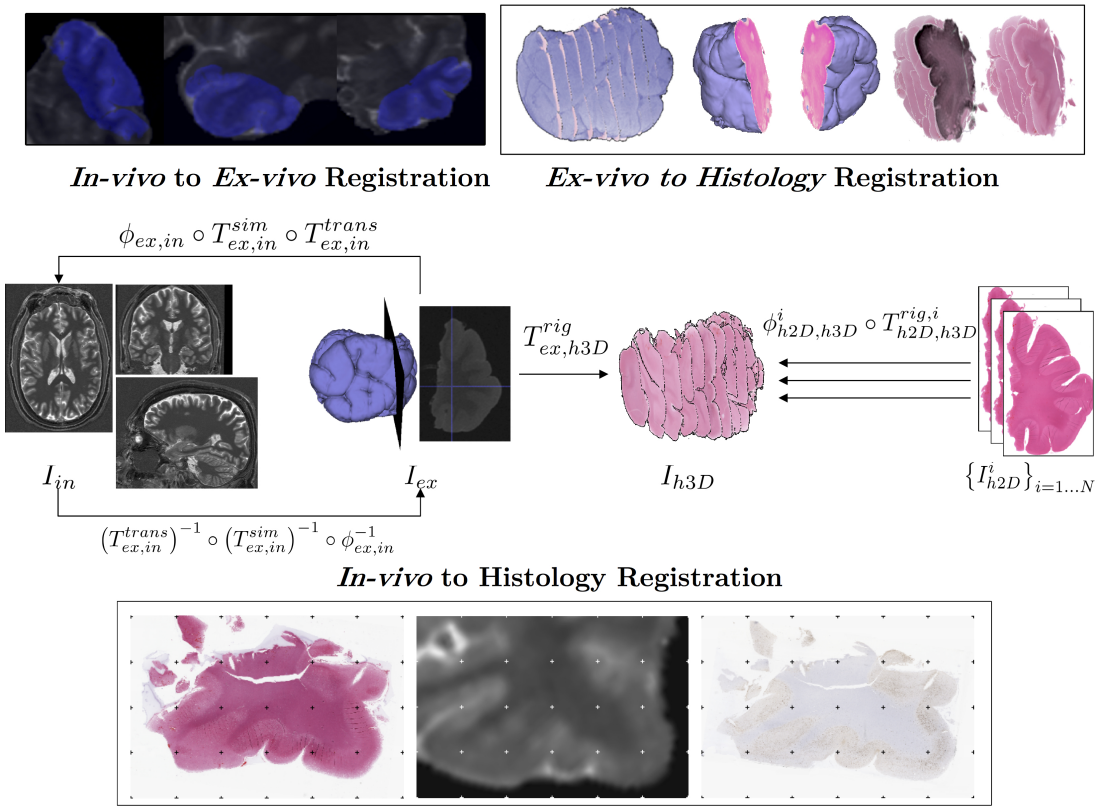

Figure 3.1: In-vivo MRI to histology registration scheme depicting the transformations obtained through each registration step and the resulting images.

coordinates in I_{in} (anterior temporal lobe, hippocampus) and the center of mass in a foreground mask obtained from I_{ex}, generating the *ex-vivo* image I_{ex}^{trans}. The *in-vivo* coordinates were found through linear registration to the montreal neurological institute (MNI) 152 brain atlas, where the center of the anterior temporal lobe and hippocampus in each respective hemisphere were labeled with MNI152 coordinates of $(25, -14, -19)$ and $(40, -2, -30)$ for the right hippocampus and temporal lobe respectively (left side coordinates had the x negated). The images, I_{ex}^{trans} and I_{in}, were then resampled to an isotropic voxel size of 0.4mm, and both cropped to the extents of I_{ex}^{trans}. This initial translation, along with the pose correction, allows for visualization of the *ex-vivo* and *in-vivo* images in the same space and greatly facilitates placement of landmarks for the following step.

Landmark-based similarity transformation

After the initial translation, alignment of the images was further refined using landmark-based registration. Landmarks were placed on the initialized *ex-vivo* and *in-vivo* images I_{ex}^{trans} and I_{in} in the open source software 3D Slicer, `http://www.slicer.org`, version 4.2.1. For the hippocampal specimens, on average up to 10 anatomical landmarks were chosen on orthogonal image planes within the hippocampus proper and the hippocampal subfields, specifically the dentate gyrus, with the guidance of the hippocampal sulcus, as well as the parahippocampal gyrus depending on the extents of the resection. For the neocortical specimens, the anatomical landmarks were chosen on the surface of both the *in-vivo* brain and *ex-vivo* specimen using 3D surface models and photographs from pathological grossing of the specimen. A surface-based approach was chosen since the rich set of cortical surface features visible on both images was amenable

to localization of corresponding landmarks. Surface visualization of the *in-vivo* brain was accomplished with volume-rendering of the skull-stripped and bias-corrected T1-weighted SPGR image (flip angle 18°). An average of 15 landmarks were placed on the surface of each neocortical specimen. The mean number of placed landmarks on the surface of the neocortical specimens was 15 landmarks per specimen. Figures 3.2 and 3.3 demonstrate an example of corresponding anatomical landmarks on both the *in-vivo* T1 map and the *ex-vivo* hippocampi and neocortices, and their distribution within each specimen, respectively.

After placement of landmarks the optimal transformation, $\mathbf{T}^{\mathbf{sim}}_{\mathbf{ex,in}}$ (7 dof rigid transform plus scaling), aligning the *ex-vivo* to the *in-vivo* set was found. The scale factor was employed to allow more flexibility than a rigid transformation to account for physical contraction of the tissue, while restricting unrealistic shearing that would be present in an affine transformation. The similarity transformation was estimated with the *Fiducial Registration* module in Slicer 4 and applied to the translated *ex-vivo* images I^{trans}_{ex} to produce, I^{sim}_{ex}.

Non-rigid registration: Hippocampus

A non-rigid transformation, $\phi_{\mathbf{ex,in}}$, is required to account for deformations of the hippocampi during and after surgery. We chose a user-guided landmark-based approach to account for these deformations since there is a great deal of variability in how much of the anterior hippocampus and the proximal mesial structures is retrieved from case to case, in part due to the fact that some of the tissue is lost through aspiration. Subsequent to the landmark-based similarity transform, we performed a deformable landmark-based registration for our hippocampal specimens using radial basis functions (RBF)

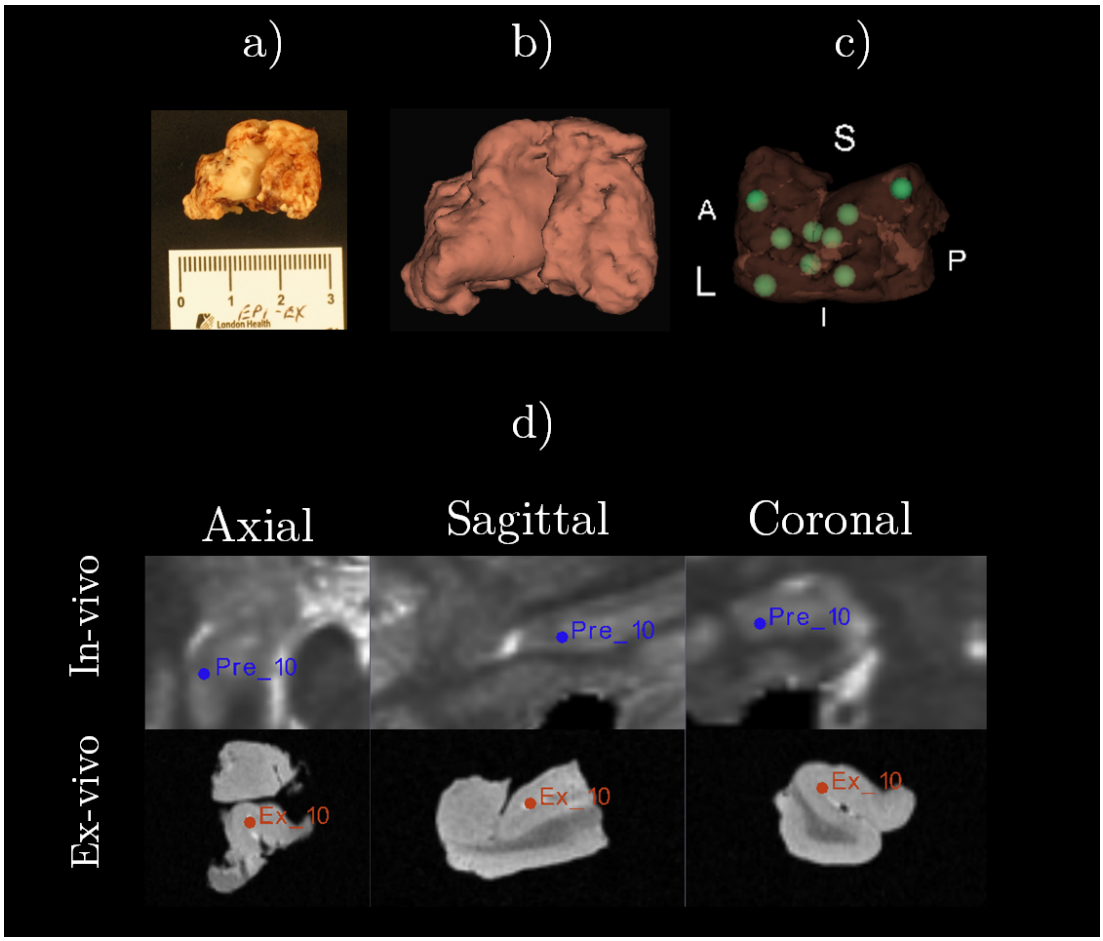

Figure 3.2: Landmark placement for *in-vivo* to *ex-vivo* registration of hippocampal specimens. a) An example hippocampus before grossing. b) Surface rendering of the *ex-vivo* MR of the specimen. c) Distribution of landmarks (green) within the volume of the specimen. d) Three pairs of corresponding landmarks chosen on orthogonal planes of *in-vivo* (blue) and *ex-vivo* (red) images.

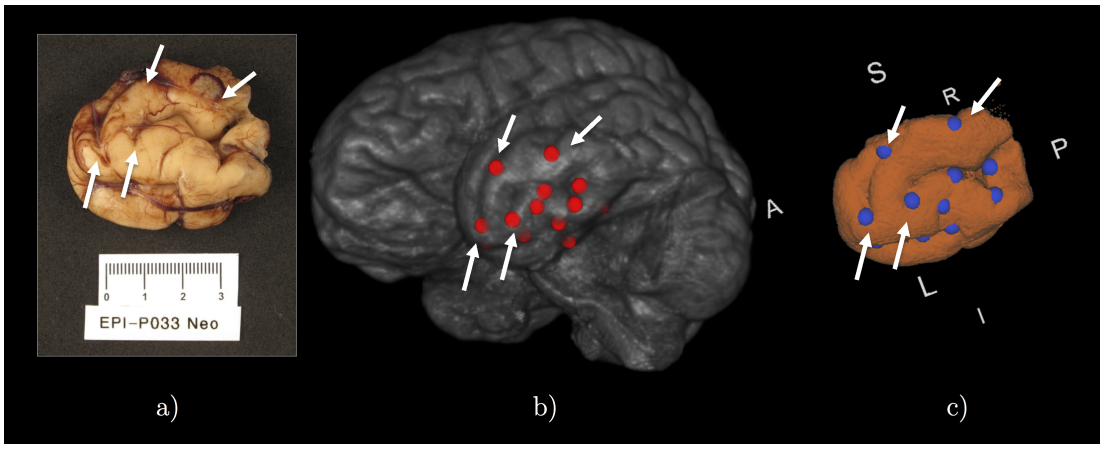

Figure 3.3: Landmark placement for rigid registration of neocortical specimens. The white arrows point to homologous points and their corresponding gyri. a) Neocortex specimen before grossing. b) Volume rendering of the *in-vivo* MR image of the patient with registration landmarks overlaid on top (red). c) Surface rendering of the *ex-vivo* MR image of the specimen with registration landmarks overlaid on top (blue).

for local corrections as implemented in the *Plasti match* plug-in [25] in 3D Slicer. Two new sets of corresponding landmarks were placed, on I_{ex}^{sim} and I_{in}, in coronal MR slices to match the coronally slice histology. Applying the similarity transform before choosing a second set of landmarks for non-rigid registration helps identify landmarks more readily since the anatomy is better aligned at this stage and thus the search space is restricted. After testing a range of parameters and visual analysis of the results, we performed the deformable landmark-based registration using a Gaussian RBF radius of 50 mm and a regularization weight of 0.1. In some cases the regularization parameter was increased, by 0.1 increments, to ensure smoothness of the resulting deformation in regions where errors in landmarks correspondence might warp the images inappropriately. A average of 12 landmarks were used per specimen to perform the registration. Since the *Hist3D* space was chosen as the target space for bringing *in-vivo* MRI and histology into alignment, the inverse deformation field $\phi_{\mathbf{ex,in}}^{-\mathbf{1}}$ was computed using the *Inverse warp* tool in FSL. This inverse warp was afterwards composed with the inverse

transforms, $\mathbf{T}^{\mathbf{sim}}_{\mathbf{ex,in}}$ and $\mathbf{T}^{\mathbf{trans}}_{\mathbf{ex,in}}$, generated in the previous sections, as well as $\mathbf{T}^{\mathbf{rig}}_{\mathbf{ex,h3D}}$ to bring the *in-vivo* image, I_{in}, to the *Hist3D* space, as depicted in Figure 3.1. The resulting composite deformation was applied to the T2 quantitative map, the FA and MD diffusion maps and structural images acquired at 7T as well as clinical 1.5T scans, if available, to warp them to the *Hist3D* space for visualization and analysis.

Non-rigid registration: Neocortex

Since the neocortex specimens are larger in size, deform more regularly, and contain many salient features in the cortical folding patterns, a more automated image-based approach was chosen to provide the analogous non-rigid deformation. We performed a fast non-rigid registration on the rigidly aligned images, I^{sim}_{ex} and I_{in}, that makes use of a B-spline deformation field, and a normalized mutual information (NMI) cost-function [26, 27] (NiftyReg,`http://sourceforge.net/projects/niftyreg/`). The algorithm estimates the transformation, $\phi_{\mathbf{ex,in}}$, that maps the *ex-vivo* image to the *in-vivo* images such that the NMI cost function is minimized, with a regularization term based on the bending energy at each control point. A symmetric implementation was employed that also generates an inverse warp, $\phi^{\mathbf{inv}}_{\mathbf{ex,in}}$, for warping images in the opposite direction. The B-spline registration employed a three-level multi-resolution image pyramid with final control point spacing of 7 voxels or 2.8 mm, small enough to account for local deformations encountered and sufficiently large to avoid noise and provide a smooth deformation. We set the deformation penalty term (bending energy of the spline at a control point) as $1e^{-4}$. As employed for the hippocampal specimens, a composite deformation field, generated by combining $\phi_{\mathbf{ex,in}}$ and the transformations described in previous sections, was applied to our 3T quantitative maps, the 7T high resolution anatomical

scans, if available, and clinical 1.5T scans to warp them to the *Hist3D* space.

In-vivo MRI to Histology registration

Transformations obtained via the methodology outlined in chapter 2 [2] were used to reconstruct a 3D histology stack and register the ex-vivo MRI to this stack. This work also described a supplementary co-registration to bring additional immunohistochemistry (IHC) stains, such as neuronal nuclei (NeuN) and glial fibrillary acidic protein (GFAP), into alignment with the H&E stains used for registration with the MRI. We reconstructed three dimensional RGB histology volumes from downsampled two dimensional sections (20 μm and 100 μm) and warped them using the previously described deformation fields to the intermediate Hist3D space, as shown in Figure 3.8(c).

3.2.6 Registration validation & statistical analysis

Validation of our registration protocol, was achieved by computing target registration error (TRE) based on manually-identified corresponding intrinsic landmarks on *in-vivo* and *ex-vivo* MR images. A set of landmarks, different from those used in the registration steps, was employed to validate our target registration accuracy to assess the accuracy of the registration at both the rigid and deformable stages of the protocol. Matching point landmarks were chosen throughout the hippocampus and neocortex using anatomical structures on the three orthogonal imaging planes. All validation landmarks were placed on the MR images in their original space. To assess significant differences between the rigid and deformable registrations, we computed a Wilcoxon matched-pairs signed-rank test with a two-tailed α value of 0.05 between the mean

TRE values of both registrations. Statistical analyses were performed in Prism 5.04 (GraphPad Software, San Diego, CA).

We also assessed the sensitivity of our registration protocol to using different sets of landmarks for computing the rigid and non-rigid transformations, by performing the registration on three hippocampal specimens, using two independent landmark sets. The two resulting transformations for each specimen were applied to a single set of validation landmarks to assess the differences between TRE.

There is also human error associated with placement of the landmarks used for validation, and this error effectively contributes to the TRE. To quantify this target localization error (TLE) we evaluated the reproducibility of landmark placement on the *in-vivo* MRI given a single set of *ex-vivo* landmarks. TLE was calculated as an unbiased estimator of the standard deviation of repeated localizations of the same landmark by the same rater [28], or the intra-rater variability, described by (1) below:

$$TLE = \sqrt{\frac{1}{J}\sum_{j=1}^{J}\frac{1}{K-1}\sum_{K=1}^{K}\|P_{j,k} - \frac{1}{K}\sum_{k=1}^{K}P_{j,k}\|^2} \tag{3.1}$$

where $P_{j,k}$ is the $k-$th localization of the $j-$th landmark. A total of three localization ($K = 3$) of fifteen landmarks ($J = 15$) was performed.

In addition to the landmark-based validation of registration errors, we performed region based by employing the Dice similarity coefficient, between delineated regions of interests (ROIs) on the histology and MRI, to further validate the registration accuracy. The cortical gray matter crown and adjacent white matter were chosen as ROIs for neocortical specimens, whereas the entorhinal cortex and combined cornu Ammonis (CA) subfields were chosen as targets for hippocampal specimens. Root mean square

error (RMSE) was computed as well for the chosen ROIs in all the specimens. The two dimensional Dice coefficient and RMSE results are summarized in table A.1.

Table 3.4: Summary of Dice similarity metric coefficient and root mean squared error (RMSE) for both tissue types (GM & WM)

	Neocortex		Hippocampus	
	GM	WM	GM	WM
Dice	0.875 ± 0.009	0.851 ± 0.038	0.854 ± 0.027	0.838 ± 0.039
RMSE (mm)	0.335 ± 0.118	0.405 ± 0.239	0.338 ± 0.175	0.375 ± 0.296

3.3 Results

Our registration protocol produced a mean TRE of 1.46 ± 0.30 mm and 1.35 ± 0.11 mm for rigid and non-rigid registrations of neocortical specimens respectively, as shown in Figure 3.4. Similarly, we computed a TRE of 1.71 ± 0.36 mm and 1.41 ± 0.33 mm for rigid and non-rigid registrations of hippocampal specimens respectively. The mean landmark localization error was 0.23 mm, which is small relative to an isotropic 1 mm voxel size of our T1 maps, $\mathbf{I_{in}}$, while the mean difference of TRE for our repeatability experiment of two independent landmark sets was 7% and %11 deviation form previous mean for rigid and non-rigid registrations respectively. The Wilcoxon matched-pairs signed-rank test confirmed that the deformable registration significantly improved the registration accuracy for the neocortex ($P_{neo} = 0.0019$, 95% CI of difference $[-0.20, -0.027]$) and the hippocampus. ($P_{hp} = 0.0011$, 95% CI of difference $[-0.54, -0.038]$).

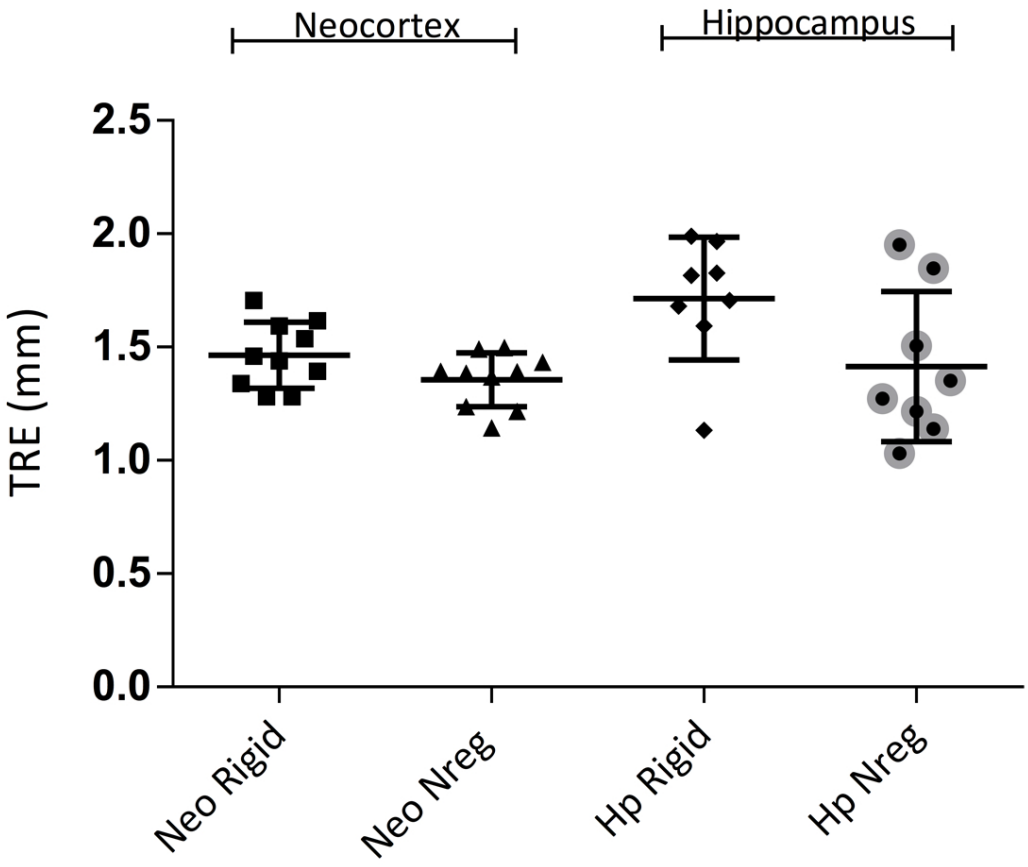

Figure 3.4: Boxplots with standard deviation of Hippocampal and Neocortical registration target registration errors at rigid and non-rigid registration stages.

The results of the landmark-based rigid and non-rigid registrations for the hippocampi are depicted on an example specimen in Figure 3.5. Purple (Figure 3.5(b)) and red (Figure 3.5(c)) represent rigidly and non-rigidly registered hippocampi respectively. The white arrows in the figure show areas were deformable registration outperformed rigid registration. The last row (Figure 3.5(f)) depicts the difference in shape and volume between the hippocampus specimen after rigid transformation and deformable warping. Figure 3.6 shows a comparison between the results of the rigid landmark-based and deformable image-based neocortical registration on an example specimen. As with the hippocampus, the white arrows highlight regions were the non-rigid registration produced a more optimal fit between the images. The figure highlights the high specimen deformations that occur during surgery and thus motivates the use of a free-form deformation model within the registration protocol.

This complete registration pipeline, allows *in-vivo* MR images to be registered to histology of surgically resected specimens, and brings both modalities to an intermediate reference space, based on *ex-vivo* MR images. After generating the deformation fields that bring pre-operative images to the *ex-vivo* space, we warped all the pre-operative scans acquired in the 3 Tesla MRI scanning session, as well as those acquired using the 7T scanner if available. Figure 3.7 presents 7T, 3T, as well as clinical 1.5T scans from a single subject registered to the excised neocortical sample. Registered histological slices of a coronal section of the neocortex are also shown. The figure highlights the effect of signal-to-noise (SNR) and image resolution on the quality of registration. It also highlights the potential of warping quantitative T1 and T2, as well as diffusion maps to histology for use in region of interest (ROI) or voxel-based analysis. A warped, reconstructed 3D stack of consecutive H&E stained slices of a neocortical specimen is shown registered to the *ex-vivo* MRI in Figure 3.8(c). This figure highlights

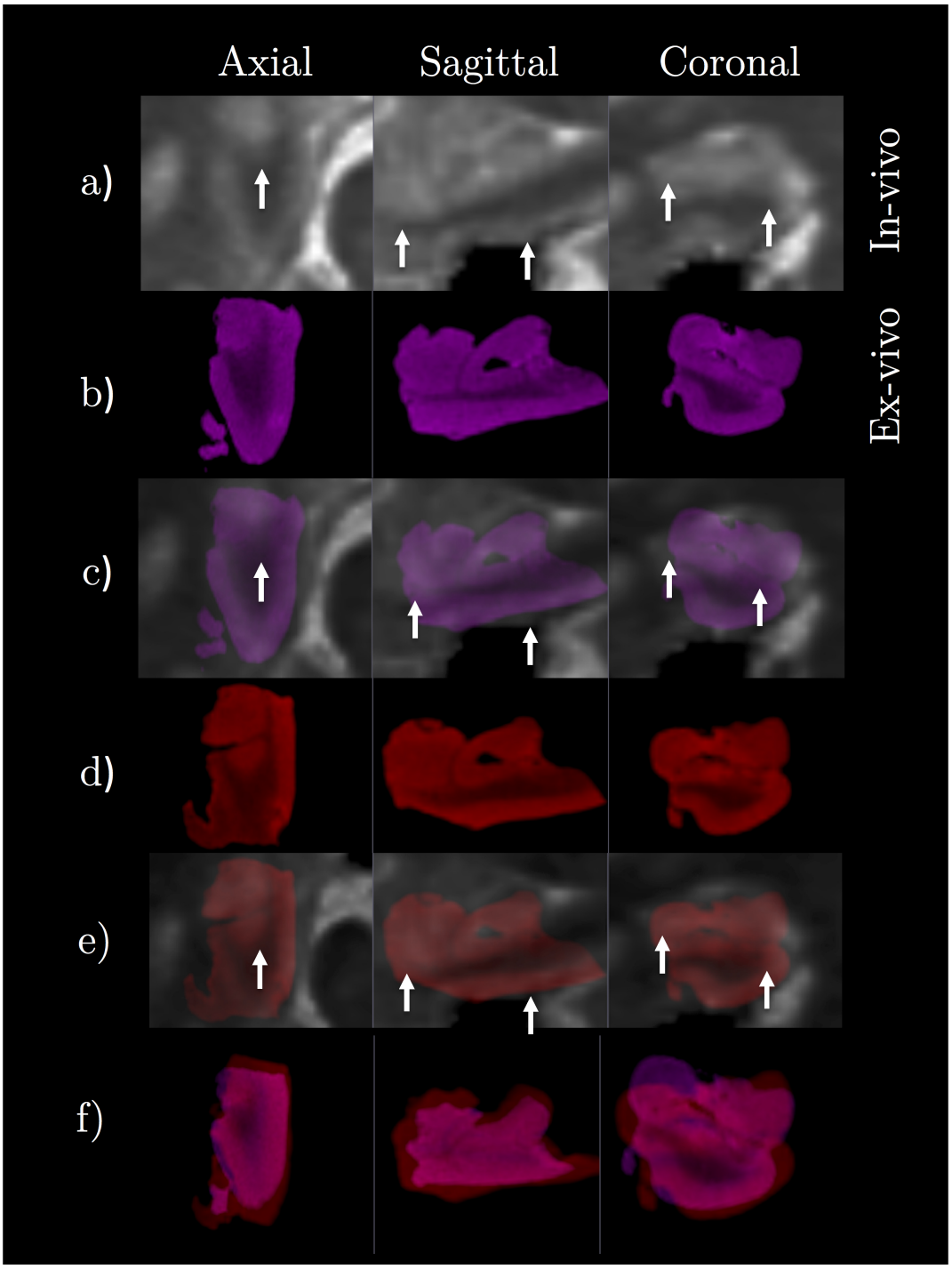

Figure 3.5: Comparison of landmark-based rigid and non-rigid registrations for the hippocampus. The white arrows depict areas where deformable registration outperformed rigid registration. a) Cropped *in-vivo* MR image, I_c, b) Rigidly registered *ex-vivo* specimen (purple), c) Merged view of rigidly registered *ex-vivo* to *in-vivo* image, d) Non-rigidly registered *ex-vivo* specimen (red), e) Merged view of non-rigidly registered *ex-vivo* to *in-vivo* image, f) Difference in shape and volume between the hippocampus specimen after rigid transformation and deformable warping.

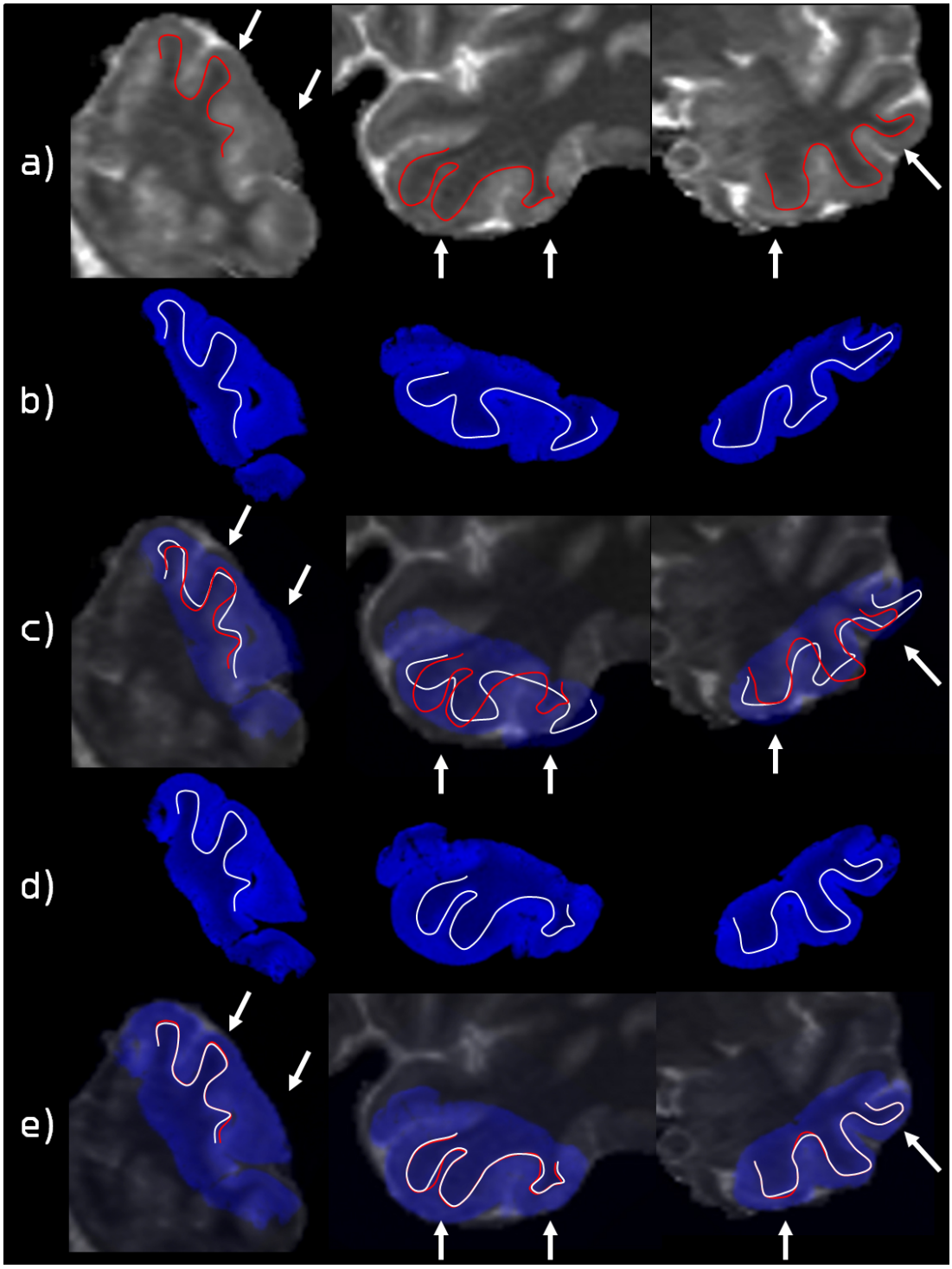

Figure 3.6: Comparison of landmark-based rigid and non-rigid registrations for the neocortex. The white arrows depict areas where deformable registration outperformed rigid registration. a) Cropped *in-vivo* MR image, I_c, b) Rigidly registered *ex-vivo* specimen, c) Merged view of rigidly registered *ex-vivo* to *in-vivo* image, d) Non-rigidly registered *ex-vivo* specimen, e) Merged view of non-rigidly registered *ex-vivo* to *in-vivo* image.

as well the 2D affine registration between H&E and other IHC stained sections (f-i).

3.4 Discussion

The presented in-vivo to ex-vivo MR registration protocol resulted in a target registration error (TRE) of 1.35 ± 0.11mm and 1.41 ± 0.33mm for neocortical and hippocampal specimens respectively. We have previously demonstrated [2] that the errors for the intermediate ex-vivo to histology registration were 0.98 ± 0.60mm and 0.76 ± 0.66mm for neocortical and hippocampal specimens respectively, resulting in a cumulative total error close to 2.33 mm and 2.17 mm for the in-vivo to histology registration. Performing voxel-based registration allows for spatially-local comparison of MRI and histology, and the scale of this analysis is dependent on the achievable registration accuracy. Many previous studies in MRI and histology registration (see Table 1) did not report accuracy or TRE [15, 29, 5, 11, 18, 1, 12, 19], and furthermore many previous studies were proof-of-concept works that included evaluation on only one dataset [16, 15, 29, 30, 5, 11, 18, 19, 8]. Of the studies that did report accuracy on more than one dataset, TRE ranged from sub-millimeter [7, 9, 13] to 3-5mm [14, 17]. Techniques that reported sub-millimeter TRE were applied on either whole brain sections of rodents or serially sectioned histology of primates, thus the smaller scale of anatomy and lack of variable resection boundaries can explain the lower TRE relative to this work. For a more relevant comparison, Singh et al. [17] performed registration of human in-vivo and post-mortem whole brain specimens and reported a TRE of 5.1mm. The only existing work that dealt with resected temporal lobe specimens was [21], however they only aimed to find corresponding slices between MRI and histology, and reported inter- and

intra-observer variability ($< 2mm$) instead of an accuracy measure. This work builds upon these efforts and provides a means to perform voxel-based MRI and histology studies in both neocortical and hippocampal specimens.

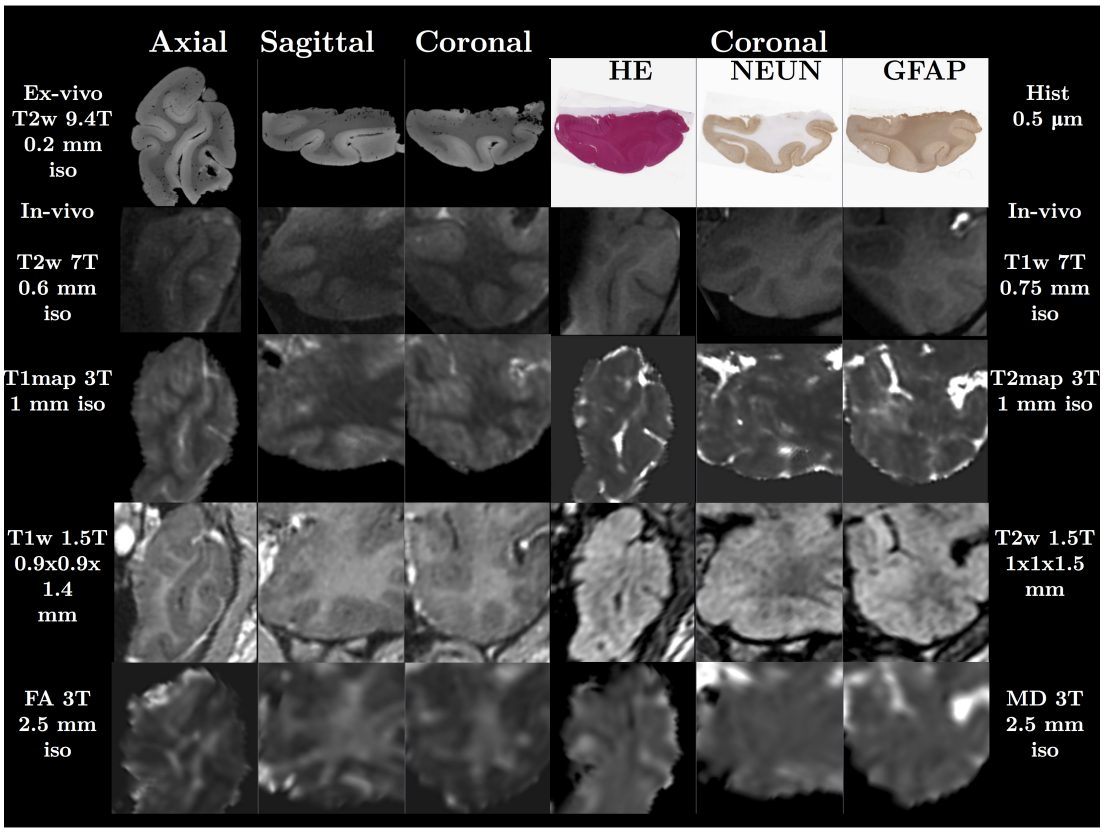

Figure 3.7: Mapping of *in-vivo* MR images to the *aligned* space for a neocortical specimen. The spatial resolution decreases vertically (top to bottom) in the figure. The top row depicts the *ex-vivo* MR (left) and three stains of a histological section (right). The 2^{nd}, 3^{rd} and 4^{th} rows show warped images taken at 7, 3 and 1.5 Tesla respectively. The last row demonstrates warped diffusion maps (FA= fractional anisotropy, MD= mean diffusivity).

There has been a recurring theme of using registration features as segmented contours or surfaces [9, 18, 7, 13], as well as landmarks [30, 19, 8, 14] to find similarities between the images to aid the registration algorithm. Although, manual landmark placement can be time consuming and user-dependent, user anatomical expertise can

enforce registration constraints with placed landmarks when similarity metrics fail to find sufficient correspondences between both modalities. I have also shown that the landmark registration protocols are reproducible across different attempts using two independent sets for the same hippocampal specimens. An implementation of a fully automated deformable registration algorithm based on image features would have decreased the amount of time required for performing the registration tasks; however, it may not have improved the registration accuracy specifically for smaller highly deformed specimens.

Many studies correlating MRI and histology have been done without the use of computational methods for 3D image registration [21, 31, 32]. These rely on visual matching of anatomy or lesions, usually on a slice by slice basis, and are suitable if the tissue of interest (lesion, or anatomy) can be reliably identified in both modalities. However, this is not possible in cases where the visibility or boundaries of the lesion in MRI are different than in histology, or if there is no apparent lesion (as is the case in paradoxical TLE). It is in these cases where MRI-histology registration is crucial, since allows for quantitative investigation of imaging correlates in these lesions that can ultimately improve MRI-based detection and delineation. Another drawback of visual matching is that it becomes more challenging to find corresponding slices when there are 3D deformations present, as the anatomy in a histology slice may not be fully present in a single MRI slice, even if obliquely resampled. Registration methods that can deal with, and compensate for, 3D deformations take the guesswork out of the inherently 2-dimensional visual matching task by using the salient features in the images to define the 3D transformations. Many registration protocols, including ours, also employ specialized tissue handling and slicing protocols designed to minimize deformations and maximize consistency; these are helpful in many cases but do not

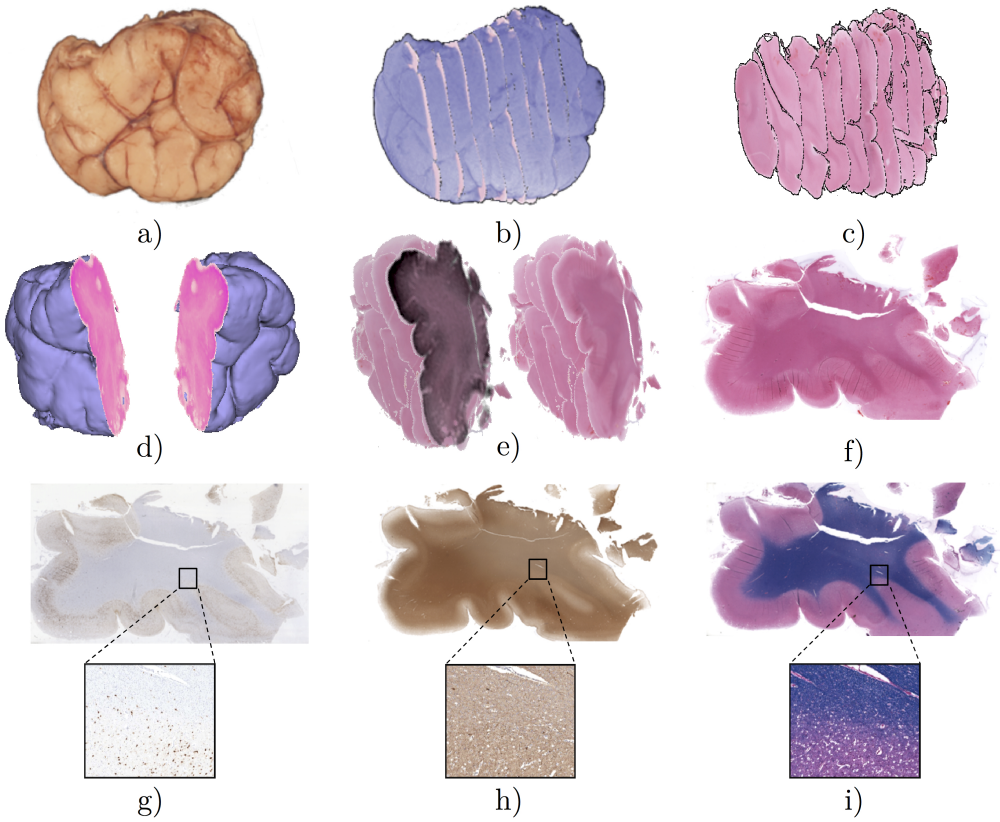

Figure 3.8: 3D histological reconstruction and registration to MR. a) A resected temporal lobe neocortical specimen from epilepsy surgery. b) Rendering of the specimen from a 9.4T MR image registered to histological slices. c) 3D consecutive histology slices in the MR space. d) Rendering of both sides of the specimen where a histology slice was cut. e) Registered MRI slice to the cut histology slice. Four different immunohistochemistry and staining techniques are shown as well for the cut histology section: f) Hematoxylin & Eosin (H&E), g) Neuronal Nuclei (NeuN), h) Microtubule associated protein (MAP)2 and i) Luxol fast blue (LFB).

preclude the use of further image-based or landmark-based registration to obtain greater accuracy.

We have presented and evaluated a detailed protocol for relating in-vivo MRI and histology, however, a true test of its generalizability would be to implement and validate this protocol in another clinical research setting. There are several limitations which could make translation of this technique difficult. For one, this protocol requires close co-operation with both neurosurgery and pathology departments. En-bloc resections are not always performed for temporal lobectomies, and the use of ultrasonic aspirators results in fragmented tissue that is difficult or impossible to deal with in histology correlation studies. A final issue is the reliance on sophisticated imaging resources, such as high-field and ultra-high field magnets for pre-operative and ex-vivo imaging. Despite these limitations, the deployment of this protocol in our unique clinical and research environment allows us to investigate specific clinical questions that can significantly influence our understanding and treatment of temporal lobe epilepsy. The histological basis of focal alterations of relaxometry and diffusion in epilepsy, both proximal and distal to the seizure focus, are important questions that have yet to be resolved [33, 34] and could also impact the clinical use of such sequences in assessing laterality or localization of epileptogenicity. Future work will involve a registration-based correlation of MRI and histology whereby spatial clusters of abnormal T1, T2, fractional anisotropy, or mean diffusivity, could be compared against histological measures such as neuronal density, gliosis, and myelination. The investigation of HS and its sub-types is another area of research which may impact clinical treatment and prediction of surgical outcomes [35]. The presented registration of hippocampal specimens is a critical step in the exploration of imaging and histology correlates in sub-regions of the hippocampus and could lead to better pre-operative assessment of hippocampal sub-types and

perhaps greater sensitivity to subtle changes in early stages of HS.

Bibliography

[1] Julien Dauguet, Thierry Delzescaux, Françoise Condé, Jean-François Mangin, Nicholas Ayache, Philippe Hantraye, and Vincent Frouin. Three-dimensional reconstruction of stained histological slices and 3D non-linear registration with in-vivo MRI for whole baboon brain. *Journal of neuroscience methods*, 164(1): 191–204, 2007.

[2] Maged Goubran, Cathie Crukley, Sandrine de Ribaupierre, Terence M Peters, and Ali R Khan. Image registration of ex-vivo MRI to sparsely sectioned histology of hippocampal and neocortical temporal lobe specimens. *Neuroimage*, 83:770–781, 2013.

[3] A Ward, C Crukley, C McKenzie, J Montreuil, E Gibson, J Gomez, M Moussa, G Bauman, and A Fenster. Registration of in vivo prostate magnetic resonance images to digital histopathology images. *Prostate Cancer Imaging. Computer-Aided Diagnosis, Prognosis, and Intervention*, pages 66–76, 2010.

[4] Jonathan Chappelow, B. Nicolas Bloch, Neil Rofsky, Elizabeth Genega, Robert Lenkinski, William DeWolf, and Anant Madabhushi. Elastic registration of multimodal prostate mri and histology via multiattribute combined mutual information. *Medical Physics*, 38(4):2005, February 2011. doi: 10.1118/1.3560879. URL `http://link.aip.org/link/MPHYA6/v38/i4/p2005/s1{&}Agg=doi`.

[5] Grégoire Malandain, Eric Bardinet, Koen Nelissen, and Wim Vanduffel. Fusion of autoradiographs with an MR volume using 2-D and 3-D linear transformations. *Neuroimage*, 23(1):111–27, 2004.

[6] Michael S Breen, Tanya L Lancaster, and David L Wilson. Correcting spatial distortion in histological images. *Comput Med Imaging Graph*, 29(6):405–17, 2005.

[7] Can Ceritoglu, Lei Wang, Lynn D Selemon, John G Csernansky, Michael I Miller, and J Tilak Ratnanather. Large Deformation Diffeomorphic Metric Mapping Registration of Reconstructed 3D Histological Section Images and in vivo MR Images. *Front Hum Neurosci*, 4:43, 2010.

[8] Ann S Choe, Yurui Gao, Xia Li, Keegan B Compton, Iwona Stepniewska, and Adam W Anderson. Accuracy of image registration between mri and light microscopy in the ex vivo brain. *Magnetic resonance imaging*, 29(5):683–692, 2011.

[9] M A Jacobs, J P Windham, H Soltanian-Zadeh, D J Peck, and R A Knight. Registration and warping of magnetic resonance images to histological sections. *Med Phys*, 26(8):1568–78, 1999.

[10] J L Humm, D Ballon, Y C Hu, S Ruan, C Chui, P K Tulipano, A Erdi, J Koutcher, K Zakian, M Urano, P Zanzonico, C Mattis, J Dyke, Y Chen, P Harrington, J A O'Donoghue, and C C Ling. A stereotactic method for the three-dimensional registration of multi-modality biologic images in animals: NMR, PET, histology, and autoradiography. *Med Phys*, 30(9):2303–14, 2003.

[11] Charles R Meyer, Bradford A Moffat, Kyle K Kuszpit, Peyton L Bland, Paul E Mckeever, Timothy D Johnson, Thomas L Chenevert, Alnawaz Rehemtulla, and

Brian D Ross. A methodology for registration of a histological slide and in vivo MRI volume based on optimizing mutual information. *Mol Imaging*, 5(1):16–23, 2006.

[12] J Lebenberg, A S Hérard, A Dubois, J Dauguet, V Frouin, M Dhenain, P Hantraye, and T Delzescaux. Validation of MRI-based 3D digital atlas registration with histological and autoradiographic volumes: An anatomofunctional transgenic mouse brain imaging study. *Neuroimage*, 51(3):1037–1046, 2010.

[13] Zhengyi Yang, Kay Richards, Nyoman D Kurniawan, Steven Petrou, and David C Reutens. Mri-guided volume reconstruction of mouse brain from histological sections. *Journal of neuroscience methods*, 211(2):210–217, 2012.

[14] Yutong Liu, Balasrinivasa R Sajja, Mariano G Uberti, Howard E Gendelman, Tammy Kielian, and Michael D Boska. Landmark optimization using local curvature for point-based nonlinear rodent brain image registration. *Journal of Biomedical Imaging*, 2012:1, 2012.

[15] T Schormann, A Dabringhaus, and K Zilles. Statistics of deformations in histology and application to improved alignment with MRI. *IEEE Transactions on Medical Imaging*, 14(1):25–35, 1995.

[16] T.S Kim, M Singh, W Sungkarat, C Zarow, and H Chui. Automatic registration of postmortem brain slices to MRI reference volume. *Nuclear Science, IEEE Transactions on*, 47(4):1607–1613, 2000.

[17] M Singh, A Rajagopalan, T-S Kim, D Hwang, H Chui, X-L Zhang, A-Y Lee, and C Zarow. Co-registration of In-Vivo Human MRI Brain Images to Postmortem

Histological Microscopic Images. *Int. J. Imaging Syst. Technol.*, 18(5-6):325–335, 2008.

[18] J Yelnik, E Bardinet, D Dormont, G Malandain, S Ourselin, D Tandé, C Karachi, N Ayache, P Cornu, and Y Agid. A three-dimensional, histological and deformable atlas of the human basal ganglia. I. Atlas construction based on immunohistochemical and MRI data. *Neuroimage*, 34(2):618–638, 2007.

[19] Sergey Osechinskiy and Frithjof Kruggel. Slice-to-Volume Nonrigid Registration of Histological Sections to MR Images of the Human Brain. *Anatomy Research International*, 2011, 2010.

[20] Katrin Amunts, Claude Lepage, Louis Borgeat, Hartmut Mohlberg, Timo Dickscheid, Marc-Étienne Rousseau, Sebastian Bludau, Pierre-Louis Bazin, Lindsay B Lewis, Ana-Maria Oros-Peusquens, et al. Bigbrain: an ultrahigh-resolution 3d human brain model. *Science*, 340(6139):1472–1475, 2013.

[21] Sofia H Eriksson, Samantha L Free, Maria Thom, William Harkness, Sanjay M Sisodiya, and John S Duncan. Reliable registration of preoperative MRI with histopathology after temporal lobe resections. *Epilepsia*, 46(10):1646–53, 2005.

[22] Sean C L Deoni. High-resolution T1 mapping of the brain at 3T with driven equilibrium single pulse observation of T1 with high-speed incorporation of RF field inhomogeneities (DESPOT1-HIFI). *J Magn Reson Imaging*, 26(4):1106–11, 2007.

[23] Sean C L Deoni. Transverse relaxation time (T2) mapping in the brain with off-resonance correction using phase-cycled steady-state free precession imaging. *J Magn Reson Imaging*, 30(2):411–7, 2009.

[24] M Jenkinson and S Smith. A global optimisation method for robust affine registration of brain images. *Medical Image Analysis*, 5(2):143–56, 2001.

[25] Csaba Pinter, Andras Lasso, An Wang, David Jaffray, and Gabor Fichtinger. Slicerrt: Radiation therapy research toolkit for 3d slicer. *Medical physics*, 39 (10):6332–6338, 2012.

[26] D Rueckert, L I Sonoda, C Hayes, D L Hill, M O Leach, and D J Hawkes. Non-rigid registration using free-form deformations: application to breast MR images. *IEEE Transactions on Medical Imaging*, 18(8):712–21, 1999.

[27] Marc Modat, Gerard R Ridgway, Zeike A Taylor, Manja Lehmann, Josephine Barnes, David J Hawkes, Nick C Fox, and Sébastien Ourselin. Fast free-form deformation using graphics processing units. *Computer methods and programs in biomedicine*, 98(3):278–84, 2010.

[28] J M Fitzpatrick, J B West, and C R Maurer. Predicting error in rigid-body point-based registration. *IEEE Trans Med Imaging*, 17(5):694–702, 1998.

[29] E Bardinet, S Ourselin, D Dormont, G Malandain, D Tandé, K Parain, N Ayache, and J Yelnik. Co-registration of histological, optical and mr data of the human brain. *Medical Image Computing and Computer-Assisted Intervention—MICCAI 2002*, pages 548–555, 2002.

[30] Roee S Lazebnik, Tanya L Lancaster, Michael S Breen, Jonathan S Lewin, and David L Wilson. Volume registration using needle paths and point landmarks for evaluation of interventional MRI treatments. *IEEE Transactions on Medical Imaging*, 22(5):653–60, 2003.

[31] Georgia Lockwood-Estrin, Maria Thom, Niels K Focke, Mark R Symms, Lillian Martinian, Sanjay M Sisodiya, John S Duncan, and Sofia H Eriksson. Correlating 3T MRI and histopathology in patients undergoing epilepsy surgery. *Journal of Neuroscience Methods*, 205(1):182–9, 2012.

[32] Rita Garbelli, Gloria Milesi, Valentina Medici, Flavio Villani, Giuseppe Didato, Francesco Deleo, Ludovico D'Incerti, Michela Morbin, Giulia Mazzoleni, Anna Rita Giovagnoli, Annalisa Parente, Ileana Zucca, Alfonso Mastropietro, and Roberto Spreafico. Blurring in patients with temporal lobe epilepsy: clinical, high-field imaging and ultrastructural study. *Brain*, 135(Pt 8):2337–49, 2012.

[33] Fergus J Rugg-Gunn, Sofia H Eriksson, Mark R Symms, Gareth J Barker, Maria Thom, William Harkness, and John S Duncan. Diffusion tensor imaging in refractory epilepsy. *Lancet*, 359(9319):1748–51, 2002.

[34] G D Jackson, A Connelly, J S Duncan, R A Grünewald, and D G Gadian. Detection of hippocampal pathology in intractable partial epilepsy: increased sensitivity with quantitative magnetic resonance T2 relaxometry. *Neurology*, 43(9):1793–9, 1993.

[35] Ingmar Blümcke, Roland Coras, Hajime Miyata, and Cigdem Ozkara. Defining clinico-neuropathological subtypes of mesial temporal lobe epilepsy with hippocampal sclerosis. *Brain Pathol*, 22(3):402–11, 2012.

Chapter 4

Correlation of Neocortical MRI and histology

4.1 Introduction

The registration protocol described in chapters 2 & 3 between histology - currently considered as the ground truth - and in-vivo MRI of resected tissue is a key component towards achieving MRI and histology correlation by bringing together information from both domains. Studies involving MRI and histology correlation from neocortical specimens in TLE have been used to better understand the relationships between the two. Garbelli et al. [1] investigated blurred cortical boundaries in the temporal pole with immunohistochemistry (IHC), and found it to be related to degeneration of fiber bundles. With visually-matched GM and WM ROIs in the middle temporal gyrus,

This chapter is adapted from Goubran et al. "MRI and histology correlation in the neocortex of temporal lobe epilepsy." Annals of neurology. Under-review

Eriksson et al. [2] found a significant negative correlation between GM fast FLAIR T2 (FFT2) and neuronal nuclear antigen (NeuN). A follow-up study [3] investigating GM probability maps with NeuN and glial fibrillary acidic protein (GFAP) did not find any correlations. Similarly, Lockwood-Estrin et al. [4] also incorporating FLAIR (normalized intensities) and DTI still failed to find any correlations. Such data suggest that the pathological basis of abnormal MRI signals is still poorly understood in focal epilepsy.

There may be several reasons why the studies at higher field strength with a larger number of subjects failed to reveal significant correlations between MRI and histology. One potential factor is that errors in the visual matching of slices and regions between MRI and histology, induced by rater error and non-rigid tissue deformations, could have led to different tissue being sampled in MRI and histology ROIs. Another factor could be the use of pseudo-quantitative MRI parameters, such as normalized FLAIR intensities, instead of quantitative relaxometry, since these approaches are more likely to include variability specific to the scan session and scan parameters, and may not precisely represent the intrinsic tissue parameters.

The objective of this chapter is to investigate the histopathological correlates of quantitative relaxometry and DTI from neocortical specimens of intractable TLE patients, while directly addressing these potential confounding issues. I make use of a validated non-rigid image registration protocol to obtain accurate correspondences between quantitative in-vivo MRI and histology images. Quantitative histology parameters from the grey and white matter in each NeuN (representing neuron integrity) and GFAP (representing gliosis) IHC slide are sampled, and then image registration is employed to obtain the corresponding MRI parameters from high-resolution quantitative T1 and T2 maps along with DTI.

4.2 Materials & Methods

4.2.1 Patients and Samples

Our study cohort included 13 TLE (5 males, 8 females, age: 34 ± 15 (range: 18-56)) who underwent anterior temporal lobectomy (ATL) surgery. This project, part of an ongoing research study at the Robarts Research Institute, was cleared by the Health Sciences Research Ethics Board of Western University, and informed consent was obtained from all patients prior to their participation in the study. Patients had preoperative investigations including neuropsychological testing and 1.5T clinical MRI scans, which included T1-weighted, T2-weighted, FLAIR, and diffusion-weighted sequences. Patients were monitored with video-scalp EEG telemetry for seizure characterization, with three patients requiring subdural electrodes placement. In addition to the 1.5T clinical MRI scans performed as part of their clinical diagnosis, patients underwent a series of scans on a 3T MRI research scanner as described in the in-vivo MRI imaging subsection. Table 4.1 summarizes the age at the time of the last consultation prior to surgery, gender, age at seizure onset, electrographic seizure origin as well as clinical MRI and pathology findings for our patient cohort.

4.2.2 *In-vivo* Magnetic Resonance Imaging

All patients underwent pre-operative imaging, comprising relaxation mapping and DTI, on a 3 Tesla Discovery MR750 scanner (General Electric, Milwaukee, WI, U.S.A.) with a 32 channel head coil. In-vivo image acquisition sequences and scanning parameters are described in details in chapter 3. Briefly, the imaging protocol comprises:

Table 4.1: Patient demographics and clinical information including age, gender, onset age, seizure origin as well as clinical MRI and pathology findings for our patient cohort. MTS = mesial temporal sclerosis, MAA= minor architectural abnormalities, Neo. Path. = Neocortical Pathology, Hp. Path. = Hippocampal Pathology,† Previous resection of left temporal lobe tumour (DNET), * not enough tissue to make diagnosis of MTS

ID	Sex	Age	Age of Onset	Sz Origin	Sz Freq.	MRI	Neo. Path.	Hp. Path	Engel outcome	Yrs since surgery
1	F	25	17	L	2	Normal †	Gliosis, Ki67-positive cells in WM	Gliosis	3	2
2	M	20	3	L	16	MTS	Gliosis, MAA	MTS	2	2.1
3	M	18	14	R	32	Possible MTS	Gliosis, MAA	Gliosis*	1	2.1
4	F	48	36	L	28	MTS	Gliosis	MTS	1	1.7
5	F	50	47	L	20	GM/WM blurring	Gliosis	Gliosis*	1	1.6
6	M	31	28	R	2	Normal	Mild gliosis, MAA	Negligible gliosis	1	1.3
7	F	32	19	L	2	MTS	Gliosis	MTS	1	1.2
8	F	43	3	R	4	MTS	Gliosis	MTS	2	1.4
9	F	26	19	R	12	Cortical tubers	Dysplastic lesion, cortical tuber	Gliosis	2	2.5
10	M	34	15	L	2	MTS	Gliosis, focal MAA	MTS	3	1.2
11	F	40	7	R	20	MTS, Porencephaly	Gliosis, MAA	MTS	2	2.5
12	F	56	15	R	8	Normal	Gliosis, arteriosclerosis	Gliosis*	1	1
13	M	23	18	L	12	Normal	Gliosis, MAA, possible FCD type 1a	Gliosis	1	1

1) the DESPOT1-HIFI technique [5] for T1 mapping whereby two SPGR sagittal T1-weighted scans and an inversion-prepared SPGR for B1 mapping are acquired, 2) the DESPOT2-FM approach [6] which relies on five bSSFP scans with different flip angles and phase cycling patterns and 3) an axial SE EPI to obtain DTI. Quantitative T1 and T2 maps were then reconstructed from the weighted images using their signal equations as described in Deoni [5], Deoni et al. [7], and FMRIB's Diffusion Toolbox (FDT) was used for diffusion tensor estimation, Eddy-current correction (EPI distortion) and computation of diffusion indices. We subsequently transformed and resampled the resulting diffusion maps (FA & MD) to the coordinate system defined by the 1mm isotropic T1 map.

4.2.3 Histological processing and quantitative histology

The specimens underwent histological processing (grossing, slicing, embedding, sectioning and digitization) according to the protocol described in chapter 2. Field fraction estimates (proportion of all pixels in the field that were positively-stained) were used to quantify the NeuN and GFAP IHC. These estimates been used in previous studies to represent neuronal integrity and gliosis [2, 3, 4] and is sensitive to the packing density and cell-size of neuronal cell bodies and processes (NeuN) or astrocytes (GFAP). The positive pixel count algorithm (Aperio Technologies, Vista, CA, USA) was employed for this purpose and employs color-based thresholding for hue, saturation, and intensity to determine whether or not a pixel is immuno-positive. Slides were batch processed using scripts written in MATLAB (The MathWorks Inc., Natick, MA, USA), processing the full resolution images in blocks of 100 μm x 100 μm. Hue and saturation thresholds were fixed (Hue value = 0.1, Hue width = 0.2 and saturation = 4x10-2)

and the intensity threshold was chosen for each case to visualize the immuno-positive pixels and account for staining variability between slides.

Field fraction measurements involving dysplastic cortex could be less sensitive when reductions in packing density are accompanied by cyto-morphological size changes, since each would affect the field fraction in opposing directions. To better decouple these factors, we developed a method for segmenting the neuronal cell bodies to provide local estimates of neuron density and size. This procedure first employs colour deconvolution [8] to extract the colour component related to immuno-positive staining, then performs a watershed-based segmentation procedure [9] for splitting joined or connected neurons, removes objects smaller than a predefined area defined as noise (less than 14 μm^2). This provides a segmentation of each individual neuron cell body that can be used to determine the neuron density in this field (# of neurons/field) and the mean size of neuron cell bodies in the field. To further discriminate between neurons, we also categorized them as either small-calibre (granular cells) or large-calibre (pyramidal cells) using an area threshold of 125 μm^2 and reported the density of each of these in the field. This procedure inherently allows analysis for laminar specificity since larger neurons are typically found in layers 3 and 5, and smaller neurons in layer 2 and 4. NeuN slides were batch-processed with scripts written in MATLAB, to extract the neuron-specific quantitative features in each 100 μm x 100 μm field. Figure 4.1 illustrates this procedure and demonstrates the six different quantitative histological features: NeuN field fraction, neuron density, mean neuron size, small neuron density, large neuron density, and GFAP field fraction.

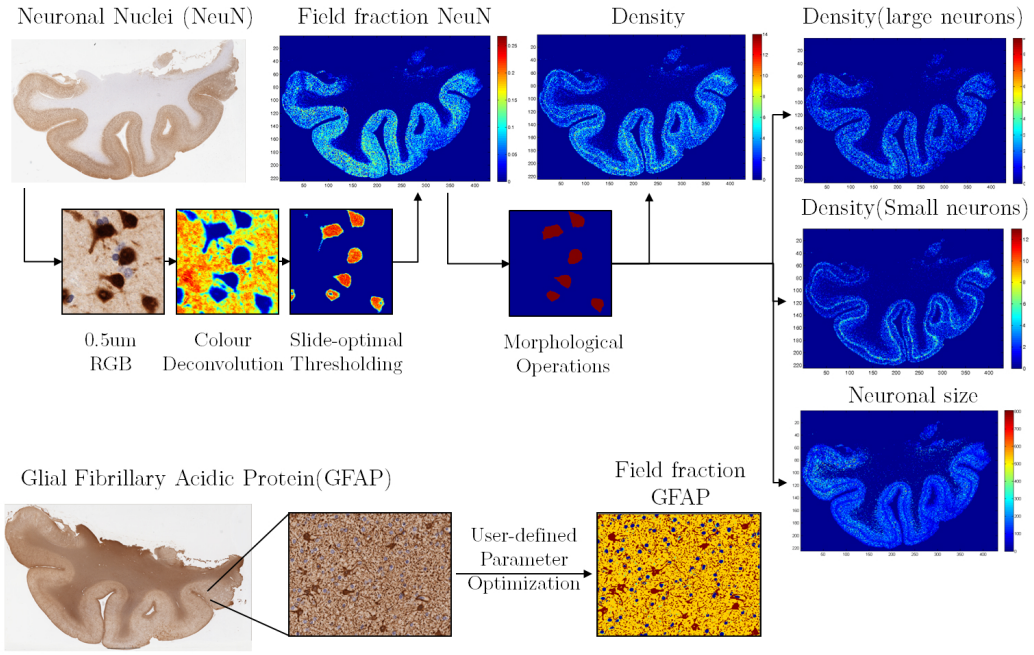

Figure 4.1: Histological processing and semi-quantitative features extraction, for both NeuN and GFAP IHC stains.

4.2.4 ROI Placement and Image Registration

To quantitatively correlate in-vivo MRI parameters and corresponding histological features, we relied on region of interest (ROI) analysis as a means of extracting the desired parameters and features from homologous regions. Histology ROIs were delineated on 100 μm downsampled H&E histology slices using ITKsnap [10]. Since the middle temporal gyrus was present in all available resections, ROIs were defined on the histology slides at the crown of the gyrus comprising grey matter (GM) and white matter (WM) sub-regions (Figure 4.2), as was also done by Eriksson et al. [2]. The edges of the WM ROIs were constrained to be 2 mm from the grey/white boundary and were not delineated inside the high curvature regions of the gyrus. The boundaries of the GM ROI were limited to a distance of 1mm from the pia to avoid partial volume effects on the in-vivo MRI images. A total of 55 ROIs: 29 GM and 26 WM (one patient had no WM

ROIs as the resection did not include sufficient tissue), were segmented on histology slices.

To ensure that equivalent ROIs were analyzed in each modality, we employed non-rigid image registration to map the H&E defined histology ROIs to the IHC slides and the in-vivo MRI. Non-rigid image registration was performed between the in-vivo MRI and histology images, using an ex-vivo MRI scan of the specimen as an intermediate reference image to effectively split the registration in two steps. After surgical resection, each specimen was oriented by the operating neurosurgeon, photographed and transported on ice to the imaging lab for ex-vivo scanning, which was performed after overnight fixation in 10% formalin. Each specimen was wrapped in gauze for stabilization, transferred to suitably-sized containers for imaging, and immersed in a fluorine-based 'fluid Christo-lube MCG 1046^{TM}' (Lubrication Technology, Inc) prior to imaging to avoid susceptibility artifacts at the tissue boundaries. The specimen scanning was performed on the same 3 T MR scanner employed for patient imaging, using a 6 channel coil designed to image the carotid artery. The sequences used for images that are part of the registration pipeline are described in detail below. The T2-weighted images were acquired with the fast imaging employing steady state acquisition (FIESTA) sequence (TR = 8.17ms, TE = 4.08ms, flip angle = $40^{c}irc$, N = 2, matrix = 200×200, slice thickness = 0.4, FOV = 70 mm) with a resolution of $0.35 \times 0.35 \times 0.4$mm. For cases where overnight imaging was feasible and not disruptive to the clinical work flow (N=4), scanning was performed on a 9.4T small bore Agilent MR magnet (Agilent, Santa Clara, CA, U.S.A) for improved image resolution and signal-to-noise ratio (SNR), as an alternative to the 3T scan. The specimens were scanned with an in-house developed coil for a total time of sixteen hours. For this protocol, images were acquired with the TrueFisp sequence (TR = 7.6 ms, TE = 3.8 ms, flip angle = $30^{c}irc$) with an

isotropic resolution of 0.2 mm and a FOV of $(50 \times 26 \times 44)$ voxels.

First, we aligned the histology images from each specimen to the corresponding slice within the 3D ex-vivo MRI volume [11]. Next, the in-vivo and ex-vivo MR images were aligned using a combination of image-based and landmark-based 3D deformable registration. The image-based registration made use of a B-spline deformation field and a normalized mutual information (NMI) cost-function [12], while the landmark registration relied on Gaussian radial basis functions [13].Validation of our registration protocol was achieved by computing target registration error (TRE) based on manually-identified corresponding intrinsic anatomical landmarks, demonstrating registration errors of 0.98 ± 0.60 mm and 1.35 ± 0.11 mm for histology to ex-vivo and ex-vivo to in-vivo registrations respectively [11]. The IHC slides (NeuN and GFAP) were linearly co-registered to the H&E slides using downsampled grayscale images of each slide, with registration accuracy better than 0.5 mm [11]. To avoid oblique resampling of the anisotropic histology images, for the purposes of visualization and analysis, the in-vivo and ex-vivo images were ultimately transformed to the space of the 3D reconstructed histology, Hist3D, where the reconstructed coronal histology slides are stacked parallel to the anterior-posterior axis. Figure 4.3 illustrates the four different spaces of MRI and histology, and registration results to bring both modalities in alignment. All in-vivo quantitative maps (T1, T2, FA, MD, AD and RD) were warped to the Hist3D space using the resultant deformation fields. Similarly, the histology ROIs were mapped to the IHC slides and the intermediate space, and underwent a final step of manual correction, if needed, to account for potential registration errors and to circumvent partial volume effects. ROIs transformed to in-vivo MRI space were used to obtain estimates of the mean MRI parameter T1, T2, FA, MD, AD, and RD at each location in the plane corresponding to the histology slides.

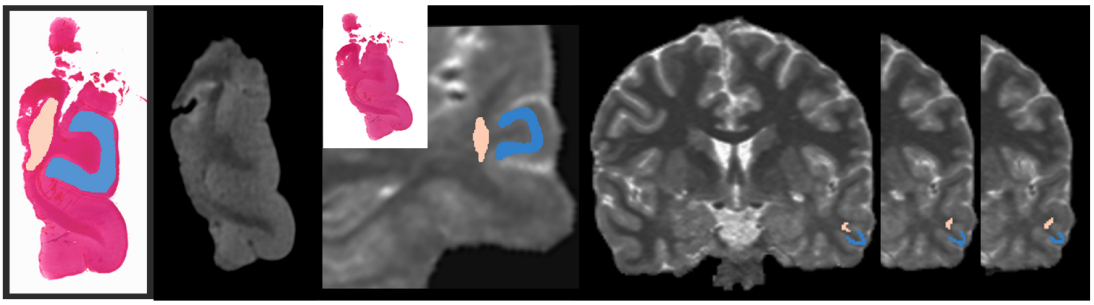

a) b) c) d)

Figure 4.2: ROI placement and MRI parameters extraction. A) Grey matter and white ROI on 100um H&E histology slice in histology native space. B) Registered ex-vivo MRI slice corresponding to the histology slice in Hist3D space. C) Warped ROIs overlaid on the registered and obliquely resampled T1 map in Hist3D space where MRI parameters extraction is performed. The registered histology slice is shown in the top left corner. D) Warped ROIs in the native in-vivo MRI space overlaid on three consecutive slices of the T1 map for illustration purposes.

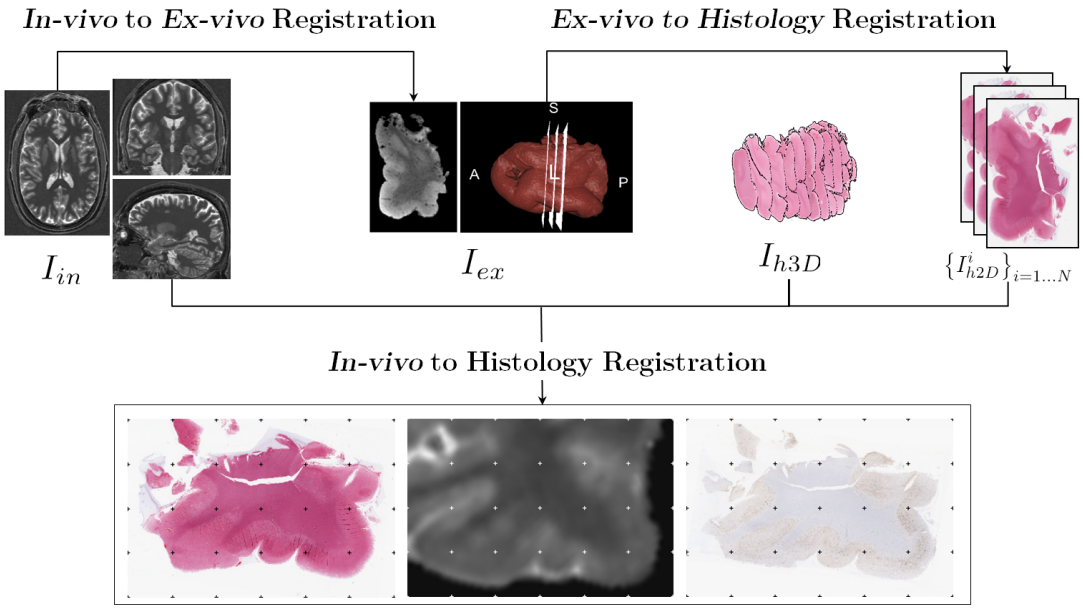

Figure 4.3: Overview of our registration pipeline depicting registration results and the four different spaces of MRI and histology including the intermediate Hist 3D space where reconstructed histology slices are stacked parallel to the A-P axis.

4.2.5 Statistical analysis

To assess the Gaussianity of the distribution of MRI samples, we employed the D'agostino & Pearson omnibus normality test. Linear mixed effects with random effects were employed to test for relationships between MRI parameters and histological features. For these analyses the histological features (stain field fraction, neuron size and neuron counts) were entered as dependent variables and MRI parameters (T1, T2, FA, MD) from patients and slices as the independent variables, whereas variables for both patient and slice were entered as repeated measures. In addition, a random effect for subject was included to account for lower variance of MRI parameters within a single (across slices) subject as compared to between subjects. For fixed effects, we first fitted a model that included all MRI parameters as explanatory variables. We employed Wald statistics for covariance structure selection. In addition, we assessed the correlations between each of the above variables as well as seizure frequency, age at the time of the last consultation prior to surgery, age of seizure onset, duration of epilepsy, and side of onset/resection. We also looked at correlations between each MRI parameter and every other MRI parameter, as well as those between histological features.

To investigate whether white matter MRI abnormalities are related to adjacent cortical histology, we also employed linear mixed models between MRI parameters from each WM ROI with histology features from its neighbouring GM ROI. Statistical analyses were performed in IBM SPSS statistics 20 (IBM, Armonk, NY). To test whether combining multiple MRI parameters leads to better prediction of histological features, multi-parametric models were compared against simpler univariate models using likelihood ratio tests.

4.3 Results

4.3.1 MRI parameters-Histology features correlation

The registration protocol enabled us to determine precise correspondences between MR and histology slices, and hence parameters from each slice were not averaged per patient and were instead employed as unique data points in the analysis. P-values from the linear mixed effects model analysis for the following histological features: neuron density, density (big neurons), density (small neurons), NeuN field fraction, are summarized in Table 4.2. T1 was found to be a significant predictor of total neuronal density in GM (Figure 4.4), as well as NeuN field fraction in the GM. Moreover, when assessing different sub-types of neurons, T1 and FA were both found to be predictors of neuronal density of large-caliber neurons (pyramidal cells) in the GM. Furthermore, only T1 was found to be a predictor of small-caliber neurons (granular cells) in the GM. There were no significant associations between the GFAP field fraction and any MRI parameter in either GM or WM. Similarly, no significant associations were seen between histology and MRI parameters in the white matter.

4.3.2 Multivariate vs. univariate MRI

To test whether combining multiple MRI parameters leads to better prediction of histological features, multi-parametric mixed effects models were compared against nested univariate models using likelihood ratio tests and the chi-squared distribution. Multiple linear regression analysis demonstrated that combining T1 and FA values predicted GM neuronal density of large-caliber neurons with a better fit than T1 or FA on their own

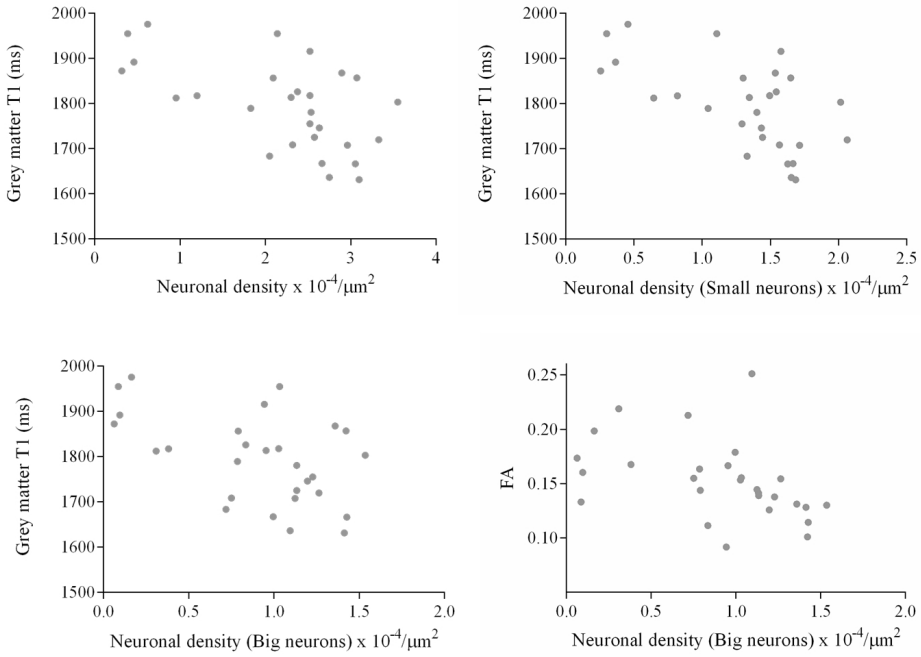

Figure 4.4: Relationships between quantitative MRI parameters (T1 and FA) and neuronal density in GM (Top left: Total neuronal density, Top right: Neuronal density for small-caliber neurons, Bottom: Neuronal density for large-caliber neurons).

Table 4.2: Results of the linear mixed-effects models with random effects for subjects, showing parameter estimates (β), standard error (SE) and p-values for all variables. Density (L.N)= Large Neurons, Density (S.N) = Small Neurons, NeuN F.F = Field Fraction. * Variable with fixed effect significant at $p < 0.05$, ** Variable with fixed effect significant at $p < 0.01$

	Total density		Density (L.N)		Density (S.N)		NEUN F.F	
Grey matter	β (SE)	p	β (SE)	p	β (SE)	p	β (SE)	p
T1	**-0.427** (0.064)	**0.008**	**-0.387** (0.066)	**0.021**	**-0.517** (0.122)	**0.004**	**-0.531** (0.137)	**0.003**
T2	0.038 (0.112)	0.733	0.085 (0.062)	0.227	-0.101 (0.122)	0.422	-.118 (0.113)	0.526
FA	-0.091 (0.077)	0.101	**-0.446** (0.031)	**0.009**	-0.022 (0.087)	0.209	-0.282 (0.048)	0.089
MD	-0.049 (0.107)	0.649	0.065 (0.050)	0.243	0.044 (0.123)	0.722	-0.067 (0.108)	0.549

(-2 log likelihood difference: 12.06, $p < 0.001$). Other multi-parametric combinations however failed to demonstrate similar predictive improvements. Figure 4.5 plots the samples in the space spanned by T1 and FA, revealing that combining both parameters provides better discrimination of density of large neurons in neocortical GM. Each dot in this plot refers to a grey matter ROI on a histology slide, with representative dots being labeled with patient IDs from Table 4.1. It is clear from the figure that low and high neuron densities are not well separated when using T1 or FA (see projections on horizontal and vertical axes), but in the two-dimensional space the data demonstrate are more clearly separable (demonstrated by the dashed line), suggesting that multivariate or multi-parametric analysis would be more beneficial in predicting or classifying pathology in-vivo. Since the presented ROIs are extracted from sparsely sectioned histology slices (4 mm apart), this figure highlights the potential of imaging parameters in detecting local pathology within the neocortex.

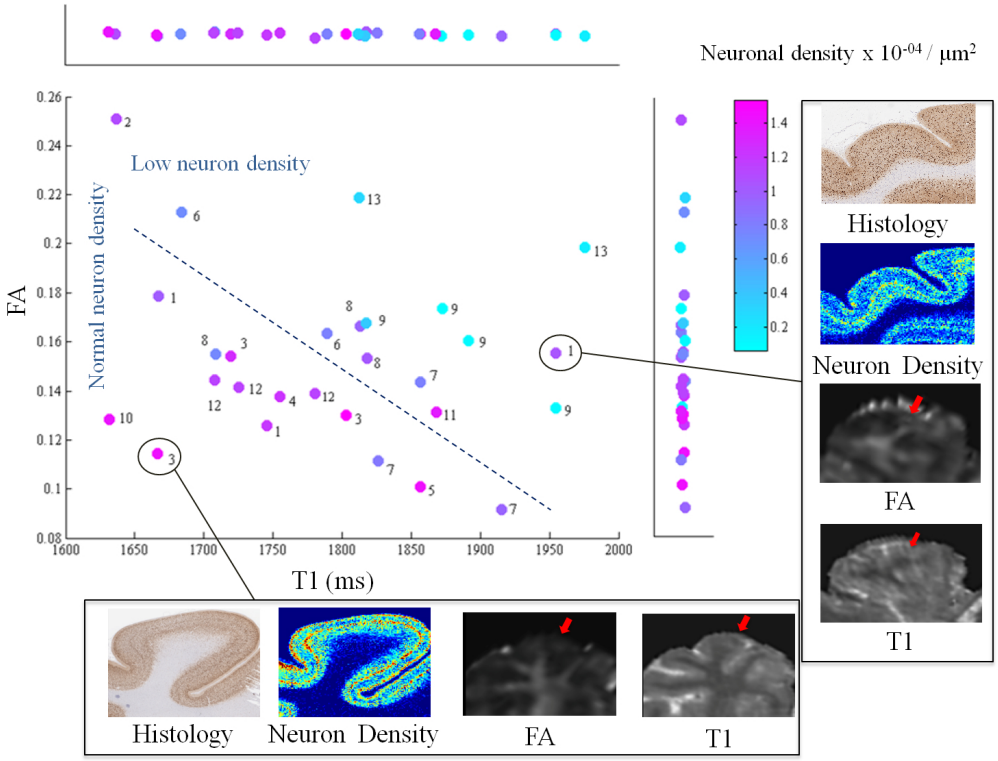

Figure 4.5: Representation of T1-FA multi-parametric space, revealing that combining T1 and FA provides better discrimination of normal and abnormal neuron density in neocortical grey matter. Each dot in this plot refers to a grey matter ROI on a histology slide, with representative dots being labeled with patient IDs from Table 1. It is clear from the figure that low and high neuron densities are not well separated when using T1 or FA (see projections on horizontal and vertical axes), but in the two-dimensional space the data demonstrate are more clearly separable (demonstrated by the dashed line), suggesting that multivariate or multi-parametric analysis would be more beneficial in predicting or classifying pathology in-vivo. Since the presented ROIs are extracted from sparsely sectioned histology slices (4 mm apart), this figure highlights the potential of imaging parameters in detecting local pathology within the neocortex.

4.3.3 Correlation with clinical variables

Correlations with clinical variables revealed significant positive correlations between neuronal density and age (rs = 0.726, pfwe = 0.021). Finally there were significant correlations with side of seizure onset, with left TLE patients exhibiting increased GM T1 (rs = 0.671, pfwe = 0.042). Clinical variables did not correlate with either the MRI parameters or histological features in white matter.

4.3.4 MRI-MRI parameters correlation

Table 4.3 summarizes the correlations between all MRI parameters within both tissue types (GM and WM). When assessing the relationships between diffusion and relaxometry parameters, there was a negative correlation between T1 and FA in WM, as well as a positive correlation between T1 values and MD in WM. When assessing the relationships between diffusion parameters (FA vs. MD) and also relaxation parameters (T1 vs. T2) no significant correlations were found after multiple comparison correction. Figure 4.6 demonstrates the significant relationships between diffusion and relaxometry MRI parameters.

4.3.5 Histology-Histology features correlation

As for the histological features, we found a positive correlation between neuronal density and NeuN field fraction in GM (rs = 0.929, p = 4.0x10-09), as shown in Figure 4.6. Similarly, neuronal density was positively correlated with densities of both large and small neurons in GM when analyzed separately (rs = 0.93, p = 1.4x10-09 and rs = 0.95,

Table 4.3: Significance of Spearman Rho correlations between MR parameters. All p-values were corrected for family wise error.

Grey matter parameters	**T1**	**T2**	**FA**	**MD**
T1		r = 0.323 P = 0.428	r = 0.207 P = 0.515	r = 0.129 P = 0.843
T2			r = 0.316 P = 0.463	r = 0.036 P = 0.931
FA				r = 0.188 P = 0.612
MD				
White matter parameters	**T1**	**T2**	**FA**	**MD**
T1		r = 0.464 P = 0.144	r = 0.806 **P = 1.73e-04***	r = 0.643 **P = 0.032**
T2			r = 0.229 P = 0.639	r = 0.381 P = 0.241
FA				r = 0.527 P = 0.147
MD				

p = 1.4x10-10). In addition, a slightly higher correlation was detected between NeuN field fraction and density of larger neurons in GM (rs = 0.96, p = 1.5x10-11), than with density of smaller neurons in GM (rs = 0.83, p = 1.8x10-05). Finally, the association between both measurements of densities proved positively correlated as well in GM (rs = 0.80, p = 1.1x10-04).

4.4 Discussion

4.4.1 Neurobiological interpretations and considerations

A significant finding of this chapter was the negative association between T1 values and neuronal integrity measures (NeuN field fraction, neuronal density) in the grey

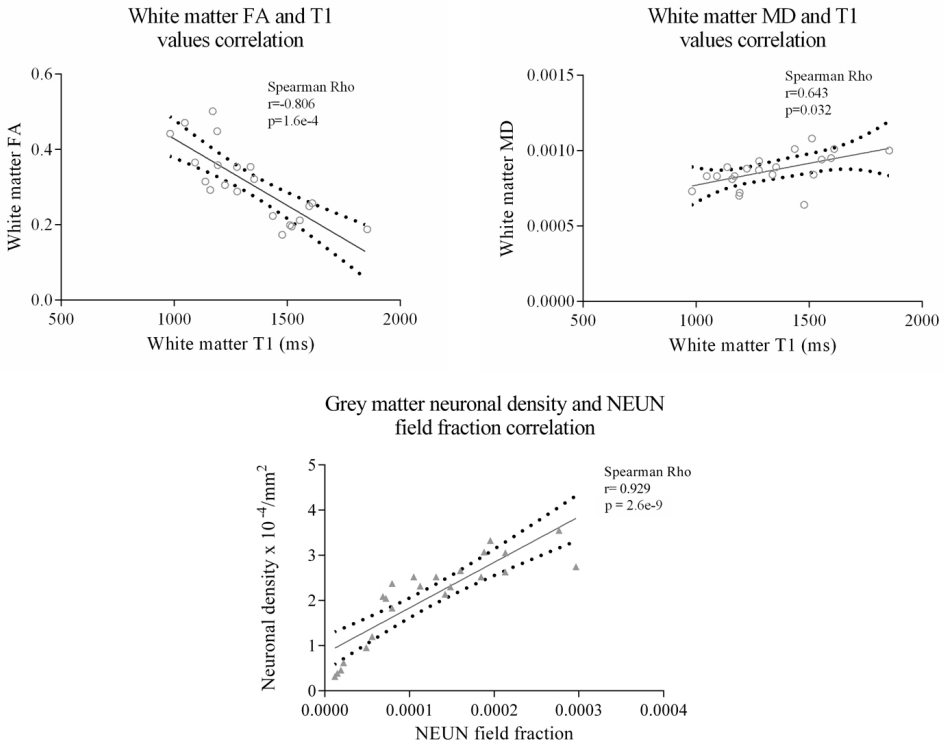

Figure 4.6: Significant relationships between diffusion and relaxometry MRI parameters, as well as the association between neuronal density and NeuN field fraction.

matter. T1 relaxation is related to many factors in the tissue, including macromolecular integrity and the relationship between free and bound water. Neuronal loss will likely result in an overall loss of macromolecules and an increase in the extra-cellular space (thus increased amount of extra-cellular water and decreased amount of intra-cellular water), all of which would act to increase T1 [14]. A similar relationship between ex-vivo GM T1 values and neuronal density has been described in patients with multiple sclerosis [15]. Our study is the first to observe this relationship with in-vivo quantitative T1 mapping and in temporal lobe resections. Eriksson et al. [2] found correlations between T2 and grey matter NeuN field fraction, employing a dual-echo fast FLAIR T2 (FFT2) mapping at 1.5T with a 5 mm slice thickness. One possible explanation why we did not observe this trend with our T2 maps could be because of differences in the mapping protocols; our protocol is at 3T, has significantly thinner slices, and did not use a fluid-attenuated inversion recovery (FLAIR) sequence. We plan to compare the relationship between our T1 and T2 maps and FLAIR sequences in future work to better understand the effectiveness of each technique in assessing pathology.

We also found that FA was a predictor of neuronal density of large-calibre (layer 3/5) neurons in the cortical gray matter. While this seems counterintuitive to our expectations in white matter, where a decrease in FA is usually associated with pathology, the cyto- and myelo-architecture in the cortex is considerably different from that in the white matter. Moreover, an increase in anisotropy was previously reported [16] within the dentate gyrus in an animal model of seizing rats, as compared to naive controls. Diffusion anisotropy is low and not typically examined in the cortical grey matter, with some exceptions [17]. However high-resolution diffusion studies on post-mortem brains have shown that the fiber configuration can be complex, with both fibers parallel and perpendicular to the cortical surface observed, along with areas of fiber crossings

[18]. In a region of low anisotropy due to fiber-crossing, such as the cortex, selective loss of one type of fibers would lead to an increase in anisotropy (i.e. a shift to a simpler fiber configuration). This phenomenon has been observed previously in a region of white matter fiber-crossing, where Douaud et al. [19] demonstrated an increase of FA could be explained by a relative preservation of motor-related projection fibers crossing the association fibers of the superior longitudinal fasciculus in mild cognitive impairment subjects. Thus, the increase in FA we observed, coinciding with a loss of only large-calibre neurons, could be explained by the selective loss of fibers running either parallel or perpendicular to the cortical surface), as depicted in the simplified schematic representation in Figure 4.7. Given the limitations of in-vivo DTI data we cannot precisely assess the nature of the architectural changes related to FA, however we hope to explore these issues further using high-resolution ex-vivo DTI of the resected specimens.

In the white matter, increases in T1 were positively correlated with MD and negatively with FA. This agrees with previous studies that have also demonstrated reduced FA and increased MD in the ipsilateral white matter in TLE [20, 21, 22, 23, 24, 25]. These changes may be due to degeneration of axons, reduced packing, or demyelination [26] which may facilitate isotropic diffusion and accumulation of free water in the extracellular space, which would lengthen T1 as well. A similar trend of prolonged T1 times and decreased FA was reported in white matter hyperintense regions of Alzheimer's patients [27], where they showed that increased T1 reflected a range of pathological findings including axon and myelin loss and microglial activation, whereas the strongest predictor of decreased FA was axonal loss. In addition to affecting relaxation and diffusion parameters, reactive gliosis has also been previously associated with neuronal loss [28]; however we did not observe any significant correlations with GFAP

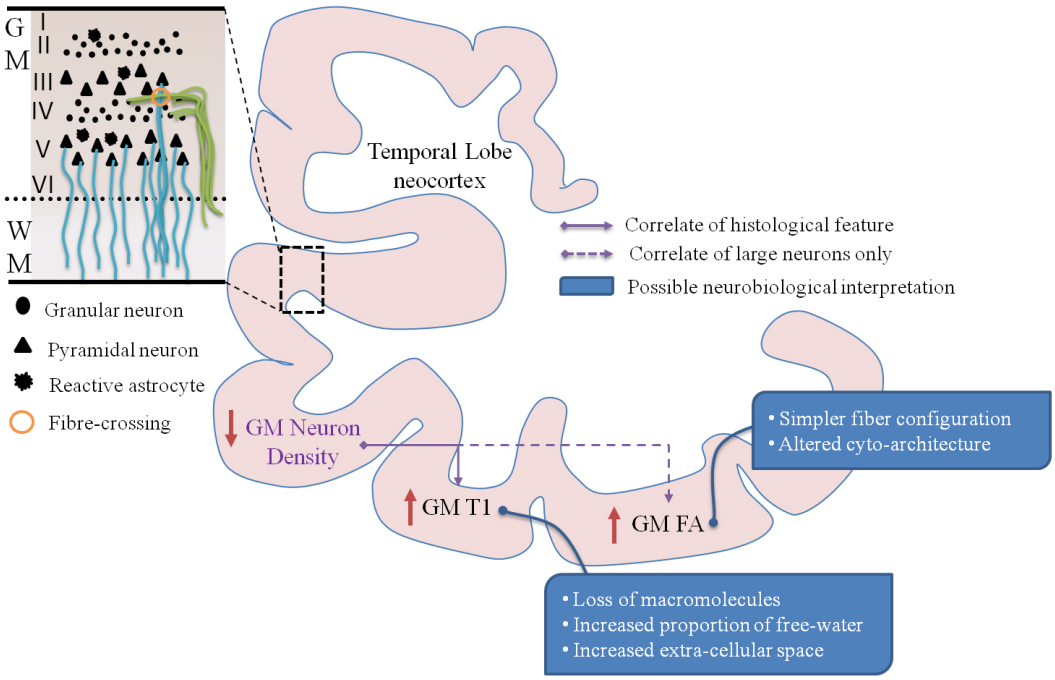

Figure 4.7: Summary of MRI parameters and histological features correlations in both tissues of the temporal lobe neocortex, along with possible neurobiological explanations for the highlighted relations.

IHC in either GM or WM.

The positive correlation reported between age and neuronal density has been shown previously in a healthy aging population [29], and was attributed to atrophy (volume loss) without accompanied neuronal loss. This has potential implications on the detection of neuronal integrity, since if age-related atrophy (density increases) and neuron loss (density decreases) occur simultaneously, there may be no net change in density, and thus no change in MRI signal. Finally, we found significant differences in left-onset TLE patients, who demonstrated had increased T1 and decreased FA in the grey matter. Asymmetry has also been found in other recent DTI studies [30, 31] with left-onset patients having more significant and widespread abnormalities and greater hippocampal atrophy [32], and have been speculated to be due to the greater vulnerability to early injury and the progressive effect of seizures on the left hemisphere. These asymmetric structural differences could also be related to the inherent functional lateralization, including language dominance [33].

4.4.2 Benefit of registration-based correlation

Many studies correlating MRI and histology have been performed without the use of computational methods for 3D image registration, relying instead on visual matching of ROIs. However, this is difficult in cases where the visibility or boundaries of the lesion in MRI and histology differ and where no definitive lesion is apparent (as in paradoxical TLE). Another drawback of visual matching is that it becomes more challenging to find corresponding slices when there are 3D deformations present, as the anatomy in a histology slice may not be fully present in a single MRI slice, even if obliquely resampled.

If no registration is employed and the tissue is subjected to non-rigid deformations, the samples from both modalities may represent different parts of the same anatomical region, which could potentially lead to abnormal sub-regions of one modality being correlated with normal elements of the other. When image registration is employed, the degree of mismatch between regions of both modalities becomes dependent on the registration error. For example, an image registration error between in-vivo MRI and histology of 1 mm would produce an overlap of 70% between two regions of interests with a volume of 140 mm3 on each modalities, (roughly the size of a very small FCD) [34].

4.4.3 Limitations and future work

The current study is limited to the investigation of neuronal integrity and gliosis through field fractions and measurements of neuronal size and density. Since focal neuronal loss and gliosis are thought to be related to epileptogenicity, correlation of these measures with MRI is an important step in validating quantitative imaging techniques. Additional insight might also be gained through the use of myelin-specific stains (Luxol fast blue, or myelin basic protein), since their relationship with both T1 [35] and T2 [15] has been previously demonstrated. Another limitation of this preliminary work is the lack of normative control data for histology, which we plan to address in future studies with tissue obtained from post-mortem specimens. The lack of control non-epileptic specimens makes it difficult to validate that the observed pathological changes directly relate to seizure generation.

In addition to histopathology, correlation with electrophysiology obtained with intracranial EEG (iEEG) could be used to further validate these techniques and better

understand the relationship with epileptogenicity, imaging, and histology. However, there are some issues with using iEEG as a gold-standard for validating imaging methods, since localization is limited to placement of the electrodes and abnormal iEEG may not actually have an altered structural substrate that can be detected. For these reasons, it may still be more beneficial to investigate the histopathological correlates instead of iEEG, specifically of cortical dysplasia, which often go undetected and have a higher risk for seizure recurrence [36]. We intend as well to correlate our imaging findings (specifically abnormalities found on T1 and FA maps) with long-term seizure outcomes, and investigate whether the absence of such lesions provides more favourable outcomes for patients undergoing surgery due to hippocampal sclerosis. Future work should as well investigate whether these neocortical abnormalities are related to the epileptogenicity in those patients, possibly though correlation of the imaging abnormalities with depth electrode recordings. Better quantification and characterization of these lesions in histology, based on neuronal- and laminar-centric analysis, could be used to improve detection and precise delineation with MRI, and could improve surgical outcomes through more complete resection of the underlying pathology [37]. Our future work in this direction will build upon histological image processing techniques and ex-vivo MR microscopy to accurately quantify and characterize these lesions for correlation with MRI.

Bibliography

[1] Rita Garbelli, Gloria Milesi, Valentina Medici, Flavio Villani, Giuseppe Didato, Francesco Deleo, Ludovico D'Incerti, Michela Morbin, Giulia Mazzoleni, Anna Rita Giovagnoli, Annalisa Parente, Ileana Zucca, Alfonso Mastropietro,

and Roberto Spreafico. Blurring in patients with temporal lobe epilepsy: clinical, high-field imaging and ultrastructural study. *Brain*, 135(Pt 8):2337–49, 2012.

[2] S H Eriksson, S L Free, M Thom, L Martinian, M R Symms, T M Salmenpera, A W McEvoy, W Harkness, J S Duncan, and S M Sisodiya. Correlation of quantitative MRI and neuropathology in epilepsy surgical resection specimens–T2 correlates with neuronal tissue in gray matter. *Neuroimage*, 37(1):48–55, 2007.

[3] S H Eriksson, S L Free, M Thom, M R Symms, L Martinian, J S Duncan, and S M Sisodiya. Quantitative grey matter histological measures do not correlate with grey matter probability values from in vivo MRI in the temporal lobe. *Journal of neuroscience methods*, 181(1):111–8, 2009.

[4] Georgia Lockwood-Estrin, Maria Thom, Niels K Focke, Mark R Symms, Lillian Martinian, Sanjay M Sisodiya, John S Duncan, and Sofia H Eriksson. Correlating 3T MRI and histopathology in patients undergoing epilepsy surgery. *Journal of Neuroscience Methods*, 205(1):182–9, 2012.

[5] Sean C L Deoni. High-resolution T1 mapping of the brain at 3T with driven equilibrium single pulse observation of T1 with high-speed incorporation of RF field inhomogeneities (DESPOT1-HIFI). *J Magn Reson Imaging*, 26(4):1106–11, 2007.

[6] Sean C L Deoni. Transverse relaxation time (T2) mapping in the brain with off-resonance correction using phase-cycled steady-state free precession imaging. *J Magn Reson Imaging*, 30(2):411–7, 2009.

[7] Sean C L Deoni, Brian K Rutt, Tarunya Arun, Carlo Pierpaoli, and Derek K Jones.

Gleaning multicomponent T1 and T2 information from steady-state imaging data. *Magn Reson Med*, 60(6):1372–87, 2008.

[8] Arnout C Ruifrok and Dennis A Johnston. Quantification of histochemical staining by color deconvolution. *Analytical and quantitative cytology and histology/the International Academy of Cytology [and] American Society of Cytology*, 23(4): 291–299, 2001.

[9] Pierre Soille. *Morphological image analysis: principles and applications*. Springer-Verlag New York, Inc., 2003.

[10] Paul A Yushkevich, Joseph Piven, Heather Cody Hazlett, Rachel Gimpel Smith, Sean Ho, James C Gee, and Guido Gerig. User-guided 3D active contour segmentation of anatomical structures: significantly improved efficiency and reliability. *Neuroimage*, 31(3):1116–28, 2006.

[11] Maged Goubran, Cathie Crukley, Sandrine de Ribaupierre, Terence M Peters, and Ali R Khan. Image registration of ex-vivo MRI to sparsely sectioned histology of hippocampal and neocortical temporal lobe specimens. *Neuroimage*, 83:770–781, 2013.

[12] Marc Modat, Gerard R Ridgway, Zeike A Taylor, Manja Lehmann, Josephine Barnes, David J Hawkes, Nick C Fox, and Sébastien Ourselin. Fast free-form deformation using graphics processing units. *Computer methods and programs in biomedicine*, 98(3):278–84, 2010.

[13] Csaba Pinter, Andras Lasso, An Wang, David Jaffray, and Gabor Fichtinger. Slicerrt: Radiation therapy research toolkit for 3d slicer. *Medical physics*, 39 (10):6332–6338, 2012.

[14] Alina Jurcoane, Marlies Wagner, Christoph Schmidt, Christoph Mayer, Rene-Maxime Gracien, Marc Hirschmann, Ralf Deichmann, Steffen Volz, Ulf Ziemann, and Elke Hattingen. Within-lesion differences in quantitative mri parameters predict contrast enhancement in multiple sclerosis. *Journal of Magnetic Resonance Imaging*, 38(6):1454–1461, 2013.

[15] Klaus Schmierer, Harold G Parkes, Po-Wah So, Shu F An, Sebastian Brandner, Roger J Ordidge, Tarek A Yousry, and David H Miller. High field (9.4 tesla) magnetic resonance imaging of cortical grey matter lesions in multiple sclerosis. *Brain*, 133(3):858–867, 2010.

[16] Mansi B Parekh, Paul R Carney, Hector Sepulveda, Wendy Norman, Michael King, and Thomas H Mareci. Early mr diffusion and relaxation changes in the parahippocampal gyrus precede the onset of spontaneous seizures in an animal model of chronic limbic epilepsy. *Experimental neurology*, 224(1):258–270, 2010.

[17] Do-Hyung Kang, Hang Joon Jo, Wi Hoon Jung, Sun Hyung Kim, Ye-Ha Jung, Chi-Hoon Choi, Ul Soon Lee, Seung Chan An, Joon Hwan Jang, and Jun Soo Kwon. The effect of meditation on brain structure: cortical thickness mapping and diffusion tensor imaging. *Social cognitive and affective neuroscience*, 8(1): 27–33, 2013.

[18] Christoph WU Leuze, Alfred Anwander, Pierre-Louis Bazin, Bibek Dhital, Carsten Stüber, Katja Reimann, Stefan Geyer, and Robert Turner. Layer-specific intracortical connectivity revealed with diffusion mri. *Cerebral Cortex*, 24(2): 328–339, 2014.

[19] Gwenaëlle Douaud, Saâd Jbabdi, Timothy EJ Behrens, Ricarda A Menke, Achim Gass, Andreas U Monsch, Anil Rao, Brandon Whitcher, Gordon Kindlmann, Paul M Matthews, et al. Dti measures in crossing-fibre areas: *Increased* diffusion anisotropy reveals early white matter alteration in mci and mild alzheimer's disease. *Neuroimage*, 55(3):880–890, 2011.

[20] Fergus J Rugg-Gunn, Sofia H Eriksson, Mark R Symms, Gareth J Barker, Maria Thom, William Harkness, and John S Duncan. Diffusion tensor imaging in refractory epilepsy. *Lancet*, 359(9319):1748–51, 2002.

[21] Niels K Focke, Mahinda Yogarajah, Silvia B Bonelli, Philippa A Bartlett, Mark R Symms, and John S Duncan. Voxel-based diffusion tensor imaging in patients with mesial temporal lobe epilepsy and hippocampal sclerosis. *Neuroimage*, 40 (2):728–37, 2008.

[22] Tuuli M Salmenpera, Robert J Simister, Philippa Bartlett, Mark R Symms, Philip A Boulby, Samantha L Free, Gareth J Barker, and John S Duncan. High-resolution diffusion tensor imaging of the hippocampus in temporal lobe epilepsy. *Epilepsy research*, 71(2-3):102–6, 2006.

[23] Lionel Thivard, Stéphane Lehéricy, Alexandre Krainik, Claude Adam, Didier Dormont, Jacques Chiras, Michel Baulac, and Sophie Dupont. Diffusion tensor imaging in medial temporal lobe epilepsy with hippocampal sclerosis. *Neuroimage*, 28(3):682–90, 2005.

[24] Ali R Khan, Maged Goubran, Sandrine de Ribaupierre, Robert R Hammond, Jorge G Burneo, Andrew G Parrent, and Terry M Peters. Quantitative relaxometry

and diffusion MRI for lateralization in MTS and non-MTS temporal lobe epilepsy. *Epilepsy Research*, 108:506–516, 2014.

[25] Diego Cantor-Rivera, Ali R Khan, Maged Goubran, Seyed M Mirsattari, and Terry M Peters. Detection of temporal lobe epilepsy using support vector machines in multi-parametric quantitative mr imaging. *Computerized Medical Imaging and Graphics*, 2014.

[26] Donald W Gross. Diffusion tensor imaging in temporal lobe epilepsy. *Epilepsia*, 52(s4):32–34, 2011.

[27] AA Gouw, A Seewann, H Vrenken, WM Van Der Flier, JM Rozemuller, F Barkhof, P Scheltens, and JJG Geurts. Heterogeneity of white matter hyperintensities in alzheimer's disease: post-mortem quantitative mri and neuropathology. *Brain*, 131(12):3286–3298, 2008.

[28] Michelle L Block, Luigi Zecca, and Jau-Shyong Hong. Microglia-mediated neurotoxicity: uncovering the molecular mechanisms. *Nature Reviews Neuroscience*, 8(1):57–69, 2007.

[29] Stefanie H Freeman, Ruth Kandel, Luis Cruz, Anete Rozkalne, Kathy Newell, Matthew P Frosch, E Tessa Hedley-Whyte, Joseph J Locascio, Lewis Lipsitz, and Bradley T Hyman. Preservation of neuronal number despite age-related cortical brain atrophy in elderly subjects without alzheimer disease. *Journal of neuropathology and experimental neurology*, 67(12):1205, 2008.

[30] Young-Min Shon, Yeong-In Kim, Bang-Bon Koo, Jong-Min Lee, Hye J Kim, Woo J Kim, Kook J Ahn, and Dong W Yang. Group-specific regional white

matter abnormality revealed in diffusion tensor imaging of medial temporal lobe epilepsy without hippocampal sclerosis. *Epilepsia*, 51(4):529–35, 2010.

[31] Nobuko Kemmotsu, Holly M Girard, N Erkut Kucukboyaci, Linda K McEvoy, Donald J Hagler, Anders M Dale, Eric Halgren, and Carrie R McDonald. Age-related changes in the neurophysiology of language in adults: Relationship to regional cortical thinning and white matter microstructure. *The Journal of Neuroscience*, 32(35):12204–12213, 2012.

[32] L Bonilha, C Rorden, J J Halford, M Eckert, S Appenzeller, F Cendes, and L M Li. Asymmetrical extra-hippocampal grey matter loss related to hippocampal atrophy in patients with medial temporal lobe epilepsy. *J Neurol Neurosurg Psychiatr*, 78 (3):286–94, 2007.

[33] Thomas R Barrick, I Nigel Lawes, Clare E Mackay, and Chris A Clark. White matter pathway asymmetry underlies functional lateralization. *Cereb Cortex*, 17 (3):591–8, 2007.

[34] Pierre Besson, Neda Bernasconi, Olivier Colliot, Alan Evans, and Andrea Bernasconi. Surface-based texture and morphological analysis detects subtle cortical dysplasia. In *Medical Image Computing and Computer-Assisted Intervention–MICCAI 2008*, pages 645–652. Springer, 2008.

[35] JP Mottershead, K Schmierer, M Clemence, JS Thornton, F Scaravilli, GJ Barker, PS Tofts, J Newcombe, ML Cuzner, RJ Ordidge, et al. High field mri correlates of myelin content and axonal density in multiple sclerosis. *Journal of neurology*, 250(11):1293–1301, 2003.

[36] André Palmini, Antonio Gambardella, Frederick Andermann, François Dubea,

Jaderson Costa Cos, André Olivi, Donatella Tampie, Yvon Robitaill, Eduardo Paglioli, Eliseu Paglioli Neto, et al. Operative strategies for patients with cortical dysplastic lesions and intractable epilepsy. *Epilepsia*, 35(s6):S57–S71, 1994.

[37] Susanne Fauser, Andreas Schulze-Bonhage, Juergen Honegger, Hans Carmona, Hans-Juergen Huppertz, Georgios Pantazis, Sabine Rona, Thomas Bast, Karl Strobl, Bernhard J Steinhoff, et al. Focal cortical dysplasias: surgical outcome in 67 patients in relation to histological subtypes and dual pathology. *Brain*, 127 (11):2406–2418, 2004.

Chapter 5

Correlation of Hippocampal MRI and histology

5.1 Introduction

Chapter 4 focused on correlating pathology from neocortical TLE with imaging findings. Although the landscape of epilepsy surgery is changing with more neocortical lesions and FCD resections being performed, patients with hippocampal sclerosis (HS) still compromise the majority of surgical patients. In this chapter I focus on analyzing imaging findings within the hippocampal subfields for patients with TLE due to HS. Since the early 1990s HS has been detectable on pre-operative MRI [1], where its classic hallmark is reduced hippocampal volume and increased signal intensity on T2-weighted scans and T2 relaxometry maps. A large body of research has established

This chapter is in-preparation for submission to the journal 'Annals of neurology'

the reliability of hippocampal volumetry and/or T2 signal increases in reflecting hippocampal atrophy [1, 2, 3, 4, 5, 6, 7, 8, 9, 10], and psychological functioning such as memory performance [11, 12] Subfield hippocampal volume changes in intractable TLE have also been previously described in the epilepsy literature [12, 13, 14]. Moreover, previous studies investigated diffusion changes in patients with HS and demonstrated increased MD as well as decreased FA in the ipsilateral hippocampi and white matter [15, 16, 17, 18, 19]. However, these studies lacked histological validation and the exact causal relationship between structural changes and epileptogenesis in the hippocampus is still unclear. Moreover, because of limited image resolution, as well as the lack of sensitivity of standard clinical sequences to detect hippocampal subfield atrophy, the current radiological clinical practice is to report the presence or absence of HS without mention of the subtypes or subfield atrophy and pathology. Quantitative MRI sequences such as high-resolution T2 relaxometry mapping and diffusion tensor imaging (DTI) can reveal subtle pathologies undetected on conventional or routine MRI [20, 21, 22].

To this end, there are three primary objectives of this current study. We first seek to establish the pathological substrates of hippocampal volume and intensity changes in TLE, by correlating quantitative MRI parameters including relaxation, diffusion and volumetry measures with histological features such as neuronal loss and gliosis within the subfields. We then investigate the efficacy of these quantitative MRI measures in predicting neuronal loss from in-vivo imaging, and finally compare the influence and importance of each subfield in classifying hippocampal sclerosis subtypes from preoperative MRI.

5.2 Materials & Methods

5.2.1 Patients and Samples

15 TLE (6 males, 9 females, age: 34 ± 11 (range: 20-56)), who underwent anterior temporal lobectomy (ATL) surgery, were included in this study. It should be noted that while there is overlap between the patient cohorts of this chapter and Chapter 4, the patients groups are not identical across both chapters and their inclusion criteria depended on clinical MRI and histology reports of the studied pathology (whether neocortical or hippocampal). In the ATL procedure, the mesial structures, the hippocampus and amygdala, and up to 3-5 cm of the temporal neocortex are removed. Informed consent was collected from all participants prior to their participation in the study. This project was cleared by the Health Sciences Research Ethics Board of Western University. All patients had preoperative investigations including 1.5T clinical MRI scans (T1-weighted, T2-weighted, FLAIR, and diffusion-weighted sequences) and neuropsychological testing, as part of their clinical diagnostic workup. Video-scalp EEG telemetry was employed to monitor patients for seizure characterization, with four patients needing subdural electrodes placement to better localize the seizures. In addition to the 1.5T conventional MRI sequences, patients underwent a series of scans on a 3T MRI research scanner as described in the *in-vivo* MRI imaging subsection. Table 5.1 summarizes the age at the time of the last consultation prior to surgery, gender, age at seizure onset, electrographic seizure origin, Engel outcome as well as clinical MRI and pathology findings for our patient cohort.

5.2.2 *In-vivo* MRI and Qualitative classification

All patients underwent in-vivo imaging, including relaxation (T1 & T2) mapping and DTI, on a 3T Discovery MR750 scanner (General Electric, Milwaukee, WI, U.S.A.) using a 32 channel head coil. In-vivo image acquisition sequences and scanning parameters are described in details in Chapters 3 & 4. In addition to the T2 relaxometry map, we computed normalized T2 intensity (normalized in respect to the lateral ventricle ipsilateral to the hippocampus) from one of the ssfp scans (flip angle 35). A three-level clinical hippocampal sclerosis classification of the patients was performed employing MRI and histology reports. The degree of sclerosis was stratified with no HS being scored as 1, moderate 2 and severe HS 3. This clinical classification will henceforth be referred to as 'Qualitative HS subtypes'.

5.2.3 Histological processing and quantitative histology

Two of the 15 specimens were discarded from the analysis as the hippocampi were fragmented and there was insufficient tissue to clinically assess HS or perform automated neuron analysis. The resected hippocampal specimens underwent grossing and accessioning at the Department of Pathology of the University Hospital of London Health Sciences Centre. There are numerous challenges, particularly the high complexity of en-bloc resection, as well as preservation of very small sclerotic hippocampi throughout histological processing, encountered in our pipeline to perform quantitative histology on surgical hippocampal specimens. Other technical challenges comprise the tendency of the tissue to deform and presentation of histological breakage (partially due to the differential shrinkage of gray and white matter) across the specimens. To better

Table 5.1: Patient demographics and clinical information including age, gender, onset age, seizure origin as well as clinical MRI and pathology findings for our patient cohort. HS = mesial temporal sclerosis, MAA= minor architectural abnormalities, Neo. Path. = Neocortical Pathology, Hp. Path. = Hippocampal Pathology † Previous resection of left temporal lobe tumour (DNET), ‡ not enough tissue to make diagnosis of HS

ID	Sex	Age	Onset	Sz Origin	Sz Freq. /month	MRI	Hp. Path.	Engel outcome	Yrs since surgery
1	F	22	15	R	8	Normal	Early stage HS	2	3.52
2	M	52	45	L	2	Tumour	Gliosis	2	3.37
3	F	40	7	R	20	HS, Poren-cephaly	HS	2	2.5
4	M	20	3	L	16	HS	HS	2	2.1
5	F	48	36	L	28	HS	HS	1	1.7
6	M	30	2	L	4	HS	HS	1	1.87
7	M	31	28	R	2	Normal	Negligible gliosis	1	1.3
8	F	32	19	L	2	HS	HS	1	1.2
9	F	43	3	R	4	HS	HS	2	1.4
10	M	39	22	R	2	CD	Gliosis	1	0.94
11	M	23	18	L	12	Normal	Gliosis	1	1
12	M	34	15	L	2	HS	HS	3	1.2
13	F	25	17	L	2	Normal †	Gliosis	3	2
14	F	56	15	R	8	Normal	Gliosis ‡	1	1.12
15	M	39	13	R	12	DNET or CD	Gliosis ‡	2	1.16

preserve the specimen, they were cut in half in the coronal plane and each half was embedded in agar for stabilization as well as support during slicing. The histological processing pipeline (slicing, embedding, sectioning and digitization) was identical to that described in chapter 2. Similarly, the GFAP field fraction estimation was identical to the protocol described in chapter 4.

To provide local estimates of neuron density and size we developed a method for segmenting cell bodies of pyramidal and granular neurons. This technique first extracts the colour component related to immuno-positive staining using colour deconvolution [23] preceding a watershed-based segmentation procedure [24] for splitting joined or connected neurons, and removes objects smaller than a predefined area defined as noise (less than 14 μm^2). The resulting neuron segmentations provide the neuronal density (number of neurons) per field, as well as the mean area (size) of cell bodies, within the field. To further discriminate between pyramidal neurons of the CA subfields and granular neurons of the dentate gyrus, we used area thresholds (125 μm^2 and 50 μm^2 respectively) to categorize them. NeuN slides were batch-processed with scripts written in MATLAB, to extract the neuron-specific quantitative features in each 100 μm $\times$ 100 μm field. Manual counts taken from random fields within the CA subfields as well as the dentate gyrus were employed to validate our automated cell segmentation procedure for pyramidal and granular neuron quantification. Figure 5.1 illustrates this procedure and demonstrates some of the quantitative histological features: neuron density (for both CA and DG), mean neuron size, and GFAP field fraction. Neuronal counts from the least sclerotic specimens per subfield were used as references to compute percent cell loss for each patient. A second HS subtype classification was performed based on the computed percent cell loss employing guidelines (thresholds for percent cell loss per subtype and subfield) from the new clinico-pathological classification of the different

subtypes [25]. This classification will be referred to as 'Quantitative HS subtypes' throughout the manuscript. It should be noted that five patients out of the 13 that were classified as having different grades of sclerosis, based on clinical reports, compared to that identified via histological cell loss, as shown in Table 5.2.

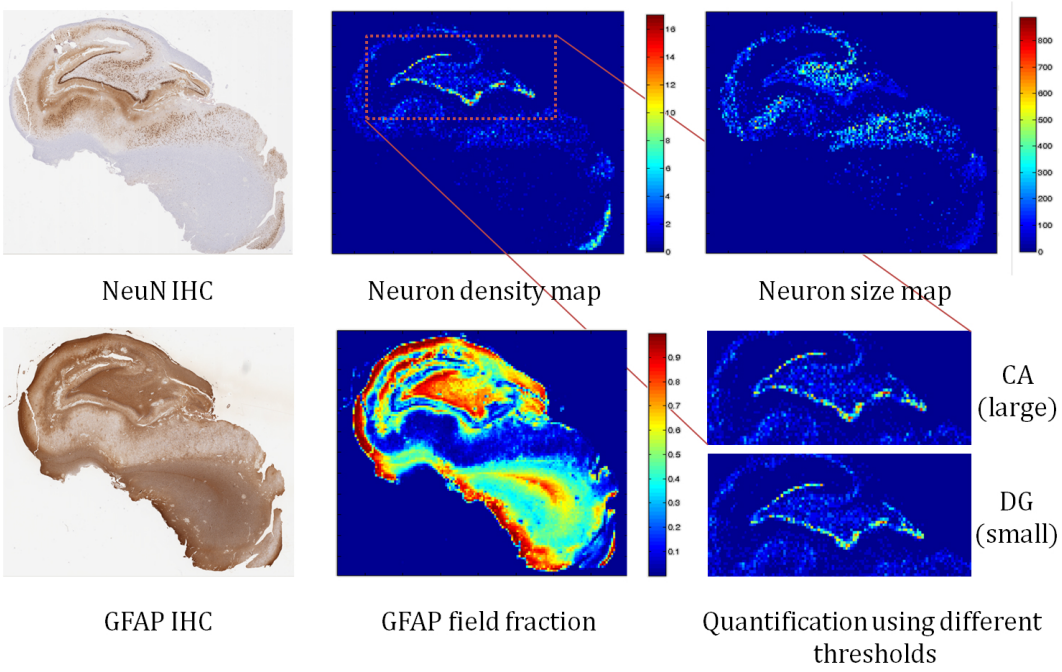

Figure 5.1: Overview of some of the quantitative histological features including: neuron density (for both CA and DG), mean neuron size, and GFAP field fraction.

5.2.4 Histology subfields segmentation

The hippocampal subfields were subsequently manually delineated on 20 μm downsampled histology slices, using the open-software tool ITKSNAP [26] and were checked by a pathologist (R.H). This segmentation protocol is similar to that described in Appendix A [27] and is based on previous protocols proposed by Wisse et al. [28] at 7T and the Duvernoy hippocampus atlas [29]. The key difference between our previous,

Table 5.2: Percent neuron loss per subfield and qualitative and Quantitative HS subtype classifications.

Patient	CA1	CA2	CA3	CA4	Qual. HS subtype	Quant. HS subtype
1	29.1951	11.9081	27.6011	0	1	1
2	0	0	32.936	29.5362	1	1
3	67.3426	91.7395	96.1312	95.1284	3	3
4	48.4765	29.357	84.0857	97.598	2	2
5	66.3895	40.7307	88.6651	96.063	3	3
6	80.3388	39.1261	92.3729	95.5111	2	3
7	64.5315	9.96929	28.3791	15.5876	1	2
8	67.0925	52.5966	95.2398	93.5412	3	3
9	69.9437	51.275	75.3959	87.3308	2	3
10	16.7605	39.1261	0	19.9012	1	1
11	32.0994	52.1615	50.5222	44.4942	1	2
12	72.2818	53.2529	80.6291	88.398	2	3
13	69.7113	4.0401	50.6483	64.1137	3	3

and current MRI delineation protocols employing higher resolution histology images, is that a distinction was made between CA2 and CA3, as well as CA4 and dentate gyrus in the newer protocol. The marking scheme and border definitions are as follows: The border between the subiculum and CA1 was defined as a horizontal line at the edge of the subiculum extending from the inferior border of the dentate gyrus and the hippocampal sulcus. The CA1/CA2 boundary was designated as the point at which a noticeable decrease in width of the CA1 subfield was observed, following the most lateral point of the DG. The CA2/CA3 boundary was defined at the most medial point of the superior curve of the dentate gyrus where a gradient of pyramidal cells density is observed between the subfields. The opening of subfields into the globular region of the hippocampal formation formed the CA3/CA4 border. The remaining globular region of the hippocampal formation was marked as the CA4 subfield. The dentate gyrus

was divided into two labels, one encompassing the granular layer and another combining both molecular and polymorphic layers surrounding the granular cells. Figure 5.2 shows examples of subfield delineation on histology slices from three patients from our cohort with mild, moderate and severe sclerosis.

5.2.5 MRI subfields segmentation

The standard methodological convention, employed in previous correction studies of hippocampal histology and MRI, is to correlate pathology findings on one or a few histology slices with MRI findings extracted from the entire hippocampus. Work from previous chapters focusing on an image registration pipeline between both modalities provides us with the MRI slice corresponding (or registered) to the cut histology slice. Hence, instead of relying on imaging parameters from segmented subfields along the entire length of the hippocampus, I extract parameters from a selective, patient-specific, target region around the corresponding MRI slice (within the hippocampal body). Figure 5.3 presents a schematic overview of the MRI parameters extraction pipeline. A region was chosen for parameter extraction, instead of relying only on parameters from the corresponding MRI slice to incorporate registration and histological sectioning errors. The target registration error for my pipeline was previously quantified to be around 2 mm, moreover, Gibson et al. [30] quantified the variance in sectioning histology slices from the face of blocks to be 1 mm. Thus, a 3 mm radius was chosen for the target region either side in the sagittal plane from the corresponding MRI slice. In addition, instead of averaging parameters across all the slices of the target region, I took a weighted average of the parameters whereby slices closer to the corresponding MRI slice in the sagittal plane had higher weighting, in order to model the registration

uncertainty. The weighting kernel employed was sync function with a full width half maximum (FWHM) of 3 mm.

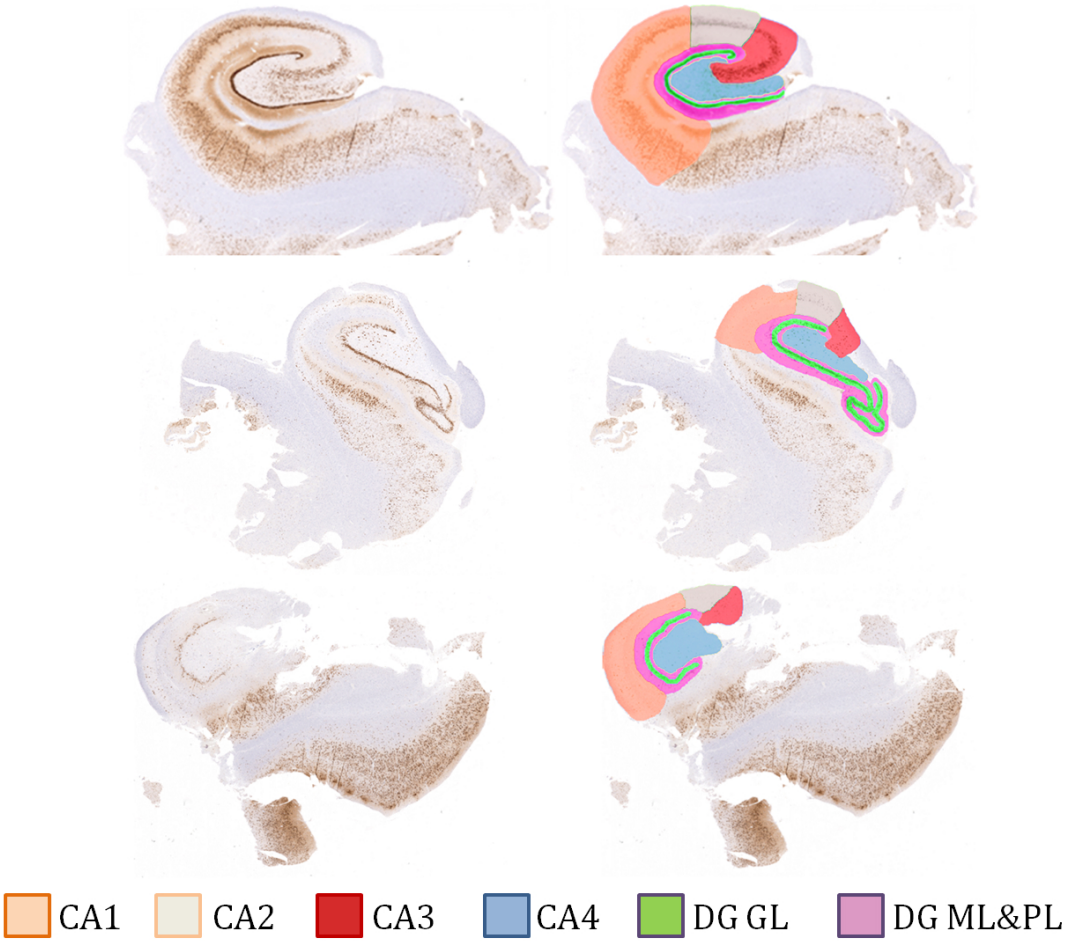

Figure 5.2: Subfield delineation on histology slices from three patients from our cohort (Top: Mild sclerosis, Middle: Moderate sclerosis, Bottom: Severe sclerosis). The labeling scheme (colour representing each subfield) is described at the bottom of the figure.

To ensure that the MRI subfields within the target region mirror those segmented on histology slices, I first initialized the labels using the automated Freesurfer subfields segmentation technique [31], then manually segmented the subfields within the chosen target region. Three main subfields were delineated using the segmentation

technique, including CA1, CA2/3 and CA4/DG. To employ the Freesurfer segmentation algorithm, I first created a synthetic T1-weighted image from the T1 map for each patient. The signal equation for the SPGR images that are employed in T1 map generation is denoted by: where $E_1 = exp(-TR/T1)$ and k is a constant proportional to the longitudinal magnetization equilibrium [32]. Synthetic T1-weighted images (SynT1) were reconstructed by substituting the calculated values back into the SPGR signal equation and using a nominal value of k = 1000 [32]. These SynT1 images (1mm isotropic) were first submitted to the automated FreeSurfer processing stream (`http://surfer.nmr.mgh.harvard.edu/`). The hippocampal subfield segmentation technique [31] was then performed on the FreeSurfer-processed images after upsampling their voxel size to 0.5 mm isotropic. This technique uses a statistical model with Markov random field priors to delineate subfield boundaries based on T1-weighted MPRAGE MR sequences [8]. It should be noted that MRI parameter extraction was performed in the intrinsic in-vivo space (1 mm isotropic) and not the upsampled space to avoid resampling the quantitative maps.

5.2.6 Statistical analysis

Our statistical analysis was stratified into three distinct experiments comprising different tests to tackle the three key objectives of the study. Firstly, we employed correlation analysis to investigate non-parametric (Spearman Rho) univariate associations between neuronal density and size vs. subfield volume, T1 and DTI, as well as between GFAP field fraction vs. T2 and DTI. This analysis was first performed using whole hippocampus MRI parameters, then employing subfield-specific parameters where only MRI and histological features from the corresponding subfield are correlated. Internal z-scores

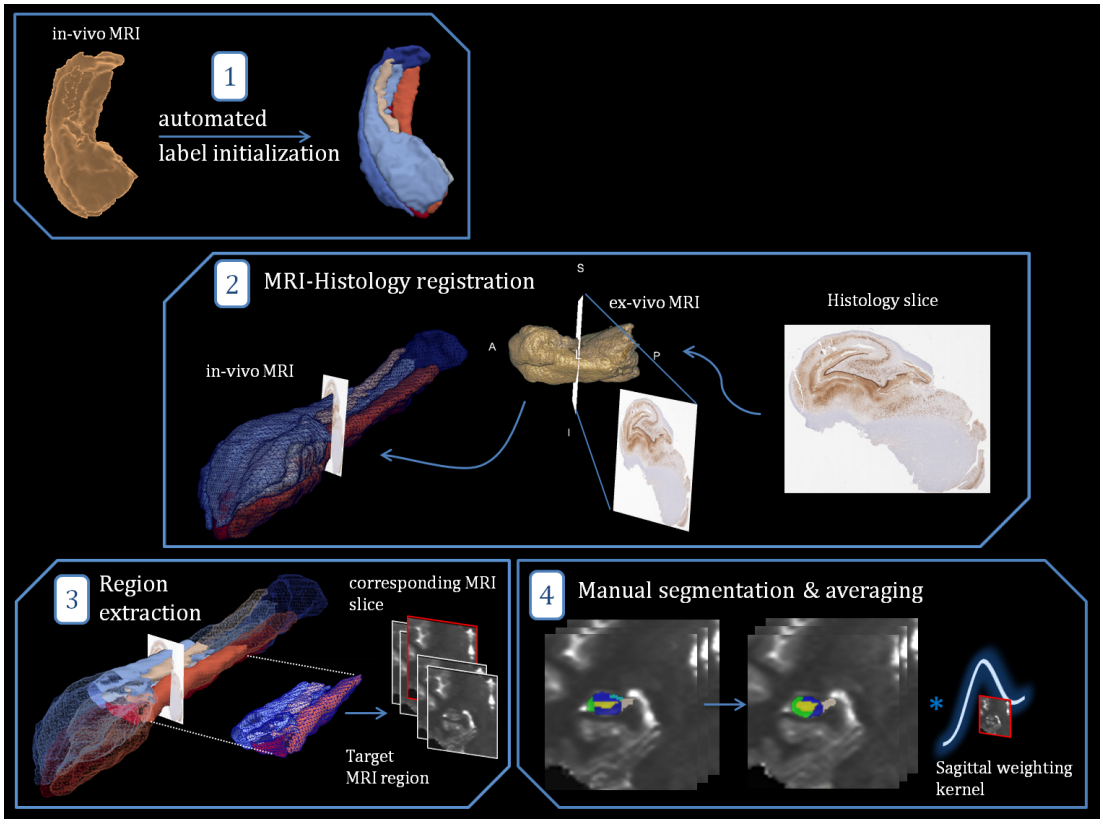

Figure 5.3: In-vivo MRI parameter extraction scheme. A target region was chosen around the corresponding (registered) MRI slice to the cut histology slice for parameter extraction. Manual segmentation of the subfields was employed within the target region and a sagittal weighting kernel was applied, whereby slices closer to the corresponding MRI slice in the sagittal plane had higher weighting.

were generated for the parameters and features and employed in the statistical analysis. We corrected for multiple comparisons in our correlation analysis with family-wise error rate (FWER) control using permutation tests [33].

To the test the efficacy of quantitative MRI parameters in pre-operatively predicting neuronal loss per subfield, multiple linear regression analysis was performed between all MRI parameters and percent loss of neurons for each subfield. Similarly to the previous experiment, regression analysis was first performed employing whole hippocampus, and then subfield parameters. We employed a forward stepwise selection procedure where variables were added sequentially to the model only if they improve the fit and the process was repeated until the addition of further variables was no longer necessary.

Finally we employed linear discriminant functional analysis to investigate the effectiveness of each subfield in accurately classifying the patients according to the quantitative HS subtype classification. The classification algorithm was performed using first the volumetric and all other quantitative parameters for whole hippocampal measures, then the same parameters for each subfield (CA1, CA2/3 and CA4 separately). Statistical analyses were performed in IBM SPSS statistics 20 (IBM, Armonk, NY) and JMP statistical software 10 (SAS, Cary, NC).

5.3 Results

Our manual count experiment to validate the automated neuron segmentation produced 98% and 96% agreements for computation of pyramidal and granular cell counts respectively. A summary of the volumetry, relaxometry and diffusion MRI data as well

as histological neuronal density, categorized by the qualitative HS subtype classification, is presented in Figure 5.4.

5.3.1 MRI-histology correlation analysis

A significant positive Spearman Rho correlation was found between whole hippocampal volume and neuronal density in CA1. A significant negative Spearman Rho correlation was also found between whole hippocampus MD on pre-operative MRI and pyramidal cell density and size of the CA2/3 and CA4 subfields. In addition, whole hippocampus T1 positively correlated with neuronal size of CA4. As for subfield-specific correlations, there was a significant positive correlation between volume on MRI and neuronal density as well as size on histology in all subfields. MD within the CA4/DG subfields was negatively correlated with pyramidal cell density. Moreover, T1 in CA4/DG was negatively correlated with neuronal size and density of the CA4 subfield. Finally, CA1 normalized T2 intensity correlated with GFAP field fraction (r=0.835, p ¡ 0.001), as shown in Figure 5.5, and CA2/3 FA was negatively correlated with GFAP field fraction. Table 5.3 summarizes the Spearman Rho correlation results for whole hippocampus as well as subfield-specific analyses respectively.

5.3.2 Correlations with clinical variables

Whole hippocampus volume negatively correlated with both qualitative and quantitative HS subtype classifications (r = -0.917, p = 0.01 and r = -0.781, p = 0.02), where higher grades indicated increased sclerosis. In addition, whole hippocampus MD correlated with the clinical qualitative HS subtype classification (r = -0.781, p = 0.04). In

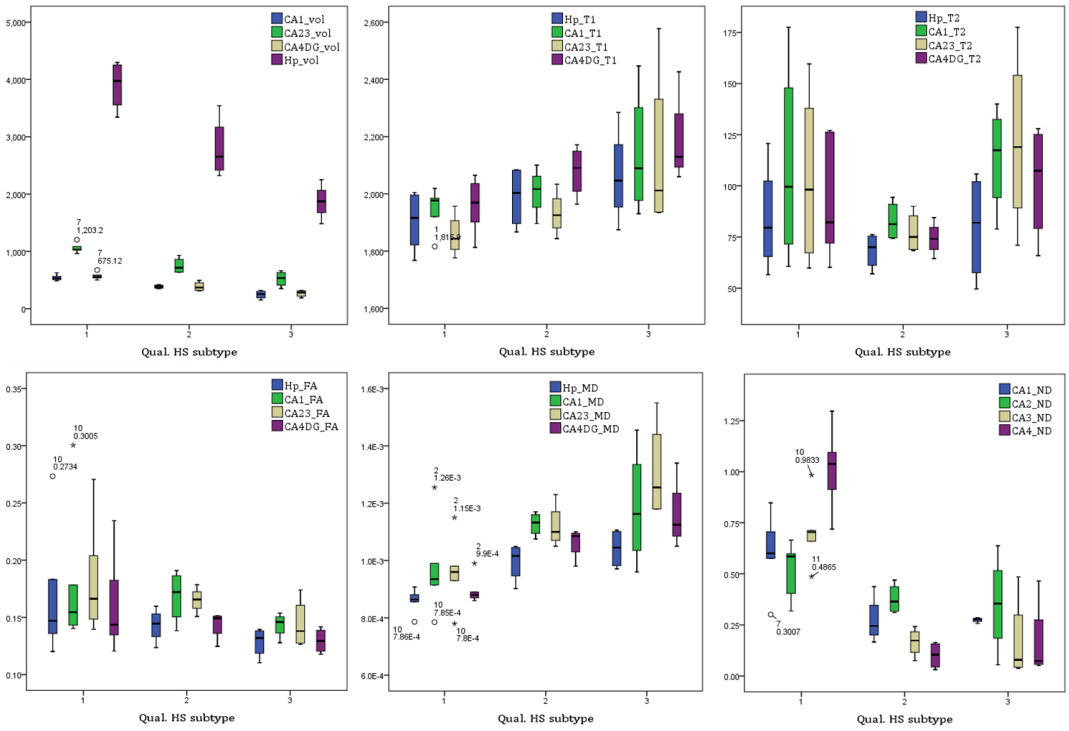

Figure 5.4: Boxplots of in-vivo MRI parameters (Volume, T1, T2, FA and MD) as well as histological neuronal density categorized by the qualitative HS subtype classification.

Table 5.3: Significance of Spearman's correlations between MR parameters and histological features for whole hippocampus and subfield-specific analyses.

		Whole hippocampus MRI parameters				
Histology features	**CA1**	**Volume**	**T1**	**T2**	**FA**	**MD**
	Density	r = 0.839 *p = 0.001*	ns	ns	ns	ns
	CA2/3	**Volume**	**T1**	**T2**	**FA**	**MD**
	Density	r = 0.586 *p = 0.035*	ns	ns	ns	r = -0.786 *p = 0.001*
	Size	ns	ns	ns	ns	r = -0.835 *p = 0.002*
	CA4	**Volume**	**T1**	**T2**	**FA**	**MD**
	Density	r= 0.611 *p = 0.027*	ns	ns	ns	r =- 0.857 *p = 0.001*
	Size	r = 0.602 *p = 0.017*	r = -0.703 p = 0.007	ns	ns	r = - 0.758 *p = 0.003*
		Subfield-specific MRI parameters				
Histology features	**CA1**		CA1			
		Volume	**T1**	**T2**	**FA**	**MD**
	Density	r = 0.910 *p < 0.001*	ns	ns	ns	ns
	Size	r = 0.731 *p = 0.005*	ns	ns	ns	ns
	CA2/3		CA2/3			
		Volume	**T1**	**T2**	**FA**	**MD**
	Density	r = 0.811 *p = 0.001*	ns	ns	ns	ns
	GFAP F.F	ns	ns	ns	r=- 0.489 *p=0.048*	ns
	CA4		CA4/DG			
		Volume	**T1**	**T2**	**FA**	**MD**
	Density	r=0.731 *p = 0.005*	r=-0.781 *p = 0.002*	ns	ns	r = -0.833 *p < 0.001*
	Size	r=0.749 *p = 0.003*	r = -0.830 *p < 0.001*	ns	ns	r = -0.841 *p = 0.039*

the subfield-specific correlation analysis, both qualitative and quantitative HS subtypes negatively correlated with volume of all the subfields. CA4 MD correlated as well with both classifications (r = 0.847, p = 0.01 and r = 0.708, p = 0.03) and CA2/3 MD correlated with the qualitative HS subtypes (r = -0.781, p = 0.04). When correlated against histological features, the qualitative HS subtype classification correlated with neuronal density in all subfields except for DG. It should be noted as well that neither qualitative nor quantitative classification of HS subtypes correlated with Engel outcomes.

5.3.3 Multiple linear regressions

A multiple linear regression analysis was performed to predict percentage neuron loss per subfield from quantitative and volumetric whole hippocampus MRI parameters. Whole hippocampus volume and T2 predicted percent pyramidal cell loss in CA1 with meager accuracy (adjusted R^2 = 0.433). Only hippocampal volume added significantly to the prediction. Whole hippocampus MD and T2 predicted percent pyramidal cell loss in CA2/3 with high accuracy (adjusted R^2 = 0.853). Only hippocampal MD added significantly to the prediction. Similarly, MD, T2 and volume accurately predicted percent pyramidal cell loss in CA4 (adjusted R^2 = 0.853). Both MD and T2 added significantly to the prediction. Table 5.4 summarizes the multiple linear regression fit for predicting percent neuron loss from whole hippocampus parameters.

In the subfield-specific experiment, CA4/DG volume as well as CA1 T1 and FA, predicted CA1 percent neuronal loss with high accuracy (adjusted R^2 = 0.904). Only volume added significantly to the model with standardized coefficients. Volume and T1 parameters from CA2/3 as well as CA4/DG MD and T2 predicted CA2/3 percent

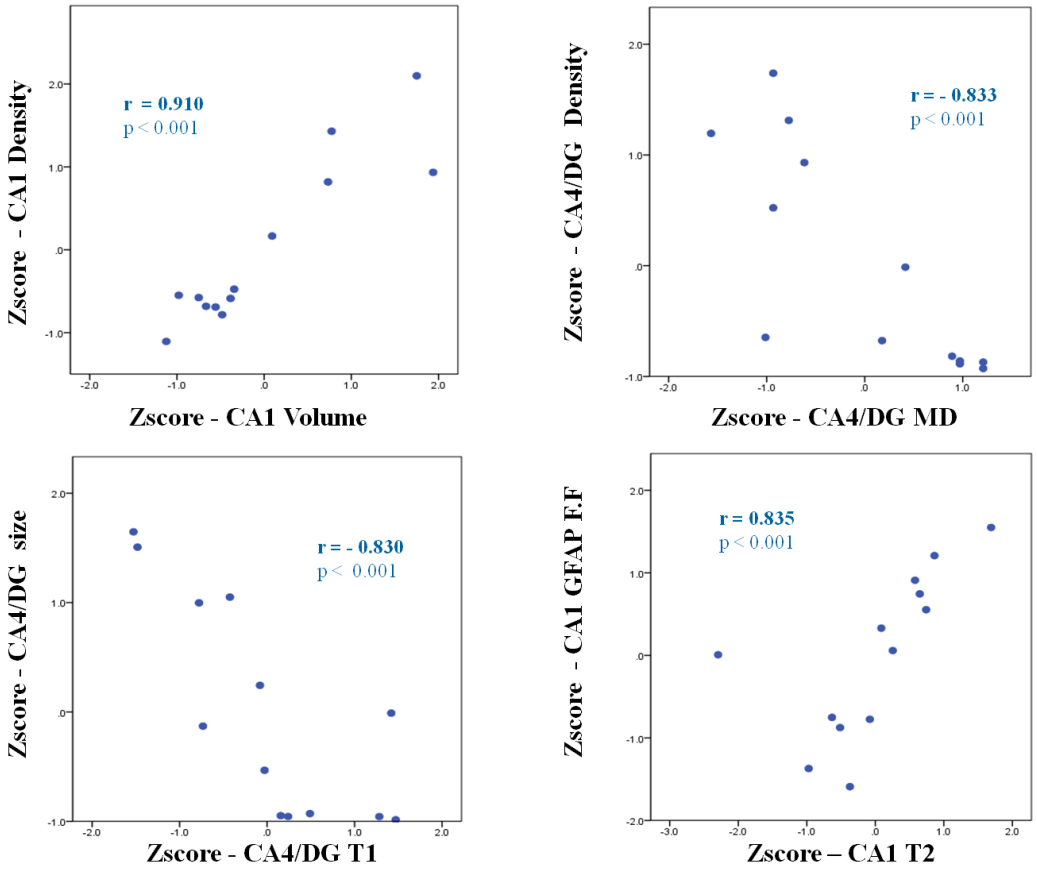

Figure 5.5: Most significant associations from Spearman's correlation analysis for subfield-specific MRI parameters with histological features.

Table 5.4: Model fit of multiple linear regression analysis for predicting percent neuron loss per subfield using whole hippocampus MRI parameters.

Dependent variable	**Independent variables**	**Standardized coefficient (β)**	p	**F**	R^2	**Adjusted R^2**	**Prob > F**
% cell loss CA1				5.588	0.528	0.433	0.023
	Volume	-0.586	0.022*				
	T2	-0.402	0.094				
% cell loss CA2/3				13.725	0.795	0.649	0.023
	MD	0.466	0.001**				
	T2	-0.395	0.043*				
% cell loss CA4				24.202	0.89	0.853	0.003
	MD	-0.537	0.001**				
	T2	-0.353	0.011*				
	Volume	-0.288	0.066				

loss with very high accuracy (adjusted R^2 = 0.958). All four parameters from CA2/3 added significantly to the prediction. Finally, loss in CA4 was predicted with equivalent accuracy using CA4/DG and CA2/3 volume and MD (adjusted R^2 = 0.971). Table 5.5 summarizes the multiple linear regression results for the subfield-specific experiment. The model fit for the prediction of neuronal loss of the four analyzed subfields from subfield-specific parameters is demonstrated in Figure 5.6.

5.3.4 Discriminant function analysis

The quantitative HS subtypes categorization was employed as the grouping variable for the discriminant function analysis. We performed three classification experiments each using the volumetry and quantitative MRI parameters of each of the three pre-

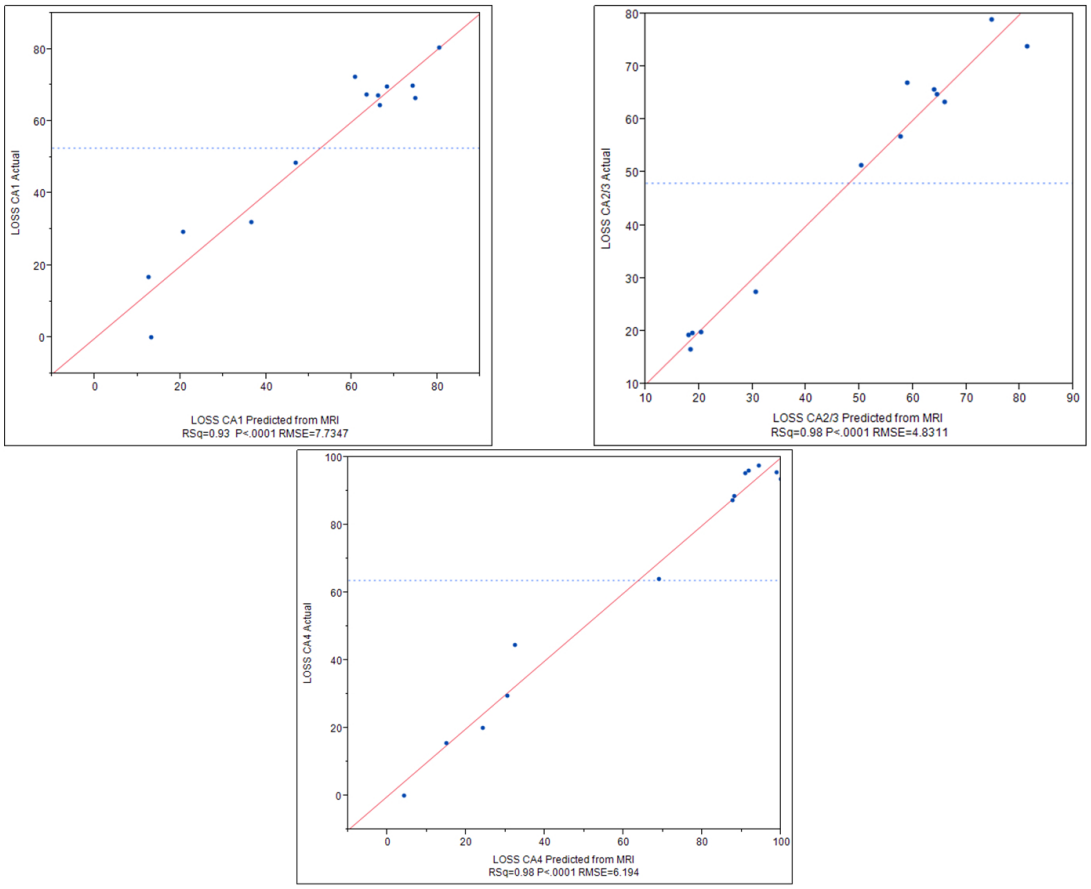

Figure 5.6: Multiple linear regression results for subfield-specific parameters depicting predicted vs. actual percent neuron loss for each of the four CA subfields.

Table 5.5: Model fit of multiple linear regression analysis for predicting percent neuron loss per subfield using subfield-specific MRI parameters.

Dependent variable	**Independent variables**	**Estimate (β)**	p	**F**	R^2	**Adjusted R^2**	**Prob > F**
% cell loss CA1				39.0	0.929	0.905	<0.001
	CA4/DG Vol	-25.211	<0.001**				
	CA1 FA	-6.714	0.039*				
	CA1 T1	-5.707	0.094				
% cell loss CA2/3				56.5	0.976	0.958	<0.001
	CA2/3 Vol	-22.754	<0.001**				
	CA 2/3 T1	-22.754	<0.001**				
	CA4/DG MD	15.316	0.006**				
	CA4/DG T2	-8.24	0.023*				
% cell loss CA4				102.8	0.980	0.971	<0.001
	CA4/DG MD	17.239	0.0008**				
	CA2/3 Vol	-40.529	<0.001**				
	CA2/3 MD	3.828	0.389				
	CA1 Vol	10.605	0.003*				

operatively segmented subfields (CA1, CA2/3 and CA4/DG) as independents. Leave-one-out cross-validation was employed whereby each patient was classified based on the functions from all other subjects. CA2/3 outperformed CA1 and CA4/DG with 92.3% (all but one) of cross-validated grouped patients correctly classified, as compared to a 84.6% (CA4/DG) and a 61.5% (CA1) accurately predicted classification.

5.4 Discussion

Numerous studies previously correlated T2 relaxometry with pathology in the context of hippocampal sclerosis. However, they only focused on whole hippocampus MRI parameters and employed relaxometry maps with low out-of-plane resolution (> 3 mm) [6, 3, 4, 5, 9, 10, 11]. This work is the first to investigate quantitative multi-modal relaxometry (T1 and T2) as well as diffusion metrics within the hippocampal subfields while employing high resolution in-vivo maps at 3T. A comprehensive protocol that validates high-resolution MRI maps with quantitative histology was employed to better understand the pathological substrates of our imaging findings. An automated quantitative histology procedure for quantification of neuronal density, size and NeuN and GFAP field fractions was also developed and validated. These features maybe more sensitive to neuronal degeneration as compared to qualitative assessment or quantitative grading of neuronal loss as they provide a continuous measurement of pathologies.

5.4.1 Biological Interpretations

In our correlation analysis, whole hippocampus volumetry was correlated with neuronal density in all subfields. Similarly, pre-operative subfield volumetry was found

to be highly correlated with subfield density (specifically in CA1). Moreover whole hippocampal volume, as well as all subfield-specific volumes correlated with the quantitative HS subtypes, which can be thought of as a global measure of neuron loss in the subfields (since it is entirely based on percent loss). Numerous studies have reported that neuronal density within the subfield may directly relate to volume atrophy [1, 2, 3, 8, 34]. The presented subfield-specific and whole hippocampus correlation analyses confirmed these previous findings.

Mean diffusivity was the most prominent MRI metric (having the most associations) in the MRI-histology correlation analysis, whether whole hippocampus or subfield-specific within CA4. In our subfield correlation analysis, MD was negatively correlated with neuronal density and size of CA4. In addition, whole hippocampus, CA2/3 and CA4/DG MD correlated with the qualitative classification and only CA4/DG MD correlated with the quantitative HS subtypes. Such correlations demonstrate the importance of this MRI parameter in determining subtypes pre-operatively. A previous study analyzing relationships between diffusion maps and cell density in malignant brain tumours described an analogous association between MD and tumour core cell density [35]. The loss of neurons in the hippocampal subfields may lead to less restricted, or hindered, water diffusion and thus higher diffusivity. A similar interpretation can be described for the relationship between MD and neuronal size, since as neuronal cell bodies shrink water diffuses more freely and diffusivity increases. Given the limitations of in-vivo DTI data, we cannot precisely assess the nature of the architectural changes related to MD, however we hope to explore these issues further using high-resolution ex-vivo DTI of the resected specimens.

T1 and FA were also negatively correlated with neuronal density/size and GFAP field fractions respectively in CA2/3. An analogous relationship between ex-vivo GM

T1 values and neuronal density has been described in patients with multiple sclerosis [36]. Cell loss will likely result in an increase in the extra-cellular space, thus the intra-cellular water will decrease as extra-cellular water increases, which in turn would increase T1 [37]. A previous study demonstrated as well the negative correlation between FA and GFAP in a rat model of hydrocephalus pathology [38]. FA is a marker of tissue microstructure and axonal integrity and reduced FA is often accompanying neuronal degeneration [38]. Similarly, increased GFAP field fraction expression represents astrocytic and microglial proliferation of the subfields and increased reactive gliosis is observed with neuronal loss. T2 anomalies have been previously suggested to reflect gliotic changes in the dentate gyrus [34]. This relationship was not observed in our analysis, and the discrepancy in the results may be attributed to methodological differences since we relied on GFAP field fraction whereas glial cell counts (astrocytes and oligodendroglial cells) were used in that study.

5.4.2 Clinical findings and insights

Multiple linear regression analysis revealed that volume and MD are the most prominent parameters in predicting neuronal loss. This observation mirrors the correlation analysis where MD and volume were the parameters with the highest number of associations with histological features. T1 was also correlated with neuronal size and density, but a larger cohort may be needed to observe its predictive validity on neuronal density. Hippocampal neuronal loss has been previously shown to be a predictor of patient outcomes [39] and memory deficits [40]. Predicting subfield loss from in-vivo quantitative MRI has the potential to non-invasively localize pathology and determine the extent of hippocampal atrophy, with a precision so far unachievable. It may also

help classify patients into different HS subtypes and decide on the merit of their surgical candidacy. Both multiple linear regression and discriminant function analyses demonstrated, as expected, that subfield-specific analysis is more sensitive towards subfield pathology as compared to whole hippocampus measurements. Specifically, subfield-specific parameters produced more accurate prediction of percent loss in all subfields (mainly CA1 and CA2). Classifying HS subtypes revealed that MRI parameters from CA2/3 and CA4/DG act as more effective discriminating variables as compared to CA1 parameters. This effect could be due to the extent of atrophy within the subfields; the most sclerotic CA1 subfields are almost depleted of neurons by the time of surgery, while a more balanced distribution of the subtypes is observed in other subfields.

The association between the qualitative HS subtype classification and neuronal density within the CA subfields validates the accuracy of our automated neuron quantification procedure. Hippocampal sclerosis subtypes have previously been shown to have different post-operative outcomes; those with CA4 atrophy have more favourable outcomes than others [41, 42] and correlate with seizure duration and onset [43]. Therefore, the task of determining HS subtypes from in-vivo images is of great importance for pre-operative investigation of intractable TLE patients. The Engel outcomes presented in this study are reported in the short-term follow up with the average time since surgery for our cohort being just under two years (22 months). The lack of correlations between the HS subtype classification and Engel outcomes in our analysis maybe due to the small number of subjects.

5.4.3 Limitations and technical considerations

There are two steps in our processing pipeline where mis-registration between images could affect the accuracy of the results. The first is the multi-modal registration between the different quantitative maps, and the second is the registration of our quantitative maps to the Freesurfer template for subfield segmentation (part of the labeling scheme). The former should not account for significant error, as the employed correlation ratio similarity metric is robust to multi-modal registration of the same subject. The latter is mitigated by the generation of SynT1 images which have analogous intensities to T1-weighted images upon which the algorithm is optimized. Although our maps are of higher spatial resolution than standard clinical scans, a higher intrinsic resolution (sub-millimeter) is preferred to achieve superior delineation and extraction of relaxation times or diffusion signal within the subfields. Another limitation of this work, is the lack of normative control data for histology, and hence the least sclerotic specimens were used as reference for computation of percent cell loss. We also employed histological measurements from one optimal slide per subject, due to the large variability in specimen sizes, as well as effects of tissue breakage and fragmentations of the specimens, which may have biased the results. Another way to correlate pre-operative MRI and pathology is through direct registration of both modalities [44] and warping of regions of interest from histology to in-vivo space. However, for this technique to be effective, image resolution of pre-operative volumes needs to be sub-millimeter. For example, if in-vivo maps have a 1 mm isotropic resolution, smaller subfields (i.e CA2 and CA3) warped from histology would only occupy 2 or 3 voxels on a slice in the in-vivo space, which would challenge the accuracy of the results.

Bibliography

[1] Gregory D Cascino, Clifford R Jack, Joseph E Parisi, Frank W Sharbrough, Kathryn A Hirschorn, Frederic B Meyer, W Richard Marsh, and Peter C O'Brien. Magnetic resonance imaging–based volume studies in temporal lobe epilepsy: pathological correlations. *Annals of neurology*, 30(1):31–36, 1991.

[2] T Lencz, G McCarthy, R A Bronen, T M Scott, J A Inserni, K J Sass, R A Novelly, J H Kim, and D D Spencer. Quantitative magnetic resonance imaging in temporal lobe epilepsy: relationship to neuropathology and neuropsychological function. *Ann Neurol*, 31(6):629–37, 1992.

[3] W Van Paesschen, T Revesz, J S Duncan, M D King, and A Connelly. Quantitative neuropathology and quantitative magnetic resonance imaging of the hippocampus in temporal lobe epilepsy. *Ann Neurol*, 42(5):756–66, 1997.

[4] Ana Carolina Coan, Eliane Kobayashi, Li Min Li, and Fernando Cendes. Quantification of hippocampal signal intensity in patients with mesial temporal lobe epilepsy. *J Neuroimaging*, 13(3):228–33, 2003.

[5] AC Coan, B Kubota, FPG Bergo, BM Campos, and F Cendes. 3t mri quantification of hippocampal volume and signal in mesial temporal lobe epilepsy improves detection of hippocampal sclerosis. *American Journal of Neuroradiology*, 35(1): 77–83, 2014.

[6] G D Jackson, A Connelly, J S Duncan, R A Grünewald, and D G Gadian. Detection of hippocampal pathology in intractable partial epilepsy: increased sensitivity with quantitative magnetic resonance T2 relaxometry. *Neurology*, 43(9):1793–9, 1993.

[7] R I Kuzniecky, E Bilir, F Gilliam, E Faught, C Palmer, R Morawetz, and G Jackson. Multimodality MRI in mesial temporal sclerosis: relative sensitivity and specificity. *Neurology*, 49(3):774–8, 1997.

[8] Jan-Christoph Schoene-Bake, Simon S Keller, Pitt Niehusmann, Elisa Volmering, Christian Elger, Michael Deppe, and Bernd Weber. In vivo mapping of hippocampal subfields in mesial temporal lobe epilepsy: Relation to histopathology. *Human brain mapping*, pages 4718–4728, 2014.

[9] CE Mackay, JA Webb, PR Eldridge, DW Chadwick, GH Whitehouse, and N Roberts. Quantitative magnetic resonance imaging in consecutive patients evaluated for surgical treatment of temporal lobe epilepsy. *Magnetic resonance imaging*, 18(10):1187–1199, 2000.

[10] P M Gonçalves Pereira, E Oliveira, and P Rosado. Apparent diffusion coefficient mapping of the hippocampus and the amygdala in pharmaco-resistant temporal lobe epilepsy. *AJNR American journal of neuroradiology*, 27(3):671–83, 2006.

[11] SA Baxendale, W van Paesschen, PJ Thompson, A Connelly, JS Duncan, WF Harkness, and SD Shorvon. The relationship between quantitative mri and neuropsychological functioning in temporal lobe epilepsy. *Epilepsia*, 39(2):158–166, 1998.

[12] Susanne G Mueller, Kenneth D Laxer, Cathy Scanlon, Paul Garcia, William J McMullen, David W Loring, Kimford J Meador, and Michael W Weiner. Different structural correlates for verbal memory impairment in temporal lobe epilepsy with and without mesial temporal lobe sclerosis. *Human brain mapping*, 33(2):489–499, 2012.

[13] R Edward Hogan, Lei Wang, Mary E Bertrand, L James Willmore, Richard D Bucholz, A Sami Nassif, and John G Csernansky. Mri-based high-dimensional hippocampal mapping in mesial temporal lobe epilepsy. *Brain*, 127(8):1731–1740, 2004.

[14] Susanne G Mueller, Kenneth D Laxer, Jerome Barakos, Ian Cheong, Paul Garcia, and Michael W Weiner. Subfield atrophy pattern in temporal lobe epilepsy with and without mesial sclerosis detected by high-resolution MRI at 4 Tesla: preliminary results. *Epilepsia*, 50(6):1474–83, 2009.

[15] Fergus J Rugg-Gunn, Sofia H Eriksson, Mark R Symms, Gareth J Barker, Maria Thom, William Harkness, and John S Duncan. Diffusion tensor imaging in refractory epilepsy. *Lancet*, 359(9319):1748–51, 2002.

[16] Niels K Focke, Mahinda Yogarajah, Silvia B Bonelli, Philippa A Bartlett, Mark R Symms, and John S Duncan. Voxel-based diffusion tensor imaging in patients with mesial temporal lobe epilepsy and hippocampal sclerosis. *Neuroimage*, 40 (2):728–37, 2008.

[17] Lionel Thivard, Stéphane Lehéricy, Alexandre Krainik, Claude Adam, Didier Dormont, Jacques Chiras, Michel Baulac, and Sophie Dupont. Diffusion tensor imaging in medial temporal lobe epilepsy with hippocampal sclerosis. *Neuroimage*, 28(3):682–90, 2005.

[18] Ali R Khan, Maged Goubran, Sandrine de Ribaupierre, Robert R Hammond, Jorge G Burneo, Andrew G Parrent, and Terry M Peters. Quantitative relaxometry and diffusion MRI for lateralization in MTS and non-MTS temporal lobe epilepsy. *Epilepsy Research*, 108:506–516, 2014.

[19] Diego Cantor-Rivera, Ali R Khan, Maged Goubran, Seyed M Mirsattari, and Terry M Peters. Detection of temporal lobe epilepsy using support vector machines in multi-parametric quantitative mr imaging. *Computerized Medical Imaging and Graphics*, 2014.

[20] A Bernasconi, N Bernasconi, Z Caramanos, D C Reutens, F Andermann, F Dubeau, D Tampieri, B G Pike, and D L Arnold. T2 relaxometry can lateralize mesial temporal lobe epilepsy in patients with normal MRI. *Neuroimage*, 12 (6):739–46, 2000.

[21] N Bernasconi, S Duchesne, A Janke, J Lerch, D L Collins, and A Bernasconi. Whole-brain voxel-based statistical analysis of gray matter and white matter in temporal lobe epilepsy. *Neuroimage*, 23(2):717–23, 2004.

[22] B C Bernhardt, K J Worsley, H Kim, A C Evans, A Bernasconi, and N Bernasconi. Longitudinal and cross-sectional analysis of atrophy in pharmacoresistant temporal lobe epilepsy. *Neurology*, 72(20):1747–54, 2009.

[23] Arnout C Ruifrok and Dennis A Johnston. Quantification of histochemical staining by color deconvolution. *Analytical and quantitative cytology and histology/the International Academy of Cytology [and] American Society of Cytology*, 23(4): 291–299, 2001.

[24] Pierre Soille. *Morphological image analysis: principles and applications*. Springer-Verlag New York, Inc., 2003.

[25] Ingmar Blümcke, Roland Coras, Hajime Miyata, and Cigdem Ozkara. Defining clinico-neuropathological subtypes of mesial temporal lobe epilepsy with hippocampal sclerosis. *Brain Pathol*, 22(3):402–11, 2012.

[26] Paul A Yushkevich, Joseph Piven, Heather Cody Hazlett, Rachel Gimpel Smith, Sean Ho, James C Gee, and Guido Gerig. User-guided 3D active contour segmentation of anatomical structures: significantly improved efficiency and reliability. *Neuroimage*, 31(3):1116–28, 2006.

[27] Maged Goubran, David A Rudko, Brendan Santyr, Joe Gati, Trevor Szekeres, Terry M Peters, and Ali R Khan. In vivo normative atlas of the hippocampal subfields using multi-echo susceptibility imaging at 7 tesla. *Human brain mapping*, 35:3588–3601, 2013.

[28] L E M Wisse, L Gerritsen, J J M Zwanenburg, H J Kuijf, P R Luijten, G J Biessels, and M I Geerlings. Subfields of the hippocampal formation at 7 T MRI: in vivo volumetric assessment. *Neuroimage*, 61(4):1043–9, 2012.

[29] Henri M Duvernoy. *The human hippocampus: functional anatomy, vascularization and serial sections with MRI*. Springer, 2005.

[30] Eli Gibson, José A Gómez, Madeleine Moussa, Cathie Crukley, Glenn Bauman, Aaron Fenster, and Aaron D Ward. 3d reconstruction of prostate histology based on quantified tissue cutting and deformation parameters. In *SPIE Medical Imaging*, pages 83170N–83170N. International Society for Optics and Photonics, 2012.

[31] Koen Van Leemput, Akram Bakkour, Thomas Benner, Graham Wiggins, Lawrence L Wald, Jean Augustinack, Bradford C Dickerson, Polina Golland, and Bruce Fischl. Automated segmentation of hippocampal subfields from ultra-high resolution in vivo MRI. *Hippocampus*, 19(6):549–57, 2009.

[32] Sean C.L Deoni, Brian K Rutt, and Terry M Peters. Synthetic T1-weighted brain

image generation with incorporated coil intensity correction using DESPOT1. *Magnetic Resonance Imaging*, 24(9):1241–1248, 2006.

[33] David M Groppe, Thomas P Urbach, and Marta Kutas. Mass univariate analysis of event-related brain potentials/fields i: A critical tutorial review. *Psychophysiology*, 48(12):1711–1725, 2011.

[34] Regula S Briellmann, Renate M Kalnins, Samuel F Berkovic, and Graeme D Jackson. Hippocampal pathology in refractory temporal lobe epilepsy: T2-weighted signal change reflects dentate gliosis. *Neurology*, 58(2):265–71, 2002.

[35] Manabu Kinoshita, Naoya Hashimoto, Tetsu Goto, Naoki Kagawa, Haruhiko Kishima, Shuichi Izumoto, Hisashi Tanaka, Norihiko Fujita, and Toshiki Yoshimine. Fractional anisotropy and tumor cell density of the tumor core show positive correlation in diffusion tensor magnetic resonance imaging of malignant brain tumors. *Neuroimage*, 43(1):29–35, 2008.

[36] Klaus Schmierer, Harold G Parkes, Po-Wah So, Shu F An, Sebastian Brandner, Roger J Ordidge, Tarek A Yousry, and David H Miller. High field (9.4 tesla) magnetic resonance imaging of cortical grey matter lesions in multiple sclerosis. *Brain*, 133(3):858–867, 2010.

[37] Alina Jurcoane, Marlies Wagner, Christoph Schmidt, Christoph Mayer, Rene-Maxime Gracien, Marc Hirschmann, Ralf Deichmann, Steffen Volz, Ulf Ziemann, and Elke Hattingen. Within-lesion differences in quantitative mri parameters predict contrast enhancement in multiple sclerosis. *Journal of Magnetic Resonance Imaging*, 38(6):1454–1461, 2013.

[38] Weihong Yuan, Kelley E Deren, James P McAllister II, Scott K Holland, Diana M

Lindquist, Alessandro Cancelliere, Melissa Mason, Ahmed Shereen, Dean A Hertzler, Mekibib Altaye, et al. Diffusion tensor imaging correlates with cytopathology in a rat model of neonatal hydrocephalus. *Cerebrospinal fluid research*, 7(1):1–12, 2010.

[39] Anaclara Prada Jardim, Rafael Scarpa da Costa Neves, Luís Otávio Sales Ferreira Caboclo, Carmen Lucia Penteado Lancellotti, Murilo Martinez Marinho, Ricardo Silva Centeno, Esper Abrão Cavalheiro, Carla Alessandra Scorza, and Elza Márcia Targas Yacubian. Temporal lobe epilepsy with mesial temporal sclerosis: hippocampal neuronal loss as a predictor of surgical outcome. *Arquivos de neuro-psiquiatria*, 70(5):319–324, 2012.

[40] E Pauli, M Hildebrandt, J Romstöck, H Stefan, and I Blümcke. Deficient memory acquisition in temporal lobe epilepsy is predicted by hippocampal granule cell loss. *Neurology*, 67(8):1383–1389, 2006.

[41] Maria Thom, Ioannis Liagkouras, Kathryn J Elliot, Lillian Martinian, William Harkness, Andrew Mcevoy, Luis O Caboclo, and Sanjay M Sisodiya. Reliability of patterns of hippocampal sclerosis as predictors of postsurgical outcome. *Epilepsia*, 51(9):1801–1808, 2010.

[42] BV Savitr Sastri, A Arivazhagan, Sanjib Sinha, Anita Mahadevan, RD Bharath, J Saini, R Jamuna, J Keshav Kumar, SL Rao, BA Chandramouli, et al. Clinicopathological factors influencing surgical outcome in drug resistant epilepsy secondary to mesial temporal sclerosis. *Journal of the neurological sciences*, 340(1): 183–190, 2014.

[43] D Fuerst, J Shah, WJ Kupsky, R Johnson, A Shah, B Hayman-Abello, T Ergh,

Q Poore, A Canady, and C Watson. Volumetric mri, pathological, and neuropsychological progression in hippocampal sclerosis. *Neurology*, 57(2):184–188, 2001.

[44] Maged Goubran, Cathie Crukley, Sandrine de Ribaupierre, Terence M Peters, and Ali R Khan. Image registration of ex-vivo MRI to sparsely sectioned histology of hippocampal and neocortical temporal lobe specimens. *Neuroimage*, 83:770–781, 2013.

Chapter 6

Conclusions and future work

The focus of this thesis is the correlation of quantitative MRI parameters with quantitative histological features within both the hippocampus and temporal lobe neocortex of patients suffering from drug-resistant epilepsy. These correlations relied on image registration and a comprehensive pipeline to bring both modalities together and merge information from both, macro and micro, domains. Correlating MRI and histology validates novel MRI sequences and aids in better understanding the pathological substrates of our imaging findings. More importantly, I demonstrated that quantitative MRI parameters can predict pathology and neuron integrity pre-operatively, which -with further studies- can have an impact on pre-operative evaluation, patient stratification and outcome prediction. Predicting subfield loss from in-vivo quantitative MRI has the potential to non-invasively localize pathology and determine the extent of hippocampal atrophy. It may also help classify patients into different HS subtypes and decide on the merit of their surgical candidacy. These in-vivo quantitative maps can be extended

as well as a marker for degeneration of hippocampal subfields in neurodegenerative diseases such as Alzheimer's.

Chapter 2 presents a protocol for registration of *ex-vivo* specimen MRI to histopathology, specifically hippocampal and neocortical temporal lobe sections. Sub-millimeter errors have been shown for *ex-vivo* MRI to histology registration on twelve collected specimens from seven patients. A successful registration between histology - currently considered as the ground truth - and post-operative MRI of resected tissue is imperative for better understanding of focal epilepsy at both the micro and macro levels. This correspondence is a key component towards achieving MRI and histology correlation by bringing together information from both domains.

Accordingly, I implemented and validated a protocol for registration of in-vivo to ex-vivo brain MRI specimens, allowing for the first time a dense correspondence of in-vivo MR with temporal lobe histology. Image registration of surgically resected brain specimens is a unique application which presents a number of technical challenges that have not been fully addressed in previous literature. The registration accuracy reported is within an acceptable range and allows for the spatially-local and quantitative assessment of pathological correlates in MRI by the fusion of information from both modalities.

In chapter 4, I demonstrated that alterations of in-vivo T1 and FA, in the temporal lobe cortex and white matter, are predictive of neuronal integrity (density and size) that serve to delineate an epileptogenic lesion. This work is the first to quantitatively assess the relationship between MRI and histopathological features using correspondences based on image registration in focal epilepsy, and to relate in-vivo T1 and FA values to the proportion of neurons, specifically large-caliber neurons, in the neocortical gray

matter. Our registration and correlation pipeline allows for a quantitative assessment of the pathological correlates of MRI by bringing information from both modalities, and the potential prediction of pathology from in-vivo MRI.

Finally, I investigated, for the first time, quantitative multi-modal in-vivo relaxometry and diffusion parameters within the hippocampal subfields for intractable TLE patients, and also developed and validated an automated quantitative histology procedure for quantification of neuronal density, size and NeuN and GFAP field fractions. This analysis demonstrates that MD correlates with neuronal density and size, and can act as a marker for neuron integrity. More importantly, this thesis is the first to highlight the potential of subfield relaxometry and diffusion parameters (mainly T2 and MD) as well as volumetry in predicting patterns of neuronal loss and the extent of cell loss per hippocampal subfield, with a precision that has not been achieved previously, better characterizing different HS subtypes pre-operatively. These in-vivo maps provide a non-invasive means of localizing pathology and determining the degree of hippocampal subfield atrophy, which has the potential to impact pre-operative evaluation and prediction of surgical outcomes. Our results suggest that high-resolution quantitative MRI sequences could have a role in routine clinical practice for pre-operative evaluation of drug-resistant focal epilepsy.

6.0.4 Current Limitations & Future Directions

The global hypothesis of this thesis is that the signatures provided by quantitative multi-parametric MRI are able to predict pathology and ultimately provide vital guidance to the neurosurgeon during surgery. There are numerous future directions needed for this

work to achieve the ultimate goal of assisting the surgeons in localizing/resecting the seizure focus and predicting outcomes. For in-vivo maps to accurately predict pathology, many more patients need to be recruited to build a database of associated MRI parameters and pathology across different pathological substrates and sclerosis grades. Data from this large cohort would be fed into a machine learning algorithm such as a support vector machine (SVM) classifier that determines the set MR parameters most likely to represent each histological feature. Such algorithms will learn, or train for, the optimal set of features from all but the tested (new) subject in a cross-validated manner to predict pre-operatively. The resulting 'predictive' histology maps would be presented to the surgeons for minimally invasive pre-operative planning. Such maps could also be employed in an augmented reality setting as an interactive display for surgical guidance during the operation. Our imaging-histology protocol allows the development of a workflow from in-vivo imaging to the operating room that incorporates these 'predictive' maps and eventually their validation through histological analysis.

Furthermore, this work only focused on correlating structural substrates extracted from histopathology with MRI. Whether predicted structural pathology is directly related to the epileptogenicity of the tissue, and whether histopathological findings are more extensive than the epileptogenic cortex, are questions that still need to be addressed. Correlation with functional data such as electrophysiology acquired using either scalp or intracranial EEG could be used to validate the link between imaging findings and epileptogenicity and better understand the relationship between imaging, histology and seizure generation/propagation. With the moderate, current long-term success of surgery, outcome prediction and patient stratification into perspective Engel outcomes is a vital task for clinicians. Hence, it is of great importance to correlate the presented imaging findings with long-term seizure outcomes, and investigate whether

the absence of such lesions provides more favourable outcomes. Similarly, a larger set of truly negative TLE patients (where clinical MRI fails to find hippocampal, neocortical or whole-brain anomalies) needs to be examined with multi-parametric quantitative MRI to validate the effectiveness of these techniques in lesion detection for this subset of patients.

Appendix A presented a quantitative normative atlas of the hippocampal subfields using R2* and quantitative susceptibility at 7T. We aim as well to investigate these high field quantitative parameters within the subfields, in both HS-positive and negative patients, against volunteers to better understand and characterize hippocampal pathology. Another limitation of this work was the follow-up times and short-term outcomes employed for analysis. Since surgical outcomes is a major factor for these patients, performing the presented analyses/correlations between multi-parametric MRI and long-term outcomes is required for the translation of these techniques to clinical protocols. Moreover, employing control histological specimens would validate the presented histological findings and aid in interpreting whether these pathological substrates are linked to epileptogenicity of the temporal lobe in these patients.

Image resolution of in-vivo maps, whether structural or diffusion maps, is a major limiting factor for understanding pathological substrates of MRI. We plan to explore high field imaging, whether in-vivo 7T or ex-vivo 9.4T, for morphometry and diffusion changes not readily detectable at lower field strengths, which will help optimize in-vivo sequences at 1.5 and 3T. Furthermore, as advances in MRI hardware and software reconstruction continue, in-vivo scans with higher resolution and/or signal-to-noise will become available, which will allow more accurate and confident automated image registration between in-vivo MRI and histology of the hippocampus. This would in-turn

provide the opportunity to investigate MRI-histology associations employing voxel-based instead of ROI-based, or subfield-based analysis. Voxel-based analysis is superior to ROIs as it samples much more data in a bias-free manner without any priors. This technique will rely on a data-driven partitioning of the specimens, which can be compared to anatomical knowledge such as subfields in the hippocampus or cortical layers in the neocortex.

Bibliography

Appendix A

In vivo atlas of the hippocampal subfields

A.1 Introduction

The human hippocampus is the most frequently studied structure in the temporal lobe, due to its role in formation of memory and learning, among other functions. Structural abnormalities of the whole hippocampus, as assessed by volume measurements, have been studied extensively in diseases such as epilepsy [1], Alzheimer's disease (AD) [2], schizophrenia [3], depression [4] and post traumatic disorder [5]. The hippocampal formation is a compound structure. comprising the dentate gyrus (fascia dentata), the hippocampus proper and the subiculum (parahippocampal gyrus), located in the temporal lobe of the brain [6]. The hippocampus proper is further divided into

This chapter is adapted from Goubran et al. "In vivo normative atlas of the hippocampal subfields using multi-echo susceptibility imaging at 7 Tesla." Human Brain Mapping 2014;35(8):3588-3601

three subfields, Cornu Ammonis (CA) 1-3, with the fourth CA subfield or the hilus frequently considered as part of the dentate gyrus. Both pre-clinical and postmortem studies suggest that these morphologically and functionally distinct subfields are selectively affected throughout the progression of different neurological diseases. West et al. [7] for instance, demonstrated that the most distinctive neuronal loss associated with Alzheimer's disease (AD) was seen in CA1. Comparatively, Rössler et al. [8] showed that CA1 and the subiculum (SUB) are both involved in the stage-dependent neuronal loss of the disease. Pathologic stress has also been associated with atrophy in the CA3 [9]. Changes in the hippocampal subfields have also been linked to temporal lobe epilepsy (TLE). For instance, mesial temporal sclerosis (MTS), the most common underlying pathology in TLE, can be characterized according to changes in the hippocampal subfields. According to the existing literature, three types of changes can occur: type 1 (associated with sclerosis in CA1 and CA4), type 2 (defined by CA1 sclerosis), and type 3 (associated with end folium sclerosis) [10]. Since epilepsy surgical outcomes differ significantly for each of these MTS types, and because of the clear importance of the subfields in epilepsy monitoring and surgical planning, we believe that analysis of each subfield independently will lead to more accurate TLE diagnosis and improved surgical planning.

Imaging the hippocampal subfields in-vivo at 1.5 or 3.0 T is challenging due to the limited spatial resolution and signal-to-noise afforded by clinical 1.5 or 3.0 T scanners [11]. However, recent advances in ultra-high-field imaging have provided the opportunity to study the hippocampal internal architecture in-vivo at high resolution. Previous studies at 3-4.7 T [12, 13, 14] or 7T [15] have focused on standard T2-weighted sequences to attain the necessary contrast and resolution to delineate the hippocampal subfields and investigate morphometric properties. Gradient-echo MRI sequences,

such as those employed for quantitative susceptibility mapping (QSM) [16] may offer improved delineation of the hippocampus and its associated subfields. Specifically, multi-echo gradient echo sequences have the added benefit of providing additional information, such as T2* relaxation time and quantitative volume magnetic susceptibility. These quantitative metrics can be employed to better characterize structures of interest while still permitting the use of traditional volumetric and morphometric analyses. For example, T2* imaging has been employed at 7 Tesla in multiple previous reports to study the normal anatomy of the hippocampus [11, 17]. It has also been employed to analyze diseased populations as in temporal lobe epilepsy [18] or Alzheimer's disease [19].

In this appendix we investigated the potential of the high-field, susceptibility related contrast to better characterize the subfields of the hippocampus. Presently, there are no reports of QS values in the hippocampal subfields at higher fields in-vivo, and only one study quantifying R2* (1/T2*) at 7T [20]. This study presents the first attempt at in vivo quantification of susceptibility values within the subfields at 7T, and our quantitative MRI measurements provide a useful starting point for more advanced analyses of subfield composition in both healthy control and diseased populations.

Anatomical atlases derived from group-wise registration of a cohort of subjects, can provide enhanced localization and visualization for structural and functional imaging studies, as well as enable voxel-based or morphometric analysis in a broad set of applications. The objective of the work reported here was to enhance our understanding of the hippocampal subfields through the development of a high resolution normative atlas using 7 T quantitative susceptibility imaging. To this end we first developed and validated a manual labeling protocol for the hippocampal subfields to assess how well

they could be identified with our proposed imaging sequence. We then applied a group-wise registration technique to align images from seventeen healthy subjects and generated a anatomical atlas of the hippocampus and its subfields, assessing accuracy of the alignment using the manually-labeled subfields. R2* and QS maps from each subject were subsequently warped to generate R2* and QS atlases, and we evaluated these quantitative metrics both within the hippocampal subfields and in the basal ganglia for comparative purposes.

A.2 Methods

A.2.1 Materials & Imaging

The subject cohort enrolled in this study included seventeen healthy controls (10 Males, 7 Females, mean age 31.3 ± 8.7). All data were acquired on a 7 Tesla neuroimaging optimized MRI scanner (Agilent, Santa Clara, CA, U.S.A/ Siemens, Erlangen, Germany) using a 16 channel transmit-receive head coil array constructed in-house. The imaging sequence used for this study was a multi-echo gradient-echo sequence with six echoes acquired with a 0.5 mm in-plane resolution (TR=40 ms, TE1=4.57 ms, Echo spacing= 4.89 ms, flip angle=13o, N=1, matrix=256x360x80, slice thickness= 1.5 mm, FOV=128x180x120 mm, total time=12 minutes), with slices acquired perpendicular to the long axis of the hippocampus in a coronal oblique orientation. Quantitative maps of the apparent transverse relaxation rate, R2* = 1/T2*, were calculated using a Levenberg-Marquardt, least-squares fitting routine for non-linear equations. Specifically, the following mono-exponential decay function:

$$S(TE) = S_0 \times exp(-TE \times R_2^*)$$

was fit to the magnitude data on a voxel-by voxel basis. In equation [1], TE represents the echo time in ms and S the signal intensity at TE = 0. A magnitude image derived from the average of all six echoes was employed for subfield labeling and groupwise registration for atlas building. This study has been approved by the office of research and ethics of Western University, and informed consent was obtained from all volunteers prior to their recruitment in the study.

A.2.2 MRI Phase Processing

From the gradient echo data, susceptibility-weighted images (SWI), local frequency shift (LFS) and quantitative susceptibility (QS) maps were reconstructed using the following multi-step procedure. Removal of channel dependent phase offsets and channel combination was performed simultaneously by calculating the hermitian inner product between all later echoes and the first, then summing the complex data across channels. This is a customary approach for simultaneously removing the influence of channel specific and B1-induced phase errors and combining multi-channel MRI data [21]. The resulting raw phase images were then unwrapped in three-dimensions using a region-growing algorithm [22]. The phase image for each echo was then divided by its corresponding echo time to produce a local frequency shift maps and a weighted average local frequency shift map was calculated using the phase noise variances as the weights. To remove slowly-varying background field caused by tissue-air interfaces, we have implemented and applied the projection onto dipole fields (PDF) [23], as well as the

sophisticated harmonic artifact reduction on phase data (SHARP) filtering technique [24] to the Fourier transform of the unwrapped phase data. We tried a variety of multiple kernel sizes to acquire the optimal results for our application, and we obtained the best results by applying a SHARP filter with a spherical convolution kernel of size 3 mm. For edge pixels, binary erosion using a spherical structuring element with the same size as the convolution kernel was performed prior to the SHARP deconvolution operation to eliminate artifacts at the edge of the brain volume. The SHARP filter size was chosen to minimize artifacts in the hippocampal region and may not be ideal for maximizing contrast in other areas of the brain such as the basal ganglia.

A.2.3 Susceptibility Weighted Image Calculation

Susceptibility weighted images (SWI), which are preferentially sensitive to subtle tissue boundaries arising from differences in the T2* and frequency, were generated using a frequency mask (FM) derived from the MR phase information. Specifically, the unwrapped phase image was filtered using the Fourier-domain, Gaussian high-pass filter described in the previous section. The filtered phase images (one for each echo) were then combined into a single local frequency shift (LFS) map using a weighted linear regression [25]. The resulting LFS map was used to calculate a frequency mask (FM) according to the following non-linear, Hann window function:

$$FM(x) = \begin{cases} 0 & if\ x < -X \\ \frac{1}{2}\left[1 + cos\frac{\pi x}{X}\right] & if -X \leq x \leq 0 \\ 1 & if\ x > 0 \end{cases}$$

where x denotes the frequency shift of a voxel in the LFS map and X is the cutoff frequency of the Hann window function. The cutoff frequency was set to 20 Hz for this work. To acquire a susceptibility weighted contrast, the magnitude image must be multiplied by the frequency mask, an effect that is accentuated by repeated this multiplication several times. We multiplied the frequency mask by the magnitude image four times to generate the SWI maps.

A.2.4 Quantitative Susceptibility Maps

Quantitative susceptibility mapping measures the apparent magnetic susceptibility of the tissue using MR phase images, which unfortunately is an ill-conditioned inverse problem (i.e. one that does not necessarily have a unique solution). Recent research suggests that the incorporation of spatial prior information, generated from the magnitude image data, can be used to identify a meaningful solution to this problem [26]. In this recent work, computation of quantitative susceptibility from local Larmor frequency shift maps was performed using quadratic minimization of a regularized least-squares objective function. The QS minimization problem can be written in a weighted least-squares form with spatial priors as described by de Rochefort et al. [26]:

$$mix_x \left\| W(CX - \delta) \right\|_2^2 + \alpha \left\| W_0 X \right\|_2^2 + \beta^2 \left\| W_1 G X \right\|_2^2 ,$$

where X denotes the k-space local frequency shift, C the Fourier domain dipole convolution kernel and X the Fourier domain susceptibility distribution of interest. W, W_0 and W_1 are weighting matrices (spatial prior information) defined as: the magnitude

image itself (W), a binary mask of the brain of the magnitude image (W0), and the gradient norm of the magnitude image (W1). The matrix denotes the gradient operator, while and are the associated regularization constants. In our numerical implementation of QSM, a minimum quadratic form of Eq. 3 was solved using the conjugate gradient normal residual (CGNR) method [26]:

$$C^{\star}W^{\star}WCX + \alpha^2 W_0^{\star}W_0X + \beta^2 G^{\star}W_1^{\star}W_1GX = C^{\star}W^{\star}W\delta,$$

In principle, a compromise must be selected for the values of α^2 and β^2 to achieve low streaking artifact, while preserving accuracy of the maps [26, 25]. We have chosen values of α^2 and β^2 equal to 1 x 10^4, since they resulted in the smallest log residual at the transition point in the L-curve (log-log plot of the norm of a regularized solution and the norm of the corresponding residual norm) and produced realistic values of susceptibility over a range of iterative steps in the CGNR algorithm. Larger values resulted in increased smoothing and reduced streaking artifact. The CGNR algorithm outlined above was implemented in Matlab (R2012b, The MathWorks, Natick, MA, USA).

To ensure reproducibility, values of quantitative magnetic susceptibility must be reported relative to a common reference structure. Previous studies have used either CSF or frontal white matter as a reference. In this study, we employed a bilateral region of interest (ROI) in the frontal white matter, to avoid phase-related artifacts due to flow and partial volume related effects relating to reference ROIs within the CSF. All QS values in this study are reported relative to the reference susceptibility of the bilateral frontal white matter ROI.

A.2.5 Subfield Labeling

A magnitude image derived from the average of all six echoes was used to perform the subfield labeling using the ITKsnap software [27]. The hippocampus, including the hippocampus proper and subiculum, was outlined and subdivided into different fields of cornu ammonis (CA) and dentate gyrus (DG) based on an adaptation of the manual delineation protocol proposed by Mueller et al. [28], as well as the Duvernoy HM (2005) atlas. The Mueller et al. [28] protocol at 4T was extended, using the higher field advantage; by including anatomical definitions obtained from the protocol described by Wisse et al. (2012) at 7T. We did not include the entorhinal cortex (ERC), alveus and fimbria. The hippocampus was partitioned into anterior (head), posterior (tail), and mid-region (body) segments, with no further subdivision of the head and tail since the additional folds (digitations of the head) from medial bending of the hippocampus in these regions caused differentiation between subfields to be unreliable. The partitioning of hippocampal head and tail followed definitions by Yushkevich et al. (2010) and the remaining slices between them were defined as the hippocampal body and subject to further subfield delineation. For the body of the hippocampus, the following sub-regions were segmented; subiculum (SUB), Amun's horn (CA1, CA2+CA3), and CA4+dentate gyrus (DG).The border between the SUB and ERC was formed following the uncal sulcus from its fundus to the medial surface (Wisse et al., 2012). As the ERC can be found in the hippocampal fissure (Insausti et al., 1987), our SUB label may have sometimes incorporated part of the ERC. The border of the SUB with CA1 was defined as a vertical line at the edge of the SUB touching the most medial border of the DG+CA4 region, in imitation to the protocol by Mueller et al. (2007). The CA1/CA2 boundary was designated as the point at which a noticeable decrease in

width of the CA1 subfield was observed, following the most lateral point of the DG. No distinction was made between CA2 and CA3 since our images showed no visible boundary between them. Similarly, in line with the debate in histological literature as to whether CA4 belongs to the CA [6] or the DG, CA4 and DG were combined. The opening of subfields into the globular region of the hippocampal formation formed the CA2+CA3/DG+CA4 border, which was specifically identified by the continuation of a clear consistent hypointense line representing the stratum lacunosum-moleculare of CA and dendrites of the molecular layer of DG, as described by Wisse et al. [15]. The remaining globular region of the hippocampal formation was marked as CA4+DG.

A single rater applied the described manual segmentation protocol to the set of seventeen subjects. To assess the accuracy and reproducibility of our segmentation protocol, images from five volunteers were segmented a second time by an additional operator, and the resulting labels compared to the first segmentation using the Dice similarity coefficient (DSC), defined as:

$$DSC = \frac{2(R_A \cap R_B)}{R_A + R_B}$$

as well as the absolute percentage volume error ($\left|\delta V_p\right|$), defined as:

$$\left|\delta V_p\right| = \frac{|(V_A - V_B)|}{V_B}$$

The intraclass correlation coefficient (ICC) was also computed for inter-rater reliability analysis with values near unity indicating consistent volume measurements. Reported subfield volumes were normalized by the intracranial volume (ICV) as estimated

by the Freesurfer software (Buckner, 2004), using the formula: normalized volume = (raw volume / ICV) $\times$ 1000 mm^3.

A.2.6 Average Atlas construction

To construct an atlas of the hippocampal subfields, we used an iterative groupwise diffeomorphic registration as implemented in the ANTS software [29]. The atlas was created using the iterative procedure of 1) registering each image to an estimate of the average, then 2) updating the average estimate using the warped images. All images were first corrected for bias field inhomogeneities using the non-uniform intensity normalization (N3) algorithm [30] and each registration step involved affine registration followed by diffeomorphic registration. The affine initialization employed a histogram matched mutual information similarity metric to align all images to one subject of the data set, which was chosen arbitrarily. The diffeomorphic registration was performed using a cross correlation similarity metric with a window radius of 5 voxels and used a greedy symmetric transformation (greedy SyN) with Gaussian regularization (sigma=3). Each optimization was performed over three resolutions with a maximum of 30 iterations at the coarsest level (one quarter of the full resolution), 90 at the next coarsest (one half of the full resolution) and 20 at the full resolution. The average atlas construction, alternating between the registration phase and average update phase, was performed in 4 iterations, with a shape update performed at each iteration to maintain stability of the average. This shape update consisted of warping the atlas a small step size (epsilon=0.25) towards the mean of the inverse warps. After the template construction, the R2*, SWI and QS maps were warped to the atlas space, upsampled to 0.5 mm isotropic resolution and averaged. The segmented labels of each subject were warped

in the same manner and fused using a majority vote (for each voxel the label that appeared the most across subjects was chosen). To validate accuracy of the group-wise registration, we evaluated the alignment of the whole hippocampus for all subjects in the average atlas space by computing the pair-wise Dice similarity metric between the warped hippocampus labels for every pair of subjects in atlas space.

A.2.7 R2* validation

To validate our R2* values, we performed an ex-vivo scan on a resected hippocampal specimen after a surgical operation: anterior temporal lobectomy. The specimen was part of an ongoing temporal lobe epilepsy study at our center, and the hippocampus was confirmed as sclerotic by both clinical imaging and histology. The scanning was performed on a ultra-high-field 9.4T MRI scanner (Varian, Palo Alto, CA, U.S.A) using a millepede birdcage coil (Agilent, Santa Clara, CA, U.S.A.) with a multi-echo gradient-echo sequence. The specimen was imaged at a resolution of 0.1 mm isotropic. The resulting R2* values were compared with the R2* values from the patient's 7T preoperative scan within the subfields. The subfields were delineated on a representative coronal slice of the ex-vivo scan, shown in Figure A.3. This figure summarizes the preop, ex-vivo comparison. To further evaluate our R2* maps we compared values of the basal ganglia structures with those reported in Deistung et al. [31] at 7T. Manual ROI labels for the thalamus, putamen, caudate nucleus and globus pallidus were delineated on a representative coronal slice of our atlas.

A.2.8 Quantitative susceptibility validation

Since QS values of the hippocampal subfields have not been previously reported at 7 Tesla, to evaluate our quantitative maps, we compared values of the basal ganglia structures with those reported in Deistung et al. [31] and [32] at 7T. Five normal controls were scanned according to the previously described imaging protocol, with the in-plane orientation being axial instead of coronal. The phase images were filtered using SHARP with a 7 mm kernel size, otherwise the processing and susceptibility quantification was identical to our previous cohort. Manual ROI labels for the thalamus, putamen, caudate nucleus and globus pallidus were delineated on a representative axial slice of each subject. Manual segmentation was preferred to atlas-based segmentation, to avoid miss registration and partial voluming effects. The validation experiment is summarized in Figure A.4.

A.2.9 Statistical comparison

To investigate the differences between magnitude, R2* and QS maps, we performed a one-way analysis of variance (ANOVA) using the mean value over each subfield label in each subject's native-space scan. These tests were corrected using Tukey's multiple comparisons method and the alpha (p) value was set to 0.05. The magnitude images were intensity normalized with 100 being the mean intensity. The statistical analysis was performed using Prism (GraphPad, La Jolla, USA) statistical software. Table 4 summarizes the significant results found between subfields for the three different imaging techniques.

A.3 Results

Figure A.1 displays representative coronal slices of our atlas-based maps for (i) the average magnitude image across all echoes (top left), (ii) R2* (top right), (iii) SWI (bottom left) and (iv) QS (bottom right). As well, the average magnitude image for all echoes for a single subject is displayed in the center of figure A.1 to illustrate the difference between the atlas-based images and the single subject case. Magnified representations of the left hippocampus are shown for visual comparison and assessment of the contrast and sharpness of the average maps. Since inter-subject anatomical variability was accounted for using a deformable registration, it was possible to generate these group-averaged atlases (average of all 17 subjects) which serve to effectively increase the signal to noise ratio and contrast to noise ratio in the hippocampal subfields. The sharp anatomical definition in these images is evidence of the accuracy of the groupwise registration within the hippocampus and in the subcortical regions. The cortical regions do not possess the same level of alignment because of the higher variability in cortical folding patterns, which is expected, and is difficult to account for with image-based registration.

The inter-rater reliability results measured by the Dice similarity metric and volume difference (in mm3) between the labels are summarized in Table A.1. The Dice metric demonstrates good agreement between both raters across the subfields, with the Dice coefficient for the total hippocampus being 0.844 for the right side and 0.839 for the left side. The highest Dice coefficient between all subfields was 0.847 for the right side and 0.801 for the left, both representing the CA4+DG label, while the lowest was for the CA2+CA3 label, being 0.682 and 0.638 for the right and left sides respectively. Similarly, the volume difference measures outlined in Table 1 showed good agreement,

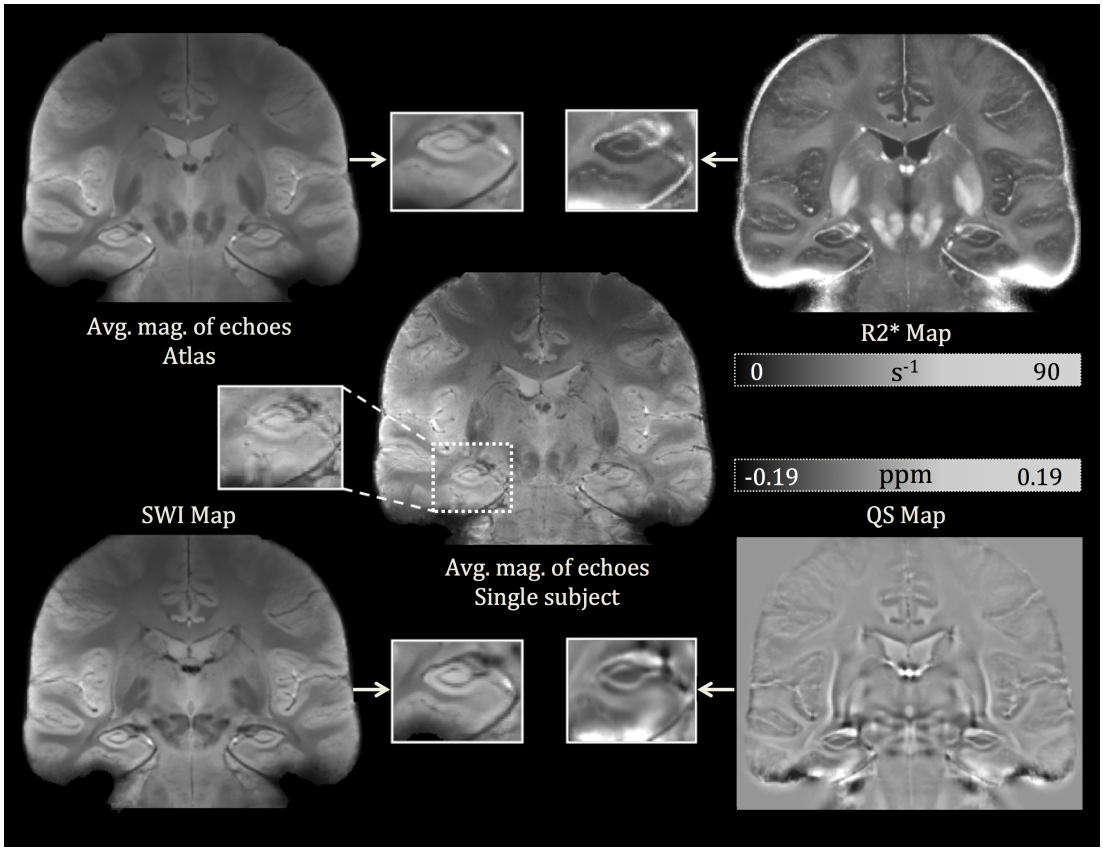

Figure A.1: Single subject (Middle) as well as atlas-based images of average magnitude across echoes (Top Left), R2* (Top Right), qualitative SWI (Bottom Left) and QS maps (Bottom Right). The adjacent image to each map shows a zoomed-in representation of a hippocampal slice in the coronal view. The same slice is chosen for all maps to compare CNR and SNR across the different maps.

on average, which validates the repeatability of our protocol. The volume of the CA1 label had showed the most agreement between the raters with a volume percentage difference of 6%. In addition, Table A.1 also displays the intraclass correlation (ICC) analysis for inter and intra-rater reliability. High consistency was observed between our raters for most of the subfields (ICC > 0.75), as well as for the repeated datasets our first rater which demonstrates the reliability of our protocol. Segmentation of the CA2+CA3 label was the least reliable with an ICC between raters of 0.624. The volumes of the subfields resulting from our manual delineation protocol were reported in Table A.2.

Table A.1: Table I: Dice similarity coefficient, absolute percentage volume error and Intra-class correlation coefficient metrics in conducted patient space

		Sub	**CA1**	**CA2+CA3**	**CA4+DG**	**Hp tail**	**Hp head**	**Total**
DSC	**L**	0.605	0.714	0.638	0.801	0.692	0.768	0.839
	R	0.734	0.796	0.682	0.847	0.706	0.814	0.844
		9.6	6	11.3	11.2	15.4	6.7	6.5
ICC Rater 1		0.949	0.973	0.781	0.966	0.813	0.984	-
ICC (between raters)		0.833	0.834	0.624	0.881	0.727	0.906	-

Table A.2: Table II: Hippocampal subfield volumes normalized by intracranial volume (ICV), reported in mm^3.

	Sub	**CA1**	**CA2+3**	**CA4+DG**	**Hp tail**	**Hp head**	**Total Hp**
Left	222.5	249.2	71.9	214.2	428.9	1263.8	2450.3
Right	233	248.4	73.4	216.5	469.8	1312.1	2553.2
Mean	227.8	248.8	72.7	215.3	449.3	1287.9	2501.8
(sd)	(-61.2)	(54.2)	(-7.9)	(47.2)	(146.3)	(196.3)	(251.2)

Figure A.2 displays coronal views of selected slices running through hippocampal body for the three major image contrasts employed in this study: the magnitude image averaged across echoes, R2* and quantitative susceptibility maps. Two sets of three

consecutive slices (Fig. 2a and 2b) are shown. The segmentation labels for the subfields are overlaid on the images. The segmentation protocol was performed using the magnitude images only. For the slices corresponding to figure A.2a (the left side of the figure), both R2* and QS showed improved delineation of the subiculum/CA1 and CA1/(CA2+CA3) boundaries compared to the magnitude image. Furthermore, the QS map defined the (CA2+CA3) subfield more clearly compared both the R2* and magnitude images based on the reduced susceptibility in this region of the hippocampus. Accuracy of the group-wise registration and the resulting average atlas was evaluated both qualitatively and quantitatively. The mean Dice metric between the hippocampus labels in the atlas space was 0.69 0.03 and ranged from 0.69 to 0.77.

Table A.3 summarizes the quantitative, intrinsic MRI measures of the hippocampal subfields, specifically R2* and quantitative susceptibility (QS). The values in table A.3 represent mean values averaged across all subjects. QS values demonstrated relatively high standard deviations within each subfield, which did not correlate with the size of the subfield. As for our R2* ex-vivo validation using a resected hippocampus from epilepsy surgery, Figure A.3 shows a very good agreement within the subfields between the pre-operative 7T scan and the 9.4T image. In addition, the R2* values for basal ganglia structures in our study are as follows (in units of s-1): thalamus (38.8), putamen (49.5), caudate nucleus (43.1) and globus pallidus (72.7). Comparatively, Deistung et al. [31] reported the following values: thalamus (41.4), putamen (49.4), caudate nucleus (42.3) and globus pallidus (83.4). Similarly, the QS validation on five normal volunteers scanned axially showed that our values (in parts-per-million of the main magnetic field, ppm) for these structures (0.0395, 0.0586, 0.0599 and 0.117) are within range of those reported in Deistung et al. [31]'s study (0.0261, 0.0380, 0.0440 and 0.131) and those reported in Wharton and Bowtell [32] at 7T (0.020, 0.060, 0.060,

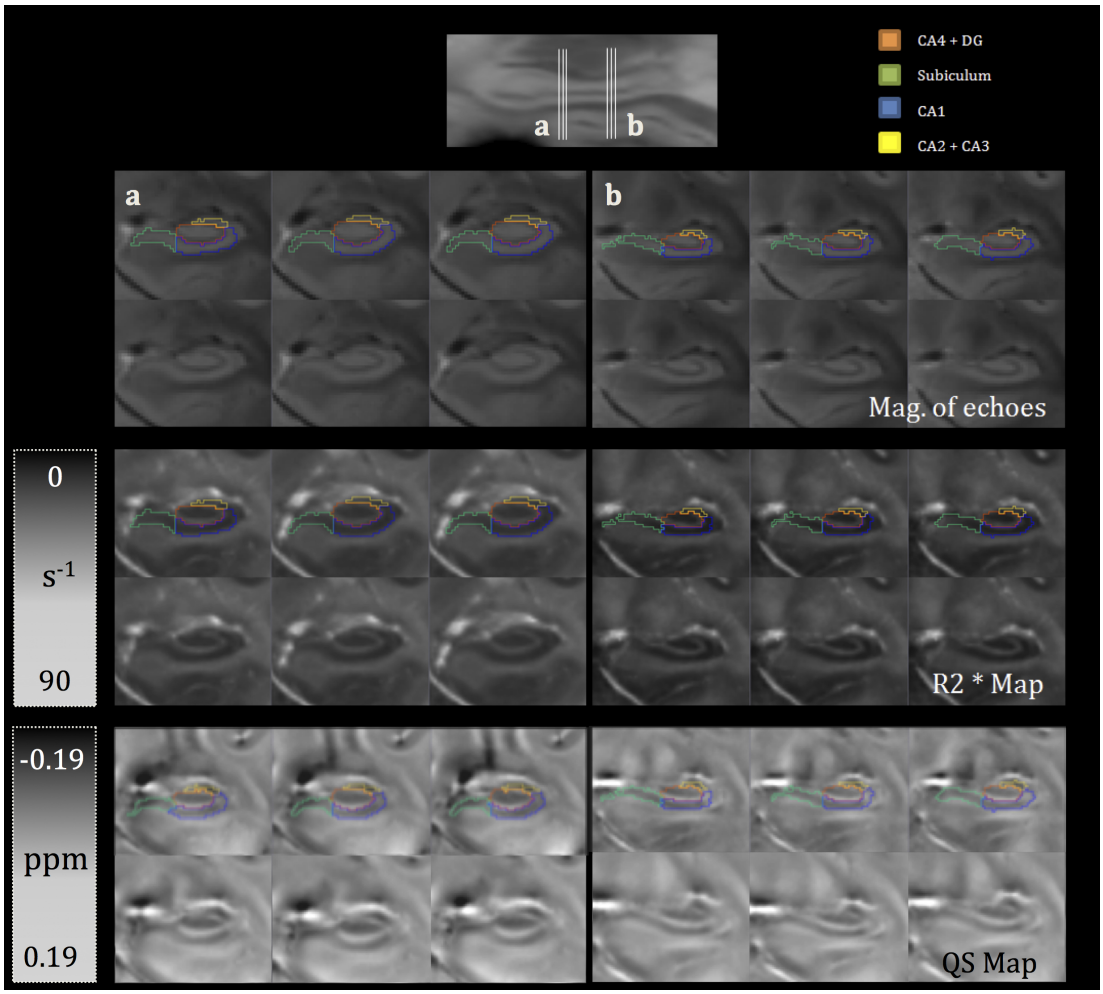

Figure A.2: Two sets of three consecutive coronal slices as seen in atlas space in the magnitude across echoes, R2* and QS maps, with the top row of each block showing segmentation labels overlaid on the images. The location of the slices is indicated on a sagittal view of the hippocampus at the top of the figure.

0.160). These values are graphed in Figure A.4 to demonstrate the agreement between our values and those reported in the literature. The ANOVA analysis showed that R2* resulted in the highest number of significant comparisons between the subfields, followed by QS; and that normalized magnitude images showed no significance for all subfield comparisons. Table A.4 summarizes all the significant comparisons for R2* and QS.

Table A.3: Table III: Subfield volumes, R2* and QS values as a mean across all subject in subject space

		Sub	**CA1**	**CA2 + CA3**	**CA4+DG**	**Hp tail**	**Hp head**
Volume (mm3)	μ	227.8	248.8	72.7	215.3	449.3	1287.9
	(σ)	(61.2)	(54.2)	(-7.9)	(47.2)	(146.3)	(196.3)
R2* (1/s)	μ	32.2	25.5	30	30.4	28.2	28.1
	(σ)	(2.3)	(2.0)	(-4.2)	(-3.3)	(-1.9)	(-2.1)
QS (ppm)	μ	-0.0216	-0.0187	-0.0376	-0.0237	-0.0134	-0.0164
	(σ)	(0.013)	(0.008)	(0.016)	(0.009)	(0.005)	(0.011)

A.4 Discussion & conclusion

Quantitative R2* maps have shown great potential as a diagnostic tool for numerous diseases affecting the hippocampus both because of the improved contrast, and through the use of voxel-based studies. Similarly, the quantitative atlas-based QS map demonstrates a unique contrast driven by the underlying magnetic susceptibility of the tissue and vasculature, which cannot be obtained using standard GRE/T2* weighted images. In-vivo susceptibility mapping can also resolve substructures of deep grey matter (GM) nuclei consistent with histological sections of post mortem brains [31]. The low variability of the R2* values within small structures as the subfields (8.5% of the mean on

Table A.4: Table IV: One-way analysis of variance (ANOVA) between all subfields for R2* and QS maps

Imaging	Subfields	Mean diff.	95% CI of diff.	Level of significance
R2*	CA4-DG vs. CA1	5.152	3.043 to 7.260	$P \leq 0.0001$
	CA4-DG vs. Hp tail	2.376	0.2673 to 4.485	$P \leq 0.05$
	CA4-DG vs. Hp head	2.556	0.4472 to 4.665	$P \leq 0.01$
	Sub vs. CA1	6.806	4.697 to 8.914	$P \leq 0.0001$
	Sub vs. Hp tail	4.03	1.921 to 6.139	$P \leq 0.0001$
	Sub vs. Hp head	4.21	2.101 to 6.319	$P \leq 0.0001$
	CA1 vs. CA2-CA3	-4.774	-6.882 to -2.665	$P \leq 0.0001$
	CA1 vs. Hp tail	-2.776	-4.884 to -0.6671	$P \leq 0.01$
	CA1 vs. Hp head	-2.596	-4.705 to -0.4872	$P \leq 0.01$
	CA2-CA3 vs. Hp head	2.178	0.06928 to 4.287	$P \leq 0.05$
QS map	CA4-DG vs. CA2-CA3	0.01383	0.004786 to 0.02288	$P \leq 0.001$
	CA4-DG vs. Hp tail	-0.01031	-0.01936 to -0.001263	$P \leq 0.05$
	Sub vs. CA2-CA3	0.01601	0.006958 to 0.02505	$P \leq 0.0001$
	CA1 vs. CA2-CA3	0.01887	0.009818 to 0.02791	$P \leq 0.0001$
	CA2-CA3 vs. Hp tail	-0.02414	-0.03319 to -0.01510	$P \leq 0.0001$
	CA2-CA3 vs. Hp head	-0.02118	-0.03022 to -0.01213	$P \leq 0.0001$

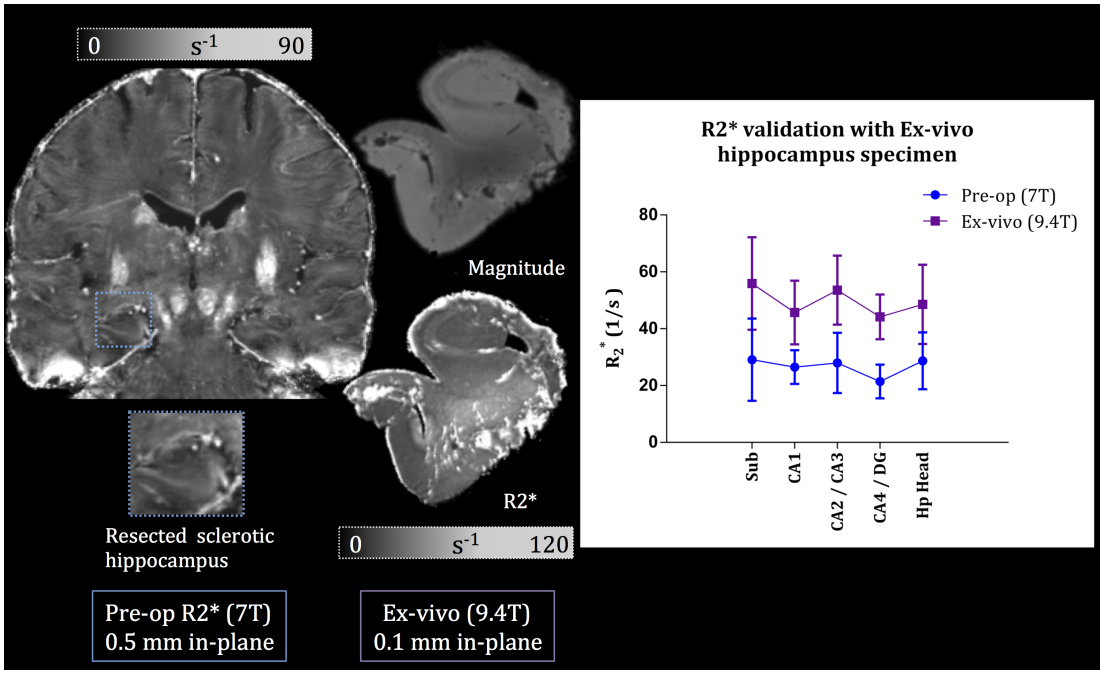

Figure A.3: Validation of pre-operative R2* with 9.4T ex-vivo imaging of a resected hippocampus. Left: Coronal slice of the pre-op R2* at 7T with a zoomed-in view of the sclerotic hippocampus before epilepsy surgery excision. Middle: Magnitude image of the patient's resected hippocampus imaged at 9.4T resulting in a 0.1 mm isotropic resolution (top); R2* image of the hippocampus, where the subfield delineation was performed (bottom). Right: Graph of comparison between pre-op (blue) and ex-vivo (purple) R2* values within the subfields.

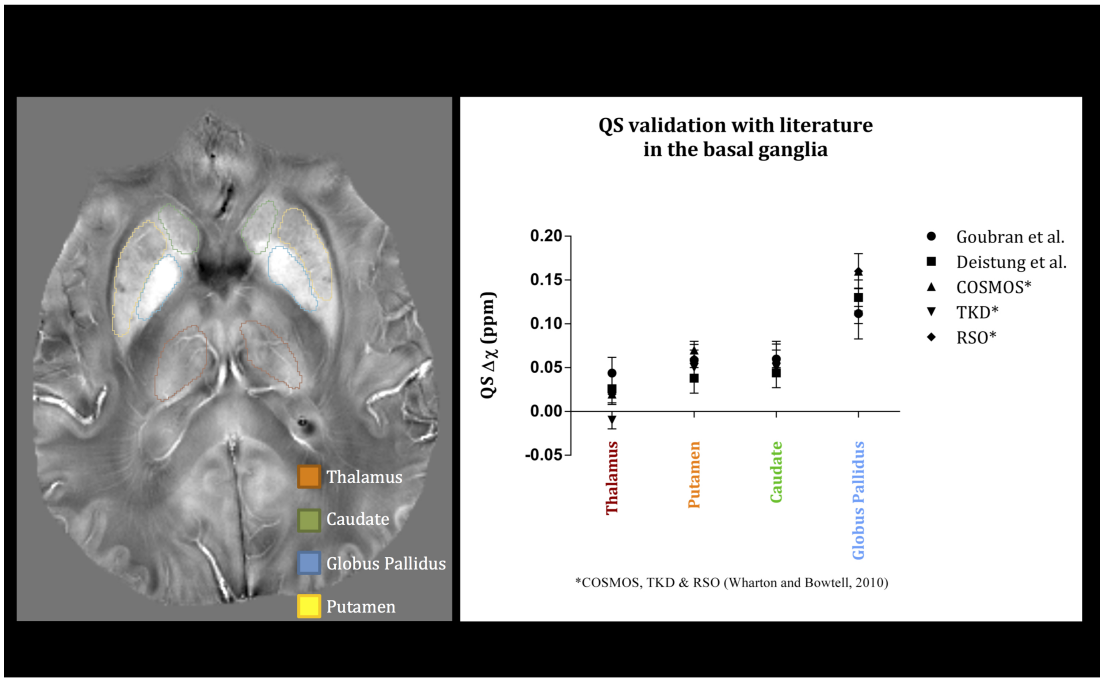

Figure A.4: Figure 4. Validation of our QS values in the basal ganglia with Deistung et al. [31] and Wharton and Bowtell [32]. Left: Axial slice of a QS map from a single subject showing the outlines of the basal ganglia structures. Right: Graph demonstrating QS values within the basal ganglia for three papers.

average across all reported subfields) demonstrates the sensitivity of this quantitative measure to local magnetic changes. The reported QS values show higher variability within each small hippocampal substructure, which could be due to phase variations from the sinus interface or reconstruction artifacts.

The ANOVA analysis suggests that there are more apparent differences between the subfields on the maps than the magnitude images. These differences between subfields can be caused by many factors, one of which may be different iron distribution within the CA1-CA3 region as compared to the CA4-DG region. Antharam et al. [33] mapped iron distribution, R2 and R2* for the subfields in three unfixed post-mortem control cases and five Alzheimer's disease (AD) specimens. They have validated the relationship between R2, R2* and tissue iron content of the hippocampal subfields and reported higher mean R2 and R2* in the CA4-DG region as compared to the CA1-CA3 region in both groups; which is consistent with our R2 values, if CA1 through CA3 are combined. Their evidence demonstrates that regions of increasing R2* correspond to regions of higher iron content, which is consistent with literature [34] and the hypothesis that iron concentration affects R2* contrast. The present work is the first in vivo quantification susceptibility values within the hippocampal subfields at 7T

It is evident at this detailed level of segmentation that the contrast cannot be attributed solely to varying iron concentrations. Other parameters affecting water diffusion and susceptibility, including the variation in compartmentalization due to cell dimensions and density of packing, and differences in hydration between gray and white matter, are also presumed relevant [33]. The changes in QS may also be due to the subependymal intrahippocampal veins and the sulcual intrahippocampal veins, which are manifested as susceptibility changes within the CA1 and the CA2/3 transition, respectively.

Yushkevich et al. [35] developed a normalized atlas of the subfields using five postmortem specimens at 9.4T. In this publication we focused on the quantification of R2* and QS values in the subfields. This quantification requires in-vivo scanning since fixation affects metal ions, protein cross-linking and water diffusion properties. Shepherd et al. [36] have shown, as well, that fixation in 4% formaldehyde results in a reduction of up to 80% in estimated T2 values. Hence, we were constrained by the requirement of imaging in-vivo unfixed tissue, with which achieving a sufficient SNR for subfield segmentation is more challenging than postmortem imaging. Figure A.3 demonstrates an example ex-vivo scan at 9.4T of a resected hippocampal specimen after anterior temporal lobectomy. This specimen represents the potential of ex-vivo imaging of excised hippocampal specimens. Previous reports have identified concerns with T2* imaging of the hippocampus. In our imaging protocol we do see loss of signal at the gyrus rectus within the medial frontal lobe due to susceptibility artifact from the sinuses; however this is only anterior to the optic chiasm and does not affect the amygdala or anterior region of the hippocampus, as shown by the sagittal slice in Figure A.2. Similarly we experienced some signal loss within the inferior region of the fusiform gyrus but this is only contained in the neocortex and does not extend past the collateral sulcus.

Cho et al. [20] reported R2* values within the subfields at 7T, as follows: Sub= 34.3, CA1= 42.59, CA2+CA3=39.2 (combining both subfields), CA4=43.66. Our values for these subfields were 32.2, 25.5, 30.0, and 30.4, respectively. Both the values reported by Cho et al. [20] and our values follow the trend of increased R2* in the CA4-DG label as compared to the combined CA1-CA3 label, demonstrated by Antharam et al. [33] on unfixed ex-vivo specimens at 14T. However, their method suffers from some limitations such as the use of only one ROI composed of 21 pixels, taken on a single coronal slice, to represent a subfield. That is pixels within the ROI may not represent

the entire subfield due to the limited sampling. Another limitation may be the use of a dual echo, instead of a multi-echo, sequence in their imaging protocol which is less effective to compute R2* values. It should also be noted, that Cho et al. [20] obtained a consistently higher standard deviation per subfield than our study. We have demonstrated, as well, the reliability of our R2* values in the basal ganglia comparison with Deistung et al. [31] and our ex-vivo 9.4T validation.

The results of our reliability analysis are presented in Table 1 and they validate repeatability of our manual segmentation protocol. One potential source of error leading to inter-rater differences is the learning curve in segmentation as Rater 2 only segmented five subjects of the dataset. As expected, the Dice coefficient was lower for the smaller subfields due to the bias of the measure towards bigger structures. It is, however, difficult to objectively assess the volumes of subfields across protocols, due to the underlying differences in the protocols, the different imaging parameters and the combination of certain subfields into a singular label depending on the protocol. For instance, [12] combined CA3 with DG in a single label while [14] combined CA1, CA2 and CA3 in a single label. Similarly, some protocols restrict subfield delineation to the body of the hippocampus [28, 12] and others [14, 15] claim that approach insufficient for detection of disease progression and instead segment the subfields along the whole length of the hippocampus. Several boundaries, such as that between the CA4/DG are not agreed upon and might require definitions based on histological detail to be resolved. Since an in-plane resolution of 0.5 mm is insufficient to resolve small detail between the subfields, we therefore decided to combine the CA4/DG label, and applied the same rationale to the CA2/CA3 boundary. Of those protocols used as comparators in this paper, only two of them attempted to resolve CA2 as a distinct subfield [15, 12], by defining the border between CA2 and CA3 as the medial side of a virtual square or

define a CA1-CA2 transition to account of the overlap of the dorsomedial part of CA1 into CA2 label.

Our average Dice values between the hippocampus labels in the atlas space, with a mean of 0.69 ± 0.03, are comparable to the best performing methods reported in a recent evaluation of nonlinear brain registration [37], which reported Dice overlaps with the SyN registration algorithm on two different datasets, CUMC (Columbia University Medical Centre) and LPBA (LONI Probabilistic Brain Atlas), made up of 12 and 40 subjects respectively. The hippocampal Dice overlaps were 0.68 and 0.75 for the CUMC12 and LPBA40 datasets respectively.

Several techniques have been presented for solving the field-to-source inverse problem for quantitative susceptibility mapping, most notably the calculation of susceptibility through multiple orientation sampling (COSMOS), truncated K-space division (TKD), and morphology enabled dipole inversion (MEDI). While maps obtained using COSMOS demonstrate high agreement with post-mortem measurements of brain iron, the method relies on multiple acquisitions with different head orientations which limits the technique for use in a clinical setting. The available single head orientation algorithms suffer to varying degrees from non-local artifacts, instability or underestimation of susceptibility values [31]. We employed the Bayesian regularized solution developed by de Rochefort et al. [26], which makes use of spatial priors from the magnitude images, and provides accurate delineation of both anatomical structure and volume magnetic susceptibility in the brain. Phase shifts induced by eddy currents, B1+ non-uniformity, or flow can introduce errors in the QS maps. However, these errors were minimized in our QS pipeline since the first echo was subtracted from all subsequent echoes using the hermitian product method. Such subtraction removes the

influence of temporally invariant background phase offsets caused by external field inhomogeneities. Flow-related errors in QS, however, are not temporally invariant. When blood flow through veins is present, the accrual of phase as a function of echo time may become non-linear. Under this condition, performing a linear fit of the phase to the echo time will not yield accurate estimates of the frequency shift. However, close inspection of our LFS and QS maps registered to the template space does not reveal significant presence of large vessels in the hippocampal subfields. For this reason, we believe the effects of venous flow artifacts in our data are minimal.

One application of the atlas-based approach presented here would be the study of quantitative intrinsic MR measures in the subfields in neurological diseases. The significant differences found in the ANOVA analysis of R2* and QS across adjacent subfields (Table 4) reveals that these quantitative maps may be superior in sensitivity to detect abnormalities in specific subfields compared to magnitude images. The subfield labels, presented in Table 2, could also be used for volumetric or morphometric analysis. Evaluation of neurological disorders that affect the hippocampal subfields, such as temporal lobe epilepsy or Alzheimer's disease, would benefit greatly from the use of these techniques. Another application could be in targeting for deep brain stimulation (DBS), since quantitative T2* [38] and susceptibility contrast [39] allow for improved visualization of commonly targeted deep GM structures. For these stereotactic neurosurgical applications, subject-atlas registration could be used to improve accuracy of electrode placement in deep GM nuclei to alleviate motoric disorders due to tremor as Parkinson's disease or dystonia.

We have constructed a normative atlas of the hippocampal subfields from in vivo susceptibility-weighted images of seventeen healthy volunteers acquired using 7T MRI.

Using our reliable manual delineation protocol of the subfields, we demonstrated the feasibility of subfield specific analyses of the hippocampus. The average atlas accurately aligns the subtle anatomical features of the hippocampus, producing high-resolution maps of quantitative susceptibility and R2*. This work represents the first in vivo quantification of susceptibility values within the hippocampal subfields at ultra-high-field strengths. It can be further complemented by investigation of these quantitative MRI parameters in patient populations where hippocampal subfields are known to be selectively affected, such as temporal lobe epilepsy or Alzheimer's disease.

Bibliography

[1] N Bernasconi, D Kinay, F Andermann, S Antel, and A Bernasconi. Analysis of shape and positioning of the hippocampal formation: an mri study in patients with partial epilepsy and healthy controls. *Brain*, 128(10):2442–2452, 2005.

[2] Josephine Barnes, Rachael I Scahill, Richard G Boyes, Chris Frost, Emma B Lewis, Charlotte L Rossor, Martin N Rossor, and Nick C Fox. Differentiating AD from aging using semiautomated measurement of hippocampal atrophy rates. *Neuroimage*, 23(2):574–81, 2004.

[3] R Grant Steen, Courtney Mull, Robert Mcclure, Robert M Hamer, and Jeffrey A Lieberman. Brain volume in first-episode schizophrenia systematic review and meta-analysis of magnetic resonance imaging studies. *The British Journal of Psychiatry*, 188(6):510–518, 2006.

[4] Loretxu Bergouignan, Marie Chupin, Yvonne Czechowska, Serge Kinkingnéhun, Cédric Lemogne, Guillaume Le Bastard, Martin Lepage, Line Garnero, Olivier

Colliot, and Philippe Fossati. Can voxel based morphometry, manual segmentation and automated segmentation equally detect hippocampal volume differences in acute depression? *Neuroimage*, 45(1):29–37, 2009.

[5] Anke Karl, Michael Schaefer, Loretta S Malta, Denise Dörfel, Nicolas Rohleder, and Annett Werner. A meta-analysis of structural brain abnormalities in ptsd. *Neuroscience & Biobehavioral Reviews*, 30(7):1004–1031, 2006.

[6] Henri M Duvernoy. *The human hippocampus: functional anatomy, vascularization and serial sections with MRI*. Springer, 2005.

[7] Mark J West, Paul D Coleman, Dorothy G Flood, and Juan C Troncoso. Differences in the pattern of hippocampal neuronal loss in normal ageing and alzheimer's disease. *The Lancet*, 344(8925):769–772, 1994.

[8] Marcus Rössler, Rosemarie Zarski, Jürgen Bohl, and Thomas G Ohm. Stage-dependent and sector-specific neuronal loss in hippocampus during alzheimer's disease. *Acta neuropathologica*, 103(4):363–369, 2002.

[9] Robert M Sapolsky, Hideo Uno, Charles S Rebert, and Caleb E Finch. Hippocampal damage associated with prolonged glucocorticoid exposure in primates. *The Journal of Neuroscience*, 10(9):2897–2902, 1990.

[10] Ingmar Blümcke, Elisabeth Pauli, Hans Clusmann, Johannes Schramm, Albert Becker, Christian Elger, Martin Merschhemke, Heinz-Joachim Meencke, Thomas Lehmann, Andreas Deimling, Christian Scheiwe, Josef Zentner, Benedikt Volk, Johann Romstöck, Hermann Stefan, and Michelle Hildebrandt. A new clinico-pathological classification system for mesial temporal sclerosis. *Acta Neuropathol*, 113(3):235–244, 2007.

[11] Bradley P Thomas, E Brian Welch, Blake D Niederhauser, William O Whetsell, Adam W Anderson, John C Gore, Malcolm J Avison, and Jeffrey L Creasy. High-resolution 7T MRI of the human hippocampus in vivo. *J Magn Reson Imaging*, 28(5):1266–72, 2008.

[12] Susanne G Mueller, Kenneth D Laxer, Jerome Barakos, Ian Cheong, Paul Garcia, and Michael W Weiner. Subfield atrophy pattern in temporal lobe epilepsy with and without mesial sclerosis detected by high-resolution MRI at 4 Tesla: preliminary results. *Epilepsia*, 50(6):1474–83, 2009.

[13] Koen Van Leemput, Akram Bakkour, Thomas Benner, Graham Wiggins, Lawrence L Wald, Jean Augustinack, Bradford C Dickerson, Polina Golland, and Bruce Fischl. Automated segmentation of hippocampal subfields from ultra-high resolution in vivo MRI. *Hippocampus*, 19(6):549–57, 2009.

[14] N V Malykhin, R M Lebel, N J Coupland, A H Wilman, and R Carter. In vivo quantification of hippocampal subfields using 4.7 T fast spin echo imaging. *Neuroimage*, 49(2):1224–30, 2010.

[15] L E M Wisse, L Gerritsen, J J M Zwanenburg, H J Kuijf, P R Luijten, G J Biessels, and M I Geerlings. Subfields of the hippocampal formation at 7 T MRI: in vivo volumetric assessment. *Neuroimage*, 61(4):1043–9, 2012.

[16] Ludovic de Rochefort, Ryan Brown, Martin R Prince, and YI Wang. Quantitative mr susceptibility mapping using piece-wise constant regularized inversion of the magnetic field. *Magnetic Resonance in Medicine*, 60(4):1003–1009, 2008.

[17] Vasthie Prudent, Arun Kumar, Songtao Liu, Graham Wiggins, Dolores Malaspina,

and Oded Gonen. Human hippocampal subfields in young adults at 7.0 T: feasibility of imaging. *Radiology*, 254(3):900–6, 2010.

[18] Tobias Breyer, Isabel Wanke, Stefan Maderwald, Friedrich G Woermann, Oliver Kraff, Jens M Theysohn, Alois Ebner, Michael Forsting, Mark E Ladd, and Marc Schlamann. Imaging of patients with hippocampal sclerosis at 7 tesla: initial results. *Academic radiology*, 17(4):421–426, 2010.

[19] Jens M Theysohn, O Kraff, S Maderwald, M U Schlamann, A de Greiff, M Forsting, S C Ladd, M E Ladd, and E R Gizewski. The human hippocampus at 7 T–in vivo MRI. *Hippocampus*, 19(1):1–7, 2009.

[20] Zang-Hee Cho, Hoon-Ki Min, Se-Hong Oh, Jae-Yong Han, Chan-Woong Park, Je-Geun Chi, Young-Bo Kim, Sun Ha Paek, Andres M Lozano, and Kendall H Lee. Direct visualization of deep brain stimulation targets in parkinson disease with the use of 7-tesla magnetic resonance imaging. *Journal of neurosurgery*, 113 (3):639, 2010.

[21] Simon Robinson, Günther Grabner, Stephan Witoszynskyj, and Siegfried Trattnig. Combining phase images from multi-channel rf coils using 3d phase offset maps derived from a dual-echo scan. *Magnetic Resonance in Medicine*, 65(6):1638–1648, 2011.

[22] Hussein S Abdul-Rahman, Munther A Gdeisat, David R Burton, Michael J Lalor, Francis Lilley, and Christopher J Moore. Fast and robust three-dimensional best path phase unwrapping algorithm. *Applied optics*, 46(26):6623–6635, 2007.

[23] Tian Liu, Jing Liu, Ludovic de Rochefort, Pascal Spincemaille, Ildar Khalidov, James Robert Ledoux, and Yi Wang. Morphology enabled dipole inversion (medi)

from a single-angle acquisition: Comparison with cosmos in human brain imaging. *Magnetic resonance in medicine*, 66(3):777–783, 2011.

[24] Ferdinand Schweser, Andreas Deistung, Berengar Wendel Lehr, and Jürgen Rainer Reichenbach. Quantitative imaging of intrinsic magnetic tissue properties using mri signal phase: an approach to in vivo brain iron metabolism? *Neuroimage*, 54(4):2789–2807, 2011.

[25] Bryan Kressler, Ludovic de Rochefort, Tian Liu, Pascal Spincemaille, Quan Jiang, and Yi Wang. Nonlinear regularization for per voxel estimation of magnetic susceptibility distributions from mri field maps. *Medical Imaging, IEEE Transactions on*, 29(2):273–281, 2010.

[26] Ludovic de Rochefort, Tian Liu, Bryan Kressler, Jing Liu, Pascal Spincemaille, Vincent Lebon, Jianlin Wu, and Yi Wang. Quantitative susceptibility map reconstruction from mr phase data using bayesian regularization: validation and application to brain imaging. *Magnetic Resonance in Medicine*, 63(1):194–206, 2010.

[27] Paul A Yushkevich, Joseph Piven, Heather Cody Hazlett, Rachel Gimpel Smith, Sean Ho, James C Gee, and Guido Gerig. User-guided 3D active contour segmentation of anatomical structures: significantly improved efficiency and reliability. *Neuroimage*, 31(3):1116–28, 2006.

[28] Susanne G Mueller, Kenneth D Laxer, Norbert Schuff, and Michael W Weiner. Voxel-based T2 relaxation rate measurements in temporal lobe epilepsy (TLE) with and without mesial temporal sclerosis. *Epilepsia*, 48(2):220–8, 2007.

[29] Brian Avants and James C Gee. Geodesic estimation for large deformation

anatomical shape averaging and interpolation. *Neuroimage*, 23 Suppl 1:S139–50, 2004.

[30] J G Sled, A P Zijdenbos, and A C Evans. A nonparametric method for automatic correction of intensity nonuniformity in MRI data. *IEEE Transactions on Medical Imaging*, 17(1):87–97, 1998.

[31] Andreas Deistung, Andreas Schäfer, Ferdinand Schweser, Uta Biedermann, Robert Turner, and Jürgen R Reichenbach. Toward in vivo histology: A comparison of quantitative susceptibility mapping (QSM) with magnitude-, phase-, and R(2)()-imaging at ultra-high magnetic field strength. *Neuroimage*, 2012.

[32] Sam Wharton and Richard Bowtell. Whole-brain susceptibility mapping at high field: a comparison of multiple-and single-orientation methods. *Neuroimage*, 53 (2):515–525, 2010.

[33] Vijay Antharam, Joanna F Collingwood, John-Paul Bullivant, Mark R Davidson, Saurav Chandra, Albina Mikhaylova, Mary E Finnegan, Christopher Batich, John R Forder, and Jon Dobson. High field magnetic resonance microscopy of the human hippocampus in alzheimer's disease: Quantitative imaging and correlation with iron. *Neuroimage*, 59(2):1249–1260, 2012.

[34] Bing Yao, Tie-Qiang Li, Peter van Gelderen, Karin Shmueli, Jacco A de Zwart, and Jeff H Duyn. Susceptibility contrast in high field mri of human brain as a function of tissue iron content. *Neuroimage*, 44(4):1259–1266, 2009.

[35] Paul A Yushkevich, Brian B Avants, John Pluta, Sandhitsu Das, David Minkoff, Dawn Mechanic-Hamilton, Simon Glynn, Stephen Pickup, Weixia Liu, James C Gee, Murray Grossman, and John A Detre. A high-resolution computational atlas

of the human hippocampus from postmortem magnetic resonance imaging at 9.4 T. *Neuroimage*, 44(2):385–98, 2009.

[36] Timothy M Shepherd, Peter E Thelwall, Greg J Stanisz, and Stephen J Blackband. Aldehyde fixative solutions alter the water relaxation and diffusion properties of nervous tissue. *Magn Reson Med*, 62(1):26–34, 2009.

[37] Arno Klein, Jesper Andersson, Babak A Ardekani, John Ashburner, Brian Avants, Ming-Chang Chiang, Gary E Christensen, D Louis Collins, James Gee, Pierre Hellier, Joo Hyun Song, Mark Jenkinson, Claude Lepage, Daniel Rueckert, Paul Thompson, Tom Vercauteren, Roger P Woods, J John Mann, and Ramin V Parsey. Evaluation of 14 nonlinear deformation algorithms applied to human brain MRI registration. *Neuroimage*, 46(3):786–802, 2009.

[38] E Elolf, V Bockermann, T Gringel, M Knauth, P Dechent, and G Helms. Improved visibility of the subthalamic nucleus on high-resolution stereotactic mr imaging by added susceptibility (t2*) contrast using multiple gradient echoes. *American journal of neuroradiology*, 28(6):1093–1094, 2007.

[39] Andreas Schäfer, Birte U Forstmann, Jane Neumann, Sam Wharton, Alexander Mietke, Richard Bowtell, and Robert Turner. Direct visualization of the subthalamic nucleus and its iron distribution using high-resolution susceptibility mapping. *Human brain mapping*, 33(12):2831–2842, 2012.

ELSEVIER LICENSE
TERMS AND CONDITIONS

Aug 20, 2014

This is a License Agreement between Maged Goubran ("You") and Elsevier ("Elsevier") provided by Copyright Clearance Center ("CCC"). The license consists of your order details, the terms and conditions provided by Elsevier, and the payment terms and conditions.

All payments must be made in full to CCC. For payment instructions, please see information listed at the bottom of this form.

Supplier	Elsevier Limited The Boulevard,Langford Lane Kidlington,Oxford,OX5 1GB,UK
Registered Company Number	1982084
Customer name	Maged Goubran
Customer address	
License number	3453090830685
License date	Aug 20, 2014
Licensed content publisher	Elsevier
Licensed content publication	NeuroImage
Licensed content title	Image registration of ex-vivo MRI to sparsely sectioned histology of hippocampal and neocortical temporal lobe specimens
Licensed content author	Maged Goubran,Cathie Crukley,Sandrine de Ribaupierre,Terence M. Peters,Ali R. Khan
Licensed content date	December 2013
Licensed content volume number	83
Licensed content issue number	n/a
Number of pages	12
Start Page	770
End Page	781
Type of Use	reuse in a thesis/dissertation
Portion	full article
Format	both print and electronic
Are you the author of this Elsevier article?	Yes
Will you be translating?	No

Title of your thesis/dissertation	Quantitative MRI correlates of hippocampal and neocortical pathology in intractable temporal lobe epilepsy
Expected completion date	Sep 2014
Estimated size (number of pages)	200
Elsevier VAT number	GB 494 6272 12
Permissions price	0.00 USD
VAT/Local Sales Tax	0.00 USD / 0.00 GBP
Total	0.00 USD
Terms and Conditions	

INTRODUCTION

1. The publisher for this copyrighted material is Elsevier. By clicking "accept" in connection with completing this licensing transaction, you agree that the following terms and conditions apply to this transaction (along with the Billing and Payment terms and conditions established by Copyright Clearance Center, Inc. ("CCC"), at the time that you opened your Rightslink account and that are available at any time at http://myaccount.copyright.com).

GENERAL TERMS

2. Elsevier hereby grants you permission to reproduce the aforementioned material subject to the terms and conditions indicated.

3. Acknowledgement: If any part of the material to be used (for example, figures) has appeared in our publication with credit or acknowledgement to another source, permission must also be sought from that source. If such permission is not obtained then that material may not be included in your publication/copies. Suitable acknowledgement to the source must be made, either as a footnote or in a reference list at the end of your publication, as follows:

"Reprinted from Publication title, Vol /edition number, Author(s), Title of article / title of chapter, Pages No., Copyright (Year), with permission from Elsevier [OR APPLICABLE SOCIETY COPYRIGHT OWNER]." Also Lancet special credit - "Reprinted from The Lancet, Vol. number, Author(s), Title of article, Pages No., Copyright (Year), with permission from Elsevier."

4. Reproduction of this material is confined to the purpose and/or media for which permission is hereby given.

5. Altering/Modifying Material: Not Permitted. However figures and illustrations may be altered/adapted minimally to serve your work. Any other abbreviations, additions, deletions and/or any other alterations shall be made only with prior written authorization of Elsevier Ltd. (Please contact Elsevier at permissions@elsevier.com)

6. If the permission fee for the requested use of our material is waived in this instance, please be advised that your future requests for Elsevier materials may attract a fee.

7. Reservation of Rights: Publisher reserves all rights not specifically granted in the combination of (i) the license details provided by you and accepted in the course of this licensing transaction, (ii)

these terms and conditions and (iii) CCC's Billing and Payment terms and conditions.

8. License Contingent Upon Payment: While you may exercise the rights licensed immediately upon issuance of the license at the end of the licensing process for the transaction, provided that you have disclosed complete and accurate details of your proposed use, no license is finally effective unless and until full payment is received from you (either by publisher or by CCC) as provided in CCC's Billing and Payment terms and conditions. If full payment is not received on a timely basis, then any license preliminarily granted shall be deemed automatically revoked and shall be void as if never granted. Further, in the event that you breach any of these terms and conditions or any of CCC's Billing and Payment terms and conditions, the license is automatically revoked and shall be void as if never granted. Use of materials as described in a revoked license, as well as any use of the materials beyond the scope of an unrevoked license, may constitute copyright infringement and publisher reserves the right to take any and all action to protect its copyright in the materials.

9. Warranties: Publisher makes no representations or warranties with respect to the licensed material.

10. Indemnity: You hereby indemnify and agree to hold harmless publisher and CCC, and their respective officers, directors, employees and agents, from and against any and all claims arising out of your use of the licensed material other than as specifically authorized pursuant to this license.

11. No Transfer of License: This license is personal to you and may not be sublicensed, assigned, or transferred by you to any other person without publisher's written permission.

12. No Amendment Except in Writing: This license may not be amended except in a writing signed by both parties (or, in the case of publisher, by CCC on publisher's behalf).

13. Objection to Contrary Terms: Publisher hereby objects to any terms contained in any purchase order, acknowledgment, check endorsement or other writing prepared by you, which terms are inconsistent with these terms and conditions or CCC's Billing and Payment terms and conditions. These terms and conditions, together with CCC's Billing and Payment terms and conditions (which are incorporated herein), comprise the entire agreement between you and publisher (and CCC) concerning this licensing transaction. In the event of any conflict between your obligations established by these terms and conditions and those established by CCC's Billing and Payment terms and conditions, these terms and conditions shall control.

14. Revocation: Elsevier or Copyright Clearance Center may deny the permissions described in this License at their sole discretion, for any reason or no reason, with a full refund payable to you. Notice of such denial will be made using the contact information provided by you. Failure to receive such notice will not alter or invalidate the denial. In no event will Elsevier or Copyright Clearance Center be responsible or liable for any costs, expenses or damage incurred by you as a result of a denial of your permission request, other than a refund of the amount(s) paid by you to Elsevier and/or Copyright Clearance Center for denied permissions.

LIMITED LICENSE

The following terms and conditions apply only to specific license types:

15. **Translation**: This permission is granted for non-exclusive world **English** rights only unless your license was granted for translation rights. If you licensed translation rights you may only translate this content into the languages you requested. A professional translator must perform all translations and reproduce the content word for word preserving the integrity of the article. If this license is to re-use 1 or 2 figures then permission is granted for non-exclusive world rights in all languages.

16. **Posting licensed content on any Website**: The following terms and conditions apply as follows: Licensing material from an Elsevier journal: All content posted to the web site must maintain the copyright information line on the bottom of each image; A hyper-text must be included to the Homepage of the journal from which you are licensing at http://www.sciencedirect.com/science/journal/xxxxx or the Elsevier homepage for books at http://www.elsevier.com; Central Storage: This license does not include permission for a scanned version of the material to be stored in a central repository such as that provided by Heron/XanEdu.

Licensing material from an Elsevier book: A hyper-text link must be included to the Elsevier homepage at http://www.elsevier.com . All content posted to the web site must maintain the copyright information line on the bottom of each image.

Posting licensed content on Electronic reserve: In addition to the above the following clauses are applicable: The web site must be password-protected and made available only to bona fide students registered on a relevant course. This permission is granted for 1 year only. You may obtain a new license for future website posting.

For journal authors: the following clauses are applicable in addition to the above: Permission granted is limited to the author accepted manuscript version* of your paper.

***Accepted Author Manuscript (AAM) Definition:** An accepted author manuscript (AAM) is the author's version of the manuscript of an article that has been accepted for publication and which may include any author-incorporated changes suggested through the processes of submission processing, peer review, and editor-author communications. AAMs do not include other publisher value-added contributions such as copy-editing, formatting, technical enhancements and (if relevant) pagination.

You are not allowed to download and post the published journal article (whether PDF or HTML, proof or final version), nor may you scan the printed edition to create an electronic version. A hyper-text must be included to the Homepage of the journal from which you are licensing at http://www.sciencedirect.com/science/journal/xxxxx. As part of our normal production process, you will receive an e-mail notice when your article appears on Elsevier's online service ScienceDirect (www.sciencedirect.com). That e-mail will include the article's Digital Object Identifier (DOI). This number provides the electronic link to the published article and should be included in the posting of your personal version. We ask that you wait until you receive this e-mail and have the DOI to do any posting.

Posting to a repository: Authors may post their AAM immediately to their employer's institutional repository for internal use only and may make their manuscript publically available after the journal-specific embargo period has ended.

Please also refer to Elsevier's Article Posting Policy for further information.

18. **For book authors** the following clauses are applicable in addition to the above: Authors are permitted to place a brief summary of their work online only.. You are not allowed to download and post the published electronic version of your chapter, nor may you scan the printed edition to create an electronic version. **Posting to a repository:** Authors are permitted to post a summary of their chapter only in their institution's repository.

20. **Thesis/Dissertation**: If your license is for use in a thesis/dissertation your thesis may be submitted to your institution in either print or electronic form. Should your thesis be published commercially, please reapply for permission. These requirements include permission for the Library and Archives of Canada to supply single copies, on demand, of the complete thesis and include permission for UMI to supply single copies, on demand, of the complete thesis. Should your thesis be published commercially, please reapply for permission.

Elsevier Open Access Terms and Conditions

Elsevier publishes Open Access articles in both its Open Access journals and via its Open Access articles option in subscription journals.

Authors publishing in an Open Access journal or who choose to make their article Open Access in an Elsevier subscription journal select one of the following Creative Commons user licenses, which define how a reader may reuse their work: Creative Commons Attribution License (CC BY), Creative Commons Attribution – Non Commercial - ShareAlike (CC BY NC SA) and Creative Commons Attribution – Non Commercial – No Derivatives (CC BY NC ND)

Terms & Conditions applicable to all Elsevier Open Access articles:

Any reuse of the article must not represent the author as endorsing the adaptation of the article nor should the article be modified in such a way as to damage the author's honour or reputation.

The author(s) must be appropriately credited.

If any part of the material to be used (for example, figures) has appeared in our publication with credit or acknowledgement to another source it is the responsibility of the user to ensure their reuse complies with the terms and conditions determined by the rights holder.

Additional Terms & Conditions applicable to each Creative Commons user license:

CC BY: You may distribute and copy the article, create extracts, abstracts, and other revised versions, adaptations or derivative works of or from an article (such as a translation), to include in a collective work (such as an anthology), to text or data mine the article, including for commercial purposes without permission from Elsevier

CC BY NC SA: For non-commercial purposes you may distribute and copy the article, create extracts, abstracts and other revised versions, adaptations or derivative works of or from an article

(such as a translation), to include in a collective work (such as an anthology), to text and data mine the article and license new adaptations or creations under identical terms without permission from Elsevier

CC BY NC ND: For non-commercial purposes you may distribute and copy the article and include it in a collective work (such as an anthology), provided you do not alter or modify the article, without permission from Elsevier

Any commercial reuse of Open Access articles published with a CC BY NC SA or CC BY NC ND license requires permission from Elsevier and will be subject to a fee.

Commercial reuse includes:

- Promotional purposes (advertising or marketing)
- Commercial exploitation (e.g. a product for sale or loan)
- Systematic distribution (for a fee or free of charge)

Please refer to Elsevier's Open Access Policy for further information.

21. **Other Conditions**:

v1.6

You will be invoiced within 48 hours of this transaction date. You may pay your invoice by credit card upon receipt of the invoice for this transaction. Please follow instructions provided at that time.
To pay for this transaction now; please remit a copy of this document along with your payment. Payment should be in the form of a check or money order referencing your account number and this invoice number RLNK501382030.
Make payments to "COPYRIGHT CLEARANCE CENTER" and send to:

Copyright Clearance Center
Dept 001
P.O. Box 843006
Boston, MA 02284-3006
Please disregard electronic and mailed copies if you remit payment in advance.
Questions? customercare@copyright.com or +1-855-239-3415 (toll free in the US) or +1-978-646-2777.

Gratis licenses (referencing $0 in the Total field) are free. Please retain this printable license for your reference. No payment is required.

JOHN WILEY AND SONS LICENSE TERMS AND CONDITIONS

Aug 20, 2014

This is a License Agreement between Maged Goubran ("You") and John Wiley and Sons ("John Wiley and Sons") provided by Copyright Clearance Center ("CCC"). The license consists of your order details, the terms and conditions provided by John Wiley and Sons, and the payment terms and conditions.

All payments must be made in full to CCC. For payment instructions, please see information listed at the bottom of this form.

License Number	3453091281597
License date	Aug 20, 2014
Licensed content publisher	John Wiley and Sons
Licensed content publication	Human Brain Mapping
Licensed content title	In vivo normative atlas of the hippocampal subfields using multi-echo susceptibility imaging at 7 Tesla
Licensed copyright line	Copyright © 2013 Wiley Periodicals, Inc.
Licensed content author	Maged Goubran,David A. Rudko,Brendan Santyr,Joe Gati,Trevor Szekeres,Terry M. Peters,Ali R. Khan
Licensed content date	Dec 13, 2013
Start page	3588
End page	3601
Type of use	Dissertation/Thesis
Requestor type	Author of this Wiley article
Format	Print and electronic
Portion	Full article
Will you be translating?	No
Title of your thesis / dissertation	Quantitative MRI correlates of hippocampal and neocortical pathology in intractable temporal lobe epilepsy
Expected completion date	Sep 2014
Expected size (number of pages)	200
Total	0.00 USD
Terms and Conditions	

TERMS AND CONDITIONS

This copyrighted material is owned by or exclusively licensed to John Wiley & Sons, Inc. or one of its group companies (each a"Wiley Company") or handled on behalf of a society with which a

Wiley Company has exclusive publishing rights in relation to a particular work (collectively "WILEY"). By clicking "accept" in connection with completing this licensing transaction, you agree that the following terms and conditions apply to this transaction (along with the billing and payment terms and conditions established by the Copyright Clearance Center Inc., ("CCC's Billing and Payment terms and conditions"), at the time that you opened your Rightslink account (these are available at any time at http://myaccount.copyright.com).

Terms and Conditions

- The materials you have requested permission to reproduce or reuse (the "Wiley Materials") are protected by copyright.

- You are hereby granted a personal, non-exclusive, non-sub licensable (on a stand-alone basis), non-transferable, worldwide, limited license to reproduce the Wiley Materials for the purpose specified in the licensing process. This license is for a one-time use only and limited to any maximum distribution number specified in the license. The first instance of republication or reuse granted by this licence must be completed within two years of the date of the grant of this licence (although copies prepared before the end date may be distributed thereafter). The Wiley Materials shall not be used in any other manner or for any other purpose, beyond what is granted in the license. Permission is granted subject to an appropriate acknowledgement given to the author, title of the material/book/journal and the publisher. You shall also duplicate the copyright notice that appears in the Wiley publication in your use of the Wiley Material. Permission is also granted on the understanding that nowhere in the text is a previously published source acknowledged for all or part of this Wiley Material. Any third party content is expressly excluded from this permission.

- With respect to the Wiley Materials, all rights are reserved. Except as expressly granted by the terms of the license, no part of the Wiley Materials may be copied, modified, adapted (except for minor reformatting required by the new Publication), translated, reproduced, transferred or distributed, in any form or by any means, and no derivative works may be made based on the Wiley Materials without the prior permission of the respective copyright owner. You may not alter, remove or suppress in any manner any copyright, trademark or other notices displayed by the Wiley Materials. You may not license, rent, sell, loan, lease, pledge, offer as security, transfer or assign the Wiley Materials on a stand-alone basis, or any of the rights granted to you hereunder to any other person.

- The Wiley Materials and all of the intellectual property rights therein shall at all times remain the exclusive property of John Wiley & Sons Inc, the Wiley Companies, or their respective licensors, and your interest therein is only that of having possession of and the right to reproduce the Wiley Materials pursuant to Section 2 herein during the continuance of this Agreement. You agree that you own no right, title or interest in or to the Wiley Materials or any of the intellectual property rights therein. You shall have no rights hereunder other than the license as provided for above in Section 2. No right, license or interest to any trademark, trade name, service mark or other branding ("Marks") of WILEY or its licensors is granted hereunder, and you agree that you shall not assert any such right, license or interest with

respect thereto.

- NEITHER WILEY NOR ITS LICENSORS MAKES ANY WARRANTY OR REPRESENTATION OF ANY KIND TO YOU OR ANY THIRD PARTY, EXPRESS, IMPLIED OR STATUTORY, WITH RESPECT TO THE MATERIALS OR THE ACCURACY OF ANY INFORMATION CONTAINED IN THE MATERIALS, INCLUDING, WITHOUT LIMITATION, ANY IMPLIED WARRANTY OF MERCHANTABILITY, ACCURACY, SATISFACTORY QUALITY, FITNESS FOR A PARTICULAR PURPOSE, USABILITY, INTEGRATION OR NON-INFRINGEMENT AND ALL SUCH WARRANTIES ARE HEREBY EXCLUDED BY WILEY AND ITS LICENSORS AND WAIVED BY YOU

- WILEY shall have the right to terminate this Agreement immediately upon breach of this Agreement by you.

- You shall indemnify, defend and hold harmless WILEY, its Licensors and their respective directors, officers, agents and employees, from and against any actual or threatened claims, demands, causes of action or proceedings arising from any breach of this Agreement by you.

- IN NO EVENT SHALL WILEY OR ITS LICENSORS BE LIABLE TO YOU OR ANY OTHER PARTY OR ANY OTHER PERSON OR ENTITY FOR ANY SPECIAL, CONSEQUENTIAL, INCIDENTAL, INDIRECT, EXEMPLARY OR PUNITIVE DAMAGES, HOWEVER CAUSED, ARISING OUT OF OR IN CONNECTION WITH THE DOWNLOADING, PROVISIONING, VIEWING OR USE OF THE MATERIALS REGARDLESS OF THE FORM OF ACTION, WHETHER FOR BREACH OF CONTRACT, BREACH OF WARRANTY, TORT, NEGLIGENCE, INFRINGEMENT OR OTHERWISE (INCLUDING, WITHOUT LIMITATION, DAMAGES BASED ON LOSS OF PROFITS, DATA, FILES, USE, BUSINESS OPPORTUNITY OR CLAIMS OF THIRD PARTIES), AND WHETHER OR NOT THE PARTY HAS BEEN ADVISED OF THE POSSIBILITY OF SUCH DAMAGES. THIS LIMITATION SHALL APPLY NOTWITHSTANDING ANY FAILURE OF ESSENTIAL PURPOSE OF ANY LIMITED REMEDY PROVIDED HEREIN.

- Should any provision of this Agreement be held by a court of competent jurisdiction to be illegal, invalid, or unenforceable, that provision shall be deemed amended to achieve as nearly as possible the same economic effect as the original provision, and the legality, validity and enforceability of the remaining provisions of this Agreement shall not be affected or impaired thereby.

- The failure of either party to enforce any term or condition of this Agreement shall not constitute a waiver of either party's right to enforce each and every term and condition of this Agreement. No breach under this agreement shall be deemed waived or excused by either party unless such waiver or consent is in writing signed by the party granting such waiver or consent. The waiver by or consent of a party to a breach of any provision of this Agreement shall not operate or be construed as a waiver of or consent to any other or subsequent breach by such other party.

- This Agreement may not be assigned (including by operation of law or otherwise) by you without WILEY's prior written consent.

- Any fee required for this permission shall be non-refundable after thirty (30) days from receipt by the CCC.

- These terms and conditions together with CCC's Billing and Payment terms and conditions (which are incorporated herein) form the entire agreement between you and WILEY concerning this licensing transaction and (in the absence of fraud) supersedes all prior agreements and representations of the parties, oral or written. This Agreement may not be amended except in writing signed by both parties. This Agreement shall be binding upon and inure to the benefit of the parties' successors, legal representatives, and authorized assigns.

- In the event of any conflict between your obligations established by these terms and conditions and those established by CCC's Billing and Payment terms and conditions, these terms and conditions shall prevail.

- WILEY expressly reserves all rights not specifically granted in the combination of (i) the license details provided by you and accepted in the course of this licensing transaction, (ii) these terms and conditions and (iii) CCC's Billing and Payment terms and conditions.

- This Agreement will be void if the Type of Use, Format, Circulation, or Requestor Type was misrepresented during the licensing process.

- This Agreement shall be governed by and construed in accordance with the laws of the State of New York, USA, without regards to such state's conflict of law rules. Any legal action, suit or proceeding arising out of or relating to these Terms and Conditions or the breach thereof shall be instituted in a court of competent jurisdiction in New York County in the State of New York in the United States of America and each party hereby consents and submits to the personal jurisdiction of such court, waives any objection to venue in such court and consents to service of process by registered or certified mail, return receipt requested, at the last known address of such party.

WILEY OPEN ACCESS TERMS AND CONDITIONS

Wiley Publishes Open Access Articles in fully Open Access Journals and in Subscription journals offering Online Open. Although most of the fully Open Access journals publish open access articles under the terms of the Creative Commons Attribution (CC BY) License only, the subscription journals and a few of the Open Access Journals offer a choice of Creative Commons Licenses:: Creative Commons Attribution (CC-BY) license Creative Commons Attribution Non-Commercial (CC-BY-NC) license and Creative Commons Attribution Non-Commercial-NoDerivs (CC-BY-NC-ND) License. The license type is clearly identified on the article.

Copyright in any research article in a journal published as Open Access under a Creative

Commons License is retained by the author(s). Authors grant Wiley a license to publish the article and identify itself as the original publisher. Authors also grant any third party the right to use the article freely as long as its integrity is maintained and its original authors, citation details and publisher are identified as follows: [Title of Article/Author/Journal Title and Volume/Issue. Copyright (c) [year] [copyright owner as specified in the Journal]. Links to the final article on Wiley's website are encouraged where applicable.

The Creative Commons Attribution License

The Creative Commons Attribution License (CC-BY) allows users to copy, distribute and transmit an article, adapt the article and make commercial use of the article. The CC-BY license permits commercial and non-commercial re-use of an open access article, as long as the author is properly attributed.

The Creative Commons Attribution License does not affect the moral rights of authors, including without limitation the right not to have their work subjected to derogatory treatment. It also does not affect any other rights held by authors or third parties in the article, including without limitation the rights of privacy and publicity. Use of the article must not assert or imply, whether implicitly or explicitly, any connection with, endorsement or sponsorship of such use by the author, publisher or any other party associated with the article.

For any reuse or distribution, users must include the copyright notice and make clear to others that the article is made available under a Creative Commons Attribution license, linking to the relevant Creative Commons web page.

To the fullest extent permitted by applicable law, the article is made available as is and without representation or warranties of any kind whether express, implied, statutory or otherwise and including, without limitation, warranties of title, merchantability, fitness for a particular purpose, non-infringement, absence of defects, accuracy, or the presence or absence of errors.

Creative Commons Attribution Non-Commercial License

The Creative Commons Attribution Non-Commercial (CC-BY-NC) License permits use, distribution and reproduction in any medium, provided the original work is properly cited and is not used for commercial purposes.(see below)

Creative Commons Attribution-Non-Commercial-NoDerivs License

The Creative Commons Attribution Non-Commercial-NoDerivs License (CC-BY-NC-ND) permits use, distribution and reproduction in any medium, provided the original work is properly cited, is not used for commercial purposes and no modifications or adaptations are made. (see below)

Use by non-commercial users

For non-commercial and non-promotional purposes, individual users may access, download, copy, display and redistribute to colleagues Wiley Open Access articles, as well as adapt, translate, text- and data-mine the content subject to the following conditions:

- The authors' moral rights are not compromised. These rights include the right of "paternity" (also known as "attribution" - the right for the author to be identified as such) and "integrity" (the right for the author not to have the work altered in such a way that the author's reputation or integrity may be impugned).

- Where content in the article is identified as belonging to a third party, it is the obligation of the user to ensure that any reuse complies with the copyright policies of the owner of that content.

- If article content is copied, downloaded or otherwise reused for non-commercial research and education purposes, a link to the appropriate bibliographic citation (authors, journal, article title, volume, issue, page numbers, DOI and the link to the definitive published version on **Wiley Online Library**) should be maintained. Copyright notices and disclaimers must not be deleted.

- Any translations, for which a prior translation agreement with Wiley has not been agreed, must prominently display the statement: "This is an unofficial translation of an article that appeared in a Wiley publication. The publisher has not endorsed this translation."

Use by commercial "for-profit" organisations

Use of Wiley Open Access articles for commercial, promotional, or marketing purposes requires further explicit permission from Wiley and will be subject to a fee. Commercial purposes include:

- Copying or downloading of articles, or linking to such articles for further redistribution, sale or licensing;

- Copying, downloading or posting by a site or service that incorporates advertising with such content;

- The inclusion or incorporation of article content in other works or services (other than normal quotations with an appropriate citation) that is then available for sale or licensing, for a fee (for example, a compilation produced for marketing purposes, inclusion in a sales pack)

- Use of article content (other than normal quotations with appropriate citation) by for-profit organisations for promotional purposes

- Linking to article content in e-mails redistributed for promotional, marketing or educational purposes;

- Use for the purposes of monetary reward by means of sale, resale, licence, loan, transfer or other form of commercial exploitation such as marketing products

- Print reprints of Wiley Open Access articles can be purchased from: corporatesales@wiley.com

Further details can be found on Wiley Online Library
http://olabout.wiley.com/WileyCDA/Section/id-410895.html

Other Terms and Conditions:

v1.9

You will be invoiced within 48 hours of this transaction date. You may pay your invoice by credit card upon receipt of the invoice for this transaction. Please follow instructions provided at that time.
To pay for this transaction now; please remit a copy of this document along with your payment. Payment should be in the form of a check or money order referencing your account number and this invoice number RLNK501382044.
Make payments to "COPYRIGHT CLEARANCE CENTER" and send to:

Copyright Clearance Center
Dept 001
P.O. Box 843006
Boston, MA 02284-3006
Please disregard electronic and mailed copies if you remit payment in advance.
Questions? customercare@copyright.com or +1-855-239-3415 (toll free in the US) or +1-978-646-2777.

Gratis licenses (referencing $0 in the Total field) are free. Please retain this printable license for your reference. No payment is required.

CURRICULUM VITAE

Maged Goubran

EDUCATION

Sep 2010-Oct 2014	**Ph.D. candidate in Biomedical Engineering,** *Medical Imaging concentration*
	Western University, London, ON, Canada
Sep 2006-May 2010	**Honors BMSc in Medical Biophysics** and Minor in French,
	with distinction, Western University, London, ON

AWARDS & HONOURS

2010 - Present	**Western Graduate Research Scholarship** (WGRS)	[$ 22,000]
2013	**ISMRM Merit Award** magna cum laude	--
2011 - 2013	NSERC award in **Computer Assisted Medical Interventions** (CAMI)	[$ 36,000]
2011	Best scientific video for summer research projects	[$ 200]
2007 - 2010	**Dean's Honor List** for a cumulative average over 80%	--
2006	Western University's **Entrance Scholarship of Excellence**	[$ 2,000]
2003 - 2005	**Top 10 of 300 graduates of the year** at the AAST, Alexandria, Egypt	[$ 300]
2003	Delegate of St. Marc School in a children rights project by the *UNESCO*	--

WORK EXPERIENCE

2013 - 2014	**Teaching Assistant,** Department of Chemical Engineering, Western University Course: Introductory Biochemistry for Engineers (*Undergraduate level*)
2012 - 2013	**Teaching Assistant,** Department of Medical Biophysics, Western University Course: Human and Animal Biomechanics (*Undergraduate level*)
2011 - 2012	**Teaching Assistant,** Department of Medical Biophysics, Western University Course: Biophysics of Transport Systems (*Undergraduate level*)
2010 - 2011	**Teaching Assistant,** Biomedical Engineering graduate program, Western University Course: Image Guided Interventions (*Graduate level*)
Summer 2010	**Research Assistant, Robarts Research Institute**, London, ON supervised by *Prof. Terry Peters*
Summer 2009	**Research Assistant, Robarts Research Institute**, London, ON supervised by *Prof. Terry Peters*
Summer 2007	**Lab assistant, Alex Scan Analysis Laboratories,** Alexandria, Egypt supervised by *Prof. Nahla Farahat*
August 2006	**Research Assistant, Medical Research Institute,** Alexandria, Egypt supervised by *Prof. Ibrahim El Akkary*

GRADUATE COURSES

2012	*Advanced digital image processing & analysis*, Department of Medical Imaging
2011	*Advanced MRI physics*, Department of Medical Biophysics *Human Physiology for Engineers*, Department of Physiology and Pharmacology
2010	*Medical Imaging*, Department of Medical Imaging *MRI physics*, Department of Medical Biophysics

PUBLICATIONS & SCHOLARLY ACTIVITIES

Journal Articles

1. **Goubran, M.,** Lau, J., Cantor-Rivera, D., Blinston, C., Hammond. R., de Ribaupierre, S., Burneo, J., Mirsattari, S., Steven, D., Parrent, A., Bernasconi, A., Bernasconi, N., Peters, T., and Khan, A.R., "Quantitative MRI correlates of hippocampal pathology in refractory mesial temporal lobe epilepsy." Target journal: *Annals of Neurology.* In-preparation.

2. **Goubran, M.,** Hammond. R., de Ribaupierre, S., Burneo, J., Mirsattari, S., Steven, D., Parrent, A., Peters, T., and Khan, A.R., "MRI and histology correlation in the neocortex of temporal lobe epilepsy." *Annals of Neurology.* Under-review. Manuscript # ANA-14-0385 [impact factor: *11.19*]

3. **Goubran, M.,** Curie, C., S., de Ribaupierre, S., Hammond. R., Parrent, A., Burneo, J., Peters, T., and Khan, A.R., "Registration of pre-operative to it ex-vivo MRI of resected specimens: a pipeline for histology to pre-op registration." *Magnetic Resonance in Medicine.* Under-review. Manuscript # MRM-13-14776 [impact factor: *3.27*]

4. **Goubran, M.,** Rudko, D., Santyr, B., Gati, J., Szekeres, T., Peters, T., and Khan, A.R., "*In vivo* normative atlas of the hippocampal subfields using multi-echo susceptibility imaging at 7 Tesla." *Human Brain Mapping* 2013; 35(8):3588-3601. doi: 10.1002/hbm.22423 [impact factor: *6.88*]

5. **Goubran, M.,** Crukley, C., S., de Ribaupierre, S., Peters, T., and Khan, A.R., "Image registration of *ex-vivo* MRI to sparsely sectioned histology of hippocampal and neocortical temporal lobe specimens." *Neuroimage* 2013: 83:770–781 [impact factor: *6.25*]

6. Santyr, B., **Goubran, M.,** de Ribaupierre, S., Peters, T., and Khan, A.R., "7-Tesla investigation of T2* and quantitative susceptibility in temporal lobe epilepsy patients." Target Journal: *Epilepsia.* In-preparation.

7. Pujol, S., Wells, W., Pierpaoli, C., Bethesda, H., Brun, C., Gee, J.C., Cheng, G., Vemuri, B., Commowick, O., Wiest-Daesske, N., **Goubran, M.,** Khan, A.R., Peters, T.M., Neher, P., Fritzche, K., Shi, Y., Tristan-Vega, A., Veni, G., Whitaker, R., Styner, M., Westin, C., Gouttard, S., Norton, I., Chauvin, L., Mamata, H., Gerig, G., Nabavi, A., Golby, A., Kikinis, R., "The DTI Tractography Challenge for Neurosurgical Planning." Target Journal: *Brain.* In-preparation.

8. Cantor-Rivera, D., Khan, A.R., Lau, J., **Goubran, M.,** Mirsattari, S.M., and Peters, T.M., "Statistical feature maps: a patient-specific analysis tool with applications in Temporal Lobe Epilepsy." Target Journal: *Neuroimage.* In-preparation.

9. Rajchl, M., Stirrat, J., **Goubran, M.,** Yu, J., Scholl, D., Peters, T., and White, A.J., "Validation and comparison of multiple myocardial scar analysis techniques for 3-dimensional late-gadolinium-

enhancement magnetic resonance imaging." *Journal of Cardiovascular Magnetic Resonance.* Under-review. Manuscript # 9186303001140234 [impact factor: *4.44*]

10. Cantor-Rivera, D., Khan, A.R., **Goubran, M.,** Mirsattari, S.M., and Peters, T.M., "Detection of Temporal Lobe Epilepsy using Support Vector Machines in multi-parametric quantitative MR imaging." *Computer Medical Imaging and Graphics:* Special Issue on Machine Learning. In-Press. [impact factor: *1.66*]

11. Khan, A.R., **Goubran, M.,** de Ribaupierre, S., Hammond, R., Burneo, J., Parrent, A., and Peters, T., "Quantitative relaxometry and diffusion MRI for lateralization in MTS and non-MTS temporal lobe epilepsy." *Epilepsy Research* 2013; 108(3):506-516. doi:10.1016/j.eplepsyres.2013.12.012. [impact factor: *2.24*]

Oral Presentations

1. **Goubran, M.,** Hammond. R., de Ribaupierre, S., Peters, T.M., and Khan, A.R., "Correlation of quantitative MRI and histology of surgical specimens in drug-resistant focal epilepsy." *11th World congress of the Society of Brain Mapping and Therapeutics*, Sydney, Australia (2014)

2. **Goubran, M.,** Curie, C., S., de Ribaupierre, S., Hammond. R., Parrent, A., Burneo, J., Peters, T., and Khan, A.R., "A pipeline for histology to in-vivo registration of surgically resected specimens in focal epilepsy." *11th World congress of the Society of Brain Mapping and Therapeutics*, Sydney, Australia (2014)

3. **Goubran, M.,** Hammond. R., de Ribaupierre, S., Peters, T.M., and Khan, A.R., "Quantitative MRI and histopathology correlation of surgical specimens in intractable focal epilepsy." *Imaging Network Ontario symposium (IMNO),* Toronto, Canada (2014)

4. **Goubran, M.,** Hammond. R., de Ribaupierre, S., Peters, T.M., and Khan, A.R., "Correlating MRI and histology in neocortical specimens of temporal lobe drug-resistant epilepsy." *London Health Research Day*, London, Canada (2014)

5. **Goubran, M.,** Santyr, B., Rudko, D., Gati, J., Szekeres, T., Peters, T., and Khan, A.R., "Ultra-high-field 7T *in vivo* normative atlas of the hippocampal subfields using susceptibility weighted imaging." *International Society for Magnetic Resonance in Medicine 'ISMRM' Proceedings,* 21th Annual Meeting, Salt Lake city, Utah, U.S.A (2013)

6. **Goubran, M.,** Buchanan, S., Peters, T.M., and Khan, A.R., "Correlating MRI and digital histopathology of temporal lobe resections in intractable epilepsy." *Society of Brain Mapping and Therapeutics*, Toronto, Canada (2012)

7. **Goubran, M.,** Khan, A.R., Crukley, C., Buchanan, S., Brendan, S., deRibaupierre, S., Peters, T.M., "Robust registration of ex-vivo temporal lobe MRI to digital histopathology" *Imaging Network Ontario symposium (IMNO),* Toronto, Canada (2012)

8. **Goubran, M.,** Khan, A.R., de Ribaupierre, S., and Peters, T.M., "Automated atlas-based seeding in cortico-spinal tractography." *Proc. DTI Tractography for Neurosurgical Planning: A Grand Challenge, Medical Image Computing and Computer Assisted Interventions 'MICCAI',* Toronto, Canada (2011)

Peer- Reviewed Conference Proceedings

1. **Goubran, M.,** Hammond, R., de Ribaupierre, S., Peters, T.M., and Khan, A.R., "Correlation of quantitative MRI and histology of surgical specimens in drug-resistant focal epilepsy." *IEEE Medicine in Biology Society,* 36th Annual Meeting, Chicago, USA (2014)

2. **Goubran, M.,** Hammond, R., de Ribaupierre, S., Peters, T.M., and Khan, A.R., "Correlation of quantitative MRI and histology of surgical specimens in drug-resistant focal epilepsy." *International Society for Magnetic Resonance in Medicine* '*ISMRM' Proceedings,* 21th Annual Meeting, Milan, Italy (2014)

3. **Goubran, M.,** Currie, C., de Ribaupierre, S., Hammond, R., Burneo, J., Parrent, A., Peters, T.M., and Khan, A.R., "A pipeline for histology to in-vivo registration of surgically resected specimens in focal epilepsy." *Organization for Human Brain Mapping* '*OHBM' Proceedings,* 20th Annual Meeting, Hamburg, Germany (2014)

4. **Goubran, M.,** Santyr, B., Rudko, D., Gati, J., Szekeres, T., Peters, T., and Khan, A.R., "Ultra-high-field 7T *in vivo normative* atlas of the hippocampal subfields using susceptibility weighted imaging." *Imaging Network Ontario,* Toronto, Canada (2013)

5. **Goubran, M.,** Peters, T.M., and Khan, A.R., "Correlations between ex-vivo MRI and hippocampal sub-field neuronal density in temporal lobe epilepsy." *International Society for Magnetic Resonance in Medicine* '*ISMRM' Proceedings,* 20th Annual Meeting, Melbourne, Australia (2012)

6. **Goubran, M.,** Khan, A.R., Crukley, C., Buchanan, S., Brendan, S., de Ribaupierre, S., Peters, T.M., "Robust registration of sparsely sectioned histology to ex-vivo MRI of temporal lobe resections." *Proc. SPIE Medical Imaging,* San Diego, U.S.A (2012), Vol. 8314, 83141V. doi: 10.1117/12.911058.

7. Khan, A.R., **Goubran, M.,** Rudko, D., Gati, J., Szekeres, T., Holmes, C., and Peters, T.M., "High-resolution 3T and 7T extension of the Colin27 atlas for deep brain targeting." *Organization for Human Brain Mapping* '*OHBM' Proceedings,* 20th Annual Meeting, Hamburg, Germany (2014)

8. Khan, A.R., **Goubran, M.,** Lau, J.C., Eagleson, R, Peters, T.M., and deRibaupierre, S., "Tensor Deflection Tractography using Local Fibre-Crossing Maps for Neurosurgical Planning" Proc. DTI Tractography for Neurosurgical Planning: A Grand Challenge, Medical Image Computing and Computer Assisted Interventions 'MICCAI', Nagoya, Japan (2013) [Oral presentation]

9. Blinston, C., Hammond, R., **Goubran, M.,** Parrent, A., Burneo, J., de Ribaupierre, S., Steven, D., Peters, T., and Khan, A.R., "Quantitative analysis of neocortical architecture in refractory temporal lobe epilepsy" *American Epilepsy Society,* Washington, D.C., U.S.A (2013)

10. Khan, A.R., **Goubran, M.,** deRibaupierre, S., and Peters, T.M., "Surface and voxel-based analysis of multi-modal quantitative MRI for pre-surgical evaluation of epilepsy patients" *International Society for Magnetic Resonance in Medicine* '*ISMRM' Proceedings,* 21th Annual Meeting, Salt Lake city, Utah, U.S.A (2013)

11. Khan, A.R., **Goubran, M.,** deRibaupierre, S., and Peters, T.M., "Pre-surgical evaluation of epilepsy patients using voxel based analysis" *Imaging Network Ontario*, Toronto, Canada (2013).

12. Khan, A.R., **Goubran, M.,** Lau, J.C., Eagleson, R., Peters, T.M., and deRibaupierre, S., "Multi-fiber tractography for tumour resection with characterization of peri-tumoural tracts." *Proc. DTI Tractography for Neurosurgical Planning: A Grand Challenge, Medical Image Computing and Computer Assisted Interventions 'MICCAI',* Nice, France (2012) [Oral presentation]

13. Khan, A.R., Oqab, H., **Goubran, M.,** and Peters, T.M., "Comparison of surface and voxel-based methods of multi-modal quantitative MRI for pre-surgical evaluation of epilepsy patients". *Society of Brain Mapping and Therapeutics*, Toronto, Canada (2012) [Oral presentation]

14. Cantor, D., **Goubran, M.,** Kraguljac, A., Mirsattari, S., Bartha, R., and Peters, T., "Detection of Small Human Cerebral Cortical Lesions with MRI under Different Levels of Gaussian Smoothing: Applications in Epilepsy." *Proc. SPIE Medical Imaging,* San Diego, U.S.A (2010), Vol. 7623, 76233S. doi: 10.1117/12.845058

Other Conference Proceedings

1. **Goubran, M.,** Khan, A.R., Hammond, R., de Ribaupierre, S., and Peters, T.M., "MRI correlates of hippocampal sclerosis in refractory focal epilepsy." *Canadian League Against Epilepsy* (CLAE), London, Ontario (2014)

2. **Goubran, M.,** Hammond, R., de Ribaupierre, S., Peters, T.M., and Khan, A.R., "Quantitative MRI correlates of hippocampal pathology in refractory temporal lobe epilepsy." *Southern Ontario Neuroscience Association* (SONA), 34th Annual meeting, London, Ontario (2014)

3. **Goubran, M.,** Santyr, B., Rudko, D., Gati, J., Szekeres, T., Peters, T., and Khan, A.R., "Ultra-high-field 7T *in vivo normative* atlas of the hippocampal subfields using susceptibility weighted imaging." *London Health Research Day,* London, Canada (2013)

4. **Goubran, M.,** Peters, T., and Khan, A.R., "Correlations between ex-vivo MRI and hippocampal sub-field neuronal density in temporal lobe epilepsy." *London Health Research Day,* London, Canada (2012)

5. **Goubran, M.,** Cantor, D., and Peters, T., "Effect of different levels Gaussian Smoothing in Statistical Parametric Mapping" *London Health Research Day,* London, Canada (2010)

6. **Goubran, M.,** Cantor, D., and Peters, T., "Modelling Mesial Temporal Lobe Epilepsy(MTLE)" *London Imaging Discovery,* London, Canada (2010)

7. Buchanan, S., **Goubran, M.,** Peters, T., and Khan, A.R., "Quantitative validation of Ex-vivo to Pre-op Temporal Lobe Registration" *London Imaging Discovery,* London, Canada (2011)

MENTORSHIP

Sep 2012 - May	Honors thesis students
2013	*Susan Buchanan*
	Project: Validation of Ex-vivo to Pre-op MRI registration of temporal lobe specimens
May 2011 - Aug	Summer Students
2012	*Brendan Santyr*
	Project: Delineation of the hippocampal subfields using high resolution *in-vivo* MRI at 7T
	Susan Buchanan
	Project: Target registration error (TRE) in Ex-vivo to Pre-op MRI registration

ACADEMIC SERVICE

Scientific Reviewer

2014 – Present	Medical Image Computing and Computer Assisted Interventions (MICCAI) conference
2013 – Present	Journal of Magnetic Resonance Imaging (JMRI)
2013 – Present	International Society for Magnetic Resonance in Medicine (ISMRM) conference
2009 - 2011	Western's Undergraduate Research Journal (WURJ) Graduate reviewer and Member of the Editorial Review Board

Conferences

2011	Conference student coordinator, Medical Image Computing and Computer Assisted Interventions (MICCAI) conference (~1000 attendees)
2011	Logistics Chair of the 6th *Canadian Student Conference on Biomedical Computing and Engineering* **(CSCBCE)**

Seminar Presentations

2010 - Present	Biomedical Engineering Seminar
2010 – 2014	Computer Assisted Medical Interventions (CAMI) program Seminar

CERTIFICATES, SKILLS & INTERESTS

Certificates	Magnetic Resonance Imaging (MRI) Operator, Red Cross Emergency First Aider Biosafety training
Languages	Fluent in *English, French* and *Arabic*
Research Interests	Medical Image Processing & Analysis, Image Guided Surgery, Neurological disorders, Epilepsy, Magnetic Resonance Imaging, Diffusion Tensor Imaging,
Other Interests	Painting and photography